Tracking water molecules and carboxylate ions in confinement using advanced vibrational spectroscopy

Korotkevich, A.

Publication date
2023

Document Version
Final published version

[Link to publication](#)
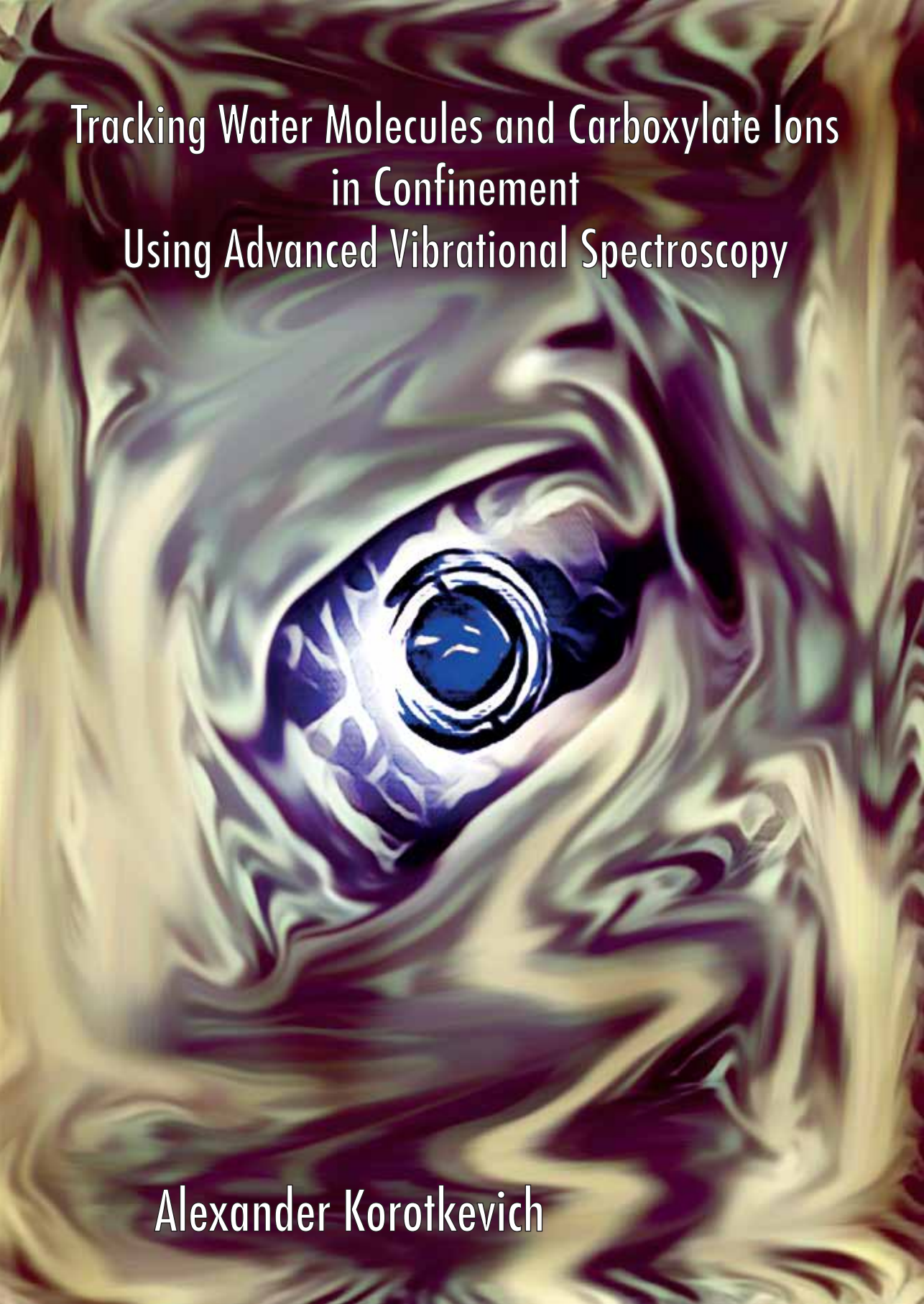
Citation for published version (APA):
Korotkevich, A. (2023). *Tracking water molecules and carboxylate ions in confinement using advanced vibrational spectroscopy*. [Thesis, fully internal, Universiteit van Amsterdam].

Tracking Water Molecules and Carboxylate Ions in Confinement
Using Advanced Vibrational Spectroscopy

Alexander Korotkevich

Tracking Water Molecules and Carboxylate Ions in Confinement Using Advanced Vibrational Spectroscopy

Alexander Korotkevich

Tracking Water Molecules and Carboxylate Ions in Confinement Using Advanced Vibrational Spectroscopy

ACADEMISCH PROEFSCHRIFT

ter verkrijging van de graad van doctor
aan de Universiteit van Amsterdam
op gezag van de Rector Magnificus
prof. dr. ir. P.P.C.C. Verbeek
ten overstaan van een door het College voor Promoties ingestelde commissie,
in het openbaar te verdedigen in de Aula der Universiteit

op vrijdag 26 mei 2023, te 14:00 uur

door

Alexander Korotkevich

geboren te Moscow

Promotiecommissie

Promotor:	prof. dr. H. J. Bakker	Universiteit van Amsterdam
Copromotor:	dr. S. Grecea	Universiteit van Amsterdam
Overige leden:	dr. E. Allarcón Lladó	Amolf
	dr. ir. A. Petrignani	Universiteit van Amsterdam
	prof. dr. W. L. Noorduin	Universiteit van Amsterdam
	prof. dr. W. J. Buma	Universiteit van Amsterdam
	prof. dr. P. G. Bolhuis	Universiteit van Amsterdam
	prof. dr. P. Vöhringer	University of Bonn
Faculteit:	Faculteit der Natuurwetenschappen, Wiskunde en Informatica	

Tracking Water Molecules and Carboxylate Ions in Confinement Using Advanced Vibrational Spectroscopy

Publications covered in this thesis:

Chapter 4: A. A. Korotkevich, H. J. Bakker *Confined Water Molecules in Binary Mixtures of Water and 2,6-Lutidine Near Lower Solution Critical Temperature*, J. Phys. Chem. B, 125, 287-296, **2021**

Chapter 5: A. A. Korotkevich, H. J. Bakker *Ultrafast vibrational dynamics of aqueous acetate and terephthalate*, J. Chem. Phys. 156 (9), 094501: 1-9, **2022**

Chapter 6: A. A. Korotkevich*, O. O. Sofronov*, O. C. M. Lugier, S. Sengupta, S. Tanase, and H. J. Bakker *Direct Probing of Vibrational Interactions in UiO-66 Polycrystalline Membranes with Femtosecond Two-Dimensional Infrared Spectroscopy*, J. Phys. Chem. Lett., 13, 9793-9800, **2022**

Chapter 7: C. J. Moll*, A. A. Korotkevich*, J. Versluis and H. J. Bakker, *Molecular orientation of small carboxylates at the water-air interface*, Phys. Chem. Chem. Phys. 24, (17), 10134-10139, **2022**

Chapter 8: A. A. Korotkevich, C. J. Moll, J. Versluis and H. J. Bakker *Molecular Orientation of Carboxylate Anions at the Water/Air Interface studied with Heterodyne-Detected Vibrational Sum-Frequency Generation*, J. Phys. Chem. B, **2023**.

*These authors contributed equally to this work.

Other collaborations:

A. Korotkevich, D. S. Firaha, A. A. H. Padua, B. Kirchner *Ab initio molecular dynamics simulations of SO_2 solvation in choline chloride/glycerol deep eutectic solvent*, Fluid Phase Equil., 448, 59-68, **2017**

E. N. Golubeva, N. A. Chumakova, S. V. Kuzin, I. A. Grigoriev, T. Kalai, A. A Korotkevich, S.E. Bogorodsky, L. I. Krotova, V. K. Popov, V. V. Lunin *Paramagnetic bioactives encapsulated in poly(D,L-lactide) microparticules: Spatial distribution and in vitro release kinetics.* J. Supercrit. Fluids, 158, 104748, **2020**

Contents

IX

x

1
Introduction

1.1 Confining environments

A chemical species can be considered as **confined** when it is localized in a small space and experiences geometrical constraints caused by the environment. Confinement takes place in various systems and plays a crucial role in material science and biochemistry. Molecular cages and containers possess nanometer-size cavities that selectively encompass guest molecules to form host-guest complexes which is a basis of supramolecular chemistry and molecular recognition. The biosynthesis of ATP molecules, playing a role of the molecular storage of chemical energy in living cells, involves electron and proton transfer processes in the sub-micron space of the mitochondria. Many chemical processes in the chemical industry rely on heterogeneous catalysis at interfaces or in nanopores and nanochannels of solid catalysts.

A key property of a confining chemical environment is that it imposes restrictions on the degrees of freedom of the enclosed compounds. This can significantly alter the chemical properties of the confined species. For example, proton hopping reactions in liquid nanodroplets are significantly slower than in the bulk of water and the rate of this process strongly depends on the size of the droplets.[1] The behaviour of molecules responsible for the formation of protein complexes and enzyme reactions differs significantly between the crowded environment of living cells and dilute solutions.[2–4] Molecular confinement in the active sites of catalysts reduces the activation energy and stabilizes the transition states of the elementary steps of chemical reactions, which enables reaction processes that are practically

impossible without catalysts.[5–7]

The great potential of confined systems stimulates the interest in the design and applications of new materials and devices involving molecular confinement. As such, it is important to identify and characterize different types of confining environments and disclose the mechanisms enabling the properties of confined systems.

1.2 Vibrational spectroscopy of confined systems

A molecular system can be thought of as a system of atoms connected by springs. Such a system has a set of **vibrations** - internal motions that do not lead to the displacement of the center of mass. The properties of molecular vibrations are primarily determined by the nature of the atoms in the system and the interactions between them. As such, by studying these vibrations we can learn about the interactions between atoms and molecules in a material of interest which is particularly important to understand the properties of confined systems.

The way to study molecular vibrations is **vibrational spectroscopy** which is based on the interactions of vibrations with electromagnetic waves, i.e. light. This field includes multiple techniques in which the frequency spectrum of light is studied after irradiation of the sample under study. Such spectra contain information about the properties of the molecular system. In **linear** spectroscopy, the material has a weak interaction with the electric field of light, leading to a response that is proportional to the amplitude of the electric field. Infrared absorption spectroscopy and Raman spectroscopy are broadly used linear spectroscopic techniques. Using these methods, we primarily investigate spectral features induced by transitions between vibrational quantum states in steady-state conditions i.e. using continuous-wave irradiation. The spectral features associated with vibrations of molecular groups are localized in quite specific frequency ranges. However, the exact position and shape often strongly depend on the inter- and intramolecular interactions involving these groups. For example, as shown in Figure 1.2, the OH-stretching vibration of liquid water has broad a absorption band centered at 3450 cm^{-1} while the non-bonded, "free" OH groups of water or metal-oxo clusters show narrow bands centered at 3600-3700 cm^{-1}.

Non-linear optical interactions can take place when a material is involved in interactions with one or more high-intensity incident fields. This can be achieved by irradiating the sample with femtosecond light pulses as these concentrate light in a very short time. Multiple non-linear spectroscopic techniques emerged in the last decades and thereby the capabilities of vibrational spectroscopy were brought to a different level. For example, with time-resolved vibrational spectroscopies such as **pump-probe** and two-dimensional infrared (**2D-IR**) spectroscopies, molecular dynamics on a picosecond time scale can be probed, and with vibrational sum-frequency generation spectroscopy (**VSFG**) surface-specific information can be
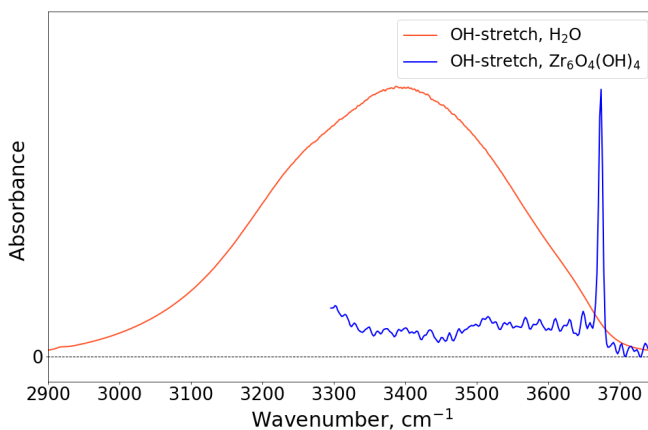
Figure 1.1. Infrared absorption spectra of the OH-stretching vibrations in liquid H_2O and $Zr_6O_4(OH)_4$ metal-oxo cluster. The absorption band in water spectrum is significantly broader and centered at lower frequency than that of the OH-groups of the metal-oxo cluster

obtained.

Vibrational spectroscopy methods provide invaluable insight into mechanisms of physical and chemical processes and have been successfully applied to investigate confined systems.[8–14]

1.3 Confined water in phase transitions

Water is essential on Earth. It acts as a universal solvent and plays a crucial role in chemical and biological processes. Water can be encountered in many natural confined environments such as nanoscale voids and pores of sedimentary rocks, and nanometer size channels of aquaporin proteins responsible for transport of water through cell membranes.[15,16]

In water molecules (H_2O), hydrogen and oxygen atoms bear strong partial positive and negative charges respectively, thus creating a polar structure. Water molecules form a dynamical network of hydrogen bonds, where the interaction is partly electrostatic and partly covalent. In pure liquid water, each water molecule can form up to four hydrogen bonds, as illustrated in Figure 1.2a

Hydrogen bonding is crucial in determining the chemical and physical properties of aqueous systems. Phase transitions in aqueous systems are important phenomena affected by hydrogen bonding. Due to the formation of strong hydrogen bonds
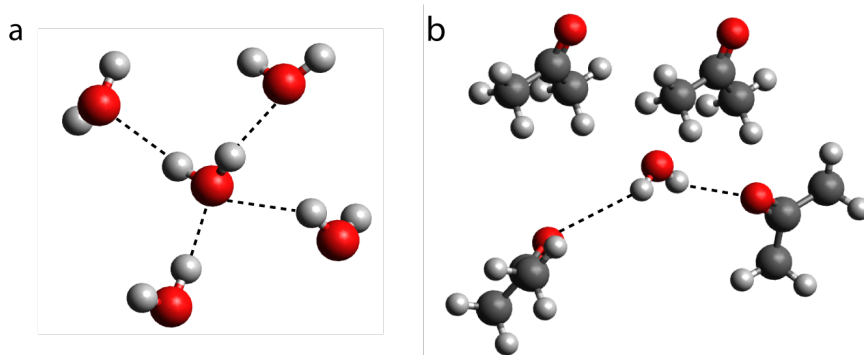
Figure 1.2. Hydrogen bonding in a. pure bulk water b. water enclosed in acetone cluster. The black, red and white spheres represent carbon, oxygen and hydrogen atoms respectively and the dashed lines represent the hydrogen bonds. Note that there are four hydrogen bonds in panel a and only two hydrogen bonds in panel b due to hydrogen bond network disruption.

water has anomalously high melting and boiling points compared to other small molecules. When water is placed in a confined environment, the hydrogen bond network gets disrupted and as a result, the phase transitions' properties are significantly altered. For example, simulations' results show that the conditions of solid-liquid phase transitions in water, filling nanoscale pores strongly depend on the pore size. Particularly, water can form stable ice phases at temperatures higher than the bulk water melting point.[17–20] Moreover, unlike in bulk water, solid and liquid phases of confined water can continuously transform into each other.[21]

In many binary mixtures of water and amphiphilic compounds, small molecular clusters enclosing water are formed as we show in Figure 1.2b. In such mixtures, orientational and hydrogen bond dynamics of water show significant retardation.[22–25] Interestingly, such mixtures often show phase separation behavior.[26–29] As such, understanding the role of confined water in phase transitions and particularly the properties of hydrogen bonding is of strong general importance. In **Chapter 4** we use polarization-resolved infrared pump-probe spectroscopy to identify confined water and study its behavior in binary mixtures with aromatic heterocyclic ampholite 2,6-lutidine that undergo phase separation at elevated temperatures.

1.4   Confined carboxylate anions

Carboxylate anion group ($-COO^-$) is one of the very abundant building blocks of organic molecules. It is often encountered in physiologically active species,
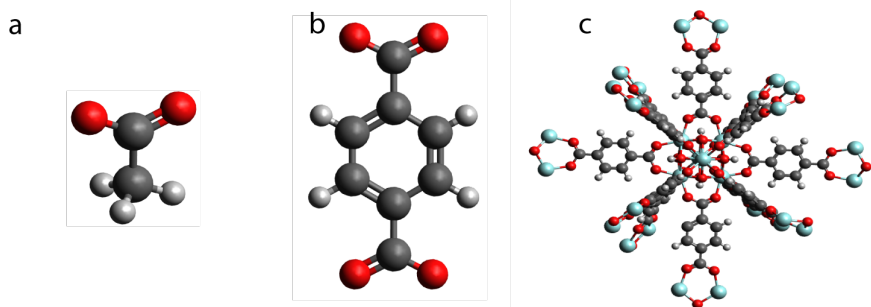
Figure 1.3. Chemical structures of a. acetate ion b. terephthalate ion c. UiO-66 fragment The white, black, red and light-blue spheres represent hydrogen, carbon, oxygen and zirconium atoms respectively.

surfactants, and (bio)polymers and plays an important role in cellular processes and functional materials.[30–35]

Recent studies include investigations of confined carboxylates showing promising properties for temperature sensing[36] and catalysis.[37] Protonation/deprotonation behavior of carboxylate groups crucial in biological processes and biotechnology are significantly affected in confinement as well.[38,39]

An important property of carboxylate ions is that they can form strong chemical bonds with metal ions which results in the formation of metal carboxylates. Furthermore, when a molecular fragment contains two or more carboxylic groups, reactions with metal cations and metal-oxo clusters often lead to the formation of the so-called coordination polymers or metal-organic frameworks (MOFs). These materials attract a lot of attention due to their potential for applications in catalysis, sensing, and separation. This is largely due to the fact that MOFs often contain well-defined nanoscale pores and channels and as a result, different molecular species can be absorbed by MOF structures becoming confined in the pores of the MOF. As such, it is important to understand the properties of the confining environment itself.

Despite the abundance and applications of species containing carboxylate anions groups, only a few time-resolved spectroscopic studies of these compounds have been performed focusing on their ultrafast vibrational and solvation dynamics.[40–43] In **Chapter 5**, we use 2D-IR spectroscopy to investigate the mechanism of vibrational coupling in abundant carboxylate ions acetate and terephthalate (1,4-benzenedicarboxylate) ions in aqueous solutions. With this we establish the framework for the analysis of more complex systems. In **Chapter 6**, we prepare polycrystalline membranes of UiO-66 metal-organic framework. This MOF consists of $Zr_6O_4(OH)_4$ metal-oxo clusters connected by terephthalate linkers as shown in Figure 1.3. We use 2D-IR to explore the properties of this confining environ-

ment by probing the vibrational and energy transfer dynamics in the terephthalate linkers that form important building blocks of the crystalline structure of UiO-66.

1.5   Molecular orientation at interfaces

Molecules and ions localized at interfaces and interfacial layers experience interactions with both adjacent media and with other interfacial species. These interactions determine the properties of various important processes that take place at phase boundaries. For instance, interfacial interactions affect the formation of atmosphere aerosol droplets[44] and the release of ions from the aerosols to the atmosphere[45]. The interfacial environment often significantly differs from both adjacent bulk phases which leads to special properties of interfacial species such as an increase of reactivity and an alteration of activation barriers of the chemical reactions.[46,47] These properties play a crucial role in the design and investigation of novel 2D materials.[48]

Chemical species adsorbed at an interface do not experience an isotropic environment. For that reason, adsorbed species often acquire a preferential orientation depending on their affinity to the components of the adjacent media. Amphiphilic species are often oriented with their charged and polar fragments toward the more polar phase while the hydrophobic fragments are pointing toward the less polar phase. Such oriented amphiphilic compounds often facilitate ion transfer between polar and non-polar phases which is crucial in organic synthesis reactions, and extraction and separation processes.[49–51] The selective orientation and binding of antifreeze proteins to the surfaces of ice crystals prevent the growth of the ice crystals,[52] which is used in cryopreservation. The orientation of DNA molecules bound to solid substrates plays an important role in the controlled patterning of cells[53] and biosensing[54,55].

As such it is clear that the determination of the molecular orientation at interfaces is of strong general importance. A perfect tool to study the orientation is
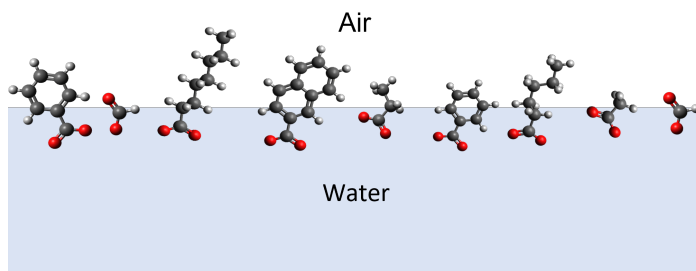
Figure 1.4. Schematic picture of carboxylates ions adsorbed at water-air interface

vibrational sum-frequency generation spectroscopy (VSFG). This method allows the detection of the vibrational response of the species localized specifically at the thin interfacial layer. The information about the molecular orientation is extracted by analyzing the second-order electric susceptibility $\chi^{(2)}$ spectra. In recent years, significant progress was made in determining the orientation of molecular species at liquid-air and solid-air interfaces using VSFG often combined with simulations.[56–63]

The molecular orientation can be determined most accurately when information related to several molecular groups is combined which is especially relevant for large molecules such as biopolymers. As pointed out in section 1.4, carboxylate anion groups (-COO$^-$) are frequently encountered in biomolecules and functional materials. In this thesis, we perform VSFG spectroscopy on carboxylate anions. In **Chapter 7** we study the adsorption of formate and acetate ions at water-air interface. In **Chapter 8** we investigate the orientation of carboxylate ions with aliphatic and aromatic substituents at the water-air interface.

2

Theory

2.1 Molecular vibrations

In this thesis, we present results of infrared spectroscopy studies of O$\cdots$D stretching vibrations of HDO molecules as well as symmetric ν_s and antisymmetric ν_{as} stretching vibrations of carboxylate anion group (R-COO$^-$). Here we present classical and quantum mechanical models to describe the properties of these molecular vibrations including their vibrational transitions.
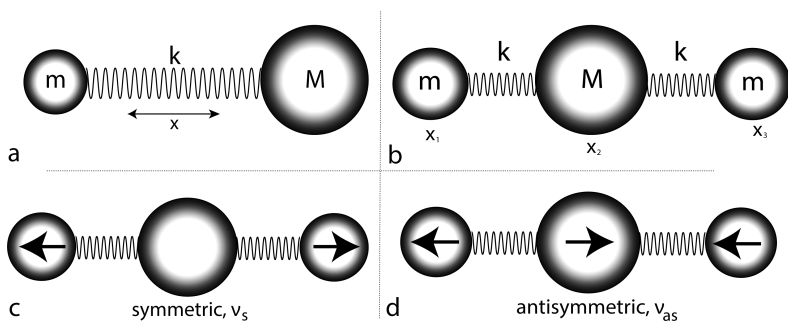
Figure 2.1. (a) Diatomic and (b) symmetric linear triatomic molecules represented as harmonic oscillators; (c,d) normal coordinates for the system (b)

2.1.1 Classical oscillators

The simplest approach to the description of molecular vibrations is considering the model of a classical harmonic oscillator for a diatomic molecule that consists of two masses m and M that are connected by a spring as shown in Figure 2.1a. When the system is displaced from equilibrium distance by amplitude x, the restoring force is proportional to the displacement $F = -kx$, where k is the spring constant (**the Hook's law**). The time-dependence of the displacement x can be found by solving the equation of motion given by Newton's second law:

$$\mu \frac{d^2 x}{dt^2} = -kx \Rightarrow x = A cos(\omega_0 t + \varphi_0) \tag{2.1}$$

The solution 2.1 represents periodical motion i.e. an oscillation the frequency of which is determined by the reduced mass $\mu = \frac{mM}{m+M}$ and the spring constant k:

$$\omega = \sqrt{\frac{k}{\mu}} \tag{2.2}$$

A slightly more complex model is obtained by connecting a third mass m to the mass M with another spring with the same spring constant k, thus representing a symmetric linear triatomic molecule, as shown in Figure 2.1b. The equation of motion for each of the masses using Hook's law is similar to the previous case:

$$m_1 \frac{d^2 x_1}{dt^2} = k(x_2 - x_1),$$
$$m_2 \frac{d^2 x_2}{dt^2} = k(x_3 - x_2) - k(x_2 - x_1), \tag{2.3}$$
$$m_1 \frac{d^2 x_3}{dt^2} = -k(x_3 - x_2)$$

The solutions of this system of coupled differential equations can be found in a form of periodic functions:[64]

$$x_1 = X_1 e^{i\omega t}, x_2 = X_2 e^{i\omega t}, x_3 = X_3 e^{i\omega t} \tag{2.4}$$

Substituting these solutions to the system of equations 2.3 yields a system of algebraic equations for frequencies ω. A linear combination of the coordinates x_1, x_2 and x_3 corresponding to the same frequency ω_i is a **normal coordinate** η_i. The solutions are:

$$\omega_1 = \sqrt{\frac{k}{m_1}}, \Rightarrow \eta_1 \propto (x_1 - x_3), x_1 = -x_3, x_2 = 0$$
$$\omega_2 = \sqrt{k(\frac{1}{m_1} + \frac{2}{m_2})} \Rightarrow \eta_2 \propto (x_1 + x_3), x_1 = x_3, x_2 = \frac{2m_1}{m_2} x_1 \tag{2.5}$$

As follows from equation 2.5, η_1 represents the displacement of masses 1 and 3 in opposite directions while mass 2 remains immobile. This motion is symmetric. η_2 represents the displacement of the masses 1 and 3 in the same direction, while sphere 2 moves in the opposite direction in such a way that the center of mass stays at the same position. This motion is antisymmetric. In Figures 2.1c and 2.1d the graphical representation of η_1 and η_2 is given. The solutions η_1 and η_2 represent ν_s and ν_{as} vibrations respectively. This model describes the case of a linear molecule, such as CO_2, however, when a nonlinear molecular fragment such as -COO^- is considered, the eigenmodes are formed by similar ν_s and ν_{as} vibrations.

Generally, for an arbitrary molecule, any pair of atoms can be considered as two masses connected with a spring. The normal coordinates are linear combinations of atomic displacements in a three-dimensional space that represent independent oscillations and any displacement of atoms can be described as a superposition of normal modes. Any non-linear molecule of N atoms has 3N-6 normal modes, while a linear molecule has 3N-5 normal modes. A more detailed description of normal modes can be found elsewhere.[65]

2.1.2 Quantum oscillators

Molecular vibrations show discrete energy levels which implies that they cannot be modeled as classical oscillators. Instead, a quantum description is required, involving a Hamiltonian with quantum operators:

$$\hat{H}_0 = \frac{\hat{p}^2}{2\mu} + \frac{1}{2}k\hat{x}^2 \tag{2.6}$$

where $\hat{p}$ and $\hat{x}$ represent the momentum and position operators.

The energy levels of the quantum-mechanical oscillator can be obtained by solving the time-independent Schrödinger equation using this Hamiltonian:

$$\hat{H}_0 \ket{\psi} = E \ket{\psi} \Rightarrow E_n = (n + \frac{1}{2})\hbar\omega_0, \tag{2.7}$$

with n an integer (positive) number. The solutions of equation 2.7 are states with an equidistant energy spacing defined by the resonance frequency ω_0 as shown in Figure 2.2. However, as shown in section 2.2.2, this result does not adequately describe the energy levels of molecular vibrations because of their anharmonic nature. The description can be improved by using anharmonic potentials instead of the harmonic potential $\hat{V}_H = \frac{1}{2}k\hat{x}^2$. A common example of such an anharmonic potential is the Morse potential:

$$\hat{V}_M = D_e(1 - e^{-\sqrt{(k_e/2D_e)}\hat{x}})^2 \tag{2.8}$$

where D_e is the depth of the potential defined with respect to the dissociation
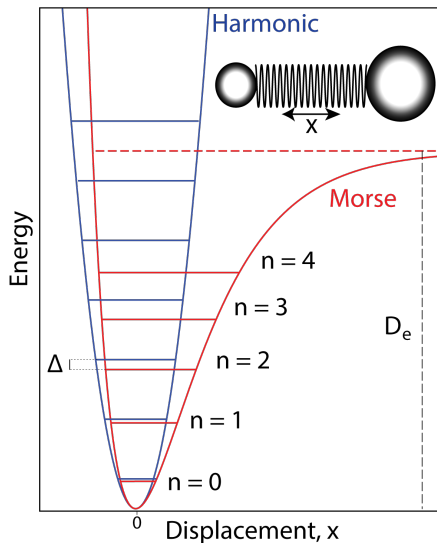
Figure 2.2. Comparison of harmonic and Morse potentials and corresponding energy levels. Note the anharmonicity (Δ) and dissociation limit (D_e) parameters

limit and k_e is the force constant. The energy levels are obtained by solving the time-independent Schrödinger equation using $\hat{V}_M$ as the potential:

$$E_n = (n + \frac{1}{2})\hbar\omega_0 - \frac{((n + \frac{1}{2})\hbar\omega_0)^2}{4D_e} \tag{2.9}$$

As follows from equation 2.9, the spacing between the energy levels of vibrational states decreases with increasing quantum number n. An important parameter that is used to characterize deviations of energy levels from the harmonic approximation is called the **anharmonicity** and is defined as:

$$\Delta = 2E_{1,H} - E_{2,A} \tag{2.10}$$

where $E_{1,H}$ is the first energy level in the harmonic approximation, while $E_{2,A}$ is the second energy level in an anharmonic approximation. The representation of the results obtained by using the Morse potential is given in Figure 2.2

Up to now, we have considered a single oscillator, while molecular systems usually form a system of oscillators as described in section 2.1.1. Molecular vibrations can be *coupled* to each other which means that when one of the coupled vibrations is driven out of equilibrium, this affects one or more of the other oscillators.

As an example, let us consider a system of two coupled oscillators. Vibrational

coupling can be described by including the coupling term to the hamiltonian:

$$\hat{H} = \hat{H}_1(\hat{x}_1) + \hat{H}_2(\hat{x}_2) + \hat{V}_c(\hat{x}_1, \hat{x}_2) \tag{2.11}$$

The simplest form of the coupling term is $\hat{V}_c(\hat{x}_1, \hat{x}_2) = k_{12}\hat{x}_1\hat{x}_2$ corresponding to *bilinear* coupling. By solving the hamiltonian, it can be shown that driving one of the coupled vibrational modes out of equilibrium changes the energy spacing of the other coupled mode. This change is primarily dependent on the anharmonicities of the coupled modes and can thus be observed only in case $\hat{H}_1$ and $\hat{H}_2$ contain anharmonic potentials.[66] This result is crucial for 2D-IR spectroscopy as shown in section 2.2.3

2.1.3 Vibrational transitions

In previous sections, we introduced a quantum mechanical model to describe molecular vibrations. Often atoms in molecules bear partial electric charges and thus strongly interact with electric fields. When a molecular system interacts with light, it can undergo transitions between vibrational states which implies that light get absorbed or amplified. To describe these transitions, let us consider that the molecule is interacting with an oscillating electric field which induces a time-dependent perturbation of the system:[67]

$$\hat{V}(t) = -\vec{\hat{\mu}} \cdot \vec{E}_0 cos(\omega t) \tag{2.12}$$

where $\vec{\hat{\mu}}$ is a dipole moment operator corresponding to the dipole moment of the molecular system. To describe the configuration of the perturbed system, the time-dependent Schrödinger equation is solved using the time-dependent molecular hamiltonian $\hat{H}(t) = \hat{H}_0 + \hat{V}(t)$.

$$\hat{H}(t)\,|\psi\rangle = i\hbar\frac{\partial\,|\psi\rangle}{\partial t} \tag{2.13}$$

Using perturbation theory to first order, the transition rate from an occupied state $|a\rangle$ to state $|b\rangle$ can be obtained (Fermi's golden rule):

$$W_{ab} = \frac{\pi}{2\hbar^2}|\langle b|\,\hat{V}\,|a\rangle|^2(\delta(\omega_{ab} - \omega) + \delta(\omega_{ab} + \omega)) \tag{2.14}$$

The transition rates W_{ab} are derived after the evaluation of amplitudes of the eigenstates of the unperturbed oscillator contributing to the perturbed wave function.[68] Equation 2.14 does not contain the time dependence initially present in the $\hat{V}(t)$ which is valid for $t \to \infty$.

As follows from equation 2.12:

$$|\langle b|\,\hat{V}\,|a\rangle|^2 = E_0^2 cos^2(\theta)|\langle b|\,\hat{\mu}\,|a\rangle|^2 \tag{2.15}$$

where θ is the angle between the vectors of electric field $\vec{E}_0$ and dipole moment $\vec{\mu}$. Assuming that the molecule stays in the same electronic state when a vibrational transition occurs, the dipole moment operator can be approximated as a function of the coordinate:

$$-\vec{\mu} \approx -\vec{\mu}_0 + \hat{x}\frac{\partial\vec{\mu}}{\partial x} \Rightarrow |\langle b| \hat{\mu} |a\rangle|^2 = (\frac{\partial\vec{\mu}}{\partial x})^2|\langle b| \hat{x} |a\rangle|^2 \tag{2.16}$$

Based on equations 2.14 - 2.16 we arrive at the selection rules for vibrational transitions:

- $W_{ab} \propto \delta(\omega_{ab} - \omega) - \delta(\omega_{ab} + \omega) \to$ the transition is possible when the field frequency is close to resonant frequency $\omega_{ab} = (E_a - E_b)/\hbar$

- $W_{ab} \propto (\frac{\partial\vec{\mu}}{\partial x})^2 \to$ the transition is possible only when atomic displacement along the vibrational coordinate leads to a change of dipole moment of the system

- $W_{ab} \propto cos^2\theta \to$ the transition is possible only when the electric field polarization direction $\vec{E}_0$ is not orthogonal to the dipole moment $\vec{\mu}$ direction

- $W_{ab} \propto |\langle b| \hat{x} |a\rangle|^2 \to$ in case the harmonic vibrational potential is used in the hamiltonian of equation 2.13 and the expansion of the dipole moment operator in equation 2.16 is limited to the linear term (dipolar approximation) the transition is only possible between the states for which $|a - b| = 1$ where a and b are the quantum number of the states.

2.2 Bulk infrared spectroscopy

Frequencies of molecular vibrations are resonant with infrared light ($\sim$ 2-10 μm), forming the basis of infrared spectroscopy. This section provides a theoretical background for steady-state and time-resolved infrared spectroscopies.

2.2.1 Absorption spectroscopy

Let us consider an infrared beam with intensity $I_0(\omega)$ passing through a layer of material with the thickness l as shown in Figure 2.3a. The intensity of light after the sample I is given by the Lambert-Beer law:

$$T(\omega) = \frac{I(\omega)}{I_0(\omega)} = e^{-\sigma(\omega)lC} \tag{2.17}$$

where $\sigma(\omega)$ is the absorption cross-section and C is the concentration of the absorbing species and $T(\omega)$ is sample transmission. The parameter $\sigma(\omega)$ is proportional to the transition rate described in section 2.1.3, thus when ω approaches
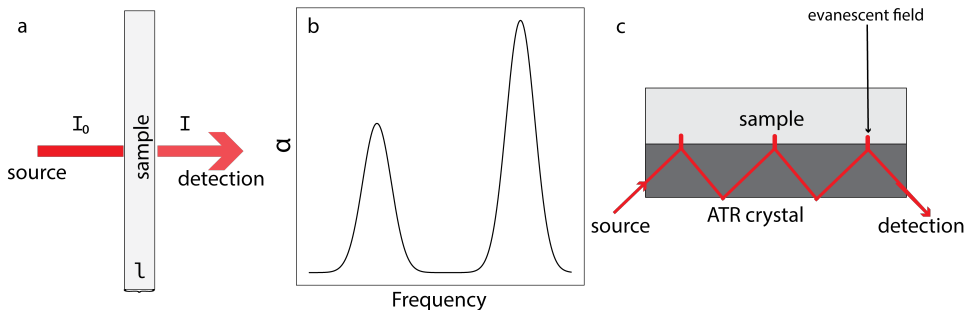
Figure 2.3. Infrared (IR) absorption experiment in a. transmission geometry b. ATR-geometry; c. Example of IR absorption spectrum containing two resonances

a resonance of a vibrational transition, attenuation of light intensity (absorption) due to vibrational transition is observed as shown in Figure 2.3b.

Taking the logarithm of equation 2.17 and accounting for multiple absorbing species the equation can be rewritten in a convenient form:

$$-ln(T) \equiv \alpha = \sum_i \sigma_i(\omega) l C_i \qquad (2.18)$$

where α is sample **absorption**, C_i is the molarity of the ith absorber, l is the sample thickness in cm and σ_i is the molar extinction coefficient given in $(L/(mol \cdot cm))$. It is clear, that when light is absorbed, α takes positive values.

The stretching vibrations of water and carboxylate anions have very high extinction coefficients. Because of that, in some cases after passing through even the thinnest layers of the materials $I(\omega)$ gets very low and cannot be reliably determined. In case the sample thickness l can no longer be reduced, it is beneficial to collect spectra in the **attenuated total reflection** (ATR) geometry. This technique is based on the phenomenon of total internal reflection which happens when light propagates from a medium with a higher refractive index n_1 to a medium with a lower refractive index n_2 at an incident angle θ which is larger than $\theta_{critical} = arcsin(\frac{n_2}{n_1})$, as follows from Snell's law. In this situation, an evanescent field is created into the medium with a low refractive index with a decay length smaller than the wavelength. As a result, the absorption spectrum is collected from a thin layer of material as shown in Figure 2.3c. A commonly used material for ATR-IR absorption measurements is diamond with a refractive index of ~ 2.4.

2.2.2 Pump-probe spectroscopy

In the previous section, we described the principles of steady-state infrared absorption spectroscopy that is based on continuous-wave irradiation of the sample.
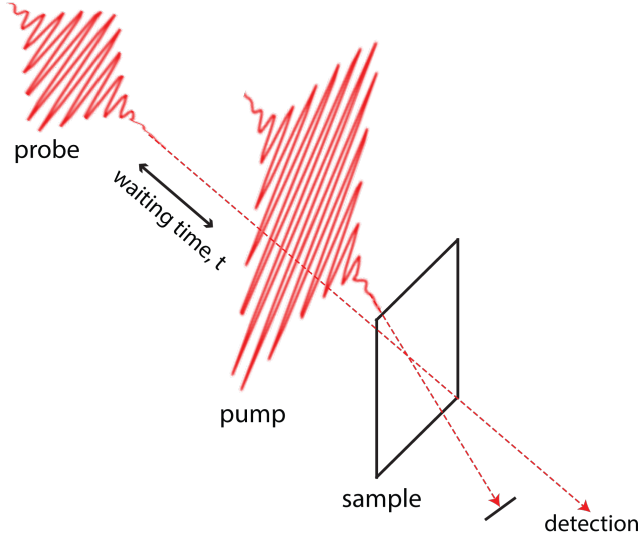
Figure 2.4. Schematic of the pump-probe experiment

Pump-probe spectroscopy, in contrast, uses femtosecond infrared pulses and thus allows obtaining information on dynamical properties.

The schematic of the experiment is shown in Figure 2.4. Firstly, an intense excitation pulse (**pump**) passes through a sample and induces vibrational excitations. After a controlled waiting time (delay time, t) (0.1 - 200 ps), a weaker detection pulse enters the sample to **probe** the evolution of the excited sub-ensemble of species. The absorption spectrum of the probe pulse is detected after excitation ($\alpha(\omega_{detection}, t)$) and compared to the absorption without excitation ($\alpha_0(\omega_{detection})$). The value $\Delta\alpha(\omega_{detection}, t)$ called **transient absorption** is used to measure the pump-induced modulation:

$$\Delta\alpha(\omega, t) = \alpha(\omega_{detection}, T) - \alpha_0(\omega_{detection}) \qquad (2.19)$$

The origin of the transient absorption spectrum is schematically represented in Figure 2.5a. The pump pulse drives the $|0\rangle \rightarrow |1\rangle$ transition at frequency ω_{01} and the sub-ensemble of species occupies the excited vibrational state $|1\rangle$. For that reason, the population of species in the vibrationally ground state decreases. This effect is called **ground state depletion**. Additionally, $|1\rangle \rightarrow |0\rangle$ transition occurs upon interaction with probe pulse at the same frequency corresponding to **stimulated emission**. Because of the ground state depletion and the stimulated emission, the sample gets more transparent around ω_{01}. Thus, $\Delta\alpha$ is negative around ω_{01}. Moreover, the excitation of $|1\rangle$ enables the $|1\rangle \rightarrow |2\rangle$ transition occur-
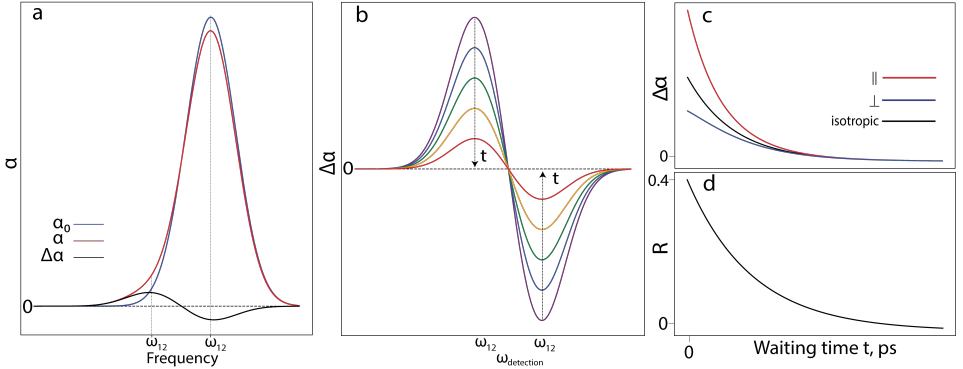
Figure 2.5. a. Origin of transient absorption $\Delta\alpha$ b. Time evolution of transient absorption spectra c. Single frequency dynamics of $\Delta\alpha_{iso}, \Delta\alpha_{||}$ and $\Delta\alpha_{perp}$ and d. Anisotropy (R)

ing at frequency ω_{12} leading to **induced absorption** of probe light around ω_{12} and hence a positive value of $\Delta\alpha$. Using N as the excited state population, and $\sigma_{01}(\omega)$, $\sigma_{12}(\omega)$ as the absorption cross-sections for the $|0\rangle \to |1\rangle$ and $|1\rangle \to |2\rangle$ transitions, respectively, $\alpha(\omega)$ can be expressed as:

$$\Delta\alpha(\omega) = -2\sigma_{01}(\omega)N + \sigma_{12}(\omega)N \qquad (2.20)$$

For a purely harmonic molecular vibration $\omega_{01} = \omega_{12}$, and $2\sigma_{01} = \sigma_{12}$, meaning that $\Delta\alpha(\omega) = 0$. For the O$\cdots$D stretching vibration of HDO molecules as well as for ν_s and ν_{as} stretching vibrations of the -COO$^-$ group, $\omega_{12} < \omega_{01}$, and $\Delta\alpha(\omega)$ shows a negative feature near ω_{01} and a positive feature near ω_{12}. It has to be noted, that due to the overlap of the negative and positive components of the transient spectrum, the positions of negative and positive peaks might not exactly match ω_{01} and ω_{12}.

With the increase of waiting time t, the excited species return to the vibrational ground state which leads to the decay of the transient signal as shown in Figure 2.5b. The dissipation of excitation energy often leads to significant heating of the excited volume. This in turn leads to a shift of the ground state absorption spectrum and results in a non-zero transient spectrum that stays constant on picosecond time scale as shown in Figure 2.6. Such spectrum is highly similar to a static **thermal difference** absorption spectrum. The magnitude of the shift is generally significantly lower than the bandwidth of the absorption bands. As a result, larger shifts due to stronger heating lead to higher amplitudes of the resulting features in the transient absorption spectrum without significantly changing its shape. In case the shift is not accompanied by a significant change of the vibrational cross-section, the resulting transient spectrum as shown in Figure 2.6a

17
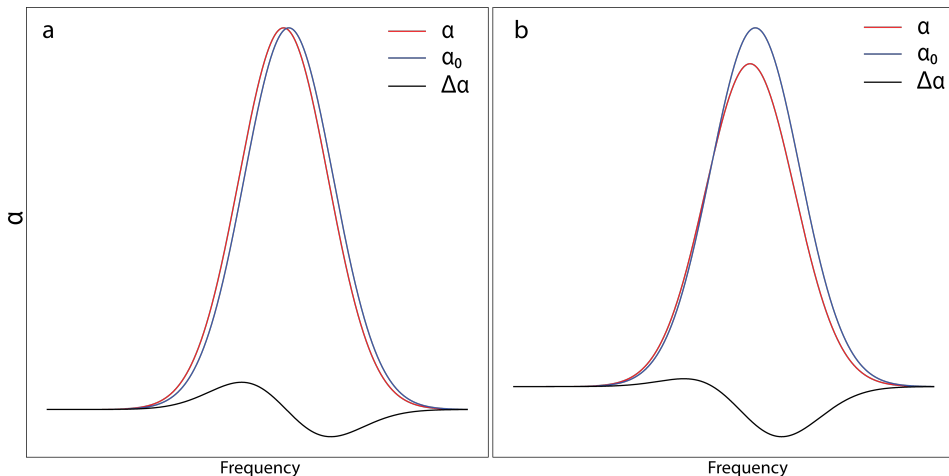
Figure 2.6. Transient absorption signals originating due to shifts of the absorption spectrum after excitation when the shift is a. not accompanied by a change of the vibrational cross-section b. accompanied by a change of the vibrational cross-section

resembles the transient absorption spectrum resulting from vibrational excitation. Transient spectra originating from vibrational excitation and the thermal effect, as well as those appearing due to vibrational coupling (section 2.2.3), have very similar shapes. Hence their origin cannot be unambiguously determined based only on the spectral features, and to find the precise origin the transient spectral information should be combined with the investigation of the vibrational dynamics. In **Chapter 6** we show how this effect is clearly pronounced for terephthalate linkers of the UiO-66 metal-organic framework. In case the thermally induced frequency shift is accompanied by a change in the vibrational cross-section, the resulting transient spectrum as shown in Figure 2.6b significantly differs from the transient spectrum following vibrational excitation. This is the case for HDO molecules reported in **Chapter 4** and in previous studies.[69,70]

As follows from section 2.1.3, the probability of vibrational transition is dependent on the mutual orientation of light polarization $\vec{E}$ and the transition dipole moment $\vec{\mu}$. Hence, when a polarized pump pulse passes through the sample, the excitation predominately takes place for the species oriented with their transition dipole moment vectors *parallel* to the polarization direction. Hence the orientational distribution of the excited species is *anisotropic*. Consequently, the time evolution of the transient absorption shown in Figure 2.5b includes both the relaxation of the excitation energy and randomization of the orientation of the excited species.

The dynamics of the two processes can be decoupled by combining transient

absorption spectra detected using two different polarizations of the probe pulse. It is common to use probe pulses polarized parallel and perpendicular with respect to excitation polarization to detect $\Delta\alpha_{||}$ and $\Delta\alpha_\perp$ respectively. At early waiting times, $\Delta\alpha_{||}$ has a higher amplitude than $\Delta\alpha_\perp$ due to the anisotropic orientational distribution of the excited molecules. By averaging the two signals, the isotropic transient absorption $\Delta\alpha_{iso}$ signal can be constructed:

$$\Delta\alpha_{iso} = \frac{1}{3}(\Delta\alpha_{||} + 2\Delta\alpha_\perp) \tag{2.21}$$

In this averaging, $\Delta\alpha_\perp$ has a larger weight as there are two non-equivalent perpendicular directions and one parallel direction with respect to excitation polarization in a three-dimensional space. $\Delta\alpha_{iso}$ does not depend on the orientational distribution of excited species and reflects properties related only to the dynamics of the excited population. Consequently, this value is convenient to use for probing vibrational dynamics.

Relaxation of the excited population to the vibrationally ground state is often a single first-order process and hence $\Delta\alpha_{iso}$, and the amplitude of the spectrum decays proportionally to $N = N_0 e^{-kt}$, where k is the vibrational relaxation rate constant and N_0 is the excited population at waiting time t = 0. In some cases, the relaxation gets frequency-dependent which can be accounted for by including additional states with different relaxation rate constants.

The energy deposited by the excitation of the sample is transferred to lower-energy vibrational states and eventually converted into thermal energy. In case the spectrum of the initially excited vibration is affected by such energy redistribution, additional contributions develop in the transient absorption spectra with the increased waiting time. A common example of such a contribution is the thermal spectrum described before. The growth of the thermal spectrum is often *delayed* with respect to the decay of the initially excited vibrations which can be accounted for in the relaxation model by including intermediate states showing no spectral response in the probed frequency region. A more detailed description of the approaches used to model the spectroscopic data is given in section 3.5.

Using $\Delta\alpha_{||}$ and $\Delta\alpha_\perp$ **anisotropy** R can be defined as a difference of $\Delta\alpha_{||}$ and $\Delta\alpha_\perp$ space normalized with respect to the isotropic absorption change $\Delta\alpha_{iso}$:

$$R = \frac{\Delta\alpha_{||} - \Delta\alpha_\perp}{\Delta\alpha_{||} + 2\Delta\alpha_\perp} = \frac{\Delta\alpha_{||} - \Delta\alpha_\perp}{3\Delta\alpha_{iso}} \tag{2.22}$$

The anisotropy depends only on the depolarization dynamics. It can be shown, that the anisotropy is proportional to the second-order orientational correlation function:[71]

$$R(t) = \frac{2}{5}\langle\frac{1}{2}(3cos^2\theta(t) - 1)\rangle \tag{2.23}$$

19

where θ is the angle between the excitation polarization and the transition dipole moment at waiting time t. At t = 0, $\theta = 0$, and R approaches a value of 0.4. At longer waiting times R decays reflecting depolarization, as shown in Figure 2.5d.

We used the decay of anisotropy to investigate the reorientation dynamics of HDO molecules. In such a case, exponential decay can be assumed.[69] However, resonant (Förster) energy transfer of the excited vibrational energy between molecules can also lead to depolarization. The Förster transfer probability is strongly dependent on the distance between the interacting dipoles and generally only plays a role in systems where the density of infrared absorbers is high. In the case of a statistical distribution of molecular vibrations with the Förster transfer rate k_F, $R(t) \propto e^{-\sqrt{k_F t}}$[72]. We observed Förster transfer between closely spaced linker ions of the UiO-66 metal-organic framework.

In this section, we presented a phenomenological description of pump-probe spectroscopy. Alternatively, this technique can be described with a density matrix formalism, considering the third-order component of the induced nonlinear polarization similar to the approach used in section 2.3.1. A detailed description of this approach can be found in the previous publication.[73]

2.2.3   Two-dimensional infrared spectroscopy (2D-IR)

2D-IR spectroscopy is a form of two-color pump-probe spectroscopy in which also the excitation frequency is varied and resolved, i.e. in this method we probe $\Delta\alpha_{||,\perp}$ $= \Delta\alpha_{||,\perp}(\omega_{excitation}, \omega_{detection}, t)$. This allows us to separate contributions that arise at a given detection frequency $\omega_{detection}$ due to the excitation of a vibrational mode at the *same* frequency $\omega_{excitation} = \omega_{detection}$ (diagonal peak signal) and due to excitation of a different vibrational mode. The signals at $\omega_{excitation} \neq \omega_{detection}$ are denoted as cross-peak signals and provide information on vibrational coupling.

The vibrational dynamics of diagonal peak signals and cross-peak signals can be characterized by studying $\Delta\alpha_{iso}$ of each of the peaks. These dynamics are dependent on the mechanism of the vibrational coupling.[74] The two main types of interaction of vibrational modes are **anharmonic coupling** and **energy transfer**. In the case of anharmonic coupling, excitation of a vibrational mode A at frequency $\omega_{excitation} = \omega_A$ leads to a perturbation of the vibrational potential of the mode B coupled to mode A. Such perturbation effectively leads to a shift in the absorption spectrum of the mode B and to a bleaching at $\omega_{excitation} = \omega_A, \omega_{detection} = \omega_B$ and an induced absorption at a slightly different (usually lower) detection frequency. Together the bleach and the induced absorption constitute the cross-peak signal. The origin of the spectrum is thus similar to that of the thermal signal described in section 2.2.2. As explained in section 2.1.2, such a shift of the absorption spectrum is only possible if the interacting vibrations are anharmonic and the magnitude of the shift is dependent on the anharmonicity of the vibration. The perturbation is present as long as mode A is excited and for that reason, the cross-peak appears
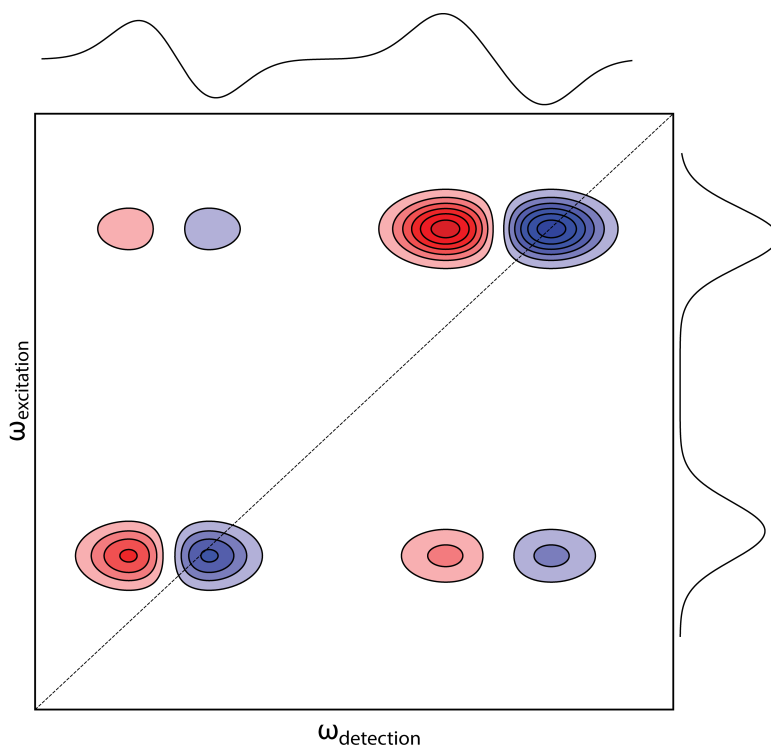
Figure 2.7. Schematic of a two-dimensional infrared spectrum of a system of two coupled vibrations. The blue and the red color correspond to negative and positive transient absorption values respectively. The dashed diagonal line corresponds to $\omega_{excitation} = \omega_{detection}$. The top inset shows the transient absorption spectrum obtained by integrating the two-dimensional spectrum along the $\omega_{excitation}$ axis. The inset on the right-hand side spectrum shows the infrared absorption spectrum
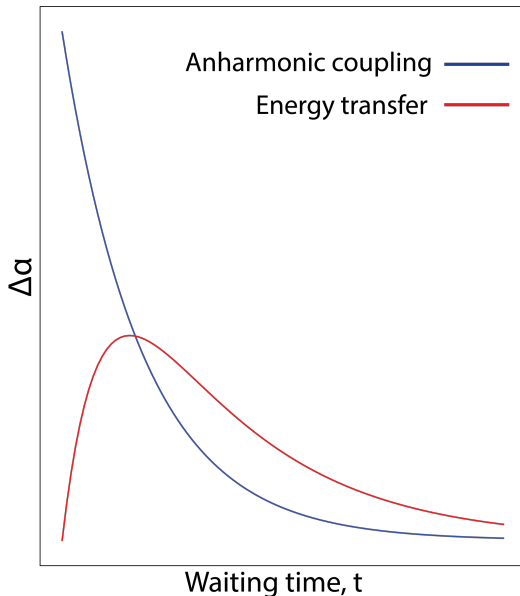
Figure 2.8. Example of dynamics of a cross-peak signal appearing due to anharmonic coupling (blue) and energy transfer (red)

instantaneously after the excitation and its dynamics follow the dynamics of mode A.

Energy transfer (or population transfer) between the modes is induced by fluctuations in the local environment leading to an equilibration of the excitation between the vibrational modes. Considering two modes A and B, the dynamics of the energy transfer can be characterized by exchange rates k_{AB} and k_{BA}. If energy transfer leads to a cross-peak signal, this signal will be *delayed* with respect to the excitation. The two mechanisms of vibrational coupling can thus be distinguished based on the dynamics of the cross-peak signals. The transfer rate (k_{AB}) and the transfer rate (k_{BA}) obey the Boltzmann ratio:

$$k_{AB} = k_{BA}e^{\frac{-\hbar \Delta \omega}{kT}} \tag{2.24}$$

where $\Delta \omega = \omega_B - \omega_A$, k is the Boltzmann constant and T is the temperature. As follows from equation 2.24, the downhill transfer is faster than the uphill transfer. In chapter 5, we present a 2D-IR study of vibrational coupling between the vibrational modes of acetate and terephthalate anions.

Similarly to $\Delta \alpha_{iso}$, the anisotropy (R) can also be probed separately for diagonal peak and cross-peak signals. In the case of a diagonal peak signal, the angle θ between the polarization direction of the excitation pulse and the transition dipole

moment vector is close to $0°$. However, for the cross-peak signal θ is dependent on the angle between the transition dipole moment vectors of the coupled modes. This later angle can thus be determined based on the anisotropy value of the cross-peak signal at t $\approx$ 0 using equation 2.23

2.3 Vibrational sum-frequency generation spectroscopy

2.3.1 Origin of sum-frequency generation

Sum-frequency generation (SFG) is a second-order nonlinear optical process in which the interaction of two electric fields oscillating with frequencies ω_1 and ω_2 leads to the generation of a new electric field oscillating with frequency $\omega_1 + \omega_2$. To understand the origin of this process, as well as other second-order non-linear processes, we need to expand the induced polarization in the applied electric field.

When an electric field interacts with a material, the displacement of charges occurs yielding in an induced material polarization $\vec{P}$ that can be expressed as power series in terms of interacting electric fields $\vec{E}$:[75]

$$\vec{P} = \sum_n \vec{P}^{(n)} = \epsilon_0 \sum_n \chi^{(n)} \vec{E}^n \tag{2.25}$$

where ϵ_0 is the vacuum permittivity. In this expansion, $\vec{P}^{(n)} = \epsilon_0 \chi^{(n)} \vec{E}^n$ is the nth order polarization. In the expression on the right-hand side, the nth order electric susceptibility tensor $\chi^{(n)}$ with rank $n+1$ transforms n interacting electric fields into a three-dimensional vector $\vec{P}^{(n)}$. The magnitude of the components of susceptibility tensors significantly decreases with increasing order n, and thus to induce higher order polarization components higher amplitudes of the electric fields are required.

$\vec{P}$ is the induced dipole oscillating at different frequencies which can act as a source of new electromagnetic waves. The propagation of the emitted wave in three-dimensional space $\vec{r}$ in non-magnetic media without free charges is described by the wave equation:

$$\nabla^2 \vec{E}(\vec{r}, t) = \frac{1}{c^2} \frac{\partial^2}{\partial t^2} (\vec{E}(\vec{r}, t) + \frac{1}{\epsilon_0} \vec{P}(\vec{r}, t)) \tag{2.26}$$

Solving the equation yields a relation between frequency components $E(\omega)$ and $P(\omega)$

$$k^2 E(\omega) = \frac{\omega^2}{c^2} (E(\omega) + \frac{1}{\epsilon_0} P(\omega)) \tag{2.27}$$

where k^2 and ω^2 are the squares of the magnitude of the wavevector and the angular frequency respectively.

Let us consider the case of two monochromatic electromagnetic waves oscillating with frequencies ω_1 and ω_2

$$\vec{E} = \vec{E}_1(\vec{r_1})cos(\omega_1 t) + \vec{E}_2(\vec{r_2})cos(\omega_2 t) \tag{2.28}$$

Describing the second-order processes requires considering the second-order polarization $\vec{P}^{(2)}$ induced by the interaction of the fields:

$$
\begin{aligned}
\vec{P}^{(2)}(\vec{r}, t) &= \epsilon_0 \chi^{(2)} \vec{E}_1(\vec{r_1}, t) \vec{E}_2(\vec{r_2}, t) = \\
&= \frac{1}{2}\epsilon_0 \chi^{(2)}(\vec{E}_1^2(\vec{r_1}) + \vec{E}_2^2(\vec{r_2}) + \vec{E}_1^2(\vec{r_1})cos(2\omega_1 t) + \\
&+ \vec{E}_2^2(\vec{r_2})cos(2\omega_2 t) + \vec{E}_1(\vec{r_1})\vec{E}_2(\vec{r_2})(cos((\omega_1 + \omega_2)t) \\
&+ cos((\omega_1 - \omega_2)t)))
\end{aligned}
\tag{2.29}
$$

In equation 2.29 we considered the polarization response of the electric fields to be instantaneous and used the angle sum trigonometric identity $cos(\alpha \pm \beta) = cos\alpha \cdot cos\beta \mp sin\alpha \cdot sin\beta$. Inserting the expression for $\vec{P}(\vec{r}, t)$ from equation 2.29 to equation 2.26 leads to the creation of electric fields with frequencies different from ω_1 and ω_2. Firstly, the process called **optical rectification** (OR) leads to the creation of a static field proportional to $\vec{E}_1^2$ and $\vec{E}_2^2$. Next, the process called a **second-harmonic generation** (SHG) yields fields oscillating with frequencies $2\omega_1$ and $2\omega_2$. Finally, sum-frequency generation and **difference-frequency generation** (DFG) lead to the creation of fields oscillating with frequencies (ω_1 + ω_2) and (ω_1 - ω_2), respectively.

In this thesis, we present the results of vibrational sum-frequency generation spectroscopy measurements (**VSFG**). In this method, a pulse centered at $\sim$ 800 nm (ω_{vis}) interacts with an infrared pulse (ω_{IR}) to generate a sum-frequency pulse ($\omega_{SFG} = \omega_{vis} + \omega_{IR}$). When ω_{IR} approaches the resonant frequencies of vibrational transitions, the SFG process will be enhanced.

For VSFG, the second-order polarization component can be expressed as:

$$\vec{P}^{(2)}(\omega_{SFG}) = \epsilon_0 \chi^{(2)}(\omega_{SFG})\vec{E}(\omega_{vis})\vec{E}(\omega_{IR}) \tag{2.30}$$

It has to be noted that equation 2.30 is valid under the assumption that the induced dipole acts as the only source of sum-frequency generation which implies that gradients of electric fields near the interfacial layers do not significantly affect $\vec{P}$. A more accurate treatment requires including higher order terms such as magnetic dipole and electric quadrupole terms in the expression for $\vec{P}$.[76]
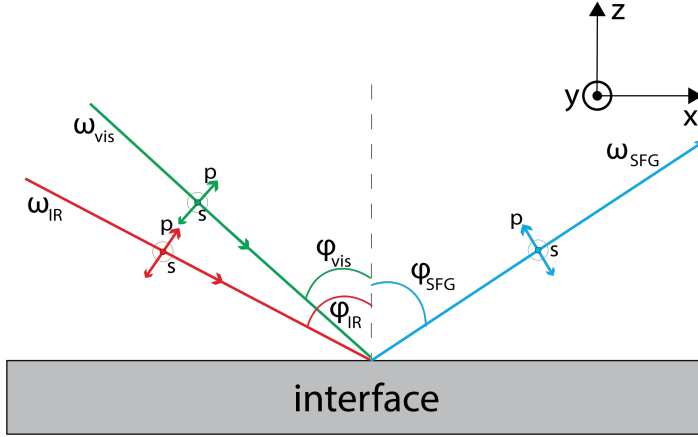
Figure 2.9. Geometry of the VSFG experiment. The directions of the y-axis and s-polarization are orthogonal to the page plane

2.3.2 Symmetry of the system and $\chi^{(2)}$

In section 2.3.1, we showed how non-linear interactions of the applied electric fields with a medium can lead to sum-frequency generation. The properties of this process are strongly dependent on the electric susceptibility tensor $\chi^{(2)}$ entering equation 2.30. In this section, we focus on properties caused by the system symmetry and geometry of the experiment. It can be showed that $\chi^{(2)} = 0$ for centrosymmetric media. That means that the inversion symmetry has to be broken to allow for sum-frequency generation.[77] This requirement is realized at interfaces of materials, thus making it possible to generate sum-frequency light exclusively from the interfacial layers. This property underlies the surface specificity of SFG-spectroscopy. However, SFG is also possible in the bulk of crystals lacking inversion symmetry. One of such crystals is α-quartz which has a trigonal crystal system. We used this crystal for reference measurements in SFG (see section 3.6).

As follows from section 2.3.1 $\chi^{(2)}$ is a third-rank tensor and thus contains 27 elements each which can be denoted as $\chi^{(2)}_{ijk}$ where i corresponds to the direction of $\vec{E}(\omega_{SF})$, j - $\vec{E}(\omega_{vis})$, k - $\vec{E}(\omega_{IR})$. To further elaborate on the properties of $\chi^{(2)}$, it is necessary to consider the geometry of the experiment that we show in Figure 2.9. The surface of a liquid sample possesses a C_∞ symmetry axis parallel to the z-axis of the laboratory coordinate system as well as a mirror symmetry plane that coincides with the XY plane. Given this, it can be shown that $\chi^{(2)}$ tensor can contain only 4 independent non-zero elements:[77]

$$\chi^{(2)}_{zzz}, \chi^{(2)}_{zxx}(= \chi^{(2)}_{zyy}), \chi^{(2)}_{xzx}(= \chi^{(2)}_{yzy}), \chi^{(2)}_{xxz}(= \chi^{(2)}_{yyz}) \tag{2.31}$$
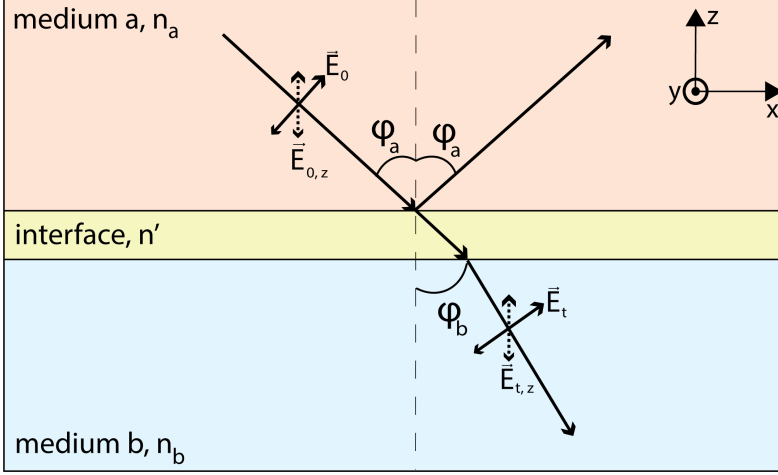
Figure 2.10. Reflection and transmission within the framework of the three-layer model. P-polarization of light as well z-component of the electric field vector are given as an example

By selecting S or P polarized $\vec{E}(\omega_{vis})$ and $\vec{E}(\omega_{IR})$ prior to the sample as defined in Figure 2.9 as well as selectively detecting S or P polarized components of SFG light, it is possible to experimentally determine $\chi^{(2)}$ components and this way probe each of the non-zero $\chi^{(2)}_{ijk}$:

$$\chi^{(2)}_{SSP} \quad \propto \quad \chi^{(2)}_{xxz}, \tag{2.32}$$

$$\chi^{(2)}_{SPS} \quad \propto \quad \chi^{(2)}_{xzx}, \tag{2.33}$$

$$\chi^{(2)}_{PSS} \quad \propto \quad \chi^{(2)}_{zxx}, \tag{2.34}$$

$$\chi^{(2)}_{PPP} \quad \propto \quad \chi^{(2)}_{xxz}, \chi^{(2)}_{xzx}, \chi^{(2)}_{zxx}, \chi^{(2)}_{zzz} \tag{2.35}$$

The order of the P and S in parentheses after $\chi^{(2)}$ corresponds to a decrease in frequency, e.g. $\chi^{(2)}_{SSP}$ means S-polarized ω_{SFG}, S-polarized ω_{vis}, and P-polarized ω_{IR}. As can be noticed, S-polarized light allows the probing of $\chi^{(2)}$ components in the XY-plane, while the P-polarized field probes the Z-component.

2.3.3 Fresnel coefficients

The amplitude of $\vec{E}(\omega_{SFG})$ depends on the amplitudes of the electric fields penetrating the interfacial layer. Since polarized light is commonly used in experiments, it is convenient to use Fresnel coefficients (L_{ii}) that express the ratio between the

amplitudes of ith components of the incident and transmitted fields, $i = x, y, z$. A model accurately describing transmission at phase boundaries is a three-layer model that explicitly includes the interfacial layer with a refractive index n' between media a and b, as shown in Figure 2.10. When incident beams enter a boundary between two media a and b with refractive indices n_a and n_b with incident angle φ_a and transmitted angle φ_b the Fresnel coefficients are given by:[76]

$$L_{xx} = \frac{E_{t,x}}{E_{0,x}} = \frac{2n_a cos\varphi_b}{n_b cos\varphi_a + n_a cos\varphi_b}, \tag{2.36}$$

$$L_{yy} = \frac{E_{t,y}}{E_{0,y}} = \frac{2n_a cos\varphi_a}{n_a cos\varphi_a + n_b cos\varphi_b}, \tag{2.37}$$

$$L_{zz} = \frac{E_{t,z}}{E_{0,z}} = (\frac{n_a}{n'})^2 \frac{2n_b cos\varphi_a}{n_b cos\varphi_a + n_a cos\varphi_b} \tag{2.38}$$

While the bulk refractive indices are commonly well-defined and can be independently determined, this is not the case for the interfacial refractive index n'. An accurate estimation of n' of liquid/air interfaces has been obtained by using the modified Lorentz model[56], which yields:

$$(\frac{1}{n'})^2 = \frac{4n_b^2 + 2}{n_b^2(n_b^2 + 5)} \tag{2.39}$$

When frequencies of the incoming fields do not match any resonances of a molecular system, the Fresnel coefficients show almost no dependence on frequency and in practice can be considered constant. However, when a resonance is approached, the dispersion of the refractive index might modulate the transmitted component of the field and thus alter the SFG amplitudes. Particularly, such behavior can be observed when ω_{IR} is in the vicinity of a vibrational resonance. This effect can be explicitly accounted for in calculations of the Fresnel coefficients by using a complex refractive index for infrared light assuming the Lorentzian shape of the resonance:

$$\tilde{n}(\omega) = n_{NR} + n(\omega) + ik(\omega) \tag{2.40}$$

$$n(\omega) \propto -\frac{(\omega - \omega_0)}{(\omega - \omega_0)^2 + \zeta}, k(\omega) \propto \frac{\sqrt{\zeta}}{(\omega - \omega_0)^2 + \zeta} \tag{2.41}$$

where ω_0 and ζ represent the resonant frequency and damping constant respectively.[78] In practice, the amplitude of the imaginary part k can be determined from infrared absorption spectra and the real part can be obtained using the Kramers-Kronig transformation.[75]

2.3.4 Molecular origin of resonant $\chi^{(2)}$

Similarly to the expansion of polarization for bulk material in equation 2.25, the expansion of an induced dipole for a single molecule can be written:

$$\vec{\mu} = \vec{\mu_0} + \alpha\vec{E} + \beta\vec{E}^2 + \gamma\vec{E}^3... \tag{2.42}$$

where α is molecular polarizability, β and γ are the first- and second-order molecular hyperpolarizabilities respectively.

The molecular property corresponding to the second-order component of the induced dipole is the **first-order hyperpolarizability** β. Near a vibrational resonance, it can be expressed as a sum of resonant and non-resonant contributions:[79]

$$\beta = \beta_{NR} + \sum_n \frac{\beta_n}{\omega_n - \omega_{IR} - i\gamma_n} \tag{2.43}$$

where β_n, ω_n, ω_{IR}, and γ_n are the nth resonance amplitude, the resonant frequency of a vibrational transition, the frequency of the infrared pulse and the damping constant of a vibration respectively. Similarly to $\chi^{(2)}$, β is a third-rank tensor containing 27 elements $\beta_{i'j'k'}$.

The amplitude of the resonant part of a hyperpolarizability component can be described as a product of transition dipole moment $\frac{\partial\mu_{k'}}{\partial x_n}$ also appearing in equation 2.16 and Raman transition moment $\frac{\partial\alpha_{i'j'}}{\partial x_n}$ of the nth vibrational mode x_n:

$$\beta_{n,i',j',k'} = -\frac{1}{2\epsilon_0\omega_n}\frac{\partial\alpha_{i'j'}}{\partial x_n}\frac{\partial\mu_{k'}}{\partial x_n} \tag{2.44}$$

$\chi^{(2)}$ can be obtained by averaging the molecular hyperpolarizabilities $\beta_{i'j'k'}$ accounting for the molecular orientation distribution:

$$\chi^{(2)}_{ijk} = \frac{N_s}{\epsilon_0}\sum_{i'j'k'} < R(\psi)R(\theta)R(\phi) > \beta_{i'j'k'} \tag{2.45}$$

where N_s is the surface population and $R(\psi)$, $R(\theta)$, $R(\phi)$ represent rotation matrices for Euler transformation from molecular to laboratory coordinate system.[80]

From equations 2.43 and 2.45 it is clear that $\chi^{(2)}$ can also be split into resonant and non-resonant components:

$$\chi^{(2)}(\omega) = \chi^{(2)}_{NR} + \chi^{(2)}_R(\omega) = A_{NR} + \sum_n \frac{A_{R,n}}{\omega_n - \omega_{IR} - i\Gamma_n} \tag{2.46}$$

From equation 2.46 it follows that when ω_{IR} approaches the resonant frequency of a vibrational mode centered at ω_n, $\chi^{(2)}$ shows a resonance with amplitude $A_{R,n}$ with the line width Γ. The real part of this expression ($\text{Re}\chi^{(2)}$) has a dispersive shape, while the imaginary part ($\text{Im}\chi^{(2)}$) is symmetric around the resonant
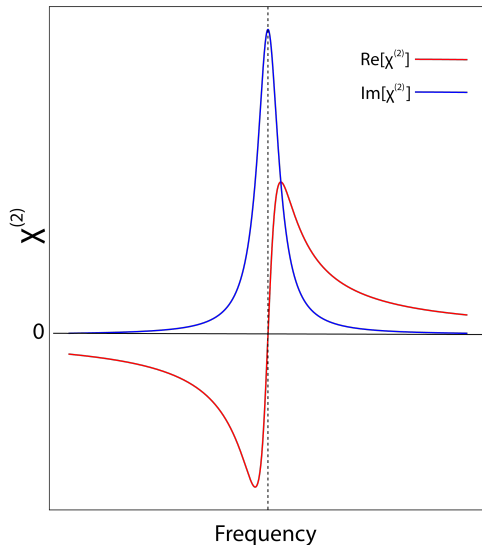
Figure 2.11. Real and imaginary parts of a resonant $\chi^{(2)}$ component in the vicinity of a vibrational resonance

frequency as shown in Figure 2.11.

As follows from equation 2.44, the $\beta_{n,i',j',k'}$ component is non-zero in case the nth vibrational mode is infrared and Raman active. Moreover, as follows from equation 2.45, $\chi^{(2)}$ is dependent on the surface density and on the angular distribution of the molecular vibrations. Thus, in order to generate sum-frequency light the following conditions are necessary to be fulfilled:

- the species are present at the surface

- the probed vibrational modes are infrared and Raman active

- the probed vibrational modes have a preferred orientation .

2.3.5 VSFG spectroscopy on carboxylate anions

In this thesis, we present the results of VSFG studies on ν_{as} and ν_s vibrational modes of the carboxylate anion group.

To study the surface adsorption and orientational properties of these ions, we performed measurements under SSP and SPS polarization experimental combinations. The experimentally determined $\chi^{(2)}$ components are related to $\chi_{xxz}^{(2)}$ and $\chi_{xzx}^{(2)}$ components in the laboratory coordinate system as follows:
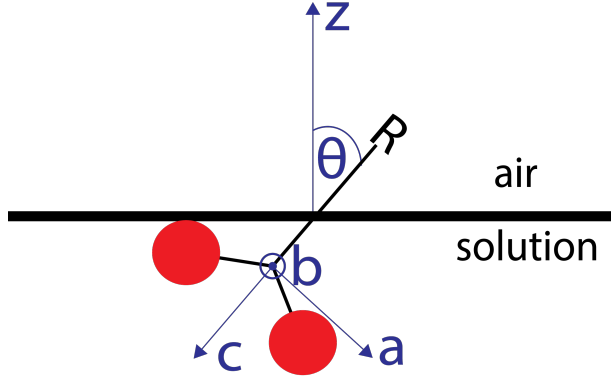
Figure 2.12. Definition of tilt angle θ for carboxylate anion group; z-axis corresponds to the laboratory coordinate system while a,b,c-axes represent molecular coordinate system where c-axis coincides with the C_2 axis of the -COO$^-$ group

$$\chi^{(2)}_{SSP} = L_{yy}(\omega_{SFG})L_{yy}(\omega_{vis})L_{zz}(\omega_{IR})sin\varphi_{IR}\chi^{(2)}_{xxz} \tag{2.47}$$

$$\chi^{(2)}_{SPS} = L_{yy}(\omega_{SFG})L_{zz}(\omega_{vis})L_{yy}(\omega_{IR})sin\varphi_{vis}\chi^{(2)}_{xzx} \tag{2.48}$$

where $\varphi_{IR,vis}$ correspond to the incidence angles of the infrared and 800 nm beams respectively.

Carboxylate anion group -COO$^-$ has C_{2v} symmetry, and the C_2 symmetry axis coincides with the molecular c-axis as displayed in Figure 2.12. Thus the averaging over the angular distribution according to equation 2.45 connects the selected $\chi^{(2)}$ components in the laboratory coordinate system to molecular hyperpolarizability components and angular distribution of the -COO$^-$ group:[79]

$$\chi^{(2)}_{xxz}, \nu_{as} = -\frac{1}{2}N_s\beta_{aca}(\langle cos\theta \rangle - \langle cos^3\theta \rangle) \tag{2.49}$$

$$\chi^{(2)}_{xzx}, \nu_{as} = \frac{1}{2}N_s\beta_{aca}\langle cos^3\theta \rangle \tag{2.50}$$

$$\chi^{(2)}_{xxz}, \nu_s = \frac{1}{4}N_s(\beta_{aac}+\beta_{bbc}+2\beta_{ccc})\langle cos\theta \rangle + \frac{1}{4}N_s(\beta_{aac}+\beta_{bbc}-2\beta_{ccc})\langle cos^3\theta \rangle \tag{2.51}$$

$$\chi^{(2)}_{xzx}, \nu_s = -\frac{1}{4}N_s(\beta_{aac} + \beta_{bbc} - 2\beta_{ccc})(\langle cos\theta \rangle - \langle cos^3\theta \rangle) \tag{2.52}$$

These expressions are obtained under the assumption of free rotation of the -COO⁻ group around the C-C (C-H) bond and contain only the tilt angle θ defined in Figure 2.12. In case the rotation is not free, $\chi^{(2)}$ acquires a dependence on the twist angle ψ.

By dividing equation 2.47 by equation 2.48 and using equations 2.49, 2.50, the experimentally determined $\chi^{(2)}$ can be expressed in terms of the orientational distribution of the ions, namely tilt angle θ, and the known properties of the experiment:

$$\frac{\chi^{(2)}_{SSP}}{\chi^{(2)}_{SPS}} = -L\frac{sin\varphi_{IR}}{sin\varphi_{vis}}\frac{\langle cos\theta\rangle - \langle cos^3\theta\rangle}{\langle cos^3\theta\rangle} \tag{2.53}$$

where L = $(L_{yy}(\omega_{vis})L_{zz}(\omega_{IR})/(L_{zz}(\omega_{vis})L_{yy}(\omega_{IR}))$ As follows from equations 2.49 - 2.52, to obtain information about the orientational properties, the angular terms $f(\theta) = \langle cos\theta\rangle$, $\langle cos^3\theta\rangle$ require integration over the orientation distribution function $F(\theta, \vec{a})$ that is unknown a priori:

$$\langle f(\theta)\rangle = \frac{\int_0^\pi d\theta f(\theta)F(\theta,\vec{a})sin\theta}{\int_0^\pi d\theta F(\theta,\vec{a})sin\theta} \tag{2.54}$$

where $\vec{a}$ is the set of the parameters defining the distribution function and the denominator is used for normalization with respect to the area of the distribution function.

The simplest assumption for the distribution function is a δ-distribution: $F(\theta) = \delta(\theta)$. In such case, the integration yields in $\langle f(\theta)\rangle = f(\theta)$.

A more complex assumption is a Gaussian distribution defined as:

$$F(\theta, \theta_c, c) = exp(-\frac{(\theta - \theta_c)^2}{2c^2}) \tag{2.55}$$

where θ_c is the expected value of the tilt angle and c determines the width of the distribution and is related to the full width at half maximum of the distribution (FWHM) as:

$$FWHM = 2\sqrt{2ln2}c \tag{2.56}$$

As the integration is performed from 0 to 180 degrees, the Gaussian distribution is truncated at 0 as discussed in Chapter 8. Further, we use the term FWHM only to refer to the full width at half maximum of the symmetric and not truncated Gaussian that is defined prior to integration over the distribution.

Generally, an arbitrary distribution function can be defined, and by integrating over this distribution according to equation 2.54 the dependence of the angular terms on the parameters $\vec{a}$ can be investigated.

3

Experiments

In this chapter, we describe the experimental setups used for the spectroscopic measurements reported in this thesis: FTIR, pump-probe, 2D-IR, and VSFG - as well as approaches used for processing and analysis of the spectroscopic data.

3.1 Infrared absorption spectroscopy

The linear infrared absorption spectra were recorded with a commercial Bruker Vertex 80v Fourier-transform infrared spectrometer with a resolution of 2 cm^{-1}. To record spectra of liquid samples described in **Chapters 4, 5, 7, 8** and solid MOF-membranes described in **Chapter 6**, we used the supplied transmission geometry accessory. The samples containing liquid hydrophilic mixtures were prepared by squeezing a droplet of the material between two circular CaF$_2$ windows (Crystran) separated by a 10-200 μm thick PTFE spacer. For less hydrophilic mixtures such as water/2,6-lutidine mixtures with high lutidine fractions described in **Chapter 4**, squeezing is complicated due to the high wettability of CaF$_2$ by hydrophobic samples. Therefore, for these samples we used drilled CaF$_2$ windows (Crystran) and injected the mixtures through the holes in the windows. An empty cell containing two CaF$_2$ windows identical to the ones used for the samples were used for background measurements. The spectra were recorded after purging the sample chamber with nitrogen gas to remove water vapors and CO$_2$ to circumvent contributions of absorption of these gases to the spectra.

Solid MOF membranes deposited on sapphire substrates were measured as is and the bare substrate was used for background measurements. The spectra were

recorded under reduced pressure ($\sim$ 5 hPa) to avoid absorption of water from the air. To record spectra of powders described in **Chapter 6**, we used the supplied Pt/diamond ATR accessory. The spectra were recorded under reduced pressure and the spectrum of empty sample chamber was used for background measurements.

3.2 Generation of femtosecond infrared pulses

In all the experimental setups used in the studies presented in this thesis, we used laser systems based on a Ti:sapphire regenerative amplifier (Coherent) seeded by the output of a mode-locked Ti:sapphire oscillator (Coherent Mantis). The systems produce $\sim$ 35 fs 800 nm pulses with a pulse energy of $\sim$ 3-6 mJ at a repetition rate of 1 kHz.

To generate femtosecond infrared pulses, we used home-built and commercial (Light Conversion) optical parametric amplifiers (OPAs), pumped by the 800 nm output ($\omega_p = 12500$ cm^{-1}) of the laser system. We used the same system to pump one or two OPAs. A small fraction of the pump ($\sim$ 1%) is sent to a sapphire plate to generate a white light continuum used as a seed for the optical parametric amplification process. After that, the seed and another fraction of the ω_p beam are collinearly overlapped in space and time in a birefringent crystal β-barium borate (BBO). In this process, light around a frequency ω_s (signal beam) of the broadband seed is amplified, and an additional frequency ω_i (idler beam) is generated so that $\omega_i = \omega_p - \omega_s$. The exact values of ω_s and ω_i are determined by the **phase matching condition**:

$$n_i\omega_i = n_p\omega_p - n_s\omega_s \tag{3.1}$$

By selecting the polarization of light before the crystal and adjusting the angle of the crystal, we tune the refractive index n experienced by ω_p and ω_i light between the ordinary index (n_o) and extraordinary index (n_e) and this way select the
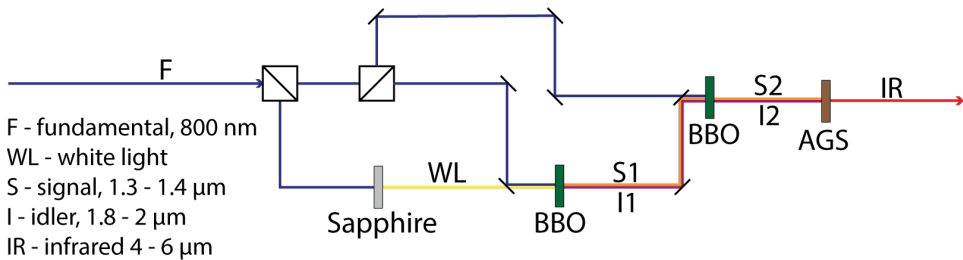

Figure 3.1. Generation of infrared pulses in the two-step optical parametric amplification and difference frequency generation processes

amplified ω_s (7000-7500 cm^{-1}) and ω_i (5000-5600 cm^{-1}). The created ω_s is used as a seed to repeat the amplification steps one or two times to obtain high-energy ω_s and ω_i pulses (150-700 μJ).

The obtained ω_s and ω_i beams are collinearly overlapped in space and time in another birefringent crystal silver gallium sulfide (AGS) to obtain the infrared beam in a difference frequency generation (DFG) process $\omega_{IR} = \omega_s - \omega_i$. In this case, by adjusting the angle of the crystal we tune the refractive index of the ω_s and ω_{IR} light to fulfill the phase-matching condition. The signal and idler beams are subsequently filtered out using a germanium filter. With this procedure, we generated the ω_{IR} (1350-2500 cm^{-1}) pulses with a power of $\sim$3-25 μJ.

3.3 Pump-probe setup

In Figure 3.2 we show a schematic picture of the two-color pump-probe setup. In the pump-probe experiments described in **Chapter 4** we generated infrared pulses in two home-built OPAs pumped using the output of the laser system split 70/30 in power. The two OPAs generate the excitation and detection pulses, respectively. In the detection path, we used a two-step parametric amplification process combined with a DFG stage to generate infrared pulses centered at 2500 cm^{-1} (4 μm) with a pulse energy of $\sim$ 3.5 μJ. The frequency of the infrared pulses corresponds to the center frequency of the OD-stretching vibration of HDO molecules. In the excitation path, we used a three-step parametric amplification process combined with a DFG stage to generate infrared pulses with a pulse energy of $\sim$ 20 μJ centered at the same frequency as the probe pulses. The output of the probe OPA is split into two beams by a ZnSe beam splitter: the probe beam and the reference beam. The probe beam is sent through a motorized delay stage to control the delay time between the pump and probe pulses.

The schematic of the measurement and detection parts of the setup is shown in Figure 3.3. The polarization of the pump pulses is set 45° with respect to that of the probe beam using a half-wave plate. The beams are focused in the sample using a parabolic mirror. While the pump and probe beams are focused in the same spot, the reference beam passes through the sample at a different position. The probe light polarized parallel or perpendicular to that of the pump is selected with a polarizer behind the sample. Subsequently, the beams are recollimated using a second parabolic mirror, dispersed by a spectrometer and detected with a liquid nitrogen-cooled 3×32 pixels array mercury-cadmium-telluride (MCT) detector. By mechanical chopping every second pump pulse before the sample, we compare the absorption of the sample with and without pump pulse excitation, thus determining the pump-induced absorption change of the probe pulse. By detecting probe pulses that are polarized parallel and perpendicular to the polarization of the pump, we obtain $\Delta\alpha_{\parallel}$ and $\Delta\alpha_{\perp}$. The reference beam is used to normalize the probe intensity in order to compensate for pulse-to-pulse power
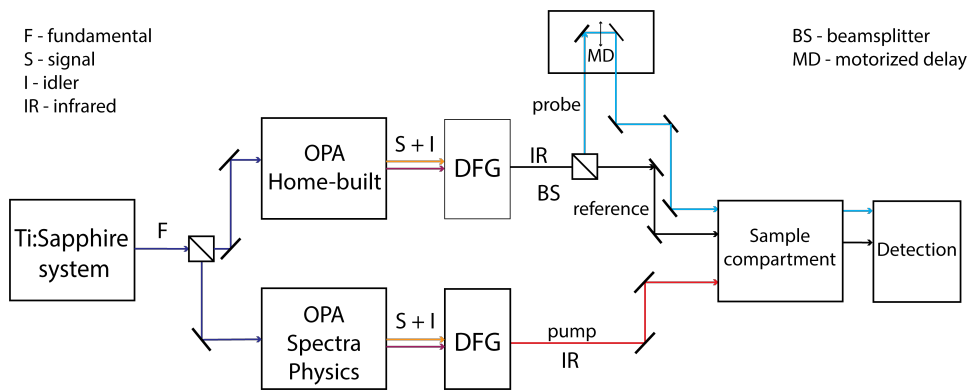
Figure 3.2. Principal scheme of the two-color pump-probe setup
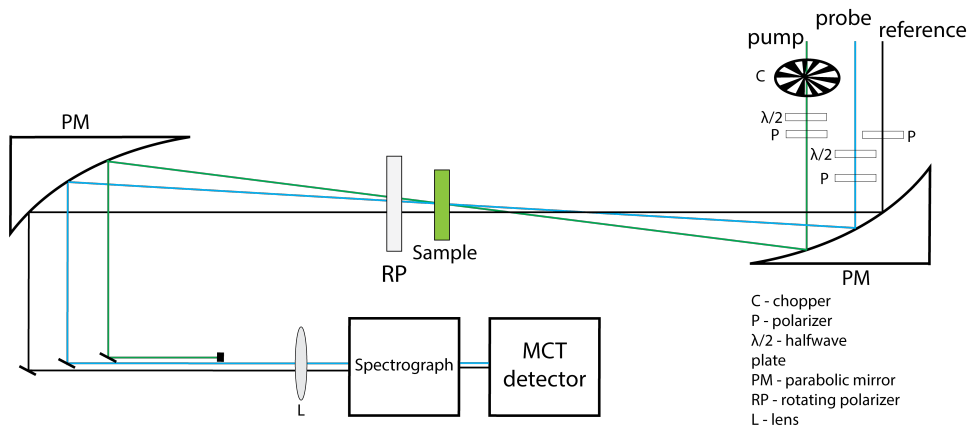
Figure 3.3. Schematic picture of measurement and detection parts of the pump-probe setup

36

fluctuations for both $\Delta\alpha_\parallel$ and $\Delta\alpha_\perp$. The resulting $\Delta\alpha$ is given by:

$$\Delta\alpha(\omega_{detection}, t) = -ln\frac{I_{probe}(\omega_{detection}, t)}{I_{ref}(\omega_{detection}, t)} + ln\frac{I_{probe,0}(\omega_{detection}, t)}{I_{ref,0}(\omega_{detection}, t)} \qquad (3.2)$$

where the first and the second terms correspond to normalized α_{pumped} and $\alpha_{unpumped}$ respectively. The samples for the pump-probe experiments are prepared similarly to the linear infrared absorption experiments in transmission geometry described in section 3.1

3.4 2D-IR setup

The principal scheme of the 2D-IR setup is shown in Figure 3.4. In the 2D-IR experiments reported in **Chapters 5, 6**, we used two commercial OPAs followed by home-built DFG stages to generate infrared pulses centered at ~ 1550 cm^{-1} (6 μm) used for excitation and detection.

In the detection path, the output of the OPA-DFG setup has an energy of 2-4 μJ. Similarly to the pump-probe setup, the infrared beam is split by a ZnSe beam splitter into probe and reference beams. The probe beam is sent through a motorized delay stage to control the delay time between the probe pulse and the static arm of the excitation pulse pair (see below).

In the excitation path, the output of the OPA-DFG setup has an energy of $\sim$ 20 μJ. The ZnSe wobbler is used to average out interference effects resulting from scattering of the excitation pulses from the sample. After the wobbler, the output is sent into a Mach-Zehnder interferometer to obtain a pulse pair with a controlled mutual delay τ. The pulse pair is used for sample excitation. An interference pattern of an identical pulse pair is simultaneously recorded with a built-in pyro-detector and the mutual delay time τ is determined by counting the interference fringes of an auxiliary HeNe laser, propagating parallel to the copy infrared pulse pair.[81,82] A mechanical chopper is used to optimize the alignment of the setup, and to calibrate the position of the motorized delay stage of the probe pulse, in order to determine pump-probe delay $t = 0$.

In Figure 3.5 we show a schematic picture of the measurement and detection parts of the 2D-IR setup. The layout is only slightly different from that of the pump-probe setup, shown in Figure 3.3. In the case of the 2D-IR setup, after the sample, instead of using a rotating polarizer to select a particular polarization direction, the probe beam is split into two beams each of which is sent through a wire-grid polarizer. One of the polarizers is set parallel to the polarization of the excitation pulses, while the other is set perpendicular to the polarization of the excitation pulses. The two mutually perpendicularly polarized probe pulses and the reference pulse are detected by a 3×32 liquid nitrogen-cooled mercury-

F - fundamental
S - signal
I - Idler
IR - infrared

⬔ - beamsplitter
MD - motorized delay
C - chopper
W - wobbler

Figure 3.4. Principal scheme of the 2D-IR setup. The inset on the bottom left shows the beam path for the excitation pulse in the Mach-Zehnder interferometer

P - polarizer
λ/2 - halfwave plate
PM - parabolic mirror
L - lens

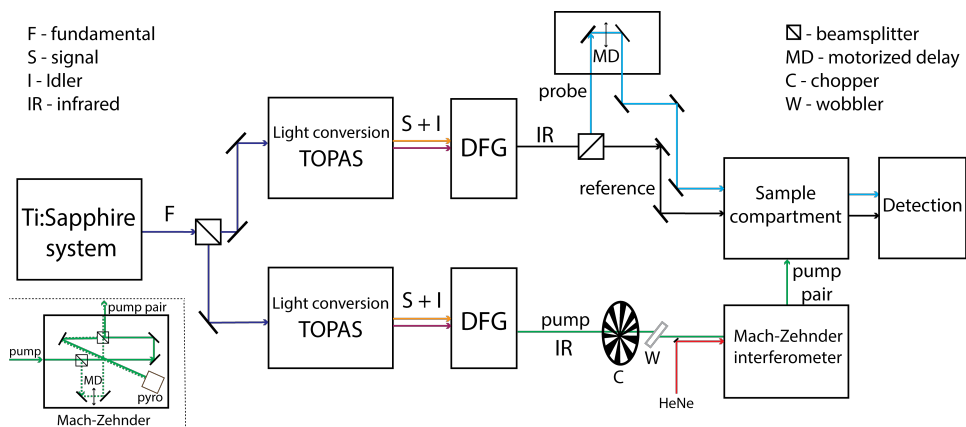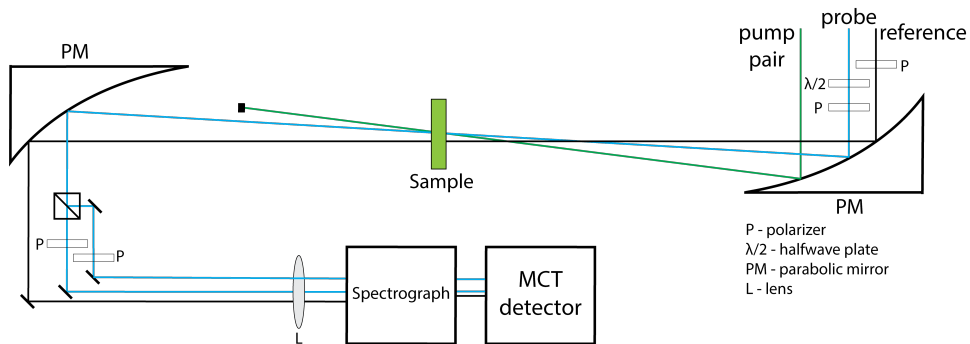**Figure 3.5.** Schematic picture of the measurement and detection parts of the 2D-IR setup

cadmium telluride (MCT) array.

The transient absorption signal is recorded as a function of the probe frequency $\omega_{detection}$, the time τ between the two excitation pulses, and the waiting time t between the probe and the static arm of the interferometer. By performing a Fourier transform with respect to τ, we obtain the dependence of the transient absorption changes on the excitation frequency, $\Delta\alpha(\omega_{detection}, \omega_{excitation}, t)$. By detecting probe pulses that are polarized parallel and perpendicular to the polarization of the pump, $\Delta\alpha_{\parallel}(\omega_{detection}, \omega_{excitation}, t)$ and $\Delta\alpha_{\perp}(\omega_{detection}, \omega_{excitation}, t)$ are obtained. The obtained two-dimensional spectra are divided by the pump spectrum that is determined from the interference pattern and detected by the pyro-detector of the Mach-Zehnder interferometer. The samples for the 2D-IR experiments are prepared similarly to the linear infrared absorption experiments in transmission geometry described in section 3.1

3.5 Analysis of the time-resolved spectroscopic data

The outcome of the time-resolved spectroscopic measurements is formed by two data sets - $\Delta\alpha_{\parallel,\perp}(\omega_{detection}, t)$ in case of the pump-probe experiment, and $\Delta\alpha_{\parallel,\perp}(\omega_{excitation}, \omega_{detection}, t)$ in case of the 2D-IR experiment. In the 2D-IR studies presented in this thesis, we analyzed the relaxation dynamics of diagonal and cross-peaks which do not show a significant dependence on the precise excitation frequency within these peaks. Therefore, we averaged certain frequency ranges of spectra along the excitation axis and thereby averaged out a potential residual dependence on $\omega_{excitation}$. As a result, the explicit excitation-frequency dependence of the 2D-IR signals vanishes, and the dimensions of the analyzed data sets are the same for the pump-probe and 2D-IR experiments. Accordingly, the combinations of $\Delta\alpha_{\parallel}$ and $\Delta\alpha_{\perp}$ yielding $\Delta\alpha_{iso}$ and R have the same dimensions. Mathematically, the obtained $\Delta\alpha$ and R can be considered as a two-dimensional matrix $n \times m$ where the number of rows n is equal to the number of probed frequencies and m is equal to the number of probed waiting times. We analyze these data sets with kinetic models that describe the vibrational relaxation and anisotropy dynamics.

To analyze the vibrational relaxation, we fit $\Delta\alpha_{iso}(\omega, t)$ with a specific kinetic vibrational relaxation model. This model usually contains several states, the populations of which $N(t)$ are evolving with waiting time t. Each of these states possesses an associated transient absorption spectrum $\sigma(\omega_{detection})$, and together the states should account for the transient isotropic absorption signal $\Delta\alpha_{iso}(\omega, t)$ at all waiting times t. $\Delta\alpha_{iso}(\omega, t)$ can thus be represented as a matrix product of a matrix of populations $N(t)$ and a matrix of spectral shapes $\sigma(\omega_{detection})$ (further $\sigma(\omega)$):

$$\Delta\alpha_{iso}(\omega, t) = \sigma(\omega)N(t) \tag{3.3}$$

The matrix $N(t)$ represents the dynamics of the populations determined by the rate equations:

$$\frac{d}{dt}N(t) = KN(t) \tag{3.4}$$

where K is the rate matrix determined by the chosen relaxation model. The solution of the rate equations is given by:

$$N(t) = Ve^{Dt}V^{-1}N(0) \tag{3.5}$$

where D is the diagonal matrix containing the eigenvalues of K, and V is the matrix composed of the eigenvectors of K. Once the population matrix is known, the spectral signatures can be retrieved by solving the system of linear equations defined by equation 3.3 to determine $\sigma(\omega)$.

Commonly, the fitting procedure starts with a computation of $N(t)$ using an initial approximation for the rate constants. Subsequently, the $\sigma(\omega)$ is determined by solving the system of linear equations of 3.3 using a linear least-squares method. The obtained $\sigma(\omega)$ spectra are used to minimize the residuals in a non-linear least-squares procedure where the rate constants are treated as free parameters:

$$\chi^2 = \left(\frac{\sum_{i,j}\Delta\alpha_{iso}(\omega_i, t_j) - \sigma(\omega_i)N(t_j)}{\xi_{i,j}^2}\right)^2 \tag{3.6}$$

where $\xi_{i,j}$ is a standard deviation for $\Delta\alpha_{iso}(\omega_i, t_j)$. With the thus obtained rate constants, $\sigma(\omega)$ can be redetermined. By repeating these steps, the set of rate constants and spectral shapes that provide the best description of the data is obtained.

Let us consider a parallel decay relaxation scheme as shown in Figure 3.6a. In this scheme two excited states, denoted as red and blue, relax to a common local hot state with different relaxation rates. For this model, the rate matrix is given by:

$$K = \begin{pmatrix} -k_r & 0 & 0 \\ 0 & -k_b & 0 \\ k_r & k_b & 0 \end{pmatrix} \tag{3.7}$$

Here the first two rows of K correspond to the dynamics of the red and blue excited states, respectively, showing population decay with rate constants k_r and k_b. The third row corresponds to the hot state, the population of which increases proportional to the decaying populations of the two excited states. The initial populations of the excited states are equal while that of the hot state is 0. Since
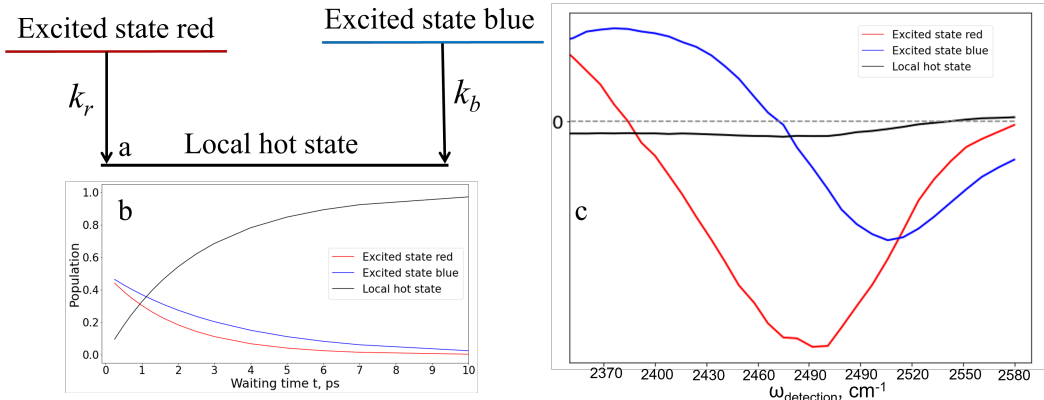
Figure 3.6. a. Parallel decay scheme b. populations dynamics and c. spectral signatures extracted from the fitting

three states are involved in the dynamics, σ has three columns, and N has three rows. In Figure 3.6b,c we show the retrieved populations dynamics and spectral signatures.

Following the determination of the vibrational relaxation model, we can subsequently assume an anisotropy relaxation model for each of the states. Often, the anisotropy does not show a pronounced frequency dependence, and hence the dependence on ω can be omitted. The total anisotropy will thus be a population-weighed sum of state-associated anisotropies:

$$R_{total}(t) = \sum_i N_i(t) R_i(t) \tag{3.8}$$

The state-associated anisotropies can then be retrieved by using the non-linear least-square procedure described before.

Alternatively, a global fitting can be performed using $\Delta\alpha_\parallel$ and $\Delta\alpha_\parallel$ by minimizing the residuals:

$$
\begin{aligned}
\chi^2 = &\left(\frac{\sum_{i,j}\Delta\alpha_\parallel(\omega_i,t_j,) - \sigma(\omega_i)N(t_j)(1+2R(t_j))}{\xi_{i,j}^2}\right)^2 + \\
&\left(\frac{\sum_{i,j}\Delta\alpha_\parallel(\omega_i,t_j,) - \sigma(\omega_i)N(t_j)(1-R(t_j))}{\xi_{i,j}^2}\right)^2
\end{aligned} \tag{3.9}
$$

Using the latter approach, the vibrational relaxation and anisotropy dynamics can be fit simultaneously.
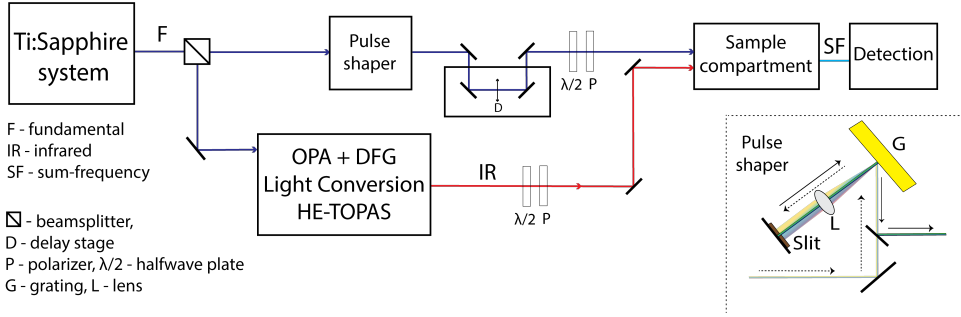
Figure 3.7. Principal scheme of the HD-VSFG setup. The laser fundamental frequency coincides with ω_{vis}. The inset on the right bottom shows the geometry of the pulse shaper, the dashed arrows correspond to the direction of the incoming ω_{vis} beam depicted as semi-transparent, while the solid arrows represent the direction of the spectrally narrow beam depicted opaque

3.6 HD-VSFG experiment

In Figure 3.7 we show the principal scheme of the HD-VSFG setup. In the experiment, the output of the amplifier is split into two parts. The first part is sent to a pulse-shaper in order to generate a spectrally narrow (~ 20 cm^{-1}) 800 nm pulse (ω_{vis}). The bandwidth can be controlled by adjusting the width of the slit of the pulse shaper. The second part of the output is sent to a commercial optical parametric amplifier and difference-frequency mixing stage (Light Conversion HE-TOPAS) to generate infrared pulses centered at ~ 1550 cm^{-1} (ω_{IR}) with a spectral width of ~ 400 cm^{-1}.

The laser and the parametric generation device deliver s-polarized ω_{vis} and p-polarized ω_{IR} light, respectively. We perform measurements in SSP and SPS polarization combinations, where the notation SS(P)P(S) refers to S-polarized light at ω_{SFG}, S(P)-polarized light at ω_{vis}, and P(S)-polarized light at ω_{IR}. The energies of the ω_{vis} and ω_{IR} pulses are $\sim$20 μJ and $\sim$15 μJ, respectively.

In Figure 3.8 we show a schematic picture of the measurement and detection compartments of the HD-VSFG setup. The ω_{vis} and ω_{IR} beams are focused and overlapped on the surface of a gold mirror to generate a local oscillator sum-frequency generation signal (LO-SFG, $\omega_{SFG} = \omega_{vis} + \omega_{IR}$). The LO-SFG light is sent through a 1 mm thick silica plate to delay it by $\sim$1.6 ps with respect to the ω_{vis} and ω_{IR} beams. All the beams are refocused on the sample surface, where the ω_{vis} and ω_{IR} beams generate the sample sum-frequency generation signal. The sample SFG and the LO-SFG are then sent to a spectrometer and their intensity is detected frequency-resolved by a thermoelectrically cooled charged-coupled device (CCD, Princeton Instruments). The sample SFG and the LO-SFG interfere and
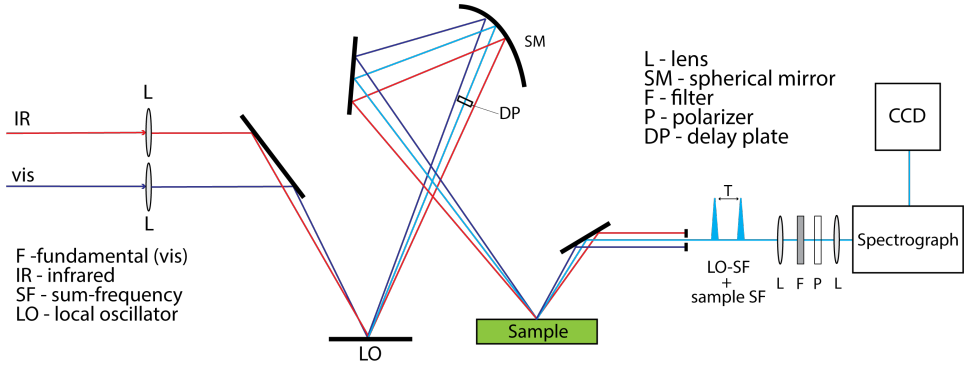
Figure 3.8. Schematic of the sample and detection compartments of the HD-VSFG setup

form an interference pattern. The real and imaginary parts of the $\chi^{(2)}$ spectrum of the sample are extracted by Fourier filtering, as shown in Figure 3.9. All samples studied in this thesis are prepared by placing 4 ml of a solution in a Teflon Petri dish with a diameter of ~ 4 cm. It is important to put a sufficient sample volume in a Petri dish to avoid significant curvature of the surface. The sample spectra are obtained by averaging five scans with an acquisition time of 120 s for each scan.

To correct the measured spectra for their dependence on the intensity spectrum of the IR pulse, we divide the sample spectra by SFG spectra measured with a reference z-cut α-quartz instead of the sample. The height of the α-quartz surface is carefully adjusted to that of the sample surface, to minimize the error in determining the phase of the sample SFG signal. We use the same normalization procedure for spectra collected in SSP and SPS polarization combinations. Since the quartz sum-frequency signals are very close in these polarization combinations,[83] the amplitudes of the SSP and SPS $\chi^{(2)}$ spectra are determined only by sample properties.

In the 1300 - 1650 cm^{-1} frequency region a strong etalon effect occurs in the CCD camera, which can significantly distort the spectra. This effect is corrected by taking two reference spectra from the quartz crystal. The phases of the two spectra differ by 180°, which is achieved by rotating the quartz crystal by 180° around its z-axis. Because of the phase difference, the addition of the two spectra yields the subtraction of the quartz sum-frequency signals and the result is thus the sum of the LO-SFG signals and the structural noise induced by the etalon effect. The structural noise can then be eliminated from the measured sample spectrum by dividing this spectrum by the sum of the two reference spectra, prior to Fourier filtering. The details of this correction procedure have been reported before.[84–86] The final $\chi^{(2)}$ spectra are given as:

43
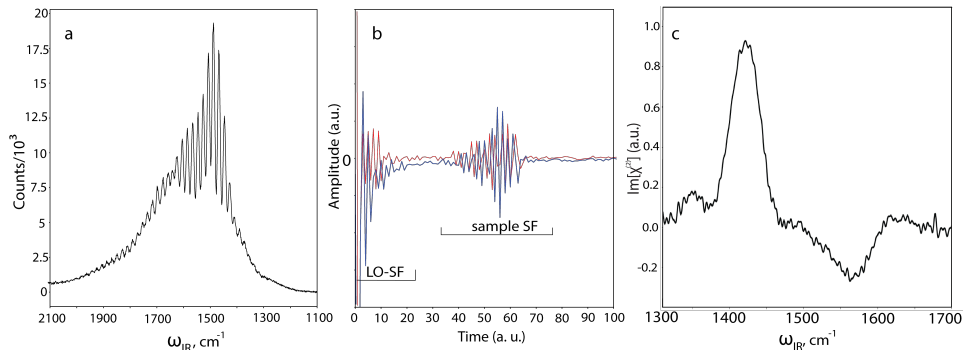
Figure 3.9. a. Example of a raw heterodyne-detected SFG spectrum b. Fourier transform of the raw heterodyne-detected SFG spectrum corrected for structural noise c. Im$[\chi^{(2)}]$ spectrum obtained after Fourier filtering and normalization with respect to quartz reference

$$S = \frac{\chi^{(2)}_{sample} \cdot e^{i\varphi}}{i\chi^{(2)}_{quartz}} \tag{3.10}$$

In this expression, i appears as a factor in the denominator to account for the theoretical phase difference of $\pi/2$ between the sum-frequency signals originating from the quartz bulk and the sample surface.[87] The experimentally determined phase can contain a small error.[88] For that reason, an additional phase correction of $\varphi = \pi/20 - \pi/10$ is sometimes applied by multiplying the spectrum with the complex exponential term in the numerator. The phase uncertainty of the experiments, therefore, does not exceed $\pi/10$ ($\sim 20°$).

3.7 Preparation and characterization of UiO-66 polycrystalline membranes

In **Chapter 6** we describe 2D-IR spectroscopy on UiO-66 polycrystalline membranes grown on c-sapphire substrates. Here we describe the sample preparation procedure used in this study.

We have cut optical grade sapphire wafers (Siegert Wafer, C-plane cut, 0.7 mm thick) with a diamond cutter (AMOLF) in 1×1 cm plates. Zirconium tetrachloride (ZrCl$_4$, Sigma Aldrich anhydrous for synthesis), 1,4-benzenedicarboxylic (terephthalic) acid (BDCH$_2$, Aldrich, 98%), N,N-dimethylformamide (DMF, Sigma-Aldrich, $\geq$ 99.8%) and acetic acid (AcOH, Sigma-Aldrich $\geq$ 99.8%) were used as received. ZrCl$_4$ was constantly stored in a glove box purged with dry air to avoid hydrolysis

44

of the salt.

We prepared the samples in a single-step anhydrous acidified solvothermal process. Before each synthesis, the plates have been thoroughly wiped with cotton wool wet with acetone and then sonicated in ethanol for 5 minutes followed by 20 min treatment in a UV-ozone cleaner. After that, the plates were placed in a Teflon sample holder (AMOLF) which was placed in a Teflon beaker of the 23 ml acid digest vessel (Parr instruments). To prepare the reaction mixture, we separately dissolved $ZrCl_4$ and $BDCH_2$ in DMF and sonicated the solutions for 5 minutes. After that, the solutions were combined, AcOH was added and the mixture was again sonicated for 10 minutes. The resulting solution contains the reactants with the following molar ratios: $ZrCl_4$:$BDCH_2$:AcOH:DMF = 1:1:200:400. The solution was after that combined with the clean sapphire plates in the Teflon beaker. We aimed for keeping the sapphire plates on air as short as possible before starting the reaction.

After combining the reactants, the reaction vessel was sealed and kept in the oven at 120°C for 24h. Then the vessel was taken out and cooled down in a water bath. The resulting polycrystalline UiO-66 membranes grown on both sides of the sapphire plates were extracted and purified by consecutive immersion in DMF(1x), water(2x), ethanol (1x) and dried at 50°C. In the spectroscopic experiments, we used only the UiO-66 sample at one side of the sapphire plate and the sample at the other side of the sapphire plate was mechanically removed since the light penetration depth does not allow to excite the samples on both sides of the sapphire plate.

To characterize the sample the remaining reaction mixture was transferred to a 15 ml Falcon tube and put in a centrifuge to extract the remaining UiO-66 powder. The precipitate was isolated by mechanical supernatant removal. The precipitate was further mixed with 10 ml of fresh DMF for washing the powder and centrifuged again. The process was repeated using consecutively 10 ml of water(2x) and ethanol (1x) for removing the unreacted species and the solvent. Finally, the powder was transferred to a clean vial and dried at 50°C. The extracted powder was used only for characterization purposes.

To confirm the crystal structure of the prepared membranes, we measured X-ray diffraction patterns with a commercial Bruker D2 Phaser diffractometer using the Cu Kα radiation.

We determined the sample thickness with profilometry measurements using KLA Tencor P-7 Stylus Profiler in the AMOLF Nanolab Amsterdam. We made a thin trench on a polycrystalline membrane with a surgical blade and scanned a line of 500 μm length crossing the trench. The trench depth represents the membrane thickness.

To quantify the density of defects in the UiO-66 membranes we performed a thermogravimetric analysis (TGA) of the powder samples. In this method, a sample is heated while continuously monitoring the sample weight to obtain the

dependence of sample mass on temperature called a thermogravimetric curve. Due to the heating, physical and chemical processes in the sample lead to mass loss. At lower temperatures, the mass loss is due to the desorption of the compounds such as water and DMF absorbed in sample pores. At higher temperatures, the mass loss is due to the decomposition of the MOF linkers and metal-oxo clusters. Given the initial mass, final mass, and the stoichiometry of the product of the thermal decomposition the initial stoichiometry can be retrieved. The details of the determination can be found in the previous UiO-66 study.[89] We further assumed that the stoichiometry of the membranes deposited on the substrate is the same as in the powder material since they originate from the same reaction mixture. We performed the analysis using a NETZSCH Jupiter STA 449F3 instrument under argon flow (20 mL/min). The samples are heated in aluminium oxide crucible from 35 °C to 700 °C at a rate of 5 K/min. We did a reference measurement in identical conditions with empty crucibles to correct for potential artifacts.

4

Confined Water Molecules in Binary Mixtures of Water and 2,6-Lutidine Near Lower Solution Critical Temperature*

We study the concentration and temperature dependence of the reorientation dynamics of water molecules in binary mixtures of water and 2,6-lutidine below the lower solution critical temperature (LSCT) with femtosecond mid-infrared pump-probe spectroscopy. The measurements reveal the presence of water molecules interacting both with the hydrophobic groups of lutidine and forming a hydrogen bond with the nitrogen atom of lutidine. Both types of molecules show a strongly decreased rotational mobility in comparison to bulk water. From the temperature dependence of the slow water fraction, we conclude that the lutidine molecules form clusters that decrease in size when the temperature is decreased further below the LSCT.

4.1 Introduction

Amphiphilic molecules contain both polar (hydrophilic) and apolar (hydrophobic) moieties, which leads to competitive behavior in aqueous solutions of these compounds. This competition drives the rearrangement of amphiphilic molecules in order to realize the interactions favorable for both the hydrophobic and hydrophilic parts. Macroscopically these rearrangements involve a delicate balance of the entropy and the enthalpy of the system leading to the existence of critical phenomena such as phase separation. Depending on the chemical and physical parameters (composition, temperature, pressure etc.) a homogeneous liquid mixture can thus reversibly separate into solute- and solvent-rich phases. This type of phase separation is ubiquitous and takes place in a broad range of systems. Recently, several studies have been reported on the role of liquid-liquid phase separations in drug delivery,[90] living cell processes (including pathological),[91,92] atmospheric chemistry[93,94].

The phase diagram of a liquid mixture in temperature (T) – solute mole fraction (X) coordinates, represents whether the compounds are miscible or not. These phase diagrams can include both lower and higher solution critical temperatures – LSCT and HSCT, respectively. By definition, below the LSCT and above the HSCT the compounds are fully miscible. While the existence of a HSCT is quite common for binary mixtures, the existence of an LSCT for aqueous solutions is limited to a few classes of organic molecules and polymers. The aqueous solutions of compounds as tetrahydrofuran, trimethylamine and isobutyric acid, which are commonly used in organic synthesis, show an LSCT.[26,95,96] Other examples include amphiphilic polymers and ionic liquids.[97–99]

Pyridine derivatives form a class of amphiphilic compounds the solvation properties of which strongly differ from their non-polar analogs. The homoarene benzene (C_6H_6) and the simplest heteroarene pyridine (C_5H_5N) differ only by the presence of a polar N atom in the structure of the latter instead of a =CH– group in the structure of the former. However, pyridine is miscible with water at any ratio at all temperatures,[100] while benzene is only weakly soluble in water[101]. The formation of OH$\cdots$N hydrogen bonds favors miscibility and the hydrophobic interactions involving the weakly polar hydrocarbon core favor demixing.[102–104] The aggregation of solute molecules driven by hydrophobic interactions can lead to the formation of molecular clusters with sizes up to several nm.[105–108] Interestingly, very subtle changes in the molecular structure of pyridine derivatives lead to a significant change in the phase diagram of its aqueous solution. Even a change of the position of an alkyl substituent in the pyridine ring significantly influences its mixing/demixing behavior.[102,103,105] Overall, a broad range of pyridine-like compounds including a natural alkaloid nicotine, show an LSCT in aqueous mixtures.[109]

A mixture of 2,6-lutidine (2,6-dimethylpyridine, lutidine) and water demonstrates a closed-loop phase diagram.[110,111] In Figure 4.1a we show a part of the

phase diagram of the 2,6-lutidine/water mixture near the LSCT. In this mixtures, LSCT $\approx$ 307K at X $\approx$ 0.062 and the composition range in which the compounds show demixing behavior is approximately $0.01 \leq X \leq 0.3$ in between the LSCT and HSCT. Interestingly, the phase diagram also depends on the isotopic composition of the water molecules and the concentration of electrolytes, both illustrating a delicate competition of intermolecular interactions in the system. [102,104,110,112] The study of the molecular properties of 2,6-lutidine/water mixtures is of strong general interest. These mixtures have recently been used in liquid templating of the aggregation of colloidal particles via bicontinuous Pickering emulsion formation. [113] A commercially important process dependent on the mixing properties with water is the transformation of alkyl pyridines to the corresponding N-oxides. [114] It is also worth noticing that in spite of the simplicity of this system, the molecular structure of 2,6-lutidine is close to the structures of pyrimidine and purine nucleobases which are present in aqueous environment in living cells forming nucleic acids such as DNA and RNA.

In this work, we use polarization-resolved femtosecond infrared pump-probe spectroscopy to study the concentration and temperature dependence of the structural and dynamical properties of water molecules solvating 2,6-lutidine. This method has been successfully applied to the study of the hydration of small organic molecules [25,115,116] and (bio)polymers [117–120]. Because of the high sensitivity of molecular vibrations to their chemical environment, this technique is capable of providing unique information on the solvation structure. In our experiments, we observe different water species showing different reorientational dynamics and vibrational relaxation rates. We use the obtained results to explain the molecular events accompanying the phase separation of 2,6-lutidine/water mixtures near the LSCT.

4.2   Experiments

2,6-Lutidine (redistilled, 99%+) was purchased from Sigma Aldrich and was used as received. Isotopically diluted water was prepared by mixing deionized water (Millipore) with D_2O (Sigma Aldrich, 99.9% D atoms) to produce a 4 molar % solution of HDO in H_2O. We find that the isotopic dilution of H_2O by adding 2 molar % D_2O does not significantly perturb the phase diagram of water/lutidine. The isotopically diluted water was mixed with an appropriate amount of the lutidine to obtain a molar fraction X of the solute of 0.02-0.75%

The experimental setups as well as the preparation of samples for infrared absorption and pump-probe measurements are described in sections 3.1, 3.2, and 3.3.
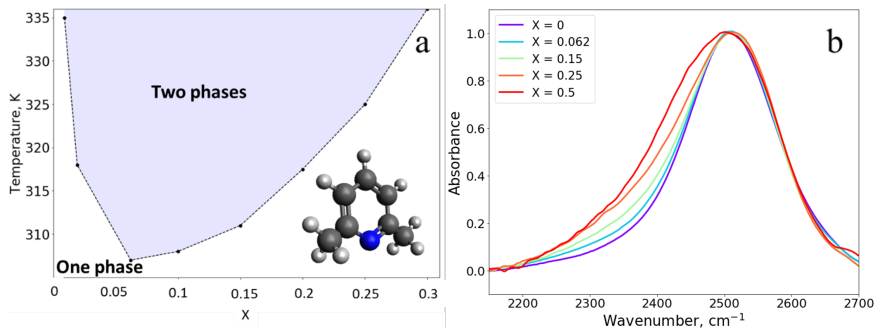
Figure 4.1. a. Phase diagram of 2,6-lutidine/water mixtures near the lower solution critical temperature (LSCT). The inset in the right bottom corner shows the structural formula of 2,6-lutidine, the black, blue and white spheres represent carbon, nitrogen and hydrogen atoms, respectively; b. Linear absorption spectra corresponding to the OD-stretch absorption band in water/lutidine mixtures, X shows the molar fraction of lutidine

4.3 Concentration dependence

4.3.1 Linear infrared absorption spectra

In Figure 4.1b we present infrared absorption spectra of the 2,6-lutidine/water mixtures in the frequency region of the OD stretch vibration of HDO. The OD-stretch absorption band of the HDO molecules overlaps with other bands assigned to H_2O and lutidine. To accurately extract the OD-stretch absorption band line shape from the raw linear infrared absorption spectrum, we used the subtraction procedure described in section 4.7. Increasing the solute concentration leads to an ingrowth of a shoulder in the red wing of the spectrum. This shoulder indicates an increased fraction of water (HDO) molecules that form stronger hydrogen bonds than the average hydrogen bond in liquid water. We assign this increasing low-frequency shoulder to the formation of OD···N hydrogen bonds, since the pyridine-type nitrogen atom of lutidine is an excellent hydrogen bond acceptor[104,105,121], 2,6-lutidine acts as a weak base (conjugated acid pKa = 6.6) in aqueous solutions[122].

4.3.2 Isotropic transient absorption

In Figure 4.2 we present isotropic transient absorption spectra ($\Delta\alpha_{iso}$) for solute fractions X = 0.02 and X = 0.3 systems. At early delay times, a negative transient absorption signal around 2500 cm^{-1} is observed corresponding to the bleaching of the ground state and stimulated emission (v = 1 ↔ 0) of the OD-stretch vibrations. The positive signal at lower frequencies corresponds to the induced v = 1 → 2
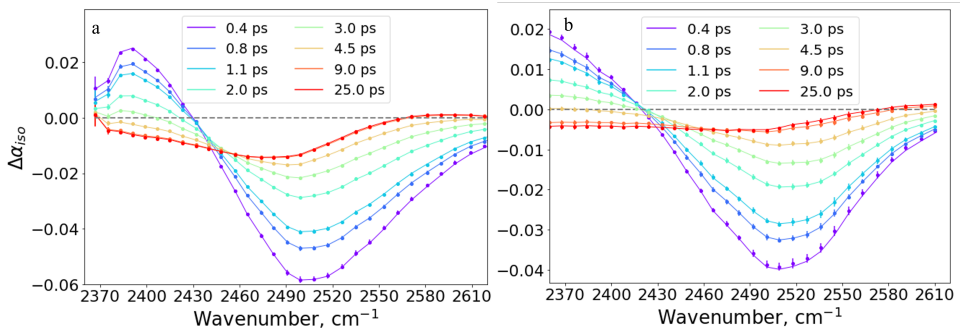
Figure 4.2. Isotropic transient absorption spectra for a. X = 0.02 and b. X = 0.3 lutidine/water mixtures. Points represent experimental values; solid lines represent the fit using the kinetic model described in the text

excited-state absorption. Due to vibrational energy relaxation, $(\Delta\alpha_{iso})$ decreases with delay time at all frequencies. At longer delay times the transient spectrum looks similar to the thermal difference spectrum of the OD-stretch absorption band (the difference of the absorption spectra measured at room temperature and at an elevated temperature). However, although the spectral shape looks similar to a thermal difference spectrum, we observe ongoing dynamics of the amplitude of the transient absorption signal, even after a relatively long delay time of 9 ps. This type of long delay time dynamics has been observed before for solutions of organic molecules in water, and indicates that the complete equilibration of the system is delayed with respect to the relaxation of the excited vibrational state.[69,123] The long delay time dynamics may be due to a repositioning of the molecules in the solution, e.g. associated with a change of the size and distribution of clusters. No further signal evolution is observed after ~ 25 ps delay time for all solute fractions, meaning that at those delay times, complete thermal equilibrium is reached within the excited volume.

A careful analysis of the transient spectra obtained for X > 0.06 reveals a blue shift of the frequency position of the maximum of the transient absorption signal with increasing delay time. This can be clearly seen by comparing for instance the signal at ≈ 0.4 ps and at 2 ps for X = 0.3 (Figure 4.2b). This observation implies that the vibrational relaxation time $(T_1 = 1/k)$ is frequency-dependent for solutions with a higher solute fraction X.

To account for the frequency dependence of the relaxation rate, we apply a kinetic relaxation model in which two excited states relax to a common state which we designate as "local hot state" (see following section). The relaxation dynamics is characterized by time constants T_{1r} and T_{1b} for the low-frequency component and for the high-frequency component, respectively (Figure 4.3a). The initial populations of the two excited states were kept equal and their spectral shapes
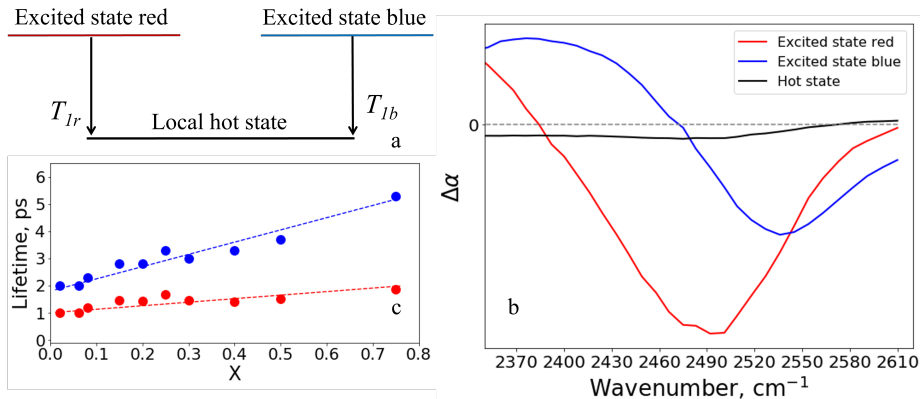
Figure 4.3. a. Representation of the kinetic model applied for the description of the vibrational energy relaxation b. Spectral shapes of the two decomposed bands extracted from an unconstrained fit of the data of the X = 0.3 mixture c. Vibrational relaxation time constants as a function of the solute fraction X at 295K. The time constants are extracted from the unconstrained fits, the dashed lines are guides to an eye.

(including the amplitudes) were varied without constraints. A similar model has been applied to the description of the vibrational energy relaxation dynamics in water/DMSO and water/acetone mixtures.[25] A more detailed description of the modeling approach can be found in ref.[25] and section 3.5.

We have applied this kinetic scheme to analyze the data obtained for all compositions. The two spectral shapes extracted from the fit for X = 0.3 mixture are presented in Figure 4.3b. Both spectra show bleaching and induced absorption signals. Figure 4.3c displays the time constants extracted from the fits for different mixtures. It is seen that the relaxation time constants increase with increasing lutidine concentration. T_{1r} increases from 1 ± 0.2 ps at X = 0.02 to 2 ± 0.3 ps at X = 0.75. T_{1r} changes from 2 ± 0.3 ps at X=0.02 to 5.3 ± 0.5 ps at X=0.75.

4.3.3 Anisotropy dynamics

The transient absorption signal contains both contributions from the excited OD vibrations and a contribution of the state that is created after the relaxation, where the latter contributions will increase with increasing delay time. In the past, such final state has been denoted as "hot ground state", representing a state in which the excitation energy has thermally equilibrated over the excited volume. Hence, this state is expected to be isotropic. To determine the delay time dependence of the anisotropy of the signal of the excited OD oscillators, the observed total absorption signal has to be corrected for the response following the relaxation of
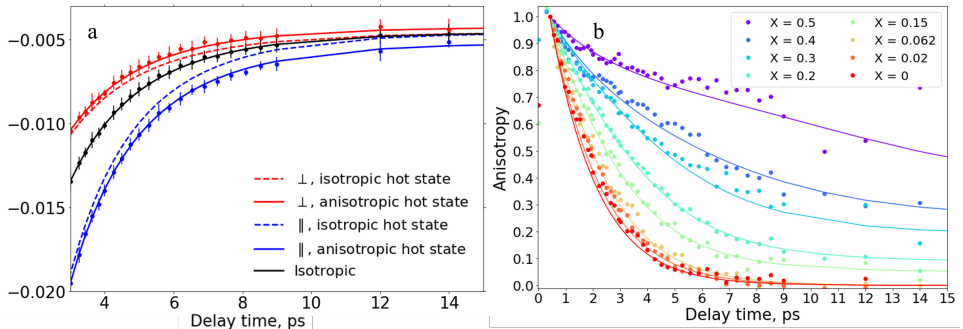
Figure 4.4. a. $\Delta\alpha_{\parallel}$ and $\Delta\alpha_{\perp}$ dynamics for X=0.3 at delay times >3 ps at the center of the bleach. The points represent the experimental results. The lines represent fits obtained with the model described in the text. b. Anisotropy dynamics measured for different concentrations of 2,6-lutidine at the center of the ground state bleach. All curves are normalized to the anisotropy value at 0.4 ps

these oscillators.[25,70,117,123] In Figure 4.4 it is seen that the assumption that the state created after the vibrational relaxation would be isotropic leads to significant differences between the curves calculated with the relaxation model (dashed lines) and the data. This assumption can even lead to a divergence of the corrected anisotropy (Figure 4.7). In Figure 4.4b, it is seen that for X ≥ 0.15 the anisotropy that is constructed directly from the measured $\Delta\alpha_{\parallel}$ and $\Delta\alpha_{\perp}$ does not completely relax even at delay times >9 ps. For X = 0.3 at 9 ps delay time, ∼ 20% of the initial anisotropy is conserved while no more than 5% of the initial excited OD population is left, and the transient absorption signal is clearly dominated by the end-level signal. Hence, we conclude that the state reached after the vibrational relaxation corresponds to an anisotropic distribution of relaxation-affected OD oscillators that remains present long after the vibrational relaxation. This indicates that the energy that is dissipated in the vibrational relaxation primarily affects the originally excited OD-oscillator, i.e. remains local. Since the spectral shape corresponding to this state is still very close to that of the thermal difference spectrum and only shows subtle amplitude dynamics, we designate this state as "local hot state".

The transient absorption signal associated with the local hot state will be anisotropic when a few conditions are met. The first condition is that the reorientation of the water molecules is slower than the vibrational relaxation, i.e. after the excitation energy is transferred into heat, the orientation of the originally excited molecule is not yet randomized. This condition is fulfilled for water molecules that are slowly reorienting due to their interaction with the hydrophobic or hydrophilic parts of the lutidine molecules. The reorientation of these molecules will also remain slow after the vibrational relaxation, i.e. when they give rise to the transient

absorption signal of the local hot state. A second important condition for the local hot state to be anisotropic is that the heating effect following the relaxation of the OD vibration has little effect on OD vibrations that were not excited. This condition is fulfilled if the equilibration of heat between excited and non-excited oscillators is slow, which will be the case if the OD oscillators are well separated and the heat diffusion is not very fast. This second condition is largely fulfilled by the isotopic dilution of the sample, which implies that the concentration of OD groups is much lower than the overall water concentration in the mixture. The separation of the OD groups will be further enhanced as a result of clustering of the lutidine/water mixture, which implies that small clusters or monomers of water molecules are embedded by lutidine molecules and thus separated from other water clusters.

To account for the anisotropy of the local hot state, we fit the experimentally observed $\Delta\alpha_{\parallel}$ and $\Delta\alpha_{\perp}$, with a combination of $\Delta\alpha_{iso,i}$, and anisotropy (R_i) values associated with each of the two excited states and the local hot state using the global minimization approach described in section 3.5.

Given the spectral shapes and relaxation rates, only the R_i values need to be fitted in this routine. We assign an identical delay-time dependent anisotropy to each of the two excited states:

$$R(t) = R_0 e^{-t/\tau_{bulk}} + R_{slow},\tag{4.1}$$

where the value (R_0) represents the fraction of bulk-like water molecules with the corresponding bulk reorientation time constant τbulk, and the offset (R_{slow}) – the fraction of slowly relaxing water molecules, for which the orientational relaxation is negligible within the accessible delay-time window of the experiment.

To describe the anisotropy of the local hot state, we used an approach akin to the one used by Rezus et. al.[69] In this approach the hot state partly inherits the anisotropic distribution of the excited OD-groups. As the bulk-like water molecules show a fast reorientation, also after their reorientation, we only consider the slow water molecules in describing the transfer of anisotropy from the excited OD vibration to the local hot state. We also assume that the anisotropy of the local hot state does not show a significant decay within the probed delay-time range. Additionally, we do not account for the heat diffusion from the excited volume which happens on a much longer time scale of microseconds and is thus not observed within the accessible experimental delay-time range. Under these assumptions the anisotropy of the local hot state can be described with the following simple expression (see section 4.7):

$$R_h = a \cdot R_{slow}\tag{4.2}$$

Here R_h is the anisotropy of the local hot state, and a is a fraction of the
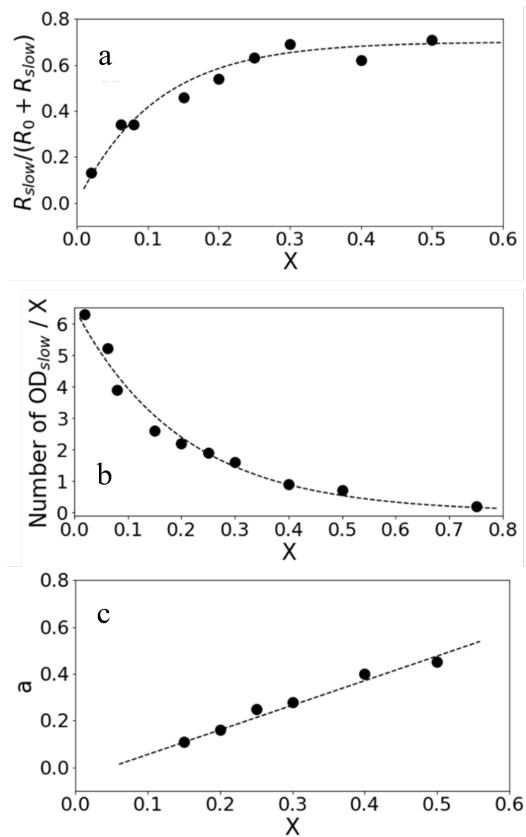
Figure 4.5. Parameters extracted from the fitting of the anisotropy dynamics of Figure 4.4. a. Fraction of slow water as a function of the fraction of 2,6-lutidine; b. Number of slow water molecules per 2,6-lutidine molecule as a function of the fraction of 2,6-lutidine; c. Fraction of the anisotropy (a) inherited by the local hot state as a function of the fraction of 2,6-lutidine; the dashed lines are guides to an eye.

anisotropy inherited. As can be clearly seen in Figure 4.4, accounting for the local hot state anisotropy leads to a significant improvement of the data description (solid line).

In Figure 4.5 we show the parameters derived from the fit as a function of the lutidine concentration. Figure 4.5a represents the fraction of slow water molecules extracted from the fit. As can be seen, this fraction increases with increasing solute concentration until X = 0.3. At X = 0.3 the slow water fraction saturates at a value of ≈ 0.7. In Figure 4.5b we show the number of slow water molecules per lutidine

molecule. At low solute fractions, on average 6 water OD-groups are slowed down per lutidine molecule. Since the hydrophobic part of lutidine has a much higher volume than its hydrophilic part, it is most likely that at low solute content, the fraction of slow water molecules is dominated by water molecules that are slowed down as a result of their interaction with the methyl groups and the aromatic ring of lutidine. It has been shown before[70] that hydrophobic hydration can lead to the slowing down of the reorientation of up to 4 water hydroxyl groups per methyl group. Increasing the concentration leads to a gradual decrease in the number of slow water OD-groups per lutidine molecule. Dilution of water with lutidine leads to an overall lower number of water molecules per lutidine molecule. Apart from that, when the concentration is increased, the lutidine molecules will cluster due to the aggregation of their hydrophobic parts. As a result, water molecules will be expelled leading to a decrease of the number of slow water hydroxyl groups per lutidine molecule. It is to be expected that even at high concentrations, water will remain interacting with the hydrophilic part of lutidine. Each lutidine molecule can create one strong OH(OD)$\cdots$N bond. Noticing the significant broadening of the shoulder in the red wing of the linear spectrum (Figure 4.1), it thus seems likely that at high solute concentration, most of the remaining slow water hydroxyl groups are slowed down because of their interaction with the nitrogen atom of lutidine.

In Figure 4.5c we show the fraction a of the anisotropy inherited by the local hot state as a function of the lutidine fraction. At low lutidine fractions, the data can be well described assuming that the local hot state is isotropic ($a = 0$). For X $\geq$ 0.15, a has a significant non-zero value and increases with increasing lutidine fraction.

4.4 Temperature-induced changes in structure and dynamics

We studied the temperature dependence of the anisotropy dynamics at three lutidine/water compositions: lower than the critical (X = 0.02), around the critical (X = 0.062), and higher than the critical concentration of 2,6-lutidine (X = 0.2). For all compositions, we observe little acceleration in the vibrational relaxation upon decreasing the temperature (Figure 4.8). This finding is in good agreement with previously reported results for aqueous solutions of small amphiphilic molecules, that showed no change in the relaxation rate[124] or only a small acceleration when the temperature is decreased[125]. The anisotropy dynamics were analyzed by fitting $\Delta\alpha_{\parallel}$ and $\Delta\alpha_{\perp}$ according to the procedure described in the previous section. The values of the bulk reorientation time constant τ_{bulk} at different temperatures are calculated with an Arrhenius equation, using an activation energy E_a of 16.5 kJ/mol, and a prefactor A of 332.7. These values are obtained
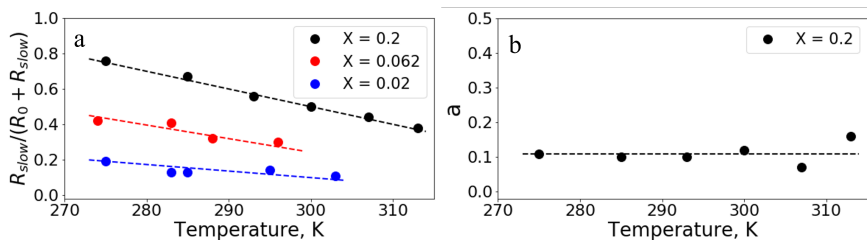
Figure 4.6. a. Temperature dependencies of the fraction of slow water molecules and b. the fraction of the inherited anisotropy, dashed lines are the guide to an eye

from a previous study of water interacting with amphiphilic molecules.[125]

The most pronounced effect induced by decreasing the temperature is the increase of the slow water fraction. This effect is very clear for X = 0.2: when the temperature is decreased from 313 K to 275 K, an increase of R_{slow} by 50% is observed. For lower solute fractions this effect is less pronounced ($\sim$ 15-20%). The value of a shows no significant temperature dependence and equals $\sim$ 0.1 for X = 0.2 (Figure 4.6b).

4.5 Discussion

A striking observation in the linear IR absorption spectrum is the rise of a shoulder in the red wing of the O-D stretch absorption band with increasing lutidine concentration. This shoulder results from the formation of a strong OD$\cdots$N hydrogen bond between HDO and the sp^2-hybridized N atom of the pyridine ring of lutidine. This observation is in good agreement with previous theoretical work.[103,126] This situation is very similar to that of the TMAO/water system in which a highly partially charged O atom is present.[123] In contrast, for tetramethyl urea, DMSO and acetone, the oxygen atoms have a weaker affinity to water hydrogen atoms.[25,70]

We find that the vibrational relaxation of the O-D stretch vibrations of the water-lutidine mixtures can be well-modeled with two O-D stretch absorption bands with different vibrational relaxation rates. These two bands account for the fact that water-lutidine mixtures contain a broad distribution of hydrogen-bond strengths, and that vibrational relaxation proceeds faster for strongly hydrogen-bonded HDO molecules (with low OD-stretch frequencies) than for weakly hydrogen-bonded HDO molecules (with high OD-stretch frequencies). A frequency-dependent relaxation rate has been observed before for DMSO/water, acetone/water and TMAO/water.[25,123] In all these cases vibrational relaxation proceeds faster in the red wing of the spectrum than in the blue.

Increasing the fraction of 2,6-lutidine leads to a deceleration of the vibrational relaxation at all frequencies. We attribute this effect to a disruption of the hydrogen

bond network by lutidine. With increasing lutidine concentration the fraction of water molecules forming hydrogen bonds with the solute increases, but the average amount of hydrogen bonds per water molecules decreases. A similar deceleration with increasing solute concentration has been observed for aqueous solutions of tetramethyl urea, DMSO and acetone. Interestingly, for the TMAO/water system no significant concentration dependence of the vibrational relaxation rate was observed, but in this case the range over which the solute fraction was varied was limited by ~ 0.15.

We observe that the fraction of slowly reorienting water molecules, as expressed by the parameter R_{slow}, increases with increasing concentration of 2,6-lutidine. This growth of R_{slow} follows from the increases of both the fraction of water interacting with the hydrophobic groups of lutidine[25,70] and the fraction of water molecules forming a hydrogen bond with the nitrogen atom of lutidine, the latter is evidenced by the rise of the red-shifted shoulder in the IR absorption spectrum.[25,123] These different types of solvating water molecules represent a broad distribution of hydrogen-bond strengths, and as both types contribute to the slow water fraction, the anisotropy of the excited OD oscillators shows very little frequency dependence. As a result, R_{slow} has the same value for the two absorption bands that we use to model the transient OD absorption spectrum. The notion that both the hydrophobic hydrating water molecules and the water molecules hydrogen-bonded to the N atom, contribute to the slow water fraction agrees with the findings of previous theoretical work, nuclear magnetic resonance[127] and small-angle scattering[105,106,108] studies of mixtures of water and different pyridine derivatives. In these studies, it was shown that water molecules interact with all hydrogen atoms and the nitrogen atom of lutidine. In previous theoretical studies, various hydration structures of lutidine have been reported.[102–104,127] It is worth noting that a water molecule can potentially coordinate two lutidine molecules. Such a molecular configuration in which a water molecule interacts with two lutidine molecules is expected to have even more constrained rotational mobility than 1:1 complexes, since in such a configuration also the rotation around the OD$\cdots$N hydrogen bond would be suppressed due to the interaction with the second lutidine molecule.

An interesting observation is that the local hot state that results from the vibrational relaxation is anisotropic, which implies that a significant fraction of the heat-affected water molecules is slowly reorienting and sufficiently isolated from other water molecules to avoid equilibration of the heating effect due to heat diffusion within the time range of our experiment. The anisotropy of the local hot state is determined by the slow water fraction R_{slow} and the parameter a that represents the transfer of this anisotropy to the local hot state, following relaxation of the OD stretch vibration. If the anisotropy would be completely retained, a would be equal to 1. There are several reasons why a is smaller than 1. In the first place, the fast local dumping of heat by the relaxation of the OD-stretch vibration likely

temporarily speeds up the reorientation, leading to a partial depolarization of the subsequent heating effect. Second, even though the water is isotopically diluted and the mixture will show microstructuring, i.e. clustering effects, for some of the excited OD groups the dissipated heat will still affect other, not excited OD groups that happen to be nearby and that have a random orientation, which will decrease the anisotropy of the heating effect. Finally, in the modeling we assumed the anisotropy of the local hot state to be time-independent to limit the number of free parameters. If this anisotropy does in fact decay on a time-scale of tens of picoseconds, either because of reorientation of the heat-affected OD group or because of heat diffusion, this will lead to a lower optimally fitted value of the parameter a.

We observe that the parameter a increases with increasing lutidine fraction as a result of several effects. In the first place, water molecules will become more isolated when the lutidine fraction increases. Hydrophobic clustering of lutidine molecules [102,128,129] has been observed for 2,6-lutidine/water and similar systems in the vicinity of the LSCT, and those clusters were reported to vary in size between 0.5 and 4 nm. [105–108] According to ultrasound absorption experiments, the lifetime of these aggregates is on the order of nanoseconds. [105] Hence within the experimentally probed time window, the water molecules will remain enclosed by lutidine molecules. With increasing lutidine concentration, the number of water molecules in the water clusters enclosed by the lutidine aggregates will decrease and the average distance between the clusters will increase. Both effects will diminish the spreading of the heating effect to other, not excited OD vibrations, following the relaxation of an excited OD vibration, and thus increase the value of the parameter a. A second reason that a increases with increasing lutidine fraction is that the reorientation of slow water molecules becomes even slower. The accessible time window of our fs-IR experiment does not allow for a quantification of this further slowing-down, but dielectric relaxation measurements have shown that the reorientation of water molecules near hydrophobic groups becomes slower when the concentration of hydrophobic groups increases, [130] probably as a result of a crowding effect. In addition, with increasing lutidine concentration the relative contribution of the water molecules forming a hydrogen bond to the N atom of lutidine will increase. These water molecules are likely even more slowly reorienting than water molecules near hydrophobic groups due to strong interaction with nitrogen. The enhanced contribution of the N-bonded water molecules to the slow water fraction will thus lead to an average slowing down of the reorientation, which increases the value of a.

A decrease of the temperature is observed to lead to an increase of R_{slow} that comprises both water molecules hydrating the hydrophobic groups of lutidine and water molecules that form a hydrogen bond to the nitrogen atom of lutidine. As the latter hydrogen bond is quite strong, we expect it to be formed at all temperatures, and thus we do not expect a strong change in the density of these hydrogen bonds

with temperature. Hence, the observed increase of the slow water fraction with decreasing temperature ($\sim 50\%$ for X = 0.2) likely originates from the increased fraction of water molecules hydrating the hydrophobic groups of the solute. This indicates that the size of the lutidine clusters decreases with decreasing temperature, thus leading to an increase of the total hydrophobic surface that is exposed to water. According to small-angle neutron scattering (SANS) experiments,[105] the size of the heterogeneities formed in a 2,6-lutidine/water system is weakly dependent on temperature, but the probed temperature range in this study was limited to only 7 K lower than the LSCT. In the same study, a significant decrease of the sizes of the heterogeneities was observed for 2-methylpyridine/water mixtures when this mixture was cooled to 40 K below the LSCT. Like 2,6-lutidine/water, 2-methylpyridine/water also possesses a closed-loop phase diagram and the structure of the solute closely resembles that of 2,6-lutidine. In the present study samples were cooled down to 30 K below LSCT, thus making it highly probable that the cluster size decreases, leading to an increase of the hydrophobic surface exposed to water, and thus of R_{slow}.

An interesting observation is that in contrast to R_{slow}, the parameter a does not show a significant temperature dependence, which can be explained by the presence of a few counteracting effects. With decreasing temperature, the reorientational dynamics of OD groups normally would become slower, which would lead to an increase of the value of a. However, with decreasing temperature the contribution of the hydrophobic hydrating OD groups to the slow water fraction increases relative to the contribution of the OD groups that are hydrogen bonded to N. The hydrophobic hydrating OD groups likely effectively have shorter reorientation dynamics, thus counteracting the increase of the reorientation time that normally would result from a decrease in temperature. The net result of the two effects is that the average reorientation time of the slow OD groups shows little variation in the studied temperature range, with the result that the parameter a does not show a significant temperature dependence.

It is interesting to consider the present findings from the perspective of the thermodynamics of the water/2,6-lutidine mixture. The mixture will be more likely in a single phase state when the Gibbs free energy difference (ΔG) of mixing is more negative. We find strong evidence for increased hydrophobic hydration when the temperature is lowered further below the LSCT. Increased hydrophobic hydration leads to a decrease of the mobility of water molecules involved, which points to a decrease of the possible orientations (realizations) of the water molecules, and thus a decrease of the entropy. Far below the LSCT the formation of lutidine clusters is not strongly pronounced which implies that there is a substantial interaction between water and the hydrophobic groups of the lutidine molecules. At a low temperature, the entropy contribution to the free energy caused by these interactions is low and is apparently compensated by the enthalpic contribution of the strong OD$\cdots$N interactions. At higher T the entropy term becomes more

important, making the expulsion of water and hydrophobic aggregation of luti-dine molecules more favorable. At the LSCT the driving force for hydrophobic aggregation becomes so strong that a full macroscopic phase separation results. At concentrations lower than the critical concentration (X < 0.062) the LSCT will be higher because the entropic effects of hydrophobic hydration and aggregation will be smaller. For X > 0.062 hydrogen bonding between water and lutidine contributes to the decrease of mixing Gibbs free energy difference and the critical temperature increases again. It is interesting to note that the OD···N hydro-gen bonds are almost unperturbed by a temperature change within the studied temperature range (down to 30K below LSCT), implying that hydrophobic hy-dration and aggregation play the most important roles in determining the phase transition conditions. Recent DFT studies indicate that the phase separation at the critical temperature is induced by the cleavage of external hydrogen bonds of 2:1 complexes of lutidine and water.[104] By combining our findings with previously reported results, we conclude that near the LSCT, water molecules that are not involved in strong interactions with the solute tend to interact with each other, rather than being located in the nearest vicinity of the solute. This result implies that the distribution of water molecules shows an increased heterogeneity near the LSCT.

4.6 Conclusions

We studied the dynamics of HDO molecules in 2,6-lutidine/water mixtures near the lower solution critical temperature (LSCT) by probing the OD stretch vibra-tions with polarization-resolved femtosecond infrared pump-probe spectroscopy. Upon the addition of 2,6-lutidine, the vibrational energy relaxation of the OD-stretch vibration is observed to proceed faster in the red wing of the spectrum than in the blue wing. This frequency dependence can be well described with a kinetic relaxation model involving two excited OD-stretch vibrational states that relax with different time constants to the common local hot state. We attributed the frequency dependence of the vibrational relaxation to an increase of the het-erogeneity of the strengths of the hydrogen bonds in the mixture with increasing lutidine concentration, likely as a result of the formation of strong OD···N hydro-gen bonds between HDO and the N-atom of lutidine. This result is corroborated by the rise of a shoulder in the red wing of the linear infrared absorption spectra with increasing 2,6-lutidine concentration. In spite of this increasing contribu-tion of strongly hydrogen-bonded OD groups, the overall vibrational relaxation rate decreases with increasing lutidine fraction, probably because of the increased perturbation and truncation of the hydrogen-bond network of the mixture. The anisotropy dynamics of the transient absorption signal show an increasing offset with increasing lutidine fraction, showing the presence of an increasing fraction of slowly reorienting water molecules. We assign these molecules to water molecules

forming a hydrogen bond to the N atom of lutidine and to water molecules hydrating the hydrophobic groups. The transient absorption signal induced by the local hot state is observed to be anisotropic when the lutidine fraction is larger than 0.15. This anisotropic character indicates that the dissipated energy primarily affects the originally excited water molecules, which implies that a significant fraction of the heat-affected water molecules are slowly reorienting and sufficiently isolated from other water molecules to avoid equilibration of the heating effect due to heat diffusion within the time range of our experiment. We describe the degree by which the anisotropy of the excited OD vibrations is retained in the local hot state with a parameter a. This parameter increases with an increase of the lutidine fraction because the reorientational dynamics of the water molecules effectively slow down and the water molecules become more isolated. This slowing down of the reorientation likely results from the increased contribution to the slow water fraction of water molecules forming hydrogen bonds with the N atom of lutidine. When the temperature of the water-lutidine mixture is decreased, the fraction of slowly reorienting water molecules increases, and no significant change in the parameter a is observed. Both observations indicate that the fraction of water molecules that hydrate the hydrophobic groups of lutidine increases, which means that with decreasing temperature the clusters decrease in size, thereby increasing the overall hydrophobic surface exposed to water.

4.7   Appendix

4.7.1   Linear infrared spectra treatment scheme

In order to accurately extract the shape of the OD-stretch absorption band we performed two series of measurements. The first series consisted of measurements of mixtures of 2,6-lutidine and isotopically diluted water and the second series consisted of solutions with the same lutidine content and normal water (no isotopical dilution). The spectra obtained in the second series were subtracted from spectra from those obtained in the first series. Since the only difference between these two series is the presence of HDO molecules, this procedure yields the spectrum of the OD-stretch vibration.

4.7.2   Description of the local hot state associated anisotropy

An approach to describe the local hot state anisotropy is based on the idea that the state created after the vibrational relaxation partly inherits the anisotropic distribution of the excited OD-groups, similar to the procedure described by Rezus et al.[69] A general expression describing this anisotropy is:

$$R_h(t) = \frac{a \cdot \int_0^t \sum dN_{e,i}(\tau) R_{e,i}(\tau) f(\tau)}{\int_0^t \sum dN_{e,i}(\tau)} \tag{4.3}$$

Here R_h is the anisotropy of the local hot state, a is the fraction of the inherited anisotropy, $R_{e,i}$ is the anisotropy of the ith excited state, $dN_{e,i}(\tau)$ is the decrement of the population of the ith excited state during the period $d\tau$ obtained from the vibrational relaxation kinetic model, and $f(\tau)$ reflects the anisotropy decay of the local hot state.

We find that the expression could be simplified in the following way:

- From equation 4.1 it follows that the anisotropy decay of the excited state is bimodal. We assume that only slow water molecules contribute to the anisotropy of the local hot state. For that reason, we excluded a time-dependent term from the expression for $R_{e,i}$

- Based on the signal-to-noise ratio at a long delay time we find that including a decay of the anisotropy of the local hot state adds an additional parameter to the model without adding an improvement in the fitting quality. For that reason, we consider anisotropy of the local hot state to be non-relaxing ($f(\tau)$ = 1).

- Based on the two previous assumptions, the integral in equation 4.3 contains only time-dependent terms of the summation of $dN_{e,i}(\tau)$ and the integral is divided out by the value $\int_0^t \sum dN_{e,i}(\tau)$. Since the identical set of parameters is used for each $R_{e,i}$, equation 4.3 simplifies to $R_h = a \cdot R_{slow}$
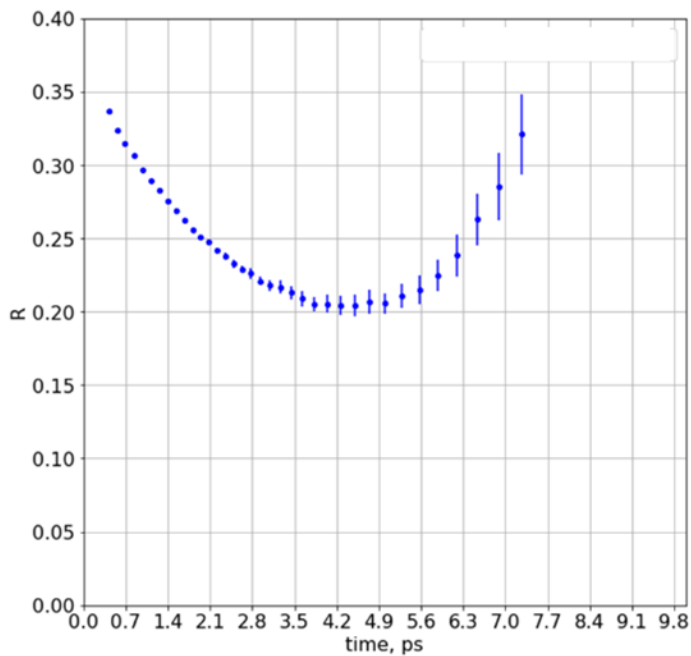
Figure 4.7. Anisotropy dynamics of an X = 0.15 mixture, constructed by subtracting an isotropic local hot state response from the $\Delta\alpha_\parallel$ and $\Delta\alpha_\perp$ data
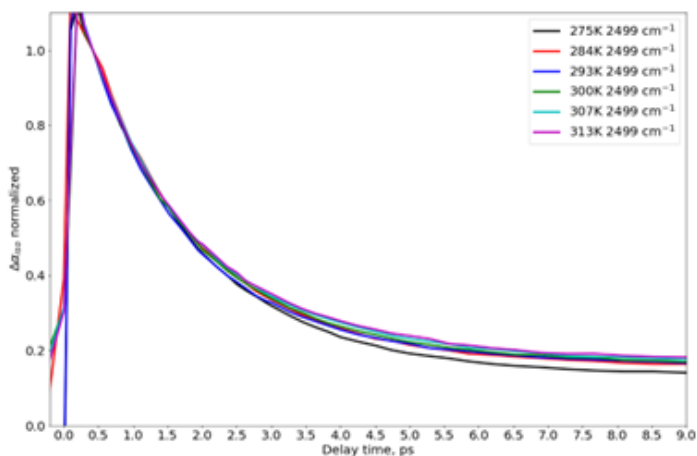
Figure 4.8. Dynamics of $\Delta\alpha_{iso}$ at the center of the bleaching signal of an X = 0.2 mixture at different temperatures

64

5

Ultrafast vibrational dynamics of aqueous acetate and terephthalate*

We study the vibrational population relaxation and mutual interaction of the symmetric stretch (ν_s) and antisymmetric stretch (ν_{as}) stretch vibrations of the carboxylate anion groups of acetate and terephthalate ions in aqueous solution with femtosecond two-dimensional infrared spectroscopy. By selectively exciting and probing the ν_s and ν_{as} vibrations, we find that the interaction of the two vibrations involves both anharmonic coupling of the vibrations and energy exchange between the excited states of the vibrations. We find that the vibrational population relaxation and the energy exchange are both faster for terephthalate than for acetate.

5.1 Introduction

Ultrafast infrared spectroscopy enables the time-resolved study of the vibrational dynamics of molecules in complex and heterogeneous condensed phases. This technique has thus been widely employed to investigate the properties of different functional groups, and their interaction with their molecular-scale environment.[131–134]

One of the most abundant functional groups in (bio)chemical species is the carboxylate group (-COO$^-$). This functional group is often present in small biologically active molecules and in the side-chains of polymers, determining their geometry and charge, thus playing a crucial role in various (bio)chemical processes.[30,32–34,135] The carboxylate group also strongly interacts with metal cations, leading to the formation of metal carboxylates with characteristic coordination numbers. These metal-carboxylate complexes often show important catalytic and photocatalytic activity.[136,137]

The carboxylate (-COO$^-$) group has two coupled vibrational modes: the symmetric C-O stretch vibration (ν_s) and the antisymmetric C-O stretch vibration (ν_{as}), both absorbing in the 6 μm region of the spectrum. These two vibrations are delocalized over the carboxylate group as a result of the sharing of negative charge by the two oxygen atoms, thus making the oxygen atoms equivalent in their binding to the carbon atom.

An interesting example of metal-carboxylate complexes are metal organic frameworks (MOFs). In many MOFs, the terephthalate (1,4 - benzenedicarboxylate) dianion and its derivatives play a crucial role as the linker between positively charged metal ions[89,138–141]. The terephthalate moiety also forms a crucial constituent of commercially produced polyesters such as polyetheleneterephthalate (PET).[142] Another important carboxylate species is acetate (CH$_3$COO$^-$). Acetate is widely used in organic synthesis reactions,[143,144] and plays an important role in many biological processes[145].

The vibrational dynamics of small carboxylates has been investigated with ultrafast infrared spectroscopy techniques, including pump-probe spectroscopy and two-dimensional infrared spectroscopy (2D-IR).[40–43,146] These studies focused on the solvation structure of the ions, their conformation, the interactions with other ions, and on the coupling of the carboxylate stretch vibrations to the C-H vibrations. It was also reported that the ν_s and ν_{as} modes of acetate are coupled.[40,43] However, the precise nature of this coupling could not be studied in detail as these studies were either performed with pump-probe spectroscopy using the same broadband mid-infrared laser pulse for excitation and detection of the separate vibrations,[40] or involved a 2D-IR spectroscopic study of only the ν_{as} mode[43].

Here we report a study of acetate and terephthalate ions in aqueous solution with femtosecond 2D-IR-spectroscopy over a wide frequency range, covering both the absorption spectra of the ν_s and ν_{as} modes. In this study, we selectively excite and probe the different vibrational modes and measure the dynamics of the resulting

nonlinear absorption signals with sub-picosecond time resolution. By measuring the dynamics of the transient absorption changes for different combinations of excited and detected vibrations, we identify the mechanisms by which the two modes interact with each other.

5.2 Experimental

We prepared aqueous solutions of 0.1 M sodium acetate (Sigma-Aldrich anhydrous for molecular biology, $\geq 99.9\%$) and 0.05 M disodium terephthalate (TCI, 99.0%) by mixing the appropriate amounts of salt with D_2O (Aldrich, 99.9 atom % D). We use D_2O instead of H_2O in order to avoid strong absorption of the bending mode of H_2O (δ_{H_2O}) in the absorption region of the ν_{as} vibration of the carboxylates.

The experimental setups as well as the preparation of samples for infrared absorption and 2D-IR measurements are described in sections 3.1, 3.2, and 3.3.

5.3 Results

In Figure 5.1 we show IR absorption spectra of solutions of sodium acetate and disodium terephthalate in D_2O. Acetate shows absorption bands centered at 1415 cm^{-1} and 1565 cm^{-1}, corresponding to the ν_s and ν_{as} vibrations of the carboxylate group. The IR absorption spectrum also shows a weak band at 1350 cm^{-1} corresponding to the CH_3 deformation vibration of acetate[147]. For terephthalate, we observe absorption bands centered at 1380 cm^{-1} and 1575 cm^{-1}, corresponding to the ν_s and ν_{as} vibrations of the carboxylate group. In addition, the spectrum contains a band at 1508 cm^{-1} band that corresponds to a skeletal deformation of the aromatic ring.[142] Potentially, for terephthalate the absorption bands of the ν_s and ν_{as} vibrations could have been split due to coupling of the two carboxylate groups of the terephthalate anion.[42,142] However, in view of the symmetry of terephthalate the in-phase ν_s and the out-of-phase ν_{as} vibrations are expected to have a negligible transition dipole moment, since the vibration-induced modulations of the dipole moment of the two carboxylate groups cancel each other.[42] As a result, only the out-of-phase ν_s and the in-phase ν_{as} vibrations are visible in the spectrum.

In Figure 5.2 we show two-dimensional spectra of a sodium acetate (a, b) and a disodium terephthalate solutions (c, d). The blue regions correspond to a negative absorption change (bleaching and stimulated emission), while the red regions reflect positive absorption changes (induced absorption). When the ν_s region is probed (Figure 5.2a, c), two clear signals are observed: a so-called diagonal signal at the excitation frequency of ν_s and a so-called cross-peak signal at the excitation frequency of ν_{as}. Similarly, when the ν_{as} region is probed (Figure 5.2b, d), we
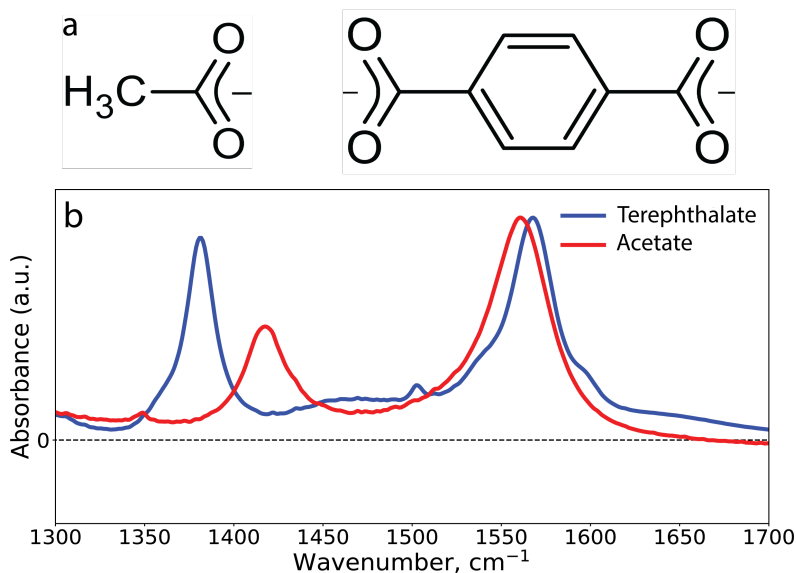
Figure 5.1. a. Chemical structures of acetate and terephthalate anions; b. Linear infrared absorption spectra of solutions of 0.1 M sodium acetate and 0.05 M disodium terephthalate in D_2O.

observe a diagonal signal at the excitation frequency of ν_{as} and a cross-peak signal at the excitation frequency of ν_s.

The bleaching and induced absorption 2D-IR signals are somewhat tilted, especially for the diagonal signals, indicating a correlation of the excitation and the detection frequencies. With increasing delay, this frequency-frequency correlation decays. The dynamics of the frequency-frequency correlation function of the ν_{as} mode of the carboxylate anion group has been extensively studied before for aqueous trifluoroacetate,[41] aqueous oxalate,[41] and aqueous acetate[43]. These dynamics provided information on the structural dynamics of the molecular environment of the carboxylate groups, in particular of the solvation shell and the dynamics of the water molecules forming the solvation shell.[41–43] In this report, we will not further elaborate on the dynamics of the frequency-frequency correlation function of the vibrations of the carboxylate group.

The cross-peak signals reflect changes in the absorption bands of vibrations that are not excited by the excitation pulse, resulting from the coupling to other vibrations that were excited by the excitation pulse. The cross-peak signals in the 2D-IR spectra of Fig. 5.2 clearly show that for both ions the ν_s and ν_{as} vibrations are coupled. We also measured the anisotropy $R(\omega_{detection}, \omega_{excitation}, T)$ of the diagonal and cross-peak signals, as shown in Figure 5.6. For the diagonal signals
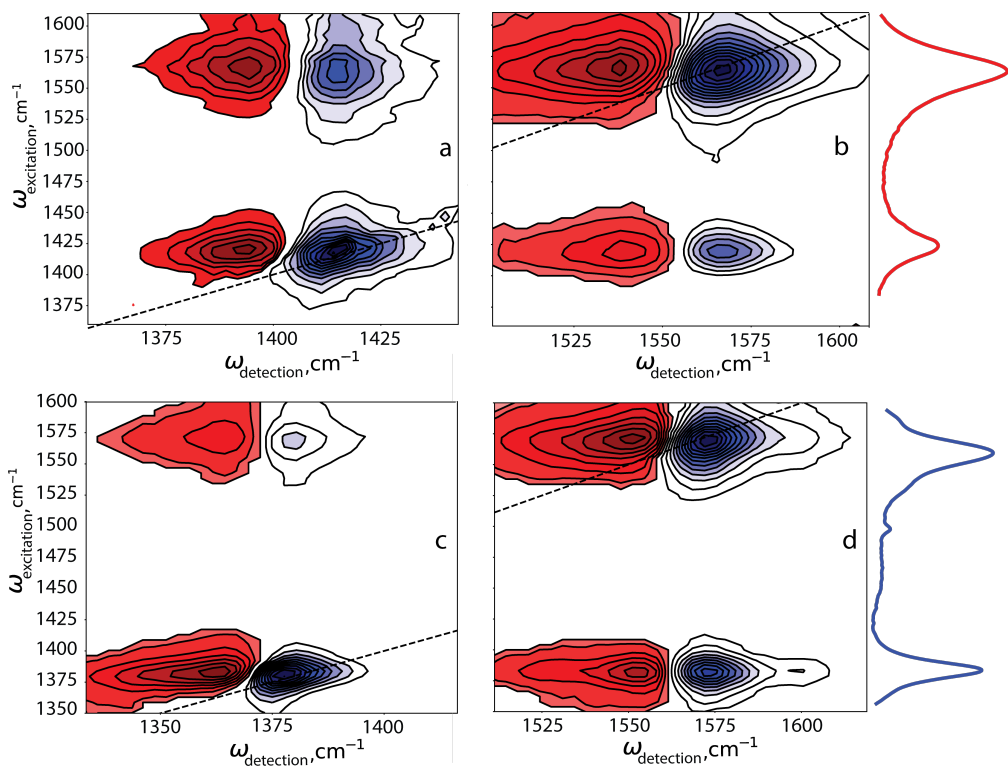
Figure 5.2. Isotropic two-dimensional infrared spectra of solutions of sodium acetate (a,b) and disodium terephthalate (c,d) at a waiting time T of 0.3 ps. The signals are presented as a function of the detection frequency (horizontal axis) and the excitation frequency (vertical axis), and are drawn as contour plots of equal signal amplitude in steps of 3%. The red and blue colors represent positive and negative absorption changes respectively. At the right-hand side, we show the linear absorption spectra to clarify the assignment.
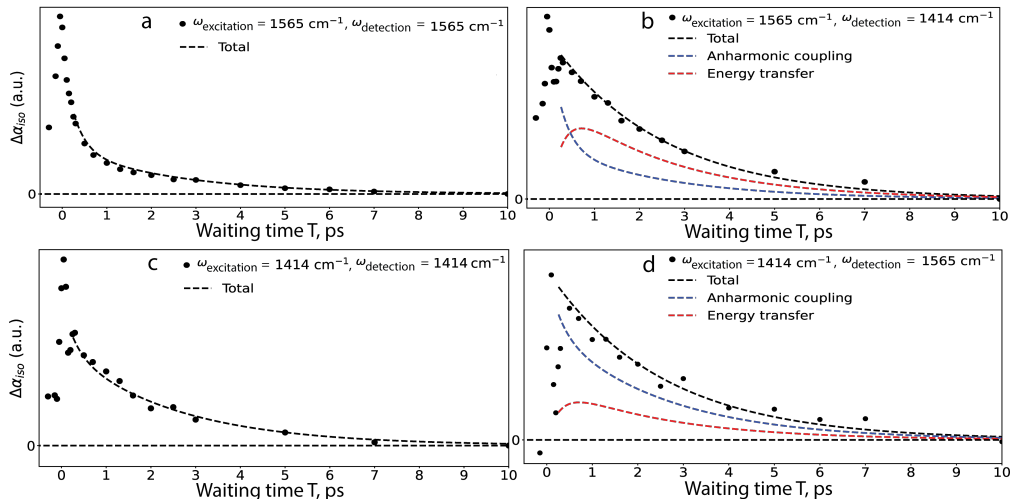
Figure 5.3. Isotropic transient absorption signals measured for a 0.1 M solution of acetate in D_2O as a function of waiting time T, detected at the maximum frequency of the ν_s/ν_{as} absorption band obtained by integrating the 2D signals over an excitation frequency interval of 100 cm^{-1} around the maximum frequency of the ν_s/ν_{as} absorption band. a. Exciting the ν_{as} signal and detecting at the maximum frequency of the ν_{as} band (diagonal ν_{as} signal); b. Exciting the ν_{as} signal and detecting at the maximum frequency of the ν_s band (downhill cross-peak signal); c. Exciting the ν_s signal and detecting at the maximum frequency of the ν_s band (diagonal ν_s signal); d. Exciting the ν_s signal and detecting at the maximum frequency of the ν_{as} band (uphill cross-peak signal). The black dashed lines represent fits to the dynamics, which in the case of the cross-peak signals contain two contributions (blue and red dashed lines), according to the model described in the text.

we observe a value of R of ~ 0.4, as expected for a system of randomly oriented dipolar oscillators. For the cross-peak signals we observe a value of R of ~ -0.2, which means that the transition dipole moment of the detected vibration is oriented at an angle of $\sim 90°$ with respect to the transition dipole moment of the excited vibration. This finding perfectly agrees with the expected mutual orientation of the ν_{as} and ν_s modes. Moreover, as we show in Figure 5.7, the anisotropy of the diagonal peaks and cross-peaks shows very little dynamics. This lack of dynamics can be explained from the large size of the acetate and terephthalate ions, making their molecular reorientation relatively slow compared to e.g. water.

To identify the precise nature of the interaction between the ν_s and ν_{as} vibrations of acetate, we investigate the dynamics of the diagonal and cross-peak signals as shown in Figure 5.3. The curves are obtained by plotting the resulting 2D-IR signal at the detection frequency that corresponds to the center of the detected

bleaching signal as a function of the waiting time T, and by integrating the 2D signals over an excitation frequency interval of 100 cm^{-1} around the maximum frequency of each absorption band.

The diagonal signal of the ν_{as} vibration shown in Figure 5.3 has bimodal dynamics (Figure. 5.3a). The initial fast decay component has also been observed in previous studies of carboxylate anions and has been assigned to energy transfer from the excited ν_{as} vibration to the ν_s vibration, enabled by fluctuations of the local environment.[40,42] Such an energy transfer between ν_{as} and ν_s is expected to lead to a delayed maximum of the cross-peak signals.[148,149] However, in Figures 5.3b, d we do not see a delayed maximum of the cross-peak signal neither for the downhill cross-peak, signal (Figure 5.3b), nor for the uphill cross-peak signal (Figure 5.3d). Both cross-peak signals are observed to rise with the cross-correlation of the excitation and detection pulses. Hence, we conclude that energy transfer is not the only mechanism leading to the cross-peak signals.

Another coupling mechanism that gives rise to cross-peak signals is anharmonic coupling of the vibrations. When two vibrations are anharmonically coupled, the excitation of one of the vibrations leads to a change of the frequency and/or cross-section of the other vibration. If this coupling mechanism dominates, the cross-peak signal closely follows the dynamics of the excited vibrations, meaning that the rise of the signal will follow the cross-correlation of the excitation and detection pulses, and the decay of the signal will follow the relaxation dynamics of the excited vibration.[133,148] The dynamics of the downhill cross-peak signal (exciting ν_{as}, detecting ν_s vibration) would thus closely follow the dynamics of the diagonal signal of the ν_{as} vibration in case the interaction of the vibrations would be dominated by anharmonic coupling. However, the dynamics of the downhill cross-peak signal clearly differ from that of the diagonal signal of the ν_{as} vibration as the cross-peak signal does not show the fast component that is observed for the diagonal signal. Based on these observations, we conclude that the cross-peak signal is the result of the combined effect of energy transfer and anharmonic coupling.

We fit the dynamics of the diagonal and cross-peak signals of Figure 5.3 with the relaxation model shown in Figure 5.4. In Figure 5.4 the different vibrational states are defined in the basis of the uncoupled symmetric and asymmetric stretch vibrations. The state (0,0) represents the ground states of the two vibrations. This model is similar to the approach that has been used to fit the population relaxation dynamics of the pump-probe dynamics of the ν_{as} mode of trifluoroacetate,[41] oxalate,[42] and acetate[43]. The model includes energy transfer between ν_s and ν_{as} with k_{sa} and k_{as}, and vibrational relaxation of the separate ν_s and ν_{as} modes to the vibrational ground state with rate constants k_s and k_a, respectively. The exchange rates obey the Boltzmann ratio $k_{sa} = k_{as} \cdot exp(-\hbar\Delta\omega/kT)$, where $\Delta\omega$ is the frequency difference between the centers of the absorption bands of ν_s and ν_{as}, which is $\sim$ 150 cm^{-1} for acetate. As the exchange rate constants are
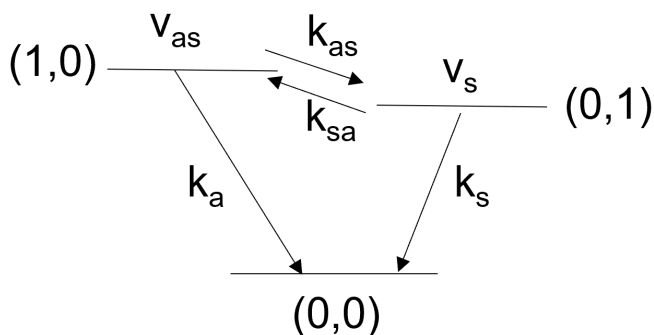
Figure 5.4. Schematic picture of the vibrational relaxation model used for fitting the dynamics of Figs. 5.3 and 5.5.

large compared to the vibrational relaxation rate constants k_s and k_a, we observe a weighted average of these latter two rate constants after the energy exchange has equilibrated, i.e. at delay times > 1 ps, which makes it impossible to determine the separate rate constants. Therefore, we took the relaxation rate constants k_s = k_a to be the same.

In fitting the data, we include an anharmonic coupling contribution to the cross-peak signals with the same amplitude for the downhill and uphill cross-peak signal. These contributions follow the dynamics of the excited vibration (i.e. the dynamics of the diagonal signal of ν_{as} for the downhill cross peak and the dynamics of the diagonal signal of ν_s for the uphill cross peak). We did not include the data at T < 0.25 ps in the fitting, as in this waiting time interval the signals show significant contributions from cross-phase modulation of the excitation and detection pulses and resonant coherent interactions (sometimes denoted as coherent artifacts).

The model of Figure 5.4 provides an excellent fit of all the data. The parameters extracted from the fit are: k_s = k_a ∼ 0.45 ps^{-1}, k_{as} ∼ $2k_{sa}$ = 1.5 ps^{-1}. We also find that the cross-peak signals are best fitted with significant contributions from both anharmonic coupling and energy transfer. The ratio between the maximum contribution resulting from energy transfer and the maximum of the contribution due to anharmonic coupling equals 0.39 and 0.19 for the downhill and uphill cross-peak signals, respectively. The difference between these ratios reflect the slower uphill energy transfer compared to the downhill energy transfer.

In Figure 5.5 we show the dynamics of the diagonal and cross-peak signals observed in the 2D-IR spectra measured for a solution of 0.05 M disodium terephthalate in D_2O. The observed dynamics are qualitatively similar to the dynamics observed for the acetate solution. The diagonal ν_{as} signal shows a bimodal decay, and the downhill cross-peak signal of Figure 5.5b differs from the diagonal ν_{as} sig-
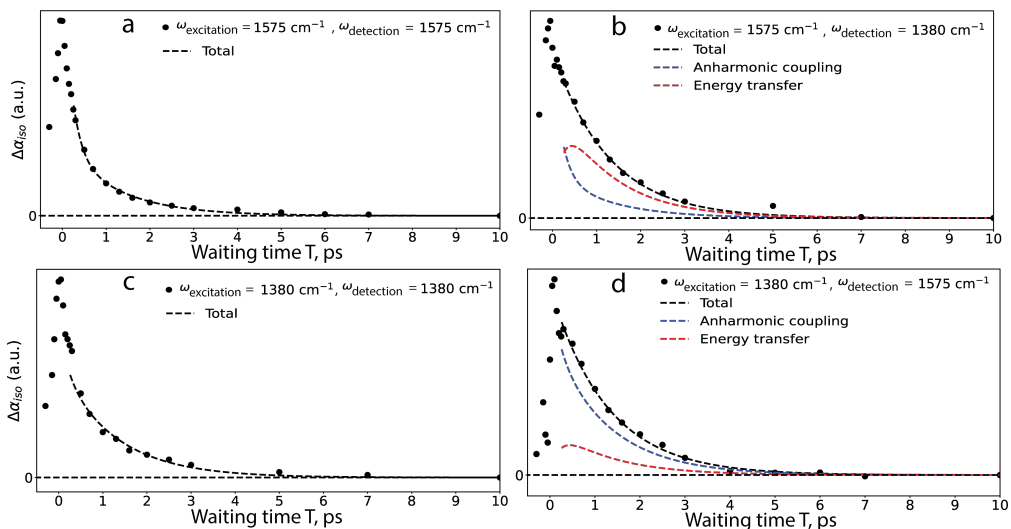
Figure 5.5. Isotropic transient absorption signals measured for a 0.1 M solution of terephthalate in D_2O as a function of waiting time T, detected at the maximum frequency of the ν_s/ν_{as} absorption band obtained by integrating the 2D signals over an excitation frequency interval of 100 cm^{-1} around the maximum frequency of the ν_s/ν_{as} absorption band. a. Exciting the ν_{as} signal and detecting at the maximum frequency of the ν_{as} band (diagonal ν_{as} signal); b. Exciting the ν_{as} signal and detecting at the maximum frequency of the ν_s band (downhill cross-peak signal); c. Exciting the ν_s signal and detecting at the maximum frequency of the ν_s band (diagonal ν_s signal); d. Exciting the ν_s signal and detecting at the maximum frequency of the ν_{as} band (uphill cross-peak signal). The black dashed lines represent fits to the dynamics, which in the case of the cross-peak signals contain two contributions (blue and red dashed lines), according to the model described in the text.

Table 5.1. Rate constants of the vibrational relaxation and energy exchange of the ν_s and ν_{as} vibrations of acetate and terephtalate obtained by fitting the experimental data of Figures 3 and 5 to the kinetic model shown in Figure 4

	$k_a = k_s$, ps^{-1}	k_{as}, ps^{-1}	k_{sa}, ps^{-1}
acetate	0.45	1.5	0.75
terephthalate	0.8	2.7	1

73

nal and does not show a delayed maximum. We fitted the dynamics of the diagonal and cross-peak signals with the model of Figure 5.4. The parameters extracted from the fit are: $k_s = k_a \sim 0.8$ ps^{-1}, $k_{as} \sim 2.7 k_{sa} = 2.7$ ps^{-1}. The larger difference in ratio between the exchange rates of terephthalate compared to acetate originates from the larger energy difference between the maxima of the absorption bands: $\Delta\omega \sim 195$ cm^{-1}. The ratio between the maximum contribution caused by energy transfer and the maximum of the contribution due to anharmonic coupling are 0.41 and 0.15 for the downhill and uphill cross-peak signals, respectively.

5.4   Discussion

The results show that the interaction between the ν_s and ν_{as} vibrations of the carboxylate anion groups of acetate and terephthalate involves both energy transfer and anharmonic coupling. These two interactions are associated with a different waiting-time dependence of the cross-peak signal, and thus potentially the spectral shape of the cross-peak signal could change as a function of the waiting time T. However, we did not observe such a dependence of the spectral shape of the cross-peak signal on T. This can be explained from the fact that the frequency shifts due to the diagonal anharmonicity and the anharmonic coupling of the vibrations are smaller than the spectral widths of the absorption bands. As a result, the spectral shape of the cross-peak signal is largely determined by the spectral width of the detected vibrational band, and the frequency shifts resulting from the diagonal anharmonicity and the anharmonic coupling only determine the amplitudes of the positive and negative signals. It would be interesting to tune the relative contributions of anharmonic coupling and energy transfer to the cross-peak signal. An obvious method to achieve this tuning would be to change the interaction with the solvent, as the energy transfer process strongly relies on the compensation of the energy mismatch by the solvent, whereas the anharmonic coupling is relatively independent of the interaction with the solvent. The interaction with the water solvent can potentially be varied by changing the temperature. However, the temperature dependence of the energy transfer processes in aqueous media is hard to predict and can be quite anomalous, i.e. slow down with increasing temperature. Another option would be to change the nature of the solvent. Varying the relative contribution of anharmonic coupling and energy transfer to the cross-peak signal will be subject of a future study.

The vibrational dynamics of acetate has been studied before, with pump-probe spectroscopy using the same broadband mid-infrared laser pulse for excitation and detection of the vibrations,[40] and with 2D-IR spectroscopy of only the ν_{as} mode[43]. In the study of Ref.[40] it was found that both ν_{as} and ν_s show a bimodal decay, with the contribution of the fast component being larger when pumping and probing the ν_{as} mode than when pumping and probing the ν_s mode. For the origin of this fast component different mechanisms were proposed, including energy transfer between

the ν_{as} and ν_s modes. However, it was not possible to make a definite assignment because in the study of Ref.[40] it was not possible to selectively excite one vibration and to detect the other vibration. In the 2D-IR study of Ref.[43] the population dynamics of the excited ν_{as} mode were fit to a relaxation model that also includes the relaxation of the ν_s mode, and the energy exchange of the two modes. However, in this study the ν_s mode was not excited and detected and only the ν_{as} mode was measured.[43] From the fit of the population dynamics of the excited ν_{as} mode, the exchange rate constant k_{as} was estimated to be 2.09 ps^{-1}, which is not very different from the value of $k_{as} \sim 1.5$ ps^{-1} that we obtain in the present work by studying the diagonal and cross-peak signals of ν_{as} and ν_s.

The rate constants resulting from the fits of data for both ions are summarized in Table I. We find that the vibrational relaxation and the energy exchange rates are both higher for terephthalate than for acetate. This difference is likely caused by the fact that the larger chemical structure of terephthalate gives rise to a much denser manifold of intramolecular vibrational combination states at the energy of the excited ν_s and ν_{as} vibrations than is the case of acetate. In particular, in terephthalate the vibrations of the carboxylate groups will be coupled to combination modes of the aromatic ring that are not present in acetate. As a result, the vibrational relaxation will be faster for terephthalate, leading to larger values for k_a and k_s than in acetate, and the compensation of the energy mismatch between the excited ν_s and ν_{as} vibrations required for the energy transfer is more efficient in terephthalate, leading to larger values for k_{as} and k_{sa}.

It is interesting to compare the vibrational relaxation and energy exchange dynamics of terephthalate with the dynamics of the oxalate anion that like terephthalate contains two carboxylate anion groups but differently from terephthalate does not contain an aromatic ring. In Ref.[42] the dynamics of the ν_{as} mode of oxalate were studied, and fitting these dynamics to an exchange model that also included the not directly observed ν_s mode, yielded a k_a of 0.98 ps^{-1}, a k_s of 0.45 ps^{-1}, and an energy exchange rate constant k_{as} of 1.55 ps^{-1}. The vibrational population relaxation rates of oxalate are thus similar to those of terephthalate and accelerated by a factor of ~ 2 compared to acetate.

Interestingly, the rate constants for energy exchange between ν_s and ν_{as} are similar for oxalate[42] and for acetate, but significantly smaller than we observe for terephthalate. It thus appears that the larger intramolecular vibrational density of states of the oxalate ion compared to acetate is effective in accelerating the vibrational population relaxation of ν_s and ν_{as}, but not in accelerating the energy exchange between these modes. The similarity in energy exchange rate of oxalate and acetate suggests that this process relies on the interaction with the solvent, i.e. the energy mismatch between ν_s and ν_{as} is compensated by low-frequency solvent modes, as this interaction is expected to be very similar for oxalate and acetate. This notion agrees with the interpretation of the origin of the decay of the frequency-frequency correlation functions of the ν_{as} modes of acetate and

oxalate. [42,43] The faster energy exchange of terephthalate compared to both oxalate and acetate suggests that the interactions between the carboxylate groups and the surrounding water molecules are enhanced by the nearby presence of the aromatic ring of the terephthalate ion. Another possible explanation for the faster energy exchange of terephthalate is that a coupling to the low-frequency modes of the aromatic ring aids in compensating the energy mismatch between the excited states of the ν_s and ν_{as} modes.

5.5   Conclusions

We performed femtosecond two-dimensional infrared (2D-IR) spectroscopy of the symmetric (ν_s) and antisymmetric (ν_{as}) vibrations of the carboxylate anion groups of acetate and terephthalate in aqueous solution. In this study we selectively excite and detect both vibrations, thus obtaining diagonal signals (exciting and detecting the same vibration), a downhill cross-peak signal (exciting ν_{as} and detecting ν_s), and an uphill cross-peak signal (exciting ν_s and detecting ν_{as}). We find that the cross-peak signals are not delayed with respect to the diagonal signals and show dynamics that differ from the dynamics of the diagonal signals. This finding indicates that the cross-peak signals result from the combined effect of energy transfer between the first excited states of the ν_s and ν_{as} vibrations, and anharmonic coupling of these two vibrations. We model the diagonal and cross-peak signals with a model in which we include the vibrational population relaxation of the first excited states of the ν_s and ν_{as} vibrations to the ground state, and their energy change with rate constants that obey detailed balance. In this modeling we include an anharmonic coupling contribution to the cross-peak signals that follows the dynamics of the excited vibration (i.e. the dynamics of the diagonal signal of ν_{as} for the downhill cross peak and the dynamics of the diagonal signal of ν_s for the uphill cross peak). From the modeling we obtain for acetate rate constants $k_s = k_a$ of ~ 0.45 ps^{-1}, and an energy exchange rate constant $k_{as} \sim 2k_{sa}$ of 1.5 ps^{-1}, and for terephthalate rate constants $k_s = k_a$ of ~ 0.8 ps^{-1}, and an energy exchange rate constant $k_{as} \sim 2.7k_{sa}$ of 2.7 ps^{-1}. We thus find that the terephthalate ion shows a faster vibrational relaxation than acetate which likely can be explained from the denser manifold of accepting vibrational combination states of the larger terephthalate ion, probably also involving the aromatic ring modes of terephthalate. The energy exchange is also faster for terephthalate than for acetate, which may be due to the effect of the aromatic ring of terephthalate on the water molecules that solvate the carboxylate anion groups, leading to a more effective compensation of the energy mismatch between the excited states of the ν_s and ν_{as}, or due to a direct coupling to low-frequency aromatic ring modes, thereby facilitating the compensation of the energy mismatch.

5.6   Appendix
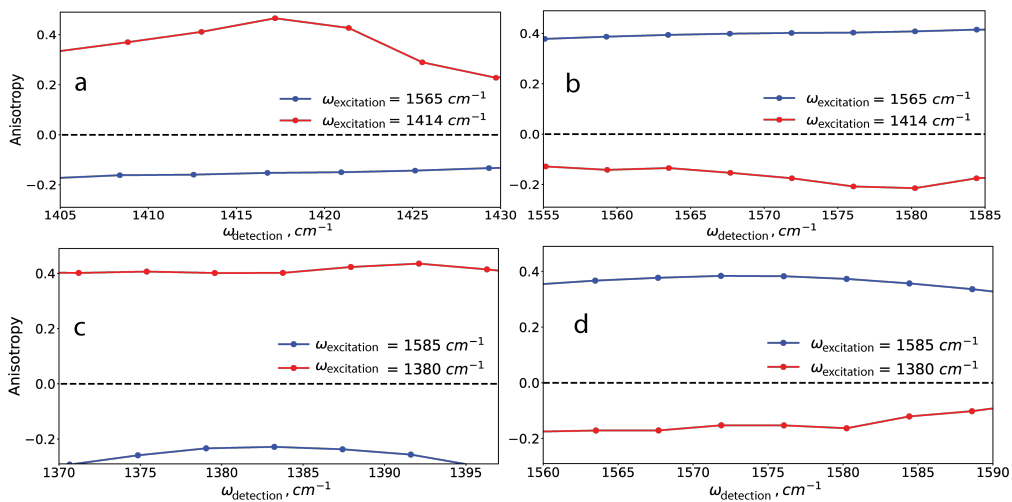
Figure 5.6. Anisotropy of the transient signals as a function of detection frequency at selected excitation frequencies for a. acetate, detecting ν_s; b. acetate, detecting ν_{as}; c. terephthalate, detecting ν_s, d. terephthalate, detecting ν_{as}
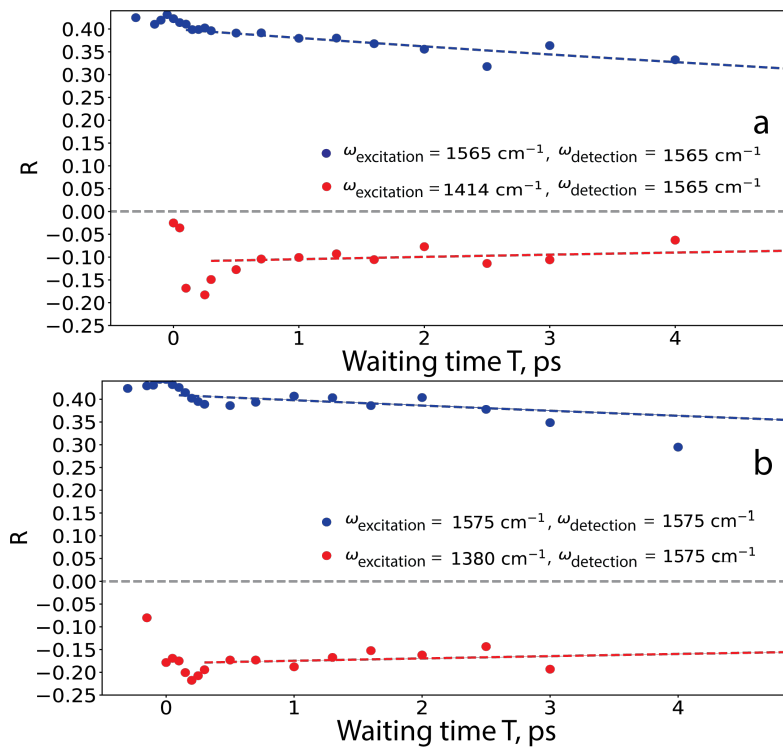
Figure 5.7. Anisotropy of the transient signals as a function of waiting time T at the center of the ground state bleach of diagonal and uphill cross-peaks for a. Acetate, detecting ν_{as}; b. terephthalate, detecting ν_{as}; dashed lines are guides to an eye

6

Direct Probing of Vibrational Interactions in UiO-66 Polycrystalline Membranes with Femtosecond Two-Dimensional Infrared Spectroscopy*

UiO-66 is a benchmark metal-organic framework (MOF) that holds great promise for the design of new functional materials. In this work, we perform 2D-IR measurements of polycrystalline membranes of UiO-66 grown on c-sapphire substrates. We study the dynamics of the symmetric and antisymmetric stretch vibrations of the carboxylate groups of the terephthalate linker ions, and find that these vibrations show a rapid energy exchange and a collective vibrational relaxation with a time constant of 1.3 ps. We also find that the symmetric vibration of the carboxylate group is strongly coupled to a vibration of the aromatic ring of the terephthalate ion. We observe that the antisymmetric carboxylate vibrations of different terephthalate linkers show rapid resonant (Förster) energy transfer with a time constant of $\sim$ 1 ps.

6.1 Introduction

Metal-organic frameworks (MOFs) are a class of crystalline materials in which metal ions or clusters of metal ions are connected by organic linkers to form extended three-dimensional structures. These materials possess well-defined nanopores and nanochannels, the size and integrity of which can be tuned over a wide range by varying the metal cations and linkers.[150–153] As such, different MOF-based functional materials have been prepared and successfully applied in catalysis[154], chemical sensing,[155] separation techniques,[156] and electrochemistry[157,158].

An important MOF family is UiO, the members of which consist of $Zr_6O_4(OH)_4$ building-blocks forming a crystal structure by 12-fold coordination with aromatic dicarboxylate linkers.[89,159] These structures show exceptional stability, even under aggressive conditions, thus making UiOs promising for multiple applications.[160,161] For example, UiO crystalline membranes have been prepared and used for water desalination, gas separation, storage, and pervaporation.[162–164] The range of applications can be further extended by preparing UiO-type MOFs for which aromatic dicarboxylate linkers are functionalized.[162,165–167] Such functionalization may thus enable the preparation of stable MOF membranes showing pronounced proton conductivity and/or redox activity, which would be highly promising for designing new fuel cells and electrocatalysis platforms.[166,168]

A crucial parameter determining the properties of UiO membranes is the number density of missing linkers, forming defects in the crystal structure. The deviation from perfect stoichiometry depends on the preparation procedure and often can be controlled, enabling a tuning of the extent of linker-metal interactions.[138,169,170] The defect content influences the adsorption and separation properties,[171,172] the catalytic activity,[173] and the Brønsted and Lewis acidity[174] of a UiO membrane. The metal-linker interactions are thus very important for the properties of UiO MOFs, and a detailed understanding of these interactions is a prerequisite for the rational design of new UiO-based materials. Various experimental and theoretical approaches have been used to study the dynamics of UiO derivatives. Recent studies addressed the proton conductivity of UiO MOFs,[175] and the role of defects in this process,[176] the dynamics of water adsorbed in the MOF pores,[177] and the relaxation kinetics following electronic excitation of the linker[178,179].

A powerful tool for obtaining structural and dynamical information of chemical systems is two-dimensional infrared spectroscopy (2D-IR). By exciting vibrational modes of molecules or ions with femtosecond infrared pulses, this method discloses unique information on the relaxation kinetics of vibrationally excited states, which in turn provides information on vibrational couplings, inter- and intramolecular energy transfer, and the reorientation dynamics of small molecular species. These processes often strongly depend on the solvation and coordination of the target functional groups. Over the last decade, 2D-IR has been successfully applied to investigate the structural elasticity of UiO-66 prepared as powder samples,[180] and

of MIL-53(Al)[181]. In this work, we present a 2D-IR investigation of polycrystalline UiO-66 membranes grown on c-sapphire plates. This MOF is the first member of the UiO series and comprises terephthalate (1,4-benzenedicarboxylate, BDC^{2-}) as a linker (Figure 2.3a).

6.2 Experiments

The experimental setups as well for infrared absorption and 2D-IR measurements are described in sections 3.1, 3.2, and 3.3. The preparation procedure of UiO-66 membranes on c-sapphire substrates and sample characterization are described in section 3.7.

6.3 Results

The preparation of UiO-66 membranes on solid substrates is a topic of strong current interest. Recently, the preparation of UiO-66 membranes and its derivatives on gold substrates,[162] sapphire rods,[163] α-Al_2O_3 disks[182], and ZrO_2@γ-Al_2O_3 fibers[183] have been reported. However, to the best of our knowledge, no protocols using flat c-sapphire substrates have been reported. We prepared UiO-66 samples by a solvothermal reaction of $ZrCl_4$ and terephthalic acid ($BDCH_2$) dissolved in DMF, using acetic acid as a growth modulator. The crystallinity of the membranes was confirmed with XRD analys shown in Figure 6.5. We find that the grains of the polycrystalline membrane have preferential (111)-orientation and that the membrane preserves cylindrical symmetry. The sample profilometry showed that the membranes have $\sim$ 600-700 nm thickness as shown in Figure 6.6. As can be seen from Figure 6.7, thermo-gravimetric analysis (TGA) shows that this preparation method results in $\sim$ 42% of missing linkers, which means that the polycrystalline film can be considered a highly defective material.

We further characterize the prepared sample with FTIR spectroscopy. In Figure 6.1b we compare the infrared absorption spectrum of the prepared UiO-66 membranes with the spectrum of a powder sample. The spectra look very similar in the frequency region above 1400 cm^{-1}, which indicates that the local environment of the linkers is very similar in the film and in the powder. We assign the bands at 1585 cm^{-1} and at 1395 cm^{-1} to the antisymmetric stretch (ν_{as}) and symmetric stretch (ν_s) vibrations of the carboxylate anion groups of the linker, respectively. The 1510 cm^{-1} band is assigned to the 19a band of the aromatic ring of the linker (further ν_{Ph}). This ring mode has the same symmetry as the ν_s vibration.[184–187] The difference between the spectra at lower frequencies is due to strong sapphire substrate absorption, which precludes a reliable determination of the film absorption values in this frequency region. In our femtosecond two-dimensional infrared (2D-IR) experiment, we excite molecular vibrations (ν_s, ν_{Ph} and ν_{as}) of
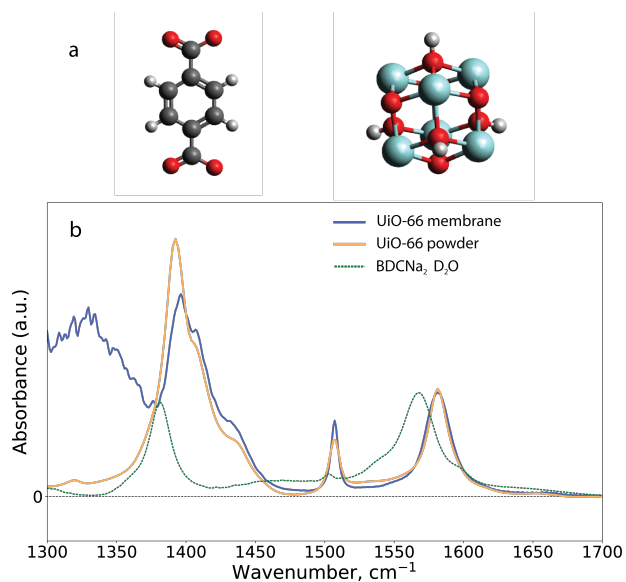
Figure 6.1. a: Chemical structures of the terephthalate (BDC^{2-}) linker (left) and $Zr_6O_4(OH)_4$ cluster (right). Black, white, red and light-blue spheres represent carbon, hydrogen, oxygen and zirconium atoms respectively. b: Linear infrared absorption spectra of UiO-66 membranes grown on a sapphire substrate measured in transmission geometry (blue), of UiO-66 powder measured in ATR geometry (orange), and of 0.4M D_2O solution of disodium terephthalate (BDCNa$_2$, green dashed line). The spectra are normalized with respect to the absorption of the ν_{as} band

the terephthalate linker of UiO-66 membranes that absorb in the 6 μm region. We measure the excitation-induced absorption change as a function of the excitation and detection frequencies, the waiting time T between the excitation and detection pulses, and their mutual polarization direction. The isotropic transient absorption dynamics provide information on the dynamics and mechanism of the interactions involving the excited vibrations. The depolarization dynamics of the transient absorption changes reveal the timescale of intermolecular energy transfer between the carboxylate groups of the linkers. An intrinsic challenge related to fs-IR experiments on solid samples is the strong scattering of the excitation light by grains of the studied polycrystalline material. This scattering can overwhelm the signal of the weaker infrared detection pulse, and thus often special techniques such as using index matching liquids[181] or advanced phase cycling schemes[180] have been used to extract reliable data. The UiO-66 membranes that we study scatter light to a much smaller extent than powder samples and the effects of the remaining scattering can be sufficiently suppressed by creating a sub-cycle delay using a wobbler. Sapphire substrates have already been successfully used to grow UiO-66 membranes,[163,164] and its broad transparency window as well as the absence of significant non-linear effects upon interaction with intense infrared pulses, enable 2D-IR experiments in transmission geometry.

In Figure 6.2 we show 2D-IR spectra of the membrane sample. Due to the limited transparency window of sapphire, we can only measure 2D-IR spectra with $\omega_{detection} > 1500$ cm^{-1} which excludes a study of the response at $\omega_{detection}$ corresponding to ν_s. However, since the membrane is superposed on the substrate, we are able to detect the transient absorption signals induced by the excitation of ν_s at $\omega_{detection}$ corresponding to ν_{Ph} and ν_{as}.

In Figure 6.2a we observe clear responses on the diagonal line at $\omega_{excitation} = \omega_{detection} = 1510$ cm^{-1} and $\omega_{excitation} = \omega_{detection} = 1585$ cm^{-1}, that correspond to the excitation and detection of ν_{Ph} and ν_{as} vibrations, respectively. We also observe several off-diagonal peaks (cross-peaks), indicating a coupling of the different vibrations. Particularly, at $\omega_{excitation} = 1395$ cm^{-1} uphill cross-peaks appear at $\omega_{detection} = 1510$ cm^{-1}, indicating vibrational coupling of the ν_s mode to the ν_{Ph} mode ($\nu_s \rightarrow \nu_{Ph}$), and at $\omega_{detection} = 1585$ cm^{-1}, indicating vibrational coupling of the ν_s mode to the ν_{as} mode ($\nu_s \rightarrow \nu_{as}$). At $\omega_{excitation} = 1585$ cm^{-1} and $\omega_{detection} = 1510$ cm^{-1} we observe a downhill cross-peak, indicating vibrational coupling between ν_{as} and ν_{Ph} ($\nu_{as} \rightarrow \nu_{Ph}$).

As can be seen from Figure 6.2b, all signals are still pronounced at a waiting time T = 7 ps, but due to vibrational relaxation their relative strengths have become different. The signal of $\nu_{Ph} \rightarrow \nu_{as}$ at $\omega_{excitation} = 1510$ cm^{-1} and $\omega_{detection} = 1585$ cm^{-1} gets more pronounced than at earlier waiting time. Figures 6.10 and 6.11 show the amplitude of this signal at shorter waiting times.

To identify the mechanism of vibrational relaxation and the nature of the vibrational coupling in UiO-66 membranes, we measure the dynamics of the diagonal

and cross-peak signals. In Figure 6.3a and 6.3b we show the dynamics of diagonal peak signal corresponding to ν_{as} and the $\nu_s \to \nu_{as}$ uphill cross-peak. We find that both dynamics can be well described with an exponential relaxation with a time constant of ~ 1.3 ps to an end-level that grows with the same time constant and that shows no further change in amplitude within 200 ps (Figures 6.11 and 6.12 of section 6.6). The fact that the diagonal ν_{as} and the $\nu_s \to \nu_{as}$ cross-peak signals show similar relaxation dynamics, points at an ultrafast equilibration between the v=1 states of the ν_{as} and ν_s vibrations, which is most likely due to energy transfer occurring within the time scale of the cross-correlate of the excitation and detection pulses. The growth of the end-level can be explained from thermal effects: the energy released as a result of the vibrational relaxation affects the shape and position of the vibrational bands, yielding a change of the transient absorption signal that is often referred to as a hot state signal.

Next, we take a closer look at the relaxation dynamics of the transient absorption signals involving the ν_{Ph} vibration. In Figure 6.3c, we show the dynamics of the diagonal peak corresponding to the excitation and detection of ν_{Ph}. Compared to the dynamics displayed in Figure 6.3a and 6.3b, this signal decays much more slowly which indicates that the v=1 state of ν_{Ph} shows a much slower relaxation than the v=1 states of the stretch vibrations of the carboxylate group. The signal decays to a negligible end-level, which means that no pronounced thermal effects are observed for the diagonal signal of the ν_{Ph} vibration.

In Figure 6.3d we present the dynamics of the $\nu_s \to \nu_{Ph}$ cross-peak signal. This signal shows a decay that cannot be well described with a single exponential time constant, and a clear non-zero end level. We find that the dynamics shown in Figure 6.3c and 6.3d can be consistently described with a model in which the v=1 state of ν_{Ph} has an intrinsic vibrational relaxation time constant of ~ 6.7 ps, and in which the ν_{Ph} vibration is coupled to the ν_s vibration by two different mechanisms: anharmonic coupling and energy transfer. The anharmonic coupling leads to an instantaneous perturbation of the vibrational potential of the ν_{Ph} following the excitation of the ν_s vibration. This perturbation leads to a frequency shift of the ν_{Ph} vibration, and thus to a transient absorption change at the detection frequency of the ν_{Ph} vibration that will follow the dynamics of the excitation of the ν_s vibration. Therefore the $\nu_s \to \nu_{Ph}$ cross-peak signal will show the 1.3 ps decay time constant of the excited ν_s vibration. This component accounts for the fast relaxation component of the cross-peak signal (Figure 6.3d, blue dashed line). The energy transfer from ν_s to ν_{Ph} leads to a contribution to the cross-peak signal that shows a delayed growth with a time constant ~ 6.9 ps, followed by a relaxation with the time constant of ~ 6.7 ps of the vibrational relaxation of the v=1 state of the ν_{Ph} vibration (Figure 6.3d, green dashed line). The uphill energy transfer time constant of ~ 6.9 ps of ν_s to ν_{Ph} is related to a downhill energy transfer time constant of ν_{Ph} to ν_s in accordance with detailed balance $k_{up} = k_{down} \cdot exp(-\hbar\Delta\omega/kT)$, where $\Delta\omega$ is the frequency difference between the

centers of the absorption bands of ν_s and ν_{Ph}, which is $\sim$100 cm^{-1}. This energy exchange process is accounted for in describing the diagonal ν_{Ph} signal dynamics in Figure 6.3c. Finally, the growth of the end-level of the cross-peak (Figure 6.3d, red dashed line) is due to both the relaxation of the ν_s vibration and the ν_{Ph} vibration, the latter getting populated as a result of the energy transfer. Given the significantly smaller contribution of the energy transfer to the cross-peak signal, the growth of the end level of the $\nu_s \rightarrow \nu_{Ph}$ cross-peak signal is dominated by the relaxation of the excited ν_s vibration. The signals of the $\nu_{as} \rightarrow \nu_{Ph}$ and $\nu_{Ph} \rightarrow \nu_{as}$ cross-peaks are much weaker than that of the $\nu_s \rightarrow \nu_{Ph}$ cross-peak, as can be seen from Figure 6.2a. By further analyzing the dynamics of these cross-peak signals (see Figure 6.12), we conclude that the vibrational coupling between ν_{as} and ν_{Ph} is much weaker than between ν_s and ν_{Ph}. The main coupling mechanism between these vibrations is anharmonic coupling, which implies that the dynamics of the cross-peak signals are determined by that of the excited vibration.

In Figure 6.4 we show the anisotropy of the excited state of the ν_{as} vibration. To obtain purely the anisotropy dynamics of this excited state, we subtracted the hot-state contributions to the measured $\Delta\alpha_{\parallel}$ and $\Delta\alpha_{\perp}$ signals prior to constructing the anisotropy parameter. The initial anisotropy value is $\sim$ 0.4, which is the value expected for isotropic materials. The anisotropy is observed to decay on a picosecond time scale. Considering that in crystalline material the terephthalate linkers are strongly bound to metal ions, reorientation is not expected to take place on a picosecond timescale. Therefore, we conclude that the observed anisotropy decay is due to excitation transfer between closely spaced and differently oriented linker species. Similarly to Nishida et al,[180] we find that these dynamics can be well described with $Ae^{-\sqrt{(t/\tau_{transfer})}}$. This expression originates from the Förster model for resonant energy exchange in isotropic materials. We obtain an excitation energy transfer time $\tau_{transfer}$ of $\sim$ 1 ps.
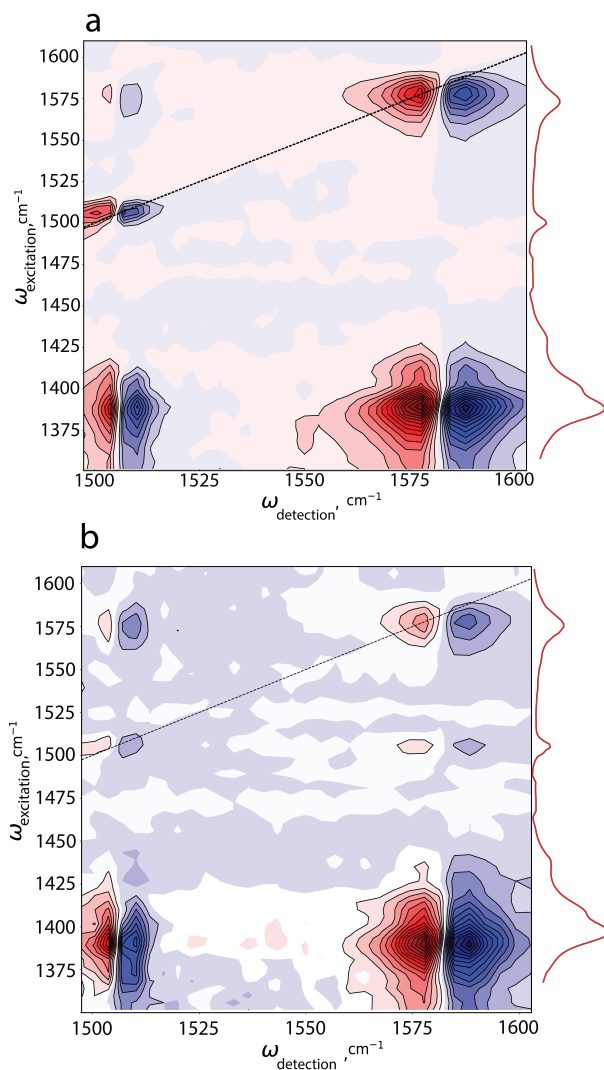
Figure 6.2. Two-dimensional infrared spectra of UiO-66 membranes grown on sapphire substrates measured at different waiting times. Figure a: T = 0.3 ps; b: T = 7 ps. The spectra are plotted as a function of the excitation frequency (vertical axis) and the detection frequency (horizontal axis). The inset on the right-hand side shows the linear infrared absorption spectrum to clarify the assignment, and the black dashed diagonal line corresponds to $\omega_{detection} = \omega_{excitation}$. The spectra are scaled relative to the transient absorption maxima at each waiting time T.
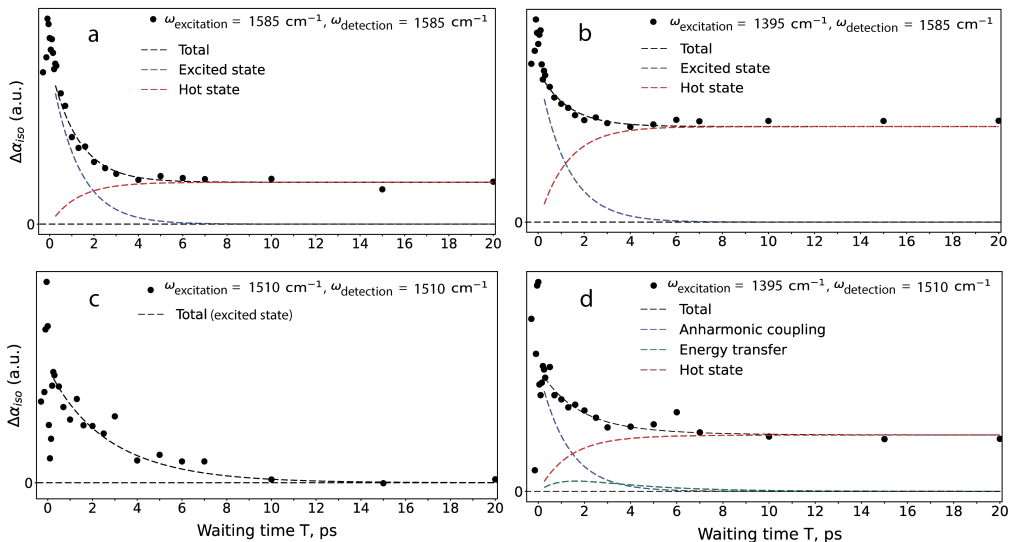
Figure 6.3. Isotropic transient absorption signals measured for UiO-66 membranes as a function of waiting time T, obtained by integrating the 2D signals over an excitation frequency interval of 20-50 cm^{-1} around the maximum frequency of the absorption bands. Figure a: Exciting ν_{as} and detecting at the maximum frequency of the ν_{as} band (diagonal ν_{as} signal); b: Exciting ν_s and detecting at the maximum frequency of the ν_{as} band ($\nu_s \rightarrow \nu_{as}$ cross-peak signal); c: Exciting ν_{Ph} and detecting at the maximum frequency of the ν_{Ph} band (diagonal ν_{Ph} signal); d: Exciting ν_s and detecting at the maximum frequency of the ν_{Ph} band ($\nu_s \rightarrow \nu_{Ph}$). The black dashed lines represent fits to the dynamics, which contain two or three signal contributions (blue, red and green dashed lines), according to the model described in the text.
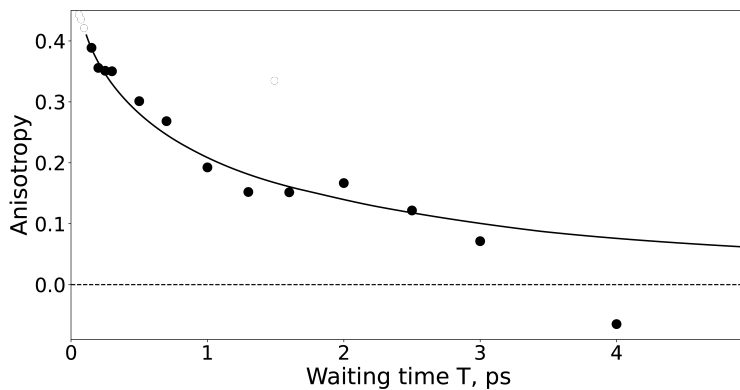
Figure 6.4. Hot state corrected anisotropy dynamics of ν_{as} diagonal peak signal. The solid line represents a fit of the data to a resonant (Förster) energy exchange model.

6.4 Discussion

The infrared absorption spectrum of the terephthalate linker in the UiO-66 structure is quite different from that of the terephthalate dianion in an aqueous solution. Firstly, the cross-section of the ν_s vibrational mode is almost twice as large as that of the ν_{as} mode in the MOF structure, while in the solution spectrum these bands have nearly the same amplitude. Interestingly, for disodium terephthalate powder the cross-section of the ν_s is also larger than that of the ν_{as} band, as can be seen in Figure 6.8. These findings show that the direct interaction of terephthalate with metal cations leads to a significant redistribution of the charge density and bond strengths in the terephthalate structure, thus significantly altering the transition dipole moments of the carboxylate stretch vibrations. We also find that the absorption band of the ν_{Ph} vibration gets much stronger in the MOF structure compared to terephthalate in aqueous solution. A similar effect is observed for solid disodium terephthalate. The ν_{Ph} vibration has the same symmetry and orientation of its transition dipole as the ν_s vibration, and the observed enhancement of the ν_{Ph} vibration is likely due to the interaction between the two vibrations and the increased cross-section of the ν_s vibration.

We find that the ν_s and ν_{as} vibrations of the terephthalate ion show an ultrafast energy equilibration when terephthalate constitutes the linker ion of UiO-66. This result differs from what was observed for the aqueous terephthalate dianion solution. The observations for aqueous solution described in chapter 5 indicated the presence of both anharmonic coupling and energy transfer that could be distinguished from each other. This means that most likely the interaction of the terephthalate linker with the Zr^{4+} cations not only changes the cross-sections of the ν_s and ν_{as} vibrations but also induces faster energy exchange between these vibrations. The intrinsic vibrational relaxation time constant of ~ 1.3 ps that we extract for the equilibrated ν_s and ν_{as} vibrations in the solid sample, is very close to the vibrational relaxation time constant of these vibrations observed for aqueous terephthalate, suggesting that the collective vibrational relaxation rate of the carboxylate stretch vibrations is only weakly dependent on the ion environment.

Thanks to the significant enhancement of the cross-section of the ν_{Ph} vibration, we also observe clear transient signals associated with this vibrational mode for UiO-66. We also observe pronounced anharmonic coupling and vibrational energy exchange between ν_{Ph} and ν_s. The interaction between ν_{Ph} and ν_{as} is observed to be much weaker, which can be explained from a simple transition dipole-dipole coupling model.[74] According to this model, the interaction is stronger for ν_{Ph} and ν_s because the transition dipole moments of these vibrational modes are parallel while the transition dipole moments of ν_{as} and ν_{Ph} are perpendicular to each other. The intrinsic vibrational relaxation of the ν_{Ph} mode is observed to be much slower than for the ν_s and ν_{as} vibrations, which indicates that this vibration has a quite different relaxation pathway.

In previous time-resolved vibrational spectroscopy studies of MOFs the relaxation of other types of vibrations was investigated. For loaded MIL-53(Al) MOFs the stretching vibration of the deuterated bridging hydroxyl referred to as μ_2-OD was found to show a relaxation time constant of $\sim$30-150 ps, depending on the degree of loading.[181] For the C-O-stretching vibration of a carbonyl probe functionalized linker in UiO-66 powder, a bimodal decay was observed, with a 4-5 ps component and a 40-60 ps component.[180] The O-D-stretching vibration of μ_2-OD in MIL-53(Al) thus shows a significantly slower relaxation compared to that in aqueous systems.[25,69] At the same time, the vibrations of carboxylate and carbonyl groups of the linker ions in the MOF structure show relaxation rates that are similar to those observed for these vibrations in aqueous or non-polar solutions.

We observe that the vibrational relaxation of the carboxylate stretch vibrations leads to a significant residual signal associated with the creation of a long-living hot state. The likely reason for this observation is that the linker density is quite high, which implies that a large amount of thermal energy will accumulate in a limited volume following vibrational excitation and relaxation. Such a heating effect is not observed for an aqueous terephthalate solution and is also much less pronounced in a MIL-53(Al) sample, which can be well explained from the much lower density of μ_2-OD groups compared to that of terephthalate linkers in the UiO-66 membranes.

The relative contribution of the hot state to the overall signal is quite different for the diagonal and cross-peak signals shown in Figure 6.3. For the ν_{as} diagonal peak we obtain a ratio between the decaying and growing contributions of $\sim$ 4, while for the $\nu_s \rightarrow \nu_{as}$ signal this ratio is $\sim$ 1.75. The diagonal signal of ν_{Ph} shows practically no end-level, while the cross-peak signal $\nu_s \rightarrow \nu_{Ph}$ shows a clear non-zero end level. The relative amplitude of the hot state signal depends on the cross-sections of the excited and detected vibrations, as well as on the strength of coupling between them. For the cross-peak signal $\nu_s \rightarrow \nu_{Ph}$, the end level is relatively high because the initial signal relies on the anharmonic coupling of the two vibrations, which yields a weaker signal than a diagonal signal, while the final signal (the hot-state end level) is determined by the total energy absorbed from the excitation pulse (see section 6.6). The excited ν_s vibration has a large cross-section meaning that a lot of energy is absorbed, thus leading to a relatively large thermal effect.

The observation of the hot state signal means that thermalization of the energy of the excited vibrations results in an immediate red-shift of the vibrational bands of the carboxylate group. Recently, similar red-shifts have been shown to indicate a loosening of metal carboxylate linkages in a broad range of carboxylate-based MOFs.[188] Hence, our results show that any heat dissipated in the MOF will lead to a loosening of the MOF linkages on a picosecond timescale. This information is important for further mechanistic studies involving MOFs with a broad range of (photo)catalytic functionalities.

We find that the anisotropy of the excitation of the ν_{as} vibration rapidly decays due to resonant energy transfer between differently oriented terephthalate ions. Interestingly, as described in **Chapter 5**, the ν_{as} vibrations of terephthalate ions in aqueous media show quite slow anisotropy dynamics, which can be explained from the much larger mutual distance of the terephthalate ions in solution. In that case the anisotropy dynamics primarily result from the reorientation of the ion. It should be noted that the energy transfer between the ν_{as} and the ν_s does not contribute to the anisotropy decay of the ν_{as}, as the accepting mode (ν_s) absorbs at a different frequency than the probed mode (ν_{as}). Hence, this energy transfer only leads to a change of the total transient absorption signal at the ν_{as} frequency, but not of the anisotropic character of this signal.

For MIL-53(Al) a limited anisotropy decay for the μ_2-OD vibration was observed, which was explained with a wobbling in a cone model, i.e. orientational diffusion within a limited solid angle.[181] Resonant (Förster) energy transfer has also been observed for the C-O stretching vibration of the carbonyl group that is attached to the aromatic ring of a fraction of terephthalate linkers in UiO-66 powders.[180] In this study an acceleration of the anisotropy and central line slope dynamics were observed upon increasing the fraction of functionalized linkers.[180] The timescale of the observed decay was significantly longer (10-50 ps), even for the highest functionalized linker loadings (14%), than the ~ 1 ps transfer time constant that we find for the anisotropy decay of the ν_{as} vibration of the carboxylate group of the terephthalate linker. This difference can be well explained from the fact that the vibrations of the carboxylate groups of the terephthalate linkers are at a much shorter relative distance than the carbonyl groups of a fraction of functionalized terephthalate linkers: in the UiO-66 structure the nearest neighboring carboxylate groups are attached to the same Zr^{4+} cation, and thus very close to each other. The transfer rate between the vibrations of the carboxylate groups is thus expected to be quite sensitive to the linker defect content, which will be the subject of future studies.

6.5 Conclusions

In summary, in this work we presented a new protocol for preparation of polycrystalline films of UiO-66 on flat c-sapphire substrates. These metal organic frameworks consist of Zr^{4+} ions connected by terephthalate linkers. The advantage of this protocol is that the samples are prepared in a single-step solvothermal process which does not involve preparation of the precursors such as Zr-based clusters. Additionally, to the best of our knowledge, no protocols using flat c-sapphire substrates have been reported. The sapphire substrates have a broad transparency window in the optical frequency range which is promising for applications in photocatalysis and electrochemistry. Furthermore, the membranes prepared according to the protocol contain high concentration of missing linkers.

Highly defective materials have been proven to be applicable in the absorptive removal of pollutants,[172] gas separation,[182] and catalysis[169].

We studied the prepared UiO-66 films with Fourier Transform Infrared (FTIR) spectroscopy and 2D-IR spectroscopy in the fingerprint region. Compared to terephthalate ions in aqueous solution, we find that the cross-sections of the ν_s carboxylate stretch vibration and the ν_{Ph} are strongly enhanced, probably as a result of the interaction with the Zr^{4+} ions. The 2D-IR studies revealed strong vibrational coupling between the ν_s and ν_{as} stretch vibrations of the carboxylate group, as well as between the ν_s vibration and the ν_{Ph} vibrational modes. We find that the ν_s and ν_{as} vibrations show an ultrafast energy exchange and thus relax together with the same effective vibrational relaxation time constant of ~ 1.3 ps. The absorption of ν_{Ph} band shows a slower intrinsic vibrational relaxation with a time constant of ~ 6.7 ps. The ν_s and ν_{Ph} modes are observed to be anharmonically coupled and to show energy exchange, with an uphill energy transfer time constant of ~ 6.9 ps. The measured transient absorption signals show a significant non-zero signal at long delay times that we attribute to a hot state resulting from the vibrational relaxation. We find that the anisotropy dynamics of the excitation of the ν_{as} vibrations can be well modelled with a Förster energy exchange model with a time constant of 1 ps. This relatively fast energy transfer can be explained from the close proximity of the carboxylate groups of differently oriented terephthalate linkers in the UiO-66 MOF.

6.6 Appendix

6.6.1 Sample characterization
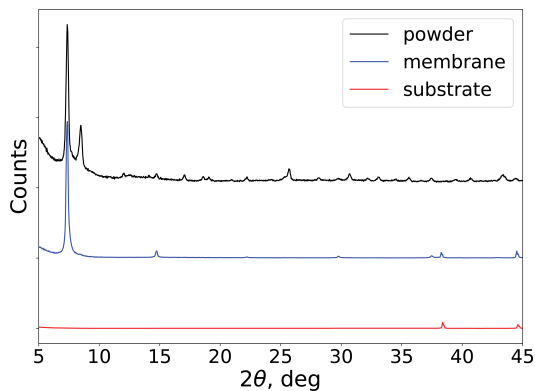
Figure 6.5. X-ray diffraction patterns of the UiO-66 prepared in the solvothermal process. The absence of the peak at $2\theta = 8.5°$ corresponding to (200)-crystallographic plane of the membrane pattern points at preferential (111)-orientation of the grains of the membrane. With such orientation the cylindrical symmetry of the sample is preserved
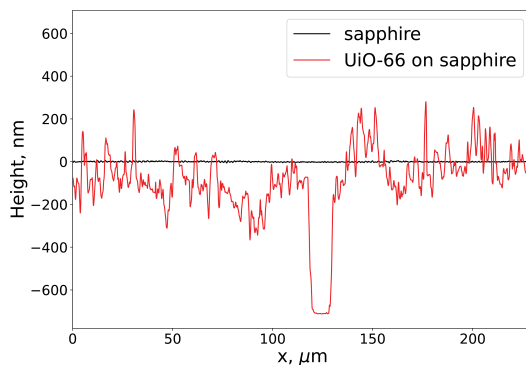
Figure 6.6. Profile of the UiO-66 polycrystalline membrane. The dip at ~ 125 μm corresponds to a trench in a film which shows ~ 700 nm thickness of the film

93
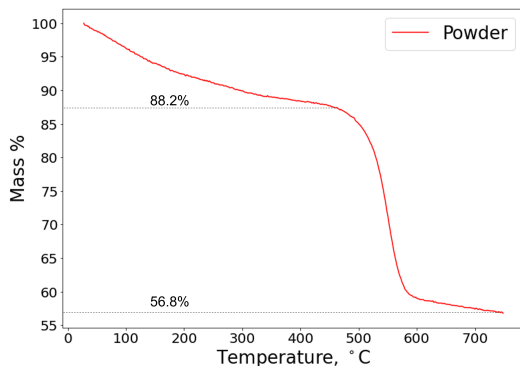
Figure 6.7. TGA curves for UiO-66 powder. The initial mass-loss of 11.8% corresponds to removal of residual DMF and acetic acid used as a solvent and a crystal growth modulator respectively. After this drop, the MOF is fully desolvated and dehydrated, and the drop of 31.5% at $\sim 550\,^\circ$C corresponds to a total MOF decomposition. For perfect MOF structure, the mass-loss of 54.6% is expected at the last step[89], which means that the material under study is missing $\sim 42\%$ of the linkers in its structure which is approximately 5 of 12 linkers per metal-oxo cluster
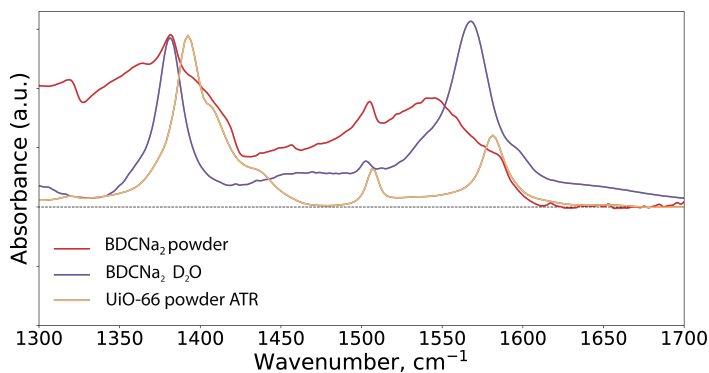
Figure 6.8. Comparison of infrared absorption spectra of aqueous disodium terephthalate, solid disodium terephthalate and UiO-66

94
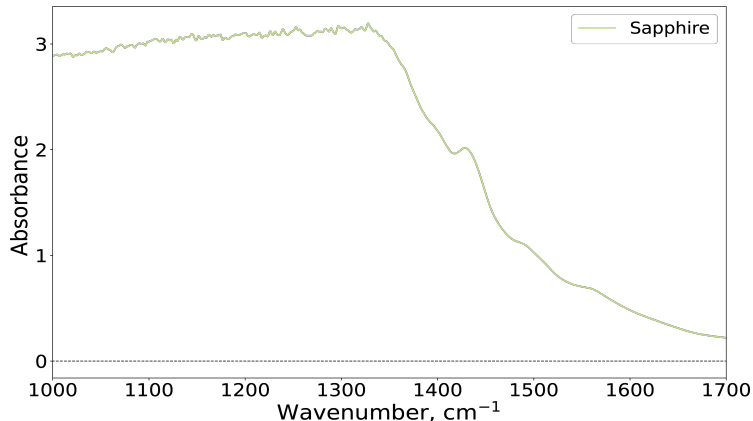
Figure 6.9. Infrared absorption spectrum of the sapphire substrate

6.6.2 Analysis of the dynamics of $\nu_{as} \rightarrow \nu_{Ph}$ and the $\nu_{Ph} \rightarrow \nu_{as}$ cross-peak signals

The dynamics of $\nu_{as} \rightarrow \nu_{Ph}$ and $\nu_{Ph} \rightarrow \nu_{as}$ cross-peak signals are analyzed in Figure 6.12. As can be clearly seen, the $\nu_{as} \rightarrow \nu_{Ph}$ and $\nu_{Ph} \rightarrow \nu_{as}$ cross-peaks show almost no relaxation and predominately consist of a small, non-relaxing end-level. These signals appear to be much weaker than $\nu_s \rightarrow \nu_{Ph}$ cross-peak as can be seen from Figure 6.2 . Moreover, neither the dynamics of ν_{as} diagonal signal nor that of the $\nu_s \rightarrow \nu_{as}$ cross-peak signal seem to be significantly influenced by the interaction with ν_{Ph}. We find that the dynamics of the $\nu_{Ph} \rightarrow \nu_{as}$ cross peak can be described as a combination of a decaying contribution with the same dynamics as the ν_{Ph} diagonal peak, followed by the hot state contribution that grows with the same rate as the decay. The dynamics of $\nu_{as} \rightarrow \nu_{Ph}$ cross-peak is also described by combining a decaying and a growing contribution but the time constant of these dynamics coincide with that of the relaxation of ν_{as}. The fact that the decaying contribution has the same dynamics as the excited vibration, points at anharmonic coupling as the interaction mechanism between the ν_{Ph} and ν_{as} vibrations.
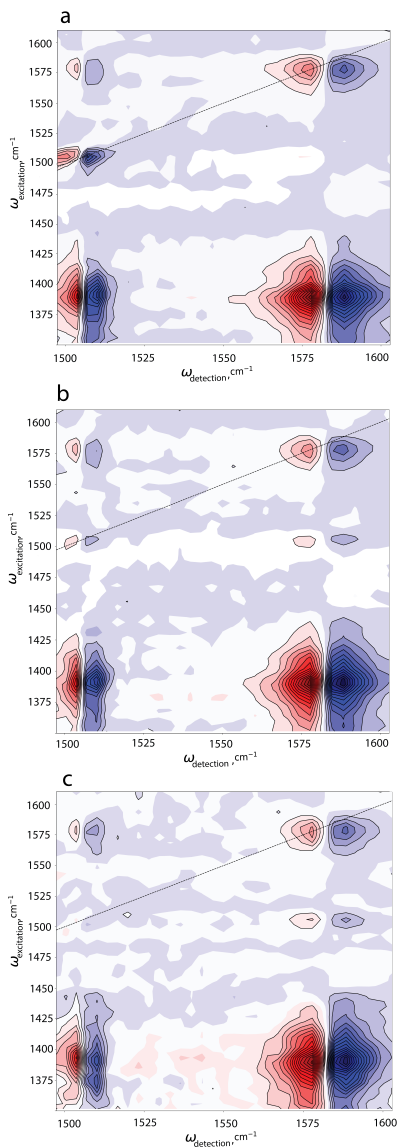
Figure 6.10. Two-dimensional infrared spectra of UiO-66 membranes grown on sapphire substrates at different waiting times a. T = 2 ps b. T = 10 ps c. T = 200 ps. The spectra are plotted as a function of the excitation frequency (vertical axis) and the detection frequency (horizontal axis). The black dashed diagonal line corresponds to $\omega_{detection} = \omega_{excitation}$. The spectra are scaled relative to the transient absorption maxima at each waiting time T.
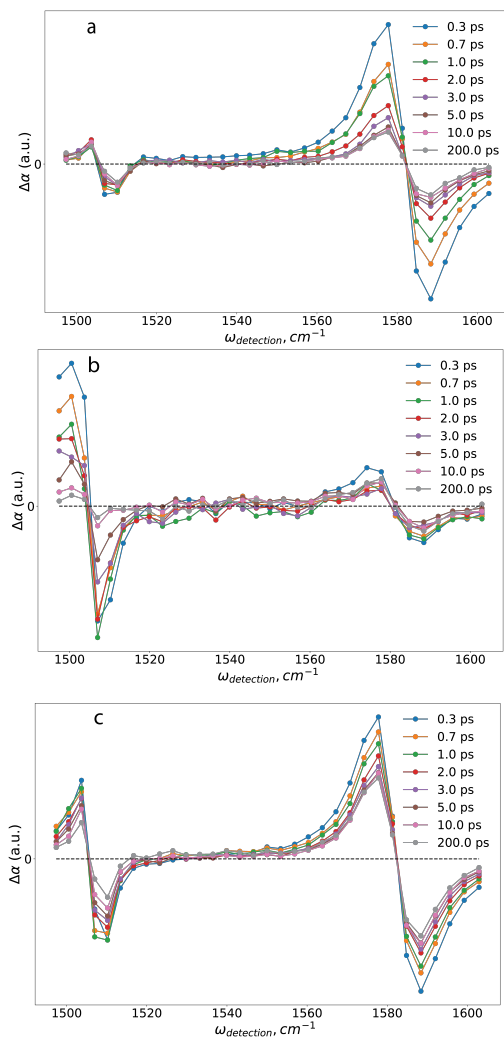
Figure 6.11. Isotropic transient absorption spectra measured for UiO-66 membranes as a function of waiting time T, and detection frequency $\omega_{detection}$ obtained by integrating the 2D signals over an excitation frequency interval of 20-50 cm^{-1} a. Exciting ν_{as} b. Exciting ν_{Ph} c. Exciting ν_s
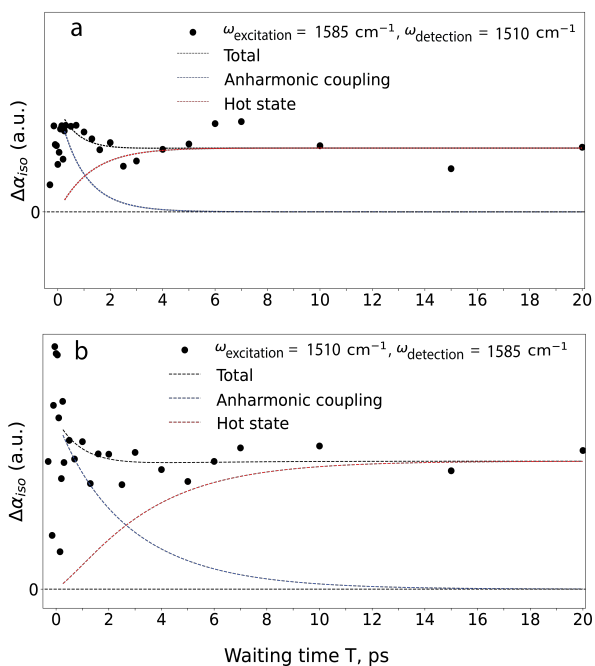
Figure 6.12. Isotropic transient absorption signals measured for UiO-66 membranes as a function of waiting time T, obtained by integrating the 2D signals over an excitation frequency interval of 20-50 cm^{-1} around the maximum frequency of the absorption bands. Figure a: Exciting ν_{as} and detecting at the maximum frequency of the ν_{Ph} band ($\nu_{as} \rightarrow \nu_{Ph}$ cross-peak signal); b: Exciting ν_{Ph} and detecting at the maximum frequency of the ν_{as} band ($\nu_{Ph} \rightarrow \nu_{as}$ cross-peak signal)

6.6.3 Analysis of the temperature dependence of the FTIR spectra of the UiO-66 membranes and interpretation of the signals at long waiting times
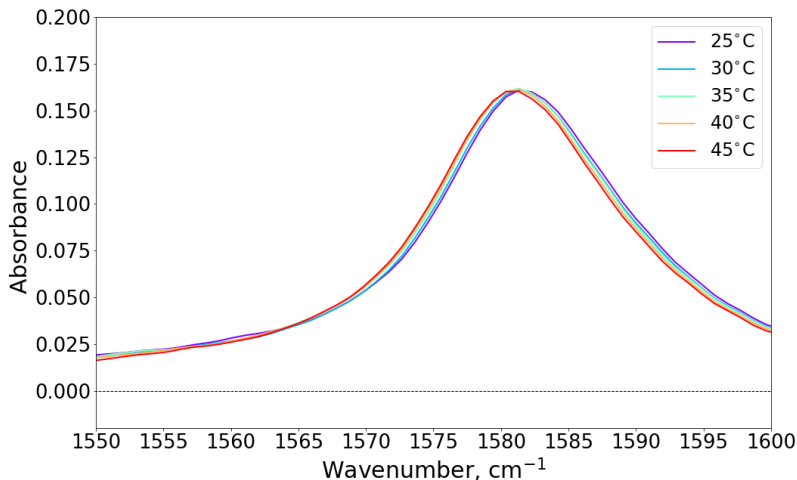
Figure 6.13. Infrared absorption spectra of UiO-66 membranes at elevated temperatures

To corroborate the thermal nature of the transient signals at long waiting time, we have performed a study of the temperature dependence of the membrane FTIR spectrum. In Figure 6.13 we show the spectra detected at elevated temperatures in the frequency region corresponding to the ν_{as} vibration. As can be clearly seen from Figure 6.13, increasing the temperature leads to a shift of the maximum of the band to lower frequencies without significantly changing the absorption cross-section. The magnitude of the shift is on the order of a few cm^{-1} and proportional to the temperature increase. By subtracting the spectrum detected at room temperature from the spectra detected at elevated temperature, we obtain the thermal difference spectra that we show in Figure 6.14. Comparison of Figure 6.14 with Figure 6.11 shows that the shape of the thermal difference spectrum is very similar to the difference absorption spectra observed at waiting times > 10 ps with 2D-IR spectroscopy. As the shift of the band is much smaller than the bandwidth, subtraction of the spectra yields an anti-symmetric dispersive shape of which the amplitude scales with the magnitude of the shift. This shape is similar to that of the excited state spectrum because the diagonal anharmonicity is also much smaller than the width of the absorption band. We calculated the
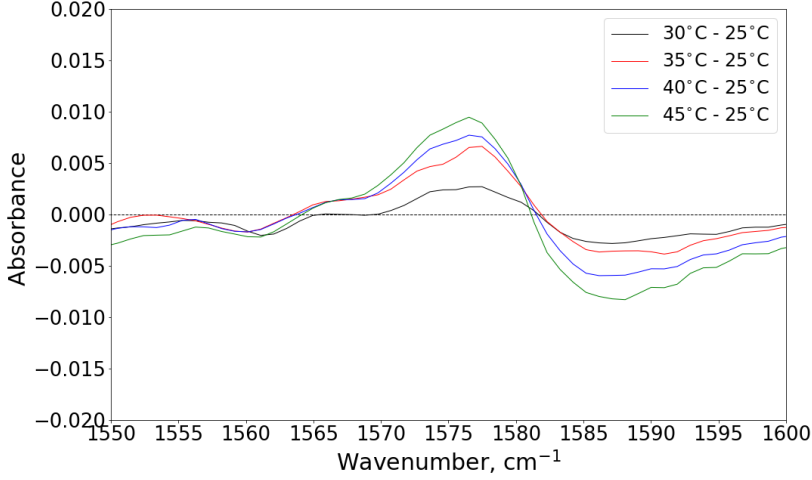
Figure 6.14. Thermal difference of the infrared absorption spectra of UiO-66 membranes displayed in Figure 6.13

temperature change in the excited volume using the following expression: $\Delta\text{T} = \text{E}_{absorbed}/(\text{c}\cdot\text{m})$, where ΔT is the temperature change, $\text{E}_{absorbed}$ is the excitation energy absorbed by the sample, c is the heat capacity and m is the mass of the volume that is excited. The absorbed energy was calculated with the following equation:

$$E_{absorbed} = E_{inc} \int_{\omega_{min}}^{\omega_{max}} d\omega((1 - 10^{-A(\omega)})S(\omega)) \tag{6.1}$$

where $A(\omega)$ is the sample absorbance determined from FTIR spectra, $S(\omega)$ the spectrum of the excitation pulse shown in Figure 6.16. We used $\omega_{min} = 1350 \text{ cm}^{-1}$, $\omega_{max} = 1450 \text{ cm}^{-1}$ and $\omega_{min} = 1540 \text{ cm}^{-1}$, $\omega_{max} = 1610 \text{ cm}^{-1}$ for ν_s and ν_{as} vibrations respectively. The incident pulse energy E_{inc} was ~ 5 μJ. To calculate the mass of the excited volume we used the beam diameter at the sample position of ~ 200 μm, the sample thickness of 700 nm (see Figure 6.6), UiO-66 density of 1200 kg/m^3 [189] and a heat capacity of 1000 J/(kg$\cdot$K) [190]. With these parameters, we calculate an increase in temperature of $\sim$10K in the case of excitation of the ν_{as} vibration and $\sim$20K in the case of excitation of the ν_s vibration. In Figure 6.15, we show pump-averaged transient spectra corresponding to the diagonal ν_{as} peak ($\omega_{excitation} = \omega_{detection} = 1585$ cm-1) and the $\nu_s \to \nu_{as}$ cross-peak ($\omega_{excitation} = 1395$ cm^{-1}, $\omega_{detection} = 1585$ cm^{-1}). Comparing Figures 6.14 and 6.15 it is clearly seen that the transient absorption spectra observed at long waiting times shown in
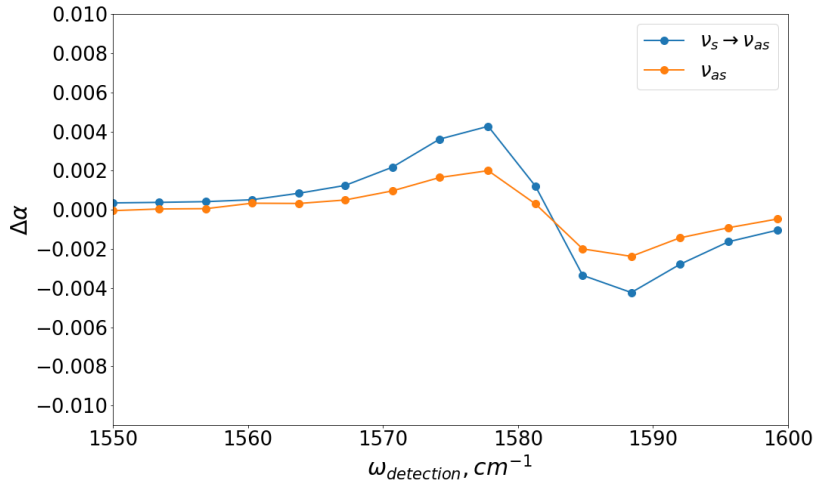
Figure 6.15. Isotropic transient absorption spectra measured for UiO-66 membranes at waiting time T = 200 ps for $\nu_s \rightarrow \nu_{as}$ cross-peak signal (blue), ν_{as} diagonal signal (orange). Note that decimal logarithm was used to calculate the transient absorption

Figure 6.15 match quite well with the thermal difference spectra shown in Figure 6.14. This result corroborates the assignment of the transient absorption spectra at waiting times >10 ps to a (local) heating effect, i.e. completed vibrational relaxation and thermal equilibration in the excited volume of the UiO-66 film.
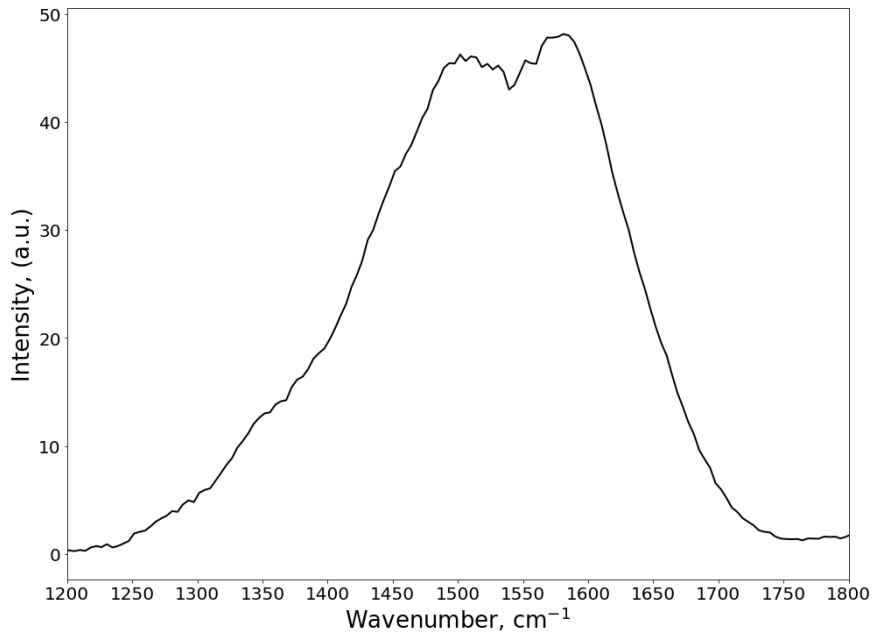
Figure 6.16. Spectral profile of the excitation pulse

7

Molecular orientation of small carboxylates at the water-air interface

We study the properties of formate (HCOO$^-$) and acetate (CH$_3$COO$^-$) ions at the surface of water using heterodyne-detected vibrational sum-frequency generation (HD-VSFG) spectroscopy. For both ions we observe a response of the symmetric (ν_s) and antisymmetric (ν_{as}) vibrations of the carboxylate group. The spectra further show that for both formate and acetate the carboxylate group is oriented toward the bulk, with a higher degree of orientation for acetate than for formate. We find that increasing the formate and acetate bulk concentrations up to 4.5 m does not change the orientation of the formate and acetate ions at the surface, and does not lead to saturation of the surface density of ions.

7.1 Introduction

Carboxylic acid (-COOH) and carboxylate (-COO$^-$) groups are involved in many important interfacial processes, such as molecular recognition at bio-membranes, protein folding, and energy conversion and storage.[31,33–35,135] The chemical and physical properties of the carboxylate anion differ strongly from those of the conjugate carboxylic acid.[191–193] Further, carboxylates form strong ionic bonds with different metal cations, giving rise to metal carboxylates as well as more elaborate structures such as carboxylate-based metal-organic frameworks.[137–141] Long-chain carboxylates are also frequently utilized as surfactants to solubilize hydrocarbons in fuel extraction.[194,195] During the last decades, the pronounced surface activity of long-chain carboxylic acids and long-chain carboxylates inspired many studies of the acid/base equilibrium, the surface propensity, and the orientation properties of these systems in dependence on the chain length, the concentration and the pH.[59,61,196–198] Surface-specific X-ray photoelectron spectroscopy (XPS) studies showed that the surface propensity increases with increasing chain length.[199] Furthermore, it has been shown that the carboxylic acid has a higher surface affinity compared to its conjugate carboxylate anion.[199] While many studies have been devoted to the properties of long-chain carboxylic acids and carboxylates at aqueous surfaces, much less attention has been given to the surface properties of small carboxylate ions like acetate and formate. Surface tension measurements and MD simulations indicate that the propensity of formate and acetate to be located at the surface of water strongly differ: while the addition of formate to water does not significantly change the surface tension, adding acetate leads to a substantial lowering of the surface tension.[200,201]

In this work we perform HD-VSFG measurements to investigate the surface properties of aqueous sodium formate and sodium acetate solutions. For both formate and acetate, we observe a vibrational surface response of the carboxylate group, and we can determine the net orientation of these ions at the solution surface. We compare our results with surface tension measurements and MD simulations.

7.2 Experiments

We prepared 0.9 - 4.5 molal (m) solutions of formate and acetate in D_2O by mixing of D_2O with the appropriate amount of salt in a vial. We used sodium formate ($\geq$99.0%, Fluka Analytical), sodium acetate (anhydrous, for molecular biology $\geq$ 99%, Sigma Aldrich) and D_2O (99.9% atom D, Aldrich) as received. The sample preparation and experimental setups used in this study are described in sections 3.1, 3.2, and 3.6
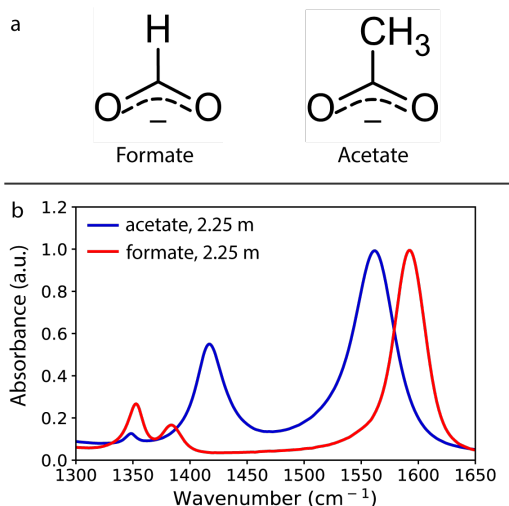
Figure 7.1. a. Chemical structures of formate and acetate ions b. Normalized FTIR spectra of 2.25 m D_2O solutions of sodium formate (red) and sodium acetate (blue) in the frequency region of 1300 -1650 cm^{-1}.

7.3 Results

In Figure 7.1, we show the normalized FTIR spectra of solutions of 2.25 m sodium formate and sodium acetate in D_2O in the 6 μm region. The high-frequency band is assigned to the antisymmetric stretch vibration (ν_{as}) of the carboxylate group. For formate this band is centered at 1590 cm^{-1} and for acetate at 1565 cm^{-1}. The low-frequency band is assigned to the symmetric stretch vibration (ν_s) of the carboxylate group and is centered at 1352 cm^{-1} for formate and at 1417 cm^{-1} for acetate. For the formate solution an additional band at 1380 cm^{-1} is observed which has been assigned earlier to the in-plane C-H bending vibration.[147] For acetate an additional band at 1350 cm^{-1} band is observed which can be assigned to the CH$_3$ deformation vibration. The symmetries of the CH vibrations and ν_s are different. (A1 and B1 respectively) and hence mixing between these bands is formally not possible.[147,202–204]

To compare the absorption strengths of the different bands, we normalize the spectra to the maximum amplitudes of the ν_{as} vibrations. We observe that the ν_s vibration is almost twice as intense for acetate than for formate. We studied the concentration dependence of the spectra, as shown in Figures 7.5 and 7.6, and found that the ratio between the ν_s of the carboxylate ions and the bending mode of D_2O (δ_{D_2O}) scales very well with the solute concentration. We also observe that for both formate and acetate, the line shapes of the carboxylate stretch vibrations
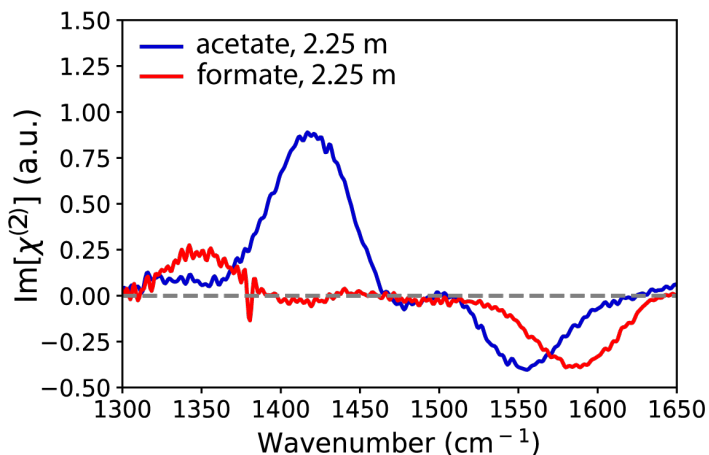
Figure 7.2. Im[$\chi^{(2)}$] spectra of a solution of 2.25 m sodium formate (red) and sodium acetate (blue) in D$_2$O in the frequency region of 1300 -1650 cm^{-1}. The measurements are taken in SSP polarization configuration.

are quite independent of the concentration.

Figure 7.2 presents the Im[$\chi^{(2)}$] spectra of solutions of 2.25 m sodium formate (red) and sodium acetate (blue) in D$_2$O obtained from HD-VSFG in the frequency region of 1300 - 1650 cm^{-1}. The Im[$\chi^{(2)}$] spectra show a positive band at 1350 cm^{-1}/1410 cm^{-1}, and a negative band at 1590 cm^{-1}/1550 cm^{-1} for formate/acetate. In line with the FTIR spectrum, we assign the low-frequency band to the ν_s vibration and the high-frequency band to the ν_{as} vibration of the carboxylate group.

In SSP polarization combination only vibrational modes with a transition dipole moment (TD) component parallel to the surface normal can be observed. Hence, considering that the TD of the ν_{as} vibration of the carboxylate group is perpendicular to that of ν_s, only the latter vibration would have been detected in case the carboxylates would have their molecular c-axis parallel to the surface normal. In earlier studies of long-chain carboxylates only the band of the ν_s vibration of the carboxylate group was observed in SSP polarization combination, indicating that for long-chain carboxylates the c-axis is indeed oriented parallel to the surface normal. For long-chain carboxylates the ν_{as} band could only be observed in SPS polarization configuration.[198] Thus, the observation of the ν_{as} band in Figure 7.2 for formate and acetate shows that for these carboxylates the molecular c-axis is at a nonzero angle with respect to the surface normal. We observe that for both carboxylate solutions, the ν_s vibrational mode has a positive sign in the Im[$\chi^{(2)}$] spectrum. As the transition dipole moment of the ν_s vibration is aligned parallel to the c-axis of the carboxylate group, this observation implies that formate

Figure 7.3. Im$[\chi^{(2)}]$ spectra of aqueous a. sodium formate and b. sodium acetate solutions in D$_2$O with different concentrations in the range of 0.9 - 4.5 m. (c-d) show the amplitudes of the bands of the ν_s and ν_{as} vibrations as a function of the carboxylate concentration.

and acetate orient with their carboxylate group toward the bulk. HD-VSFG measurements of formate and acetate solutions performed in the 3 μm region that we show in Figure 7.9, support this assignment, as these measurements show a negative sign of the C-H stretch vibration of the methine group of formate (ν_{CH}) and the symmetric CH$_3$ stretch vibration of the methyl group of acetate ($\nu_{CH_3,SS}$). These negative signs show that the C-H bonds of the carboxylate anions have a net orientation pointing toward the air.[205]

Comparing figures 7.2 and 7.1, we note that in the SFG spectrum the ν_{as} band is substantially weaker compared to the ν_s band than in the FTIR spectrum. This difference can be explained by the fact that the $\chi^{(2)}$ response measured in HD-VSFG is proportional to the product of the TD and the Raman transition matrix element. The ν_{as} vibration shows only weak Raman activity compared to the ν_s vibration[147], thus decreasing the SFG signal of the ν_{as} vibration relative to that of the ν_s vibration.

We observe in Figure 7.2 that the amplitudes of the ν_{as} bands of the sodium formate and sodium acetate solutions are almost the same. In previous studies, it was found that acetate has a quite high surface propensity, while formate was

107

found to have a very low surface propensity.[199,201] In view of this difference in surface propensity, it is quite unexpected that the VSFG response of ν_{as} is about equal in amplitude for acetate and formate solutions. The effect of the higher surface propensity of acetate is probably compensated by a larger tilt angle of the c-axis with respect to the surface normal for formate. A larger tilt angle enhances the amplitude of the band of the ν_{as} vibration. To further investigate this interpretation, we also performed HD-VSFG measurements of acetate and formate solutions in SPS polarization combination that we compare to measurements in SSP polarization combination. From the combined data, we obtain for acetate a tilt angle θ of 45° and for formate significantly larger than 45° but smaller than 90°. The SPS spectroscopic data and underlying methodology is presented in chapter 8 where we focus on the determination of orientational properties of carboxylate anions using SSP and SPS $\chi^{(2)}$ spectra.

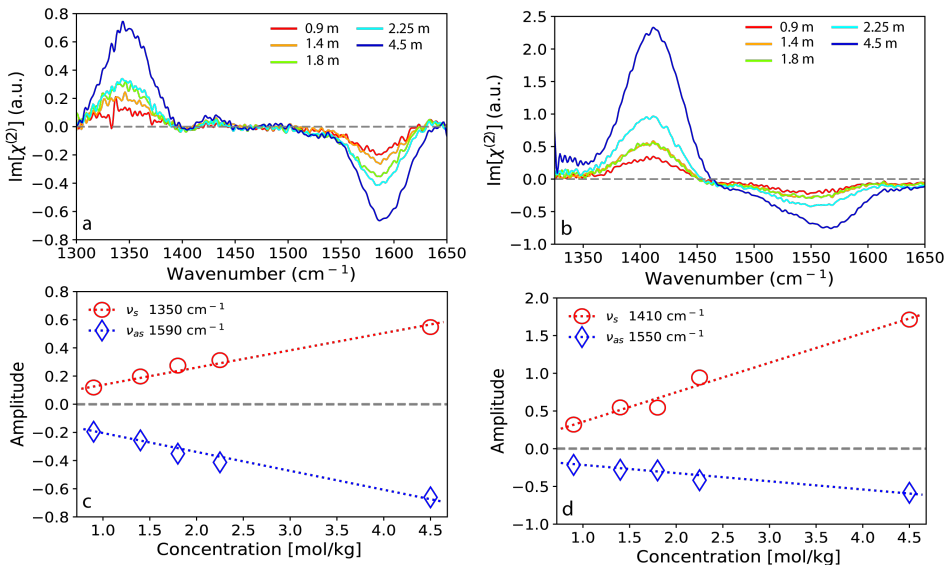In Figure 7.3 we show $\text{Im}[\chi^{(2)}]$ spectra of sodium formate and sodium acetate solutions at different concentrations in the range of 0.9 - 4.5 m and the amplitudes of the bands corresponding to the ν_s and ν_{as} vibrational modes as a function of the concentration. For both formate and acetate, we observe that the amplitudes of the ν_s and ν_{as} bands increase linearly with the bulk concentration. This result shows that the surface does not get saturated with formate/acetate ions up to bulk concentrations of 4.5 m. Sodium acetate and sodium formate are relatively small molecular ions and show a significantly lower surface propensity compared to surfactants like stearate which have long hydrophobic tails. Hence, the effect of surface adsorption becomes visible only at a relatively high salt bulk concentration (> 1 m). Another consequence of the limited surface propensity is that the surface coverage does not saturate, even at a bulk concentration of 4.5 m.

We also observe that increasing the bulk concentration of formate/acetate leads to a shift of the vibrational bands to higher frequencies, and an increasing asymmetry of the band shape. This change of the spectral shape and position is most clearly seen for the ν_{as} band and can be explained by dispersion of the refractive index in the vicinity of a vibrational resonance, which in turn affects the Fresnel factors. We modeled the VSFG response of the ν_s and ν_{as} vibrations using a three-layer model, combined with a Lorentz model to calculate the change of the refractive index of the interfacial layer with increasing carboxylate concentration. The concentration-dependent bulk refractive index was obtained from infrared absorption spectra shown in Figure 7.5 using the extinction coefficient of δ_{D_2O} vibrational band $\epsilon = 17.1 \ (M \cdot cm)^{-1}$ as described in section 2.3.3. In Figure 7.4 we compare the experimental and calculated VSFG responses for an aqueous solution of sodium acetate at different concentrations. At high ion concentrations, the infrared refractive index and the Fresnel factor of the infrared light acquire a strong frequency dependence due to the vibrational resonances. This change of the Fresnel factor leads to an increase of the high-frequency wings of the responses of the ν_s vibrations and ν_{as} vibrations. As a result, the bands become asymmetric

and the maxima shift to higher frequencies. It is also observed that the band of the ν_{as} vibration is more affected than the band of the ν_s vibration. This can be explained from the higher infrared cross-section of the ν_{as} vibration, which induces a stronger frequency dependence of the refractive index and the Fresnel factor at frequencies near the frequency of this vibration. We conclude that the three-layer model accounts very well for the experimentally observed changes in spectral shape and position. This means that these changes can be fully explained by Fresnel effects and are not caused by changes in the direct molecular environment of formate and acetate, e.g. by changes in hydrogen-bond strength or configuration upon increasing the carboxylate concentration.
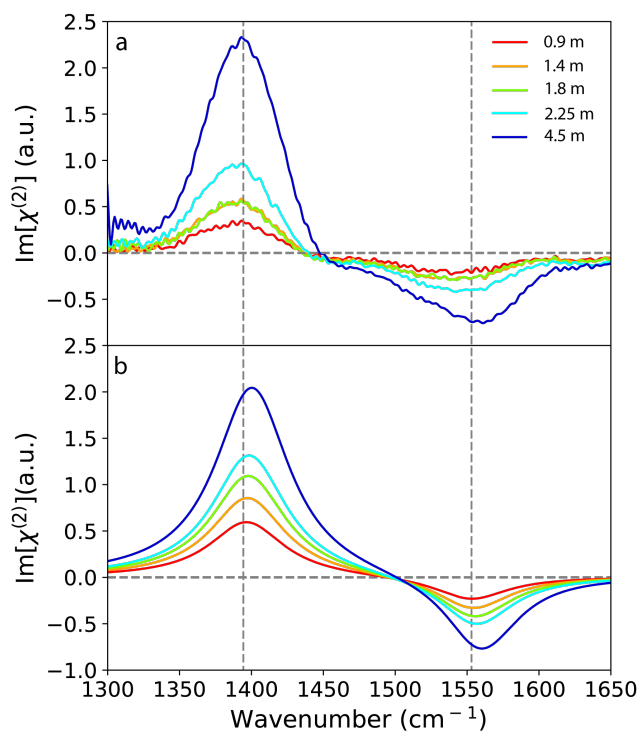

Figure 7.4. a. Experimental and b. calculated $\text{Im}[\chi^{(2)}]$ spectra of aqueous sodium acetate solutions for different concentrations in the concentration range of 0.9 - 4.5 m. The calculated $\text{Im}[\chi^{(2)}]$ spectra are obtained by accounting for the effect of acetate on the infrared Fresnel factors using the three-layer model, as described in section 2.3.3

7.4   Discussion

Previous surface tension measurements by Minofar et al. show that for aqueous acetate solutions a clear decrease in surface tension is observed with increasing concentration, indicating that acetate is surface-active.[200,201] These surface tension measurements are accompanied by MD simulations, yielding the density profile of the carboxylate ion near the surface. For acetate it is found that the density is enhanced compared to that of water at the surface, meaning that this ion has a clear surface propensity.[200,201] In addition, the MD simulations show that the acetate ions are oriented with their carboxylate groups pointing toward the bulk. Our observation of a strong positive ν_s band in the HD-VSFG spectrum of aqueous acetate, agrees well with the results of these previous surface tension measurements and MD simulations.[200,201] Interestingly, in the same study it is found that the addition of sodium formate does not lead to a significant change of the surface tension.[201] The accompanying MD simulations show that the density at the surface of formate is lower than that of water and that the formate ions do not have a preferred orientation.[201] The latter result is not in agreement with our observations. The HD-VSFG spectrum of formate shown in Figure 7.2, in particular the positive ν_s vibrational band, show that formate has a net orientation of its carboxylate group toward the bulk, albeit that the SPS data show that the degree of orientation is not very strong and much less than that of acetate. The fact that the addition of sodium formate does not significantly change the surface tension also indicates that formate is present at the surface, probably showing a very similar dependence of its density profile on the depth into the solution as water.

7.5   Conclusions

In conclusion, we performed Fourier Transform Infrared (FTIR) absorption and heterodyne-detected vibrational sum frequency generation (HD-VSFG) measurements of aqueous sodium formate and sodium acetate solutions. The HD-VSFG spectra contain responses of both the symmetric (ν_s) and the antisymmetric (ν_{as}) vibrations of the carboxylate group. The ν_s band has a positive sign which shows that formate and acetate both have a net orientation with their carboxylate group pointing toward the bulk. The observation of the ν_{as} band in the HD-VSFG spectrum of the formate and acetate solution and additional HD-VSFG measurements performed in SPS polarization configuration show that the c-axis of these ions is at a nonzero angle with respect to the surface normal. From the amplitudes of the ν_{as} bands and the SPS measurements, it follows that this angle is smaller for acetate than for formate. We find that the amplitudes of both vibrational bands increase linearly with bulk concentration up to concentrations of 4.5 m. This finding implies that, even at these high bulk concentrations, the surface is not getting saturated with carboxylate ions, and that there is no significant change of the

orientation angle of the formate and acetate ions with increasing concentration. Finally, we found that at high carboxylate concentrations the ν_s and ν_{as} bands in the HD-VSFG spectrum become asymmetric and shift to higher frequencies, which can be quantitatively explained from the change of the Fresnel factor of the infrared beam.

7.6   Appendix
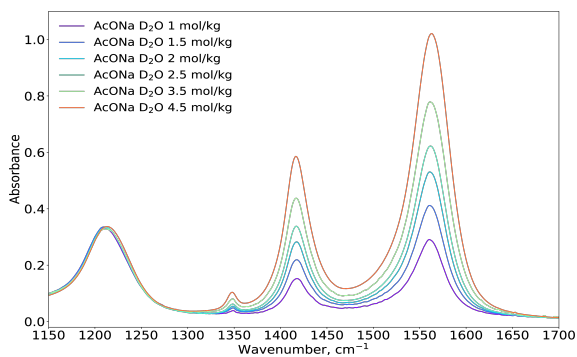
Figure 7.5.   IR absorption spectra of sodium acetate solutions in D_2O in the concentration range of 0.9 - 4.5 m in the frequency region within 1150 - 1650 cm^{-1} . The spectra are scaled with respect to the bending mode of D_2O appearing at 1210 cm^{-1}
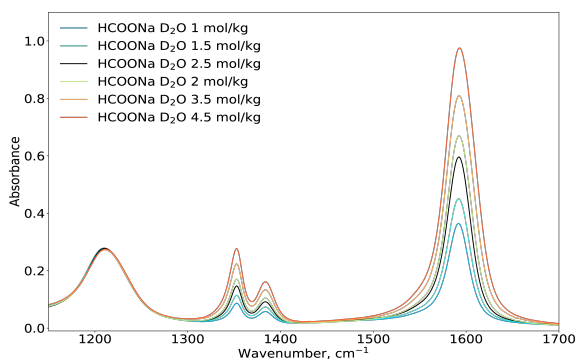
Figure 7.6. IR absorption spectra in the frequency region within 1150 - 1650 cm^{-1} The spectra are scaled with respect to the bending mode of D_2O appearing at 1210 cm^{-1}
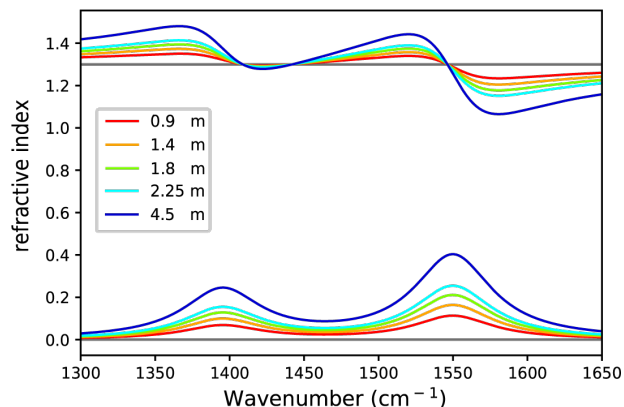
Figure 7.7. Imaginary (bottom) and real (top) parts of the refractive index in the frequency region 1300 -1650 cm^{-1} of aqueous solution of acetate at different concentrations. The cross-sections of the ν_s and ν_{as} vibrations of acetate were determined using the known cross-section of the D$_2$O bending mode centered at 1210 cm-1. The real part of the refractive index is calculated using Kramers-Kronig relation.
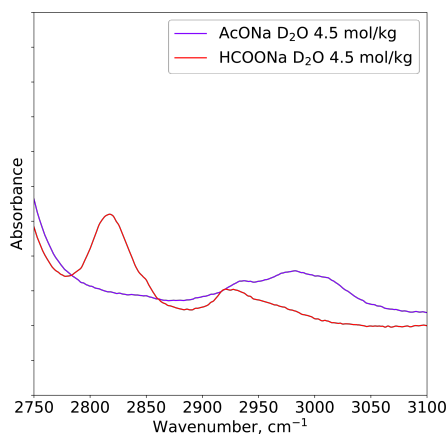
Figure 7.8. IR absorption spectra in the frequency region 2750 - 3100 cm^{-1} of 4.5 m sodium formate and sodium acetate solutions in D$_2$O.

In Figure 7.9 we show the Im[$\chi^{(2)}$] spectra in 3 μn frequency region. The spectrum of the acetate solutions in H$_2$O and D$_2$O shows two narrow negative features at 2880 cm^{-1} and 2940 cm^{-1} that we assign to the symmetric stretching vibration of the methyl group, ($\nu_{CH_3,ss}$), and the Fermi resonance of the $\nu_{CH_3,ss}$ and the overtone of the antisymmetric bending mode of the methyl group, respectively.

In addition, the spectra show a narrow positive band at 3000 cm^{-1} that we assign to the antisymmetric stretching vibration of the methyl group $(\nu_{CH_3,as})$[83,147]. For formate the spectra show a single negative band in the CH region centered at 2800 cm^{-1}, which we assign to the stretch vibration of the methine group of the formate ion (ν_{CH}). The signs of the Im[$\chi^{(2)}$] responses of the $\nu_{CH_3,ss}$ and $\nu_{CH_3,as}$ vibrations of acetate and the ν_{CH} of formate indicate that both ions have a net orientation at the water surface with their CH bonds pointing toward the air phase. Furthermore, the Im[$\chi^{(2)}$] spectrum of acetate in H$_2$O shows a positive band at 3000 - 3500 cm^{-1} that can be assigned to hydrogen-bonded OH stretch vibrations. The positive sign of the OH stretch band implies that the interfacial water molecules have a net orientation with their hydrogen atoms pointing toward the air, which can be explained from the negative charge of the acetate ions at the interface. The Im[$\chi^{(2)}$] spectrum of formate in H$_2$O shows a weak negative band in the frequency region 3000 - 3500 cm^{-1}. The amplitude of this band is smaller than that of the neat water surface. The weak response of formate solutions in the frequency region 3000 - 3500 cm^{-1} indicates that the water molecules have no clear net reorientation close to the surface upon the addition of the formate ions, which can be explained from the smaller surface propensity of formate compared to acetate. This finding is in line with previous surface tension measurements that show a negligible change in surface tension of formate solutions. In Figure 7.9 we also observe that for a solution of 4.5 m acetate the free O-H peak at 3700 cm^{-1} is no longer present while it is still observed for a solution of 4.5 m formate. This observation can be explained from the fact that for a solution of 4.5 m acetate the surface concentration of carboxylate ions is much higher than for a solution of formate. This is also in line with previous surface tension measurements showing that for aqueous acetate solutions, the surface tension decreases with increased acetate content, which is not the case for formate solutions. In addition, in the case of acetate adsorbed to the surface, a methyl group is sticking out of the surface, which is a much bulkier group than the C-H group of formate. Hence, for an aqueous solution of 4.5 m formate, much more room is left at the surface for dangling (free) water O-H groups than for an aqueous solution of 4.5 m acetate.
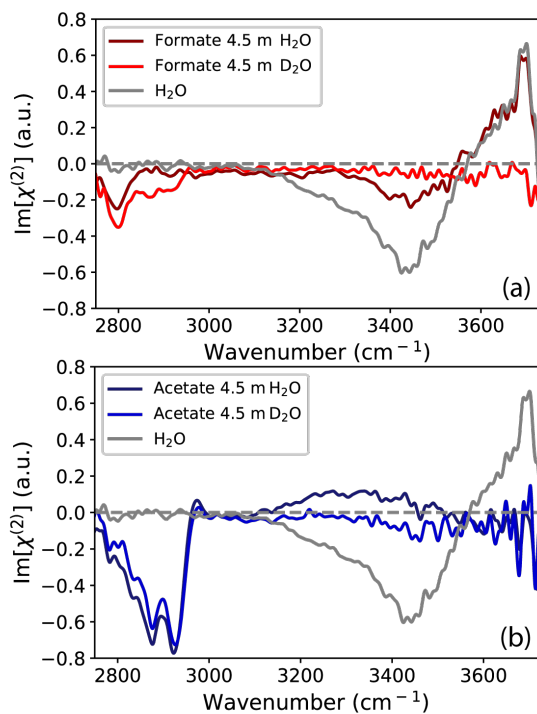
Figure 7.9. a) $\text{Im}[\chi^{(2)}]$ spectra in the frequency region 2800 - 3720 cm^{-1} of neat water (gray) and an aqueous formate solution with a concentration of 4.5 m in H_2O (dark red) and D_2O (red).(b) $\text{Im}[\chi^{(2)}]$ spectra in the frequency region within 2800 - 3720 cm^{-1} of neat water (gray) and an aqueous acetate solution with a concentration of 4.5 m in H_2O (dark blue) and D_2O (blue). All measurements are taken in SSP polarization configuration.

8

Molecular Orientation of Carboxylate Anions at the Water/Air Interface studied with Heterodyne-Detected Vibrational Sum-Frequency Generation *

The carboxylate anion group plays an important role in many (bio)chemical systems and polymeric materials. In this work, we study the orientation of carboxylate anions with various aliphatic and aromatic substituents at the water/air interface by probing the carboxylate stretch vibrations with heterodyne-detected vibrational sum-frequency generation (HD-VSFG) spectroscopy in different polarization configurations. We find that carboxylate groups with small aliphatic substituents show a large tilt angle with respect to the surface normal, and that this angle decreases with increasing size of the substituent. We further use the information on the orientation of the carboxylate group to determine the hyperpolarizability components of this group.

8.1 Introduction

Carboxylic acids and carboxylate anions are abundant in biological and abiotic systems and ubiquitous in organic synthesis reactions and industrial applications.[31,33,34,137,145,194,195,206–208] Both species can be located at aqueous interfaces, dependent on their overall hydrophobic/hydrophilic character, the subphase pH, and the ionic strength. Previous studies have focused on the degree of surface adsorption, the surface pKa of carboxylic acids,[196,199,209] the interaction of Langmuir-Blodgett monolayers of long-chain fatty acids with metal cations,[61,197,198] and the mechanisms of emulsion stabilization by carboxylic acid/-carboxylate surfactants[210]. An important property of carboxylate ions and carboxylic acids at the water-air interface concerns their orientation, as this property impacts their spatial charge distribution and solvation structure, which play an important role in atmospheric processes, the chemistry of aerosols, and soil chemistry.

Vibrational sum frequency generation spectroscopy (VSFG) is an efficient tool for investigating interfacial molecules and ions. This technique is highly surface specific and enables the characterization of the adsorption and orientation properties of species adsorbed at a phase boundary via their vibrational response. The growing interest in the molecular orientation and adsorption of molecules and ions at interfaces stimulates VSFG studies of various interfaces relevant for material design and biochemistry.[35,211–216] Previous VSFG studies have focused on the orientation of interfacial water molecules at neutral and charged interfaces,[35,57,84,217] the structure of biodegradable polymers[218] and proteins[219], the adsorption of small molecules,[56,220–222] and the molecular properties of surfactants[58,223]. VSFG spectroscopy has been used to study the orientation of formic, acetic, and hexanoic acids at the water-air interface[59,63,224]. In **Chapter 7** we applied this technique to study the orientation of formate and acetate anions probing the symmetric stretch vibration (ν_s), and the antisymmetric stretch vibration (ν_{as}) of the carboxylate group. The measured signals allowed for an estimation of the tilt angle θ of these species at the water-air interface.

The tilt angle θ is defined as the angle between the molecular c-axis and the laboratory z-axis, as shown in Figure 8.1a. The average tilt angle of the acetate ion was found to be $\sim 45°$, while that of the formate ion was found to be close to $90°$. These results appear to be in contrast with previous MD simulations that indicated that for acetate and benzoate ions the tilt angle would show a distribution with its maximum at $\sim 0°$ and a FWHM of $\sim 50\text{-}60°$. These observations stimulate further exploration of the dependence of the tilt angle of carboxylate anions on the size and structure of the substituent.

In this work, we study the molecular orientation of carboxylate anions with aliphatic substituents with different chain lengths and aromatic substituents at the water-air interface. We probe the response of the ν_{as} carboxylate stretch vibra-

116

tion with heterodyne detected vibrational sum frequency generation (HD-VSFG) spectroscopy in different polarization configurations. We combine this information with the measured responses of the ν_s carboxylate stretch vibration, which allows us to determine the relation between several of the hyperpolarizability components of the carboxylate anion group. In Figure 8.1 we show structural formulas of the carboxylate anions investigated in this work. The studied anions can be divided into two groups. The first group includes ions with aliphatic chains with a different number of carbon atoms: formate, acetate, propionate, hexanoate and octanoate. The second group includes aromatic species with different structures: benzoate and 2-naphthoate.
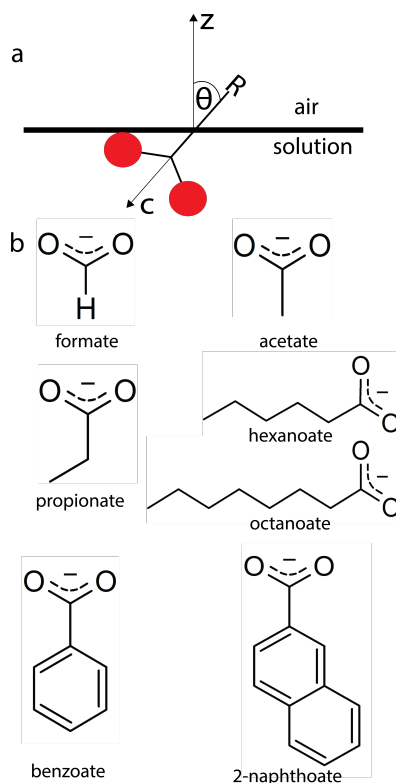
Figure 8.1. a. Definition of the tilt angle θ, red spheres represent oxygen atoms of a carboxylate anion b. Chemical structures of the carboxylates under study

8.2 Experiments

We used sodium carboxylates as received: formate ($\geq$99.0%, Fluka Analytical), acetate (anhydrous, for molecular biology $\geq$ 99%, Sigma Aldrich), propionate (minimum 99%, Sigma), hexanoate (99-100%, Sigma), octanoate ($\geq$99%, Sigma), benzoate ($>$ 99%, Sigma Aldrich), 2-naphthoate ($>$ 98%, TCI). To prepare the samples, we dissolved appropriate amounts of the salts in D_2O (99.9% atom D, Aldrich). For each carboxylate, we chose the concentration such to obtain a signal-to-noise ratio that is more than sufficient to reliably determine the amplitudes of the VSFG-responses of the ν_s and ν_{as} vibrations of the carboxylate groups in different VSFG polarization combinations.

The sample preparation and experimental setups used in this study are described in sections 3.1, 3.2, and 3.6

To extract information about the orientation of the carboxylate ions at the surface, we determine the peak amplitude of the ν_{as} vibration from the $Im[\chi^{(2)}]$ spectra collected in SSP and SPS polarization combinations, where the notation SS(P)P(S) refers to S-polarized light at ω_{SFG}, S(P)-polarized light at ω_{vis}, and P(S)-polarized light at ω_{IR}. The tilt angle θ can be determined directly from the ratio of the amplitudes of the responses of the ν_{as} vibration in the SSP and SPS $Im[\chi^{(2)}]$ spectra:

$$\frac{Im[\chi^{(2)}_{SSP,\nu_{as}}]}{Im[\chi^{(2)}_{SPS,\nu_{as}}]} = -A\frac{\langle cos\theta\rangle - \langle cos^3\theta\rangle}{\langle cos^3\theta\rangle} \tag{8.1}$$

The coefficient A is introduced to account for the ratio of the Fresnel coefficients and the ratio of the sines of the incidence angles of ω_{IR} and ω_{vis} beams. The calculation of the cosine terms on the right-hand side of equation 8.1 includes integration over the angular distribution of the carboxylate anion. In section 2.3.5 we provide a detailed theoretical background underlying the methodology.

8.3 Results

In Figure 8.2 we show linear infrared absorption spectra of the studied carboxylates in the 6 μm region. The spectra of formate, acetate and propionate are shown in Figure 8.2a. The assignment for formate and acetate can be found in **Chapter 7**. For propionate, we assign the bands centered and 1415 cm^{-1} and 1553 cm^{-1} to the ν_s and ν_{as} vibrations of the carboxylate group, respectively and the bands centered at 1374 cm^{-1} and 1468 cm^{-1} to the symmetric ($\delta_{CH_3,s}$) and antisymmetric $\delta_{CH_3,as}$) bending vibrations of the CH$_3$ group.[60,147,225]

As can be seen in Figure 8.2b, the spectra of hexanoate and octanoate look almost identical. Similarly to the propionate ion, we assign the bands centered at

Figure 8.2. Infrared absorption spectra of 1 m sodium carboxylates a. formate (purple), acetate (red), propionate (orange) b. hexanoate (green), octanoate (blue) and c. benzoate (black), 2-naphthoate (khaki). The spectra are normalized with respect to the amplitude of the band corresponding to the ν_{as} vibration

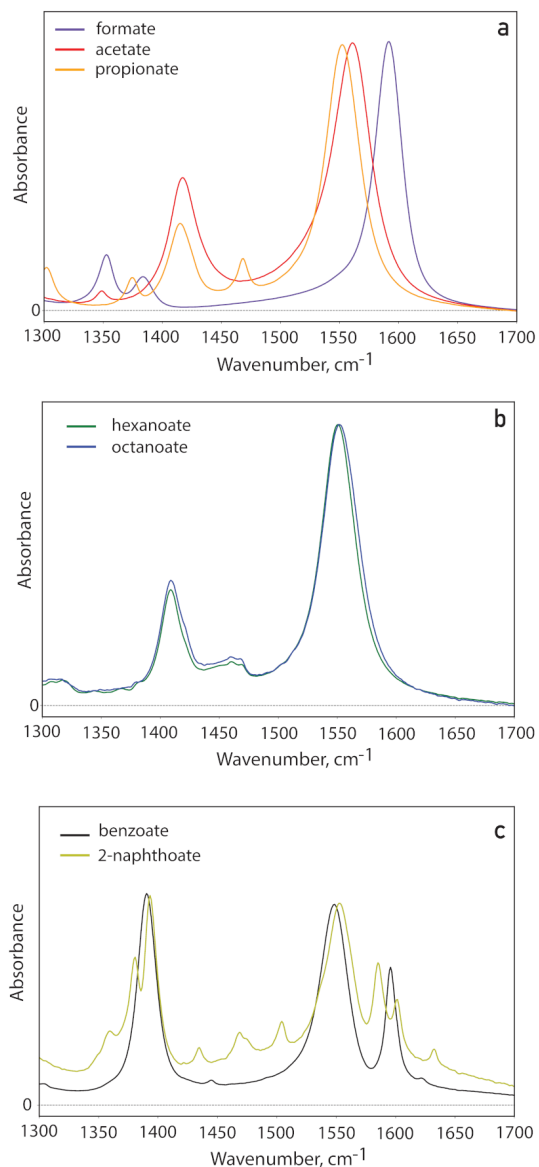1412 cm^{-1} and 1550 cm^{-1} to the ν_s and ν_{as} vibrations, respectively, and the band centered at 1462 cm^{-1} to the $\delta_{CH_3,as}$ mode.

For both benzoate and 2-naphthoate the bands corresponding to ν_s and ν_{as} vibrations are centered at 1390 cm^{-1} and 1550 cm^{-1}, respectively, and have very similar resonant frequencies, as shown in Figure 8.2c. For the benzoate ion, the band centered at 1596 cm^{-1} corresponds to a ring mode of the ion. This band is relatively strong and is thus likely of mixed character, borrowing oscillator strength from the ν_{as} vibration.[226] 2-naphthoate shows a plethora of weaker absorption bands, resulting from the coupling of the vibrations of the two-ring aromatic system with the ν_s and ν_{as} modes of the COO$^-$ group.

In Figure 8.3 we show Im[$\chi^{(2)}$] spectra of formate, acetate and propionate D$_2$O solutions, measured in SSP and SPS polarization configuration. In Figure 8.3a it is seen that the SSP-spectrum of formate shows a positive band at $\sim$ 1355 cm^{-1}, and a negative band at $\sim$ 1590 cm^{-1}, corresponding to the ν_s and ν_{as} vibrations of the carboxylate group, respectively, in agreement with the results of **Chapter 7**. The SPS spectrum of formate does not show a significant signal in this frequency region. For sodium acetate (Figure 8.3b), we also observe a positive band at $\sim$1415 cm^{-1}, corresponding to ν_s, and a negative band centered at $\sim$1565 cm^{-1}, corresponding to ν_{as} in the SSP spectrum, also in agreement with the results of **Chapter 7**. The band centered at $\sim$1350 cm^{-1} corresponds to the $\delta_{CH_3,s}$ vibration. In contrast to formate, the SPS spectrum of acetate does show a significant signal, in the form of a clear positive peak near 1560 cm^{-1}, corresponding to the ν_{as} vibration. Finally, in Figure 8.3c the SSP-spectrum of sodium propionate shows a positive band at $\sim$ 1415 cm^{-1} and a negative band at $\sim$ 1550 cm^{-1} that are assigned to the ν_s and ν_{as} vibrations, respectively. The SPS-spectrum shows a strong positive peak at 1550 cm^{-1} corresponding to the ν_{as} vibration and an additional weak positive peak at $\sim$1465 cm^{-1} that corresponds to the $\delta_{CH_3,as}$ vibration. For acetate and propionate, the absolute amplitudes of the bands corresponding to the ν_{as} vibration are very similar in the SSP and SPS spectra, whereas for formate the ν_{as} band is much stronger in SSP than in SPS. As follows from equation 8.1, these findings indicate that the tilt angle of the carboxylate group of formate is very different from that of acetate and propionate, and that the tilt angles of acetate and propionate are quite similar.

To further investigate the dependence of Im[$\chi^{(2)}$] spectra on the aliphatic chain length, we also measured the Im[$\chi^{(2)}$] spectra of hexanoate and octanoate solutions as shown in Figure 8.4. The spectra of the two ions are quite similar, and the assignment of the observed bands is the same as for propionate. The absolute amplitude of the ν_{as} band is lower in the SSP spectra than in the SPS spectrum, which indicates that the carboxylate group has a different orientation compared to acetate and propionate.

Finally, we examine the Im[$\chi^{(2)}$] spectra of the aromatic ions benzoate and 2-naphtoate as shown in Figure 8.5. The SSP spectrum of sodium benzoate shows
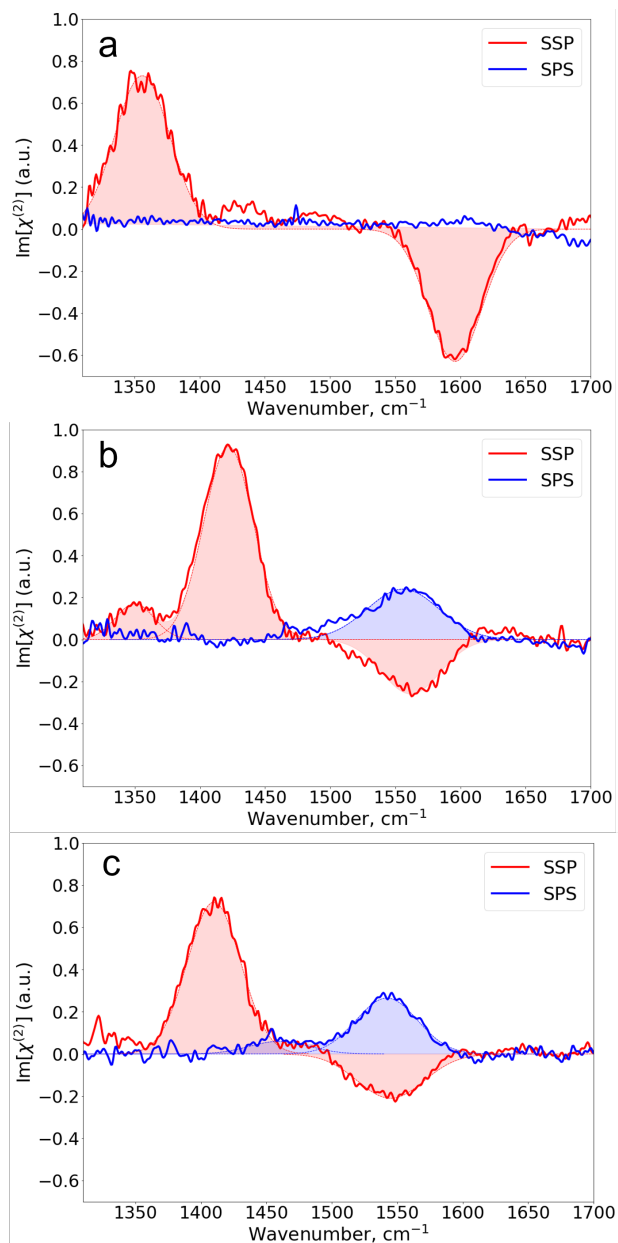
Figure 8.3. SSP and SPS Im[$\chi^{(2)}$] spectra of a. 4.5 m sodium formate b. 2.5 m sodium acetate and c. 1 m sodium propionate. The solid lines represent the experimental spectra, while the filled dashed lines represent Gaussian fits to the data

Figure 8.4. SSP and SPS Im[$\chi^{(2)}$] spectra of a. 0.2 m sodium hexanoate b. 0.04 m sodium octanoate. The solid lines represent experimental spectra, while the filled dashed lines represent Gaussian fit to the data
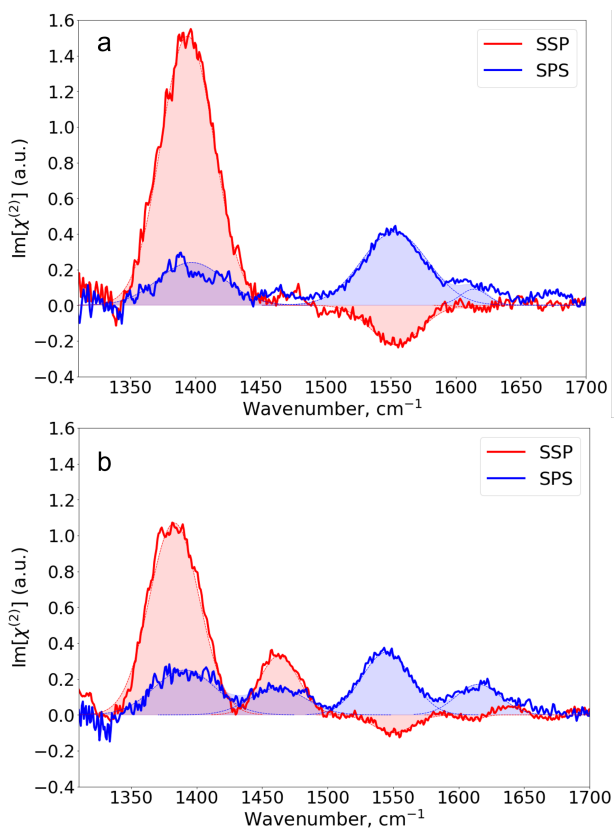
Figure 8.5. SSP and SPS $\text{Im}[\chi^{(2)}]$ spectra of a. 0.3 m sodium benzoate b. 0.075 m sodium 2-naphthoate. The solid lines represent experimental spectra, while the filled dashed lines represent Gaussian fit to the data

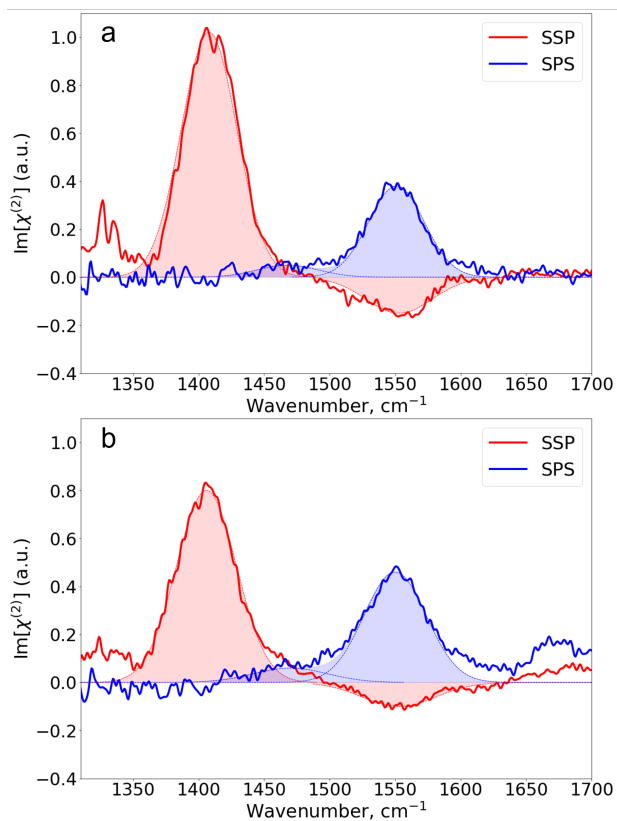**Table 8.1.** Parameters extracted from the analysis of $\text{Im}[\chi^{(2)}]$ spectra

Ion	$|A_{SSP,\nu_{as}}/A_{SPS,\nu_{as}}|$	$|A_{SSP,\nu_{as}}/A_{SSP,\nu_s}|$	$(\beta_{aac}+\beta_{bbc})/\beta_{ccc}$	β_{aca}/β_{ccc}
Formate	> 13	0.92 ± 0.06	2.0±0.2	2.0±0.2
Acetate	1.16 ± 0.19	0.3 ± 0.03	2.0±0.2	1.2 ± 0.2
Propionate	0.85 ± 0.15	0.31 ± 0.04	2.0±0.2	1.3 ± 0.2
Hexanoate	0.42 ± 0.09	0.16 ± 0.03	2.0±0.2	1.2 ± 0.2
Octanoate	0.23 ± 0.06	0.13 ± 0.04	2.0±0.2	1.2 ± 0.2
Benzoate	0.57 ± 0.08	0.14 ± 0.02	0.6 ± 0.2	0.7 ± 0.2
Naphthoate	0.31 ± 0.09	0.1 ± 0.02	-	-

a positive band at ~ 1390 cm^{-1} and a negative band centered at ~ 1555 cm^{-1}, corresponding to the ν_s and ν_{as} vibrations, respectively. The SPS spectrum of benzoate shows two bands at similar frequencies, both with a positive amplitude. In addition, we observe a weak positive band at ~ 1610 cm^{-1}. Following the assignment of the FTIR absorption spectra, we assign this band to a vibration of mixed character, involving the ν_{as} vibration of the carboxylate group and ring vibrations of the benzoate ion. The $\text{Im}[\chi^{(2)}]$ spectra of 2-naphthoate ion contain multiple bands. Similarly to the benzoate ion, the band centered at $\sim$1390 cm^{-1} corresponding to the ν_s vibration, is positive in both the SSP and SPS spectrum, while the band centered at $\sim$1555 cm^{-1} corresponding to the ν_{as} vibration, is negative in the SSP spectrum and positive in the SPS spectrum. The other bands are assigned to ring modes of the 2-napthoate ion. For both benzoate and 2-naphthoate, the ν_{as} band has a higher absolute amplitude in the SPS spectrum than in the SSP spectrum.

To obtain a quantitative determination of the tilt angle of the different carboxylate ions, we fit the bands of the $\text{Im}[\chi^{(2)}]$ spectra with Gaussian functions. As the width of the bands measured in SSP and SPS polarization combinations are similar, the ratio of the band areas is well represented by the ratio of their amplitudes. Using the extracted amplitudes we determine the $|\text{Im}[\chi^{(2)}_{SSP,\nu_{as}}]/\text{Im}[\chi^{(2)}_{SPS,\nu_{as}}]|$ ratio. This ratio is shown in Table 8.1.

We first assume a δ angular distribution and calculate the angles $\langle\theta\rangle = \theta_\delta$ using this assumption and equation 8.1. The dependence of the angular terms in the right-hand side of equation 8.1 and their ratio on the tilt angle are shown in Figure 8.6a.

For formate, it is not possible to determine amplitudes from the $\text{Im}[\chi^{(2)}]$ spectrum measured in SPS polarization combination, as this amplitude is close to 0. Considering the dependence of the angular term in the SPS-polarization combination, we conclude that this ion has a large tilt angle, close to 90°. However, the fact that we do observe a clear response in the SSP polarization combination shows that the angle must be smaller than 90°, otherwise this response should also
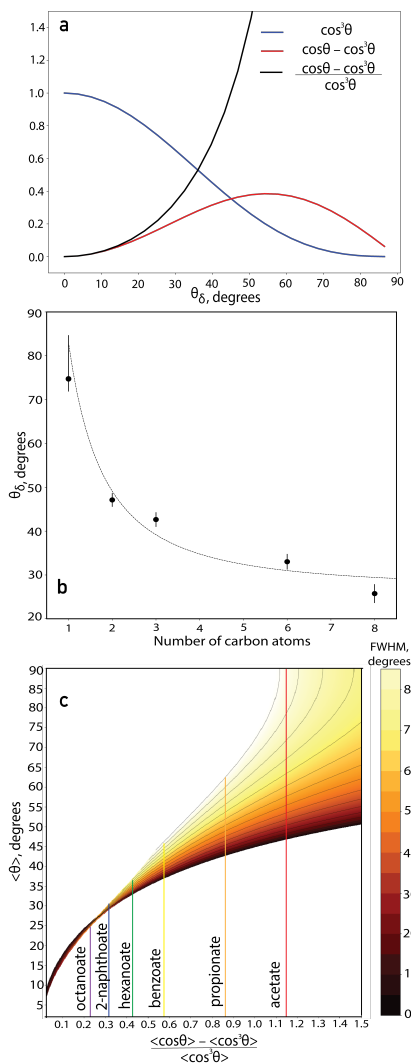
Figure 8.6. a. Calculated dependence of the angular terms for SSP and SPS polarization combinations and the $\mathrm{Im}[\chi^{(2)}_{SSP,\nu_{as}}]/\mathrm{Im}[\chi^{(2)}_{SPS,\nu_{as}}]$ ratio assuming a δ-distribution of the tilt angle θ; b. Tilt angle θ_δ extracted for aliphatic carboxylates with different chain lengths assuming a δ-distribution of the tilt angle θ; c. Dependence of the average angle $< \theta >$ on the $\mathrm{Im}[\chi^{(2)}_{SSP,\nu_{as}}]/\mathrm{Im}[\chi^{(2)}_{SPS,\nu_{as}}]$ ratio obtained by integration over the Gaussian angular distribution described in the text. The FWHM of the distribution is reflected in the colors of the contour plot and the colored solid lines correspond to the carboxylates under study: acetate (red), propionate (orange), benzoate (yellow), hexanoate (green), 2-naphthoate (blue), octanoate (purple)

125

have vanished. If we estimate the minimal detectable relative $\text{Im}[\chi^{(2)}]$ value to be 0.05, we obtain an absolute $|\text{Im}[\chi^{(2)}_{SSP,\nu_{as}}]/\text{Im}[\chi^{(2)}_{SPS,\nu_{as}}]|$ ratio > 13, which implies a tilt angle $\theta_\delta > 75°$.

For acetate and propionate the values of θ_δ are $47° \pm 2°$ and $42° \pm 3°$, respectively, meaning that these angles are similar. The long-chain carboxylates are less tilted: $\theta_\delta = 33° \pm 3°$ for hexanoate and $\theta_\delta = 26° \pm 3°$ for octanoate. For the aromatic carboxylates, we extract $\theta_\delta = 37° \pm 3°$ and $\theta_\delta = 29° \pm 4°$ for benzoate and 2-naphthoate respectively. The tilt angles of the aliphatic carboxylates are presented in Figure 8.6b as a function of the number of carbon atoms. It is clearly seen that θ_δ decreases with increasing alkyl chain length.

Using a δ angular distribution for the tilt angle is not a realistic approximation. Therefore, we also analyzed the orientation of the ions including a Gaussian angular distribution function with a central angle and a certain width. To investigate how the ratio of equation 8.1 depends on the central angle and the width of the Gaussian distribution, we integrated the angular terms in the ratio of equation 8.1 as well as the angle θ over Gaussian distribution functions with different central angles θ_c and values for the full width at half maximum of the Gaussian (FWHM) varying between $0°$ and $90°$. It should be noted that these distribution functions are not symmetric as the angle θ can only have positive values. Moreover, the θ values in the distribution near zero (i.e. perpendicular to the surface) will negligibly contribute because of the $\sin(\theta)$ term in the integration over spherical coordinates. The details of this calculation can be found in sections 2.3.5, 8.6.

Combining the calculated dependencies of $\frac{\langle \cos\theta \rangle - \langle \cos^3\theta \rangle}{\langle \cos^3\theta \rangle}$ ratio and $\langle \theta \rangle$ on the parameters of the distribution, we obtain the dependence of the average tilt angle $\langle \theta \rangle$ on the $\frac{\langle \cos\theta \rangle - \langle \cos^3\theta \rangle}{\langle \cos^3\theta \rangle}$ ratio and FWHM of the distribution which we show in Figure 8.6c. We find that for ratios < 0.4 the $\langle \theta \rangle$ value is not very sensitive to the distribution width, and thus for octanoate, 2-naphthoate and hexanoate we conclude that the average tilt angle is very close to θ_δ, irrespective of the width of the angular distribution. For ratios > 0.4, which is the case for benzoate, propionate, and acetate, the average tilt angle $\langle \theta \rangle$ has θ_δ as its minimum value and becomes larger when the width of the angular distribution increases. This effect becomes more pronounced with increasing ratio.

We further investigate the relations between the hyperpolarizability components corresponding to the vibrations associated with the carboxylate group. As follows from equation 2.52, based on the absence of the band corresponding to the ν_s vibration in the SPS spectra of the aliphatic species, we conclude that $\beta_{aac} + \beta_{bbc} \approx 2\beta_{ccc}$. For benzoate and 2-naphtoate the ν_s vibration is observed in the SPS spectra. Using the observed ratio and the values of $\langle \cos\theta \rangle$ and $\langle \cos^3\theta \rangle$, as determined from the responses measured for the ν_{as} vibration in SSP and SPS configurations, we can determine the ratio $(\beta_{aac} + \beta_{bbc})/\beta_{ccc}$ for benzoate, and we obtain for this ratio a value of 0.5 ± 0.2. We do not perform a similar analysis for 2-naphthoate ion because the character of the ν_s vibration is likely smeared

out over many different bands, as shown in Figure 8.2. We also determined the ratio between β_{aca} and β_{ccc} using the $|\text{Im}[\chi^{(2)}_{SSP,\nu_{as}}]/\text{Im}[\chi^{(2)}_{SSP,\nu_s}]|$ ratio that can be obtained by dividing equation (2.49) by equation (2.51). The results of the analysis are summarized in Table 8.1, and details of the calculations are given in section 8.6.

8.4 Discussion

In previous studies of long-chain fatty acids adsorbed at the water-air interface,[61,227] only the ν_s vibrational band of the carboxylate group was observed, and the ν_{as} band was not detected. A similar observation was done for carboxylate ions adsorbed on fluorite[60] and on nanoceria surfaces[228]. These observations contrast with the present work, for all studied carboxylates the SSP $\text{Im}[\chi^{(2)}]$ spectrum shows clear responses of both the ν_s and ν_{as} vibrations of the carboxylate group. The response of the ν_{as} band in the SSP $\text{Im}[\chi^{(2)}]$ spectrum is determined by the magnitude of the hyperpolarizability component β_{aca} and the orientation of the ion. From the angular terms of equation (2.49) it follows that the ν_{as} vibration can only be observed if the net transition dipole of the vibration is not parallel to the surface ($\langle\theta\rangle \neq 0°$). In the cited previous studies long carboxylate ions in packed monolayers and carboxylate ions adsorbed to solid surfaces in a bidentate manner were studied. In these cases, the tilt angle of the main axis will be close to zero which means that the transition dipole moment of the ν_{as} vibration is likely oriented close to parallel to the surface normal, which likely explains why this vibration was not observed in the SFG spectrum. Interestingly, for formate adsorbed to a fluorite surface, the ion has been shown to have a nonzero tilt angle but nevertheless the ν_{as} band was still not observed.[60] This latter result was attributed to low probability of Raman transition corresponding to the ν_{as} vibration which enters as a factor in the expression for β_{aca} component. Indeed, the Raman response of the ν_{as} vibration of formate in aqueous solution and in solid salts has been observed to be quite small.[147] An advantage of the technique of HD-VSFG used in the present study is that with this technique directly the complex $\chi^{(2)}$ is measured, whereas in previous intensity SFG experiments the measured response was proportional to $|\chi^{(2)}|^2$. Weak resonances like that of the ν_{as} vibration are much easier distinguished in the complex $\chi^{(2)}$ spectrum than in the $|\chi^{(2)}|^2$ spectrum, as this latter spectrum is dominated by the stronger resonances, i.e. ν_s, and usually also gets further complicated by interference effects between different resonances and between resonances and a non-resonant background.

In the SPS spectra of propionate, hexanoate, and octanoate a weak band centered at ~ 1465 cm^{-1} is observed that is assigned to the δ_{as,CH_3} band. Interestingly, this band has been observed before in the SSP spectrum of propionate, while for octanoate no clear response was detected when the ions were adsorbed to a fluorite surface.[60] This difference likely also originates from a difference in the

orientation of the carboxylate ion at the surface. The observation of δ_{as,CH_3} also requires that the net orientation of the transition dipole of the δ_{as,CH_3} vibration significantly differs from parallel to the surface.

Our results show that small carboxylate ions have their carboxylate groups significantly tilted at the water-air interface. Formate ion constitutes a special case showing a very large tilt angle. As formate does not have a clear hydrophobic part like the other carboxylates, its orientation at the water surface is not driven by preferential dehydration of its hydrophobic part. In accordance with this notion, previous MD studies point to a very low surface activity of formate and a preference for bulk-like solvation of this ion.[200] Recently, Yu et al applied HD-VSFG combined with AIMD simulations to investigate the orientation of formic acid (the protonated form of formate).[63] In this work, the tilt angle for the C-H bond of the ion, which coincides with the tilt angle defined in the present study, was found to be ~56°. This implies that the protonated carboxylic acid group is less tilted compared to the deprotonated carboxylic group of the formate.

For acetate and propionate, the tilt angles are smaller than for formate, which can be well explained by the presence of a methyl and ethyl group in their molecular structure that causes the ions to be more hydrophobic than formate. For both ions, $\theta_\delta \sim 45°$. Interestingly, in MD simulations of acetate at the water-air interface, it was found that the orientational distribution would show two maxima.[200] The first maximum is around 0° and corresponds to ions pointing with their carboxylate group maximally into the bulk while the second maximum, with a much smaller amplitude, would correspond to ions pointing into the bulk with their methyl groups. A comparison with our work is difficult because of the completely different form of the orientational distribution functions, assumed Gaussian versus doubly peaked. In previous studies it was found that the spectroscopic results could be well described with a Gaussian orientational distribution.[229,230] However, it would be of high interest if more detailed information on the shape of the orientational distribution function of various carboxylate ions could be obtained, for instance by combining spectroscopic results with molecular dynamics simulations. Such a combined approach involving VSFG measurements has recently been successfully used to elucidate the orientational distribution of formic acid at the water-air interface.[63] An interesting finding is that the tilt angles of the longer-chain hexanoate and octanoate ions are quite close to that of the 2-naphthoate ion. This is most likely because the sizes of the hydrophobic parts of these ions are very similar. For benzoate ion, the tilt angle is slightly larger (θ_δ = 37°), which can be well explained from the smaller size of its hydrophobic part. The benzoate ion has a smaller tilt angle than acetate and propionate but larger than hexanoate and octanoate and thus takes an intermediate position between long-chain and small-chain carboxylates.

The effect of including a non-zero width of the angular distribution function on the obtained values of $\langle\theta\rangle$ strongly depends on the experimental

$|\mathrm{Im}[\chi^{(2)}_{SSP,\nu_{as}}]/\mathrm{Im}[\chi^{(2)}_{SPS,\nu_{as}}]|$ ratios. For small ratios and ($\theta_\delta < 30°$), the effect is negligible, hence $\langle\theta\rangle$ has to be similar to θ_δ, irrespective of the width of the angular distribution, which applies to compounds with large substituents such as long-chain carboxylates. However, smaller ions that have a larger $\langle\theta\rangle$, require more information on the orientation distribution function for an unambiguous determination of $\langle\theta\rangle$, as a broad range of $\langle\theta\rangle$ and distribution widths can yield the same $|\mathrm{Im}[\chi^{(2)}_{SSP,\nu_{as}}]/\mathrm{Im}[\chi^{(2)}_{SPS,\nu_{as}}]|$ ratio, as determined from the VSFG experiments.

Finally, based on the information related to the orientational distribution we extract ratios of hyperpolarizability components for the carboxylate ions, namely $(\beta_{aac} + \beta_{bbc})/\beta_{ccc}$ and β_{aca}/β_{ccc}. For aliphatic species, $(\beta_{aac} + \beta_{bbc})/\beta_{ccc} \approx 2$ was extracted. Interestingly, a previous theoretical study of the hyperpolarizability components for the CH_2 group which like the carboxylate group possesses C_{2v} symmetry, yielded $\beta_{bbc} = 0$ and $\beta_{aac} = 2\beta_{ccc}$,[231] which is in close agreement with the present results for the carboxylate ion. In view of the similarity of the obtained $(\beta_{aac} + \beta_{bbc})/\beta_{ccc}$ ratios for small and intermediate chain length carboxylates, this result can likely be generalized and used for future studies of orientational properties of different species in which the -COO$^-$ group is attached to an sp^3-hybridized carbon atom such as deprotonated residues of proteins and other biomolecules. For benzoate we obtain quite different results, namely $(\beta_{aac} + \beta_{bbc})/\beta_{ccc} \approx 0.6$. This difference can probably be explained from the interaction of the π-electrons of the carboxylate group with the π-electrons of the highly polarizable aromatic ring.

8.5   Conclusions

We studied the orientation of different carboxylate anions at the water-air interface with heterodyne-detected vibrational sum frequency generation (HD-VSFG) experiments. We studied the aliphatic carboxylate anions formate, acetate, propionate, hexanoate, and octanoate and the aromatic carboxylate anions benzoate and 2-naphthoate. We probe the ν_s and ν_{as} stretching vibrations of the carboxylate group in the 6 μm region. For all ions, we observe a clear surface response of the vibrations of the carboxylate groups and the different substituents. From the ratio of the amplitudes of the responses of the ν_{as} vibration measured in SSP and SPS polarization combinations ($\mathrm{Im}[\chi^{(2)}_{SSP,\nu_{as}}]/\mathrm{Im}[\chi^{(2)}_{SPS,\nu_{as}}]$), we determine the tilt angle θ_δ of the ions at the water/air interface assuming a δ angular distribution. We find that increasing the size of the hydrophobic part of the ion leads to a decrease of the tilt angle of the carboxylate group of ions. Formate ion has a large $\theta_\delta > 75°$, while acetate and propionate have a θ_δ of $\sim$47$\pm$2$°$ and $\sim$42$\pm$3$°$, respectively. For hexanoate and octanoate we obtain tilt angles θ_δ of $33° \pm 3°$ and $\theta_\delta = 26° \pm 3°$, respectively. For the aromatic carboxylates, we extract $\theta_\delta = 37° \pm 3^o$ and $\theta_\delta = 29° \pm 4°$, for benzoate and 2-naphthoate, respectively.

We further investigated the effect of the width of the angular distribution as-

suming this distribution to be Gaussian. By integrating the cosine terms over the distribution, we obtain the relation between the average tilt angle $\langle\theta\rangle$ and the $\text{Im}[\chi^{(2)}_{SSP,\nu_{as}}]/\text{Im}[\chi^{(2)}_{SPS,\nu_{as}}]$ ratio, as is determined from the experiments. For the larger aliphatic carboxylate anions and naphthoate, we find that the average tilt angle $\langle\theta\rangle$ is independent of the width of the Gaussian angular distribution and thus equal to θ_δ. For acetate, propionate and benzoate, the average tilt angle $\langle\theta\rangle$ that follows from the measured ratio $\text{Im}[\chi^{(2)}_{SSP,\nu_{as}}]/\text{Im}[\chi^{(2)}_{SPS,\nu_{as}}]$, has θ_δ as its minimum value, and becomes larger with increasing width of the angular distribution. Finally, using the additional information encoded in the amplitudes of the peaks corresponding to the ν_s vibration we obtain $(\beta_{aac}+\beta_{bbc})/\beta_{ccc}$ and β_{aca}/β_{ccc} ratios for the carboxylate group. The $(\beta_{aac}+\beta_{bbc})/\beta_{ccc} \approx 2$ for aliphatic ions, which agrees with previous estimations for CH_2 groups. For the benzoate ion we find $(\beta_{aac}+\beta_{bbc})/\beta_{ccc} \sim 0.5$. This difference can probably be explained from the interaction of the π-electrons of the carboxylate group with the π-electrons of the highly polarizable aromatic ring. For formate, we get a ratio β_{aca}/β_{ccc} of ~ 2 which is larger than the ratio of ~ 1.2 obtained for the other aliphatic ions and the ratio of ~ 0.7 obtained for the benzoate ion.

8.6 Appendix

8.6.1 Dependence of the $\text{Im}[\chi^{(2)}_{SSP,\nu_{as}}]/\text{Im}[\chi^{(2)}_{SPS,\nu_{as}}]$ ratio on the Fresnel coefficients and the experimental geometry

The measured $\chi^{(2)}$ value is related to the $\chi^{(2)}$ in laboratory coordinate system according to equations 2.47, 2.48. Dividing equation 2.47 by equation 2.48 yields a dependence of the ratio of the SSP and SPS signals on $L_{yy}(\omega_{vis})L_{zz}(\omega_{IR})\sin\varphi_{IR}/(L_{zz}(\omega_{vis})L_{yy}(\omega_{IR})\sin\varphi_{vis})$.

We investigate the dependence of the Fresnel coefficient accounting for the change of n_{vis} and n_{IR} upon dissolving sodium carboxylates in water. We calculate the Fresnel coefficients using the three-layer model combined with the modified Lorentz model to determine the interfacial refractive index n' as described in section 2.3.3

For n_{vis}, we used refractometry data of sodium acetate solutions obtained from previous work.[232] As can be seen from Figure 8.7a, n_{vis} shows a linear increase with concentration. As can be seen from Figure 8.7b, this increase leads to <1% change in the ratio of Fresnel coefficients. Hence, the $\text{Im}[\chi^{(2)}]$ spectra of solutions with different concentrations of acetate do not show a strong variation of the Fresnel coefficient at ω_{vis}.

The concentration dependence of the Fresnel coefficients near ω_{IR} has been investigated in **Chapter 7**. The absorption of infrared light by carboxylate ions
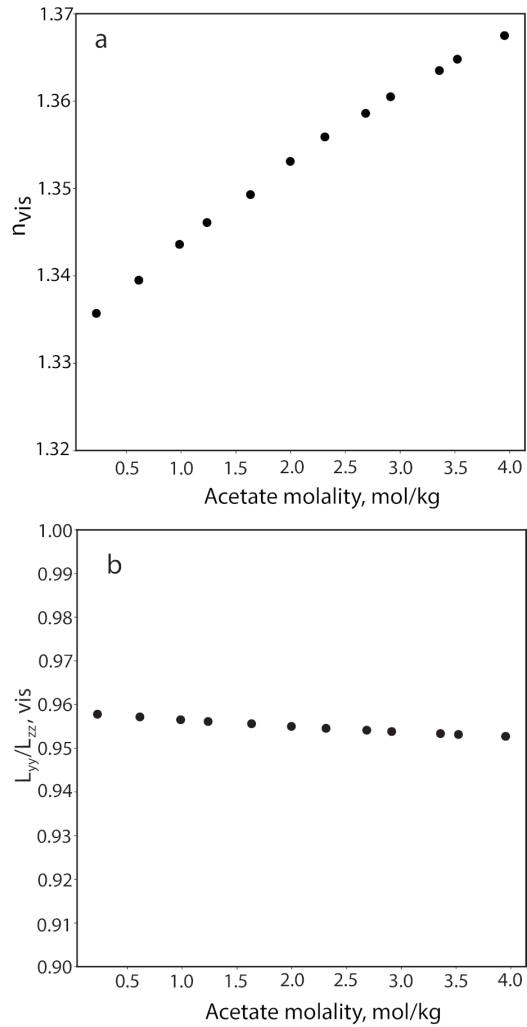
Figure 8.7. a. Dependence of the refractive index n_{vis} at ω_{vis} on the concentration of sodium acetate b. Dependence of $\mathrm{L}_{yy}(\omega_{vis})/\mathrm{L}_{zz}(\omega_{vis})$ on the concentration of sodium acetate
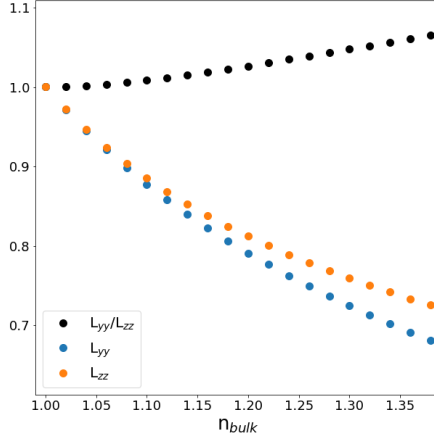
Figure 8.8. Dependence of L_{zz}, L_{yy} and the L_{zz}/L_{yy} ratio on the bulk refractive index

causes dispersion of the refractive index n_{IR}, and the magnitude of this dispersion increases with increasing carboxylate concentration. This dispersive effect primarily leads to a shift of the maximum of the spectrum of the generated sum-frequency light, and hardly affects the amplitude of the band. In Figure 8.8 we show the dependence of the ratio $L_{zz}(\omega_{IR})/L_{yy}(\omega_{IR})$ on the bulk refractive index. As can be seen, the change of the ratio $L_{zz}(\omega_{IR})/L_{yy}(\omega_{IR})$ induced by the change of the refractive index does not exceed 5%. The value of the ratio $L_{yy}(\omega_{vis})L_{zz}(\omega_{IR})/(L_{zz}(\omega_{vis})L_{yy}(\omega_{IR}))$ value will thus be close to 1 at all infrared frequencies, as can be seen from Figures 8.7 and 8.8. Hence, we conclude that the variation of $L_{yy}(\omega_{vis})L_{zz}(\omega_{IR})/(L_{zz}(\omega_{vis})L_{yy}(\omega_{IR}))$ with salt concentration has a negligible effect on the determination of the tilt angle based on the experimental $\text{Im}[\chi^{(2)}_{SSP,\nu_{as}}]/\text{Im}[\chi^{(2)}_{SPS,\nu_{as}}]$ ratio.

8.6.2 Integration of angular terms over angular distribution

To calculate the average values of $\langle\theta\rangle$, $\langle cos\theta\rangle$ and $\langle cos^3\theta\rangle$ an integration over the angular distribution function is required. The Gaussian distribution function is defined by equation 2.55 and the average value is calculated using equation 2.54.

Of course, if a δ-distribution is assumed, $\langle\theta\rangle = \theta_c \equiv \theta_\delta$, $\langle cos\theta\rangle = cos\theta_\delta$, $\langle cos^3\theta\rangle = cos^3\theta_\delta$. The dependence of the angular terms assuming a delta angular distribution

is presented in Figure 8.6b.

In Figure 8.9 we show the dependencies of angular terms determining the amplitude of the band corresponding to the ν_{as} in SSP (Figure 8.9a) and SPS (Figure 8.9b) spectra on the parameters of Gaussian distribution.

By dividing the dependence in Figure 8.9a by the dependence in Figure 8.9b we obtain the dependence of the $\frac{\langle cos\theta \rangle - \langle cos^3\theta \rangle}{\langle cos^3\theta \rangle}$ ratio that we show in Figure 8.10a. This ratio is directly related to the $\mathrm{Im}[\chi^{(2)}_{SSP,\nu_{as}}]/\mathrm{Im}[\chi^{(2)}_{SPS,\nu_{as}}]$ obtained from the measurements.

In Figure 8.10b we also show the dependence of $\langle \theta \rangle$ on the parameters of the Gaussian distribution. By combining the information displayed in Figure 8.10a and Figure 8.10b we obtain the dependence of $\langle \theta \rangle$ on the $\frac{\langle cos\theta \rangle - \langle cos^3\theta \rangle}{\langle cos^3\theta \rangle}$ ratio and the FWHM of the Gaussian distribution, shown in Figure 8.6c.

To understand the orientational properties of the formate ion, it is important to discuss the dependencies of the angular terms in Figure 8.9. As the amplitude of the band corresponding to the ν_{as} vibration in the SPS spectrum is very close to 0, the θ_δ must be quite large, as follows from Figure 2b. At the same time, as a strong negative response is observed in the SSP spectrum θ_δ must be smaller than 90°, as follows from Figure 2a. We estimate the smallest measurable relative $\mathrm{Im}[\chi^{(2)}]$ value to be 0.05 for SPS polarization, which yields a $\frac{\langle cos\theta \rangle - \langle cos^3\theta \rangle}{\langle cos^3\theta \rangle}$ ratio of ~ 13 and hence 75° as a lower boundary for θ_δ. Note that if a lower amplitude in the SPS spectrum was used in the calculations, only a larger tilt angle could be extracted. Furthermore, as follows from Figure 8.10b, with $\theta_\delta = 75°$, increasing the FWHM can only increase the $\langle \theta \rangle$, thus we conclude that $\langle \theta \rangle > 75°$ for formate.
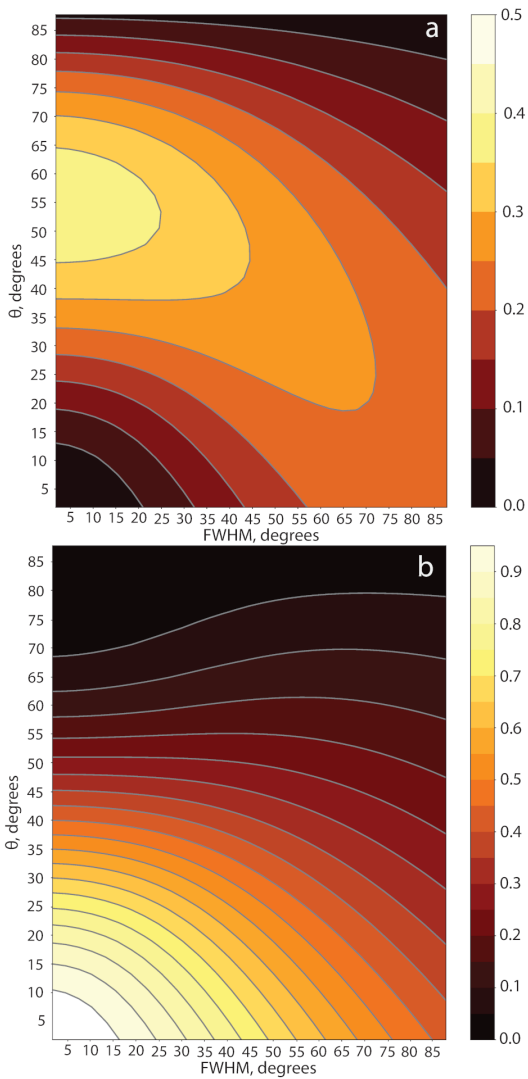
Figure 8.9. Dependence of a. $\langle cos\theta \rangle$ - $\langle cos^3\theta \rangle$ b. $\langle cos^3\theta \rangle$ on θ_c and FWHM of Gaussian distribution obtained by integration over Gaussian functions
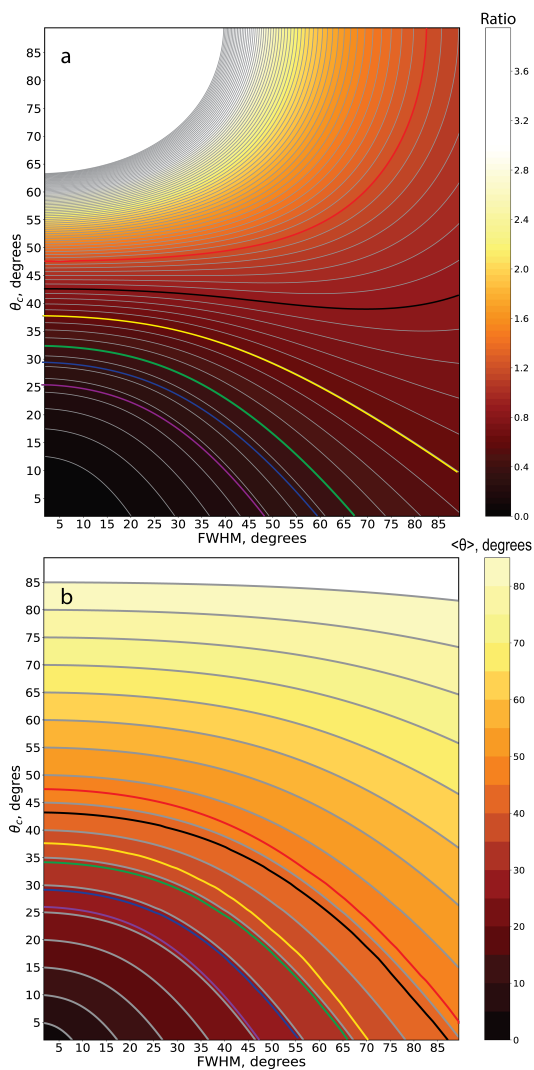
Figure 8.10. Dependence of a. $\frac{\langle cos\theta \rangle - \langle cos^3\theta \rangle}{\langle cos^3\theta \rangle}$ ratio and b. $\langle\theta\rangle$ on θ_c and the width of the Gaussian distribution obtained from equation (2.55). The colored solid lines correspond to the carboxylates under study: acetate (red), propionate (black), benzoate (yellow), hexanoate (green), 2-naphthoate (blue), octanoate (purple)

8.6.3 Determination of the relations between the hyperpolarizability components

As can be noticed directly from the measurements, the band corresponding to the ν_s vibration is absent in the SPS spectra of the aliphatic carboxylates. As follows from equation 2.52, this observation implies that $\beta_{aac} + \beta_{bbc} \approx 2\beta_{ccc}$ as the angular term is non-zero considering the non-zero amplitude of the band corresponding to the ν_{as} vibration in the SSP spectrum. Given that, it can be noted that the second term of equation 2.51 of the main text for the ν_s vibration in SSP polarization combination also must vanish and the expression thus simplifies to its first term. Hence, by dividing equation 1 of the main text by equation 3 of the main text we obtain:

$$
\begin{aligned}
\frac{Im[\chi^{(2)}_{SSP,\nu_{as}}]}{Im[\chi^{(2)}_{SSP,\nu_s}]} &\approx -\frac{2\beta_{aca}}{\beta_{aac} + \beta_{bbc} + 2\beta_{ccc}} \frac{\langle cos\theta \rangle - \langle cos^3\theta \rangle}{\langle cos\theta \rangle} \\
&\approx -\frac{\beta_{aca}}{2\beta_{ccc}} \frac{\langle cos\theta \rangle - \langle cos^3\theta \rangle}{\langle cos\theta \rangle}
\end{aligned}
\tag{8.2}
$$

Therefore, the experimental ratio depends on both the angular distribution and the ratio of the β_{aca} and β_{ccc} hyperpolarizability components. Based on the information on the angular distribution obtained from the $Im[\chi^{(2)}_{SSP,\nu_{as}}]/Im[\chi^{(2)}_{SPS,\nu_{as}}]$, we can determine the value of the $\frac{\langle cos\theta \rangle - \langle cos^3\theta \rangle}{\langle cos\theta \rangle}$ entering equation 8.2 independently. With this information, we obtain the β_{aca}/β_{ccc} for aliphatic ions.

For the aromatic species, the estimation is more elaborate as the band corresponding to the ν_s vibration is non-zero in the SPS spectrum. Dividing equation 2.49 of the main text by equation 2.52 of the main text and taking the experimental $Im[\chi^{(2)}_{SSP,\nu_{as}}]/Im[\chi^{(2)}_{SPS,\nu_s}]$ ratio yields:

$$
\frac{Im[\chi^{(2)}_{SSP,\nu_{as}}]}{Im[\chi^{(2)}_{SPS,\nu_s}]} = -\frac{2\beta_{aca}}{\beta_{aac} + \beta_{bbc} - 2\beta_{ccc}} \approx -0.92
\tag{8.3}
$$

Further, dividing equation 2.49 by equation 2.52 combined with the experimental $Im[\chi^{(2)}_{SSP,\nu_{as}}]/Im[\chi^{(2)}_{SSP,\nu_s}]$ ratio, we obtain:

$$
\begin{aligned}
\frac{Im[\chi^{(2)}_{SSP,\nu_{as}}]}{Im[\chi^{(2)}_{SSP,\nu_s}]} = &-\frac{2\beta_{aca}}{\beta_{aac} + \beta_{bbc} + 2\beta_{ccc}} \frac{\langle cos\theta \rangle - \langle cos^3\theta \rangle}{\langle cos\theta \rangle} - \\
&-\frac{2\beta_{aca}}{\beta_{aac} + \beta_{bbc} - 2\beta_{ccc}} \frac{\langle cos\theta \rangle - \langle cos^3\theta \rangle}{\langle cos^3\theta \rangle} \approx -0.14
\end{aligned}
\tag{8.4}
$$

In this equation, the ratio of the hyperpolarizability components in the second term is known from equation 8.3, and the ratios of the angular terms are ob-
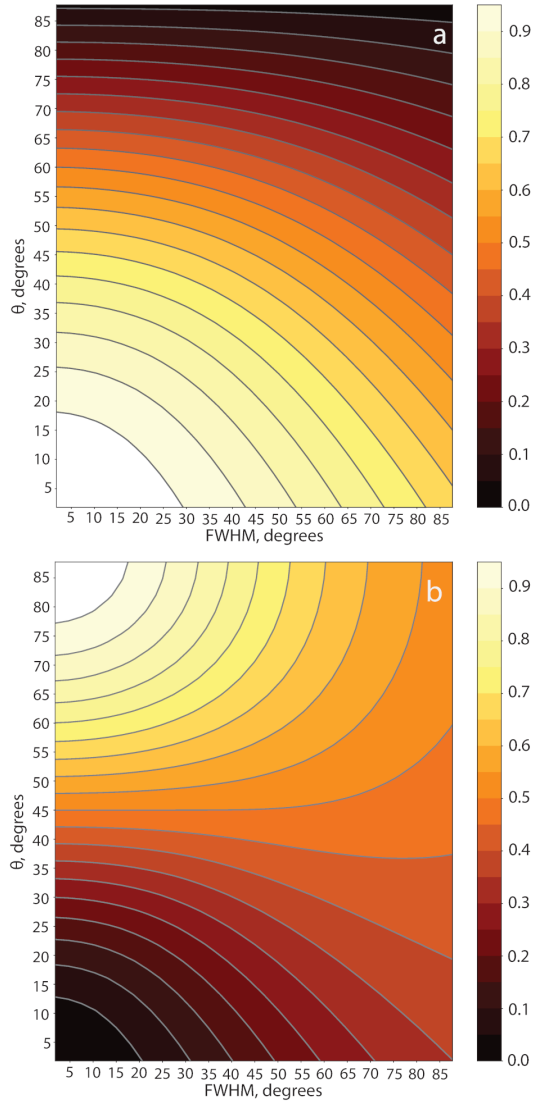
Figure 8.11. Dependence of a. $\langle cos\theta \rangle$ b. $(\langle cos\theta \rangle - \langle cos^3\theta \rangle)/\langle cos\theta \rangle$ on θ_c and the FWHM of the Gaussian distribution obtained from equation (2.55).
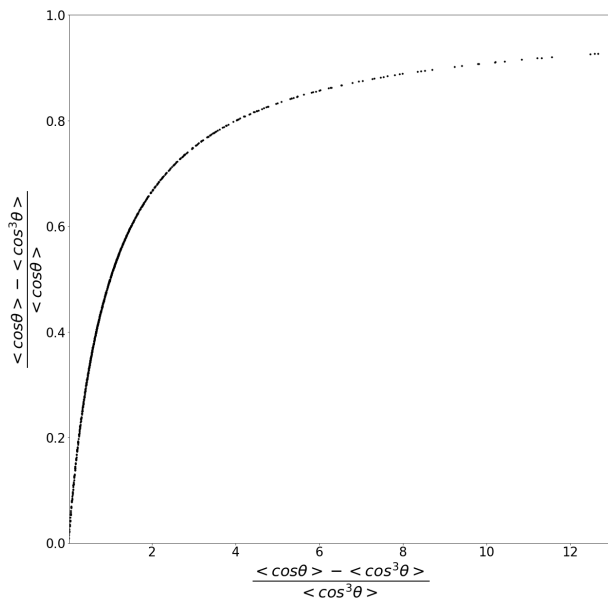
**Figure 8.12.** Dependence of $\frac{\langle cos\theta \rangle - \langle cos^3\theta \rangle}{\langle cos\theta \rangle}$ on $\frac{\langle cos\theta \rangle - \langle cos^3\theta \rangle}{\langle cos^3\theta \rangle}$ obtained from equation (2.55).

tained similarly to the case of the aliphatic carboxylates, as described before. By combining equations 8.3 and 8.4, we obtain $\frac{\beta_{aac}+\beta_{bbc}}{\beta_{ccc}} \approx 0.5$ and $\frac{\beta_{aca}}{\beta_{ccc}} \approx 0.7$

References

[1] Sofronov, O. O.; Bakker, H. J. Slow Proton Transfer in Nanoconfined Water. *ACS Cent. Sci* **2020**, *6*, 1150–1158.

[2] Zhou, H.-X.; Rivas, G.; Minton, A. P. Macromolecular Crowding and Confinement: Biochemical, Biophysical, and Potential Physiological Consequences. *Annu. Rev. Biophys.* **2008**, *37*, 375–397.

[3] Minton, A. P. The Influence of Macromolecular Crowding and Cacromolecular Confinement on Biochemical Reactions in Physiological Media. *J. Biol. Chem.* **2001**, *276*, 10577–10580.

[4] Eggers, D. K.; Valentine, J. S. Molecular Confinement Influences Protein Structure and Enhances Thermal Protein Stability. *Protein Sci.* **2001**, *10*, 250–261.

[5] Slot, T. K.; Riley, N.; Shiju, N. R.; Medlin, J. W.; Rothenberg, G. An Experimental Approach for Controlling Confinement Effects at Catalyst Interfaces. *Chem. Sci.* **2020**, *11*, 11024–11029.

[6] Dong, B.; Pei, Y.; Mansour, N.; Lu, X.; Yang, K.; Huang, W.; Fang, N. Deciphering Nanoconfinement Effects on Molecular Orientation and Reaction Intermediate by Single Molecule Imaging. *Nat. Commun.* **2019**, *10*, 1–6.

[7] Lloyd, G. O.; Forgan, R. S. *Reactivity in Confined Spaces*; Royal Society of Chemistry, 2021; Vol. 31.

[8] Dokter, A. M.; Woutersen, S.; Bakker, H. J. Inhomogeneous Dynamics in Confined Water Nanodroplets. *Proc. Natl. Acad. Sci. U.S.A.* **2006**, *103*, 15355–15358.

[9] Cringus, D.; Lindner, J.; Milder, M. T.; Pshenichnikov, M. S.; Vöhringer, P.; Wiersma, D. A. Femtosecond Water Dynamics in Reverse-Micellar Nanodroplets. *Chemi. Phys. Lett.* **2005**, *408*, 162–168.

[10] Moilanen, D. E.; Fenn, E. E.; Wong, D.; Fayer, M. D. Water Dynamics in Large and Small Reverse Micelles: From Two Ensembles to Collective Behavior. *J. Chem. Phys* **2009**, *131*, 014704.

[11] Moilanen, D. E.; Piletic, I. R.; Fayer, M. Tracking Water's Response to Structural Changes in Nafion Membranes. *J. Phys. Chem. A* **2006**, *110*, 9084–9088.

[12] Yamada, S. A.; Hung, S. T.; Thompson, W. H.; Fayer, M. D. Effects of Pore Size on Water Dynamics in Mesoporous Silica. *J. Chem. Phys* **2020**, *152*, 154704.

[13] Caporaletti, F.; Bonn, D.; Woutersen, S. Lifetime-Associated Two-Dimensional Infrared Spectroscopy Reveals the Hydrogen-Bond Structure of Supercooled Water in Soft Confinement. *J. Phys. Chem. Lett.* **2021**, *12*, 5951–5956.

[14] Hwang, A. Y.; Chikkaraddy, R.; Grys, D.-B.; Scherman, O. A.; Baumberg, J. J.; de Nijs, B. Tracking Water Dimers in Ambient Nanocapsules by Vibrational Spectroscopy. *Proc. Natl. Acad. Sci. U.S.A.* **2022**, *119*, e2212497119.

[15] Knight, A. W.; Kalugin, N. G.; Coker, E.; Ilgen, A. G. Water properties under nanoscale confinement. *Sci. Rep.* **2019**, *9*, 8246.

[16] Kozono, D.; Yasui, M.; King, L. S.; Agre, P., et al. Aquaporin Water Channels: Atomic Structure Molecular Dynamics Meet Clinical Medicine. *J. Clin. Investig.* **2002**, *109*, 1395–1399.

[17] Ghosh, S.; Ramanathan, K.; Sood, A. Water at Nanoscale Confined in Single-Walled Carbon Nanotubes Studied by NMR. *EPL* **2004**, *65*, 678.

[18] Takaiwa, D.; Hatano, I.; Koga, K.; Tanaka, H. Phase diagram of water in carbon nanotubes. *Proc. Natl. Acad. Sci. U.S.A.* **2008**, *105*, 39–43.

[19] Kolesnikov, A. I.; Zanotti, J.-M.; Loong, C.-K.; Thiyagarajan, P.; Moravsky, A. P.; Loutfy, R. O.; Burnham, C. J. Anomalously Soft Dynamics of Water in a Nanotube: a Revelation of Nanoscale Confinement. *Phys. Rev. Lett.* **2004**, *93*, 035503.

[20] Pajzderska, A.; Bilski, P.; Wąsicki, J. Phase Diagram of Water Confined in MCM-41 up to 700 MPa. *J. Chem. Phys* **2015**, *142*, 084505.

[21] Han, S.; Choi, M.; Kumar, P.; Stanley, H. E. Phase Transitions in Confined Water Nanofilms. *Nature Physics* **2010**, *6*, 685–689.

[22] Gilijamse, J.; Lock, A.; Bakker, H. Dynamics of Confined Water Molecules. *Proc. Natl. Acad. Sci. U.S.A.* **2005**, *102*, 3202–3207.

[23] Cringus, D.; Yeremenko, S.; Pshenichnikov, M. S.; Wiersma, D. A. Hydrogen Bonding and Vibrational Energy Relaxation in Water-Acetonitrile mixtures. *J. Phys. Chem B* **2004**, *108*, 10376–10387.

[24] Cringus, D.; Jansen, T. l. C.; Pshenichnikov, M. S.; Wiersma, D. A. Ultrafast Anisotropy Dynamics of Water Molecules Dissolved in Acetonitrile. *J. Chem. Phys* **2007**, *127*, 084507.

[25] Lotze, S.; Groot, C. C. M.; Vennehaug, C.; Bakker, H. J. Femtosecond Mid-Infrared Study of the Dynamics of Water Molecules in Water–Acetone and Water–Dimethyl Sulfoxide Mixtures. *J. Phys. Chem. B* **2015**, *119*, 5228–5239.

[26] Chou, Y. C.; Goldburg, W. I. Phase separation and coalescence in critically quenched isobutyric acid-water and 2,6-lutidine-water mixtures. *Phys. Rev. A* **1979**, *20*, 2105–2113.

[27] Jung, H. Y.; Jhon, M. S. Partial Miscibility in Water-Nicotine and Water-β-Picoline Systems. *Korean J. Chem. Eng.* **1984**, *1*, 59–63.

[28] Erikson, J. P. Partially Miscible Water-Triethylamine Solutions and Their Temperature Dependence. *J. Chem. Educ.* **2017**, *94*, 75–78.

[29] Muñoz-Iglesias, V.; Choukroun, M.; Vu, T. H.; Hodyss, R.; Mahjoub, A.; Smythe, W. D.; Sotin, C. Phase Diagram of the Ternary Water-Tetrahydrofuran-Ammonia System at Low Temperatures. Implications for Clathrate Hydrates and Outgassing on Titan. *ACS Earth Space Chem.* **2018**, *2*, 135–146.

[30] Istvan, E. S.; Deisenhofer, J. Structural mechanism for statin inhibition of HMG-CoA reductase. *Science* **2001**, *292*, 1160–1164.

[31] Gatej, I.; Popa, M.; Rinaudo, M. Role of the pH on Hyaluronan Behavior in Aqueous Solution. *Biomacromolecules* **2005**, *6*, 61–67.

[32] Impact of the counterion on the solubility and physicochemical properties of salts of carboxylic acid drugs. *Drug Development and Industrial Pharmacy* **2012**, *38*, 93–103.

[33] Zhang, L.; Yang, Y.; Kao, Y. T.; Wang, L.; Zhong, D. Protein hydration dynamics and molecular mechanism of coupled water-protein fluctuations. *J. Am. Chem. Soc.* **2009**, *131*, 10677–10691.

[34] Kocak, G.; Tuncer, C.; Bütün, V. pH-Responsive Polymers. *Polym. Chem.* **2017**, *8*, 144–176.

[35] Wen, Y. C.; Zha, S.; Liu, X.; Yang, S.; Guo, P.; Shi, G.; Fang, H.; Shen, Y. R.; Tian, C. Unveiling Microscopic Structures of Charged Water Interfaces by Surface-Specific Vibrational Spectroscopy. *Phys. Rev. Lett.* **2016**, *116*, 1–5.

[36] Miyagawa, A.; Harada, M.; Fukuhara, G.; Okada, T. Space Size-Dependent Transformation of Tetraphenylethylene Carboxylate Aggregates by Ice Confinement. *J. Phys. Chem. B* **2020**, *124*, 2209–2217.

[37] Deka, J. R.; Lee, M.-H.; Saikia, D.; Kao, H.-M.; Yang, Y.-C. Confinement of Cu Nanoparticles in the Nanocages of Large Pore SBA-16 Functionalized with Carboxylic Acid: Enhanced Activity and Improved Durability for 4-Nitrophenol Reduction. *Dalton Trans.* **2019**, *48*, 8227–8237.

[38] Yameen, B.; Ali, M.; Neumann, R.; Ensinger, W.; Knoll, W.; Azzaroni, O. Single Conical Nanopores Displaying pH-Tunable Rectifying Characteristics. Manipulating Ionic Transport with Zwitterionic Polymer Brushes. *J. Am. Chem. Soc.* **2009**, *131*, 2070–2071.

[39] Gao, H.-L.; Zhang, H.; Li, C.-Y.; Xia, X.-H. Confinement Effect of Protonation/Deprotonation of Carboxylic Group Modified in Nanochannel. *Electrochimica Acta* **2013**, *110*, 159–163.

[40] Banno, M.; Ohta, K.; Tominaga, K. Vibrational Dynamics of Acetate in D_2O Studied by Infrared Pump–Probe Spectroscopy. *Phys. Chem. Chem. Phys.* **2012**, *14*, 6359–6366.

[41] Kuroda, D. G.; Vorobyev, D. Y.; Hochstrasser, R. M. Ultrafast relaxation and 2D IR of the aqueous trifluorocarboxylate ion. *The Journal of Chemical Physics* **2010**, *132*, 044501.

[42] Kuroda, D. G.; Hochstrasser, R. M. Two-dimensional infrared spectral signature and hydration of the oxalate dianion. *The Journal of Chemical Physics* **2011**, *135*, 204502.

[43] Zhang, X.; Kumar, R.; Kuroda, D. G. Acetate Ion and its Interesting Solvation Shell Structure and Dynamics. *J. Chem. Phys.* **2018**, *148*, 094506.

[44] Kumar, M.; Francisco, J. S. Ion Pair Particles at the Air-Water Interface. *Proc. Natl. Acad. Sci. U.S.A* **2017**, *114*, 12401–12406.

[45] Jungwirth, P.; Tobias, D. J. Ions at the Air/Water Interface. *J. Phys Chem. B* **2002**, *106*, 6361–6373.

[46] Jordan, C. J. C.; Lowe, E. A.; Verlet, J. R. R. Photooxidation of the Phenolate Anion is Accelerated at the Water/Air Interface. *J. Am. Chem. Soc* **2022**, *144*, 14012–14015.

[47] Masaya, T. W.; Goulay, F. A Molecular Dynamic Study of the Effects of Surface Partitioning on the OH Radical Interactions with Solutes in Multicomponent Aqueous Aerosols. *J. Phys. Chem. A* **0**, *Article ASAP*, null.

[48] Boscoboinik, J. A. Chemistry in Confined Space Through the Eyes of Surface Science—2D Porous Materials. *J. Condens. Matter Phys* **2018**, *31*, 063001.

[49] Laforge, F. O.; Sun, P.; Mirkin, M. V. Shuttling Mechanism of Ion Transfer at the Interface between Two Immiscible Liquids. *J. Am. Chem. Soc.* **2006**, *128*, 15019–15025.

[50] Duong, Q.; Tan, Y.; Corey, J.; Anz, S.; Sun, P. Mechanism of the Transfer of $AuCl_4^-$ and TOA^+ Ions Across the Liquid/Liquid Interface. *J. Phys. Chem. C* **2015**, *119*, 10365–10369.

[51] Koizumi, A.; Tahara, H.; Hirano, T.; Morita, A. Revealing Transient Shuttling Mechanism of Catalytic Ion Transport through Liquid–Liquid Interface. *J. Phys. Chem. Lett.* **2020**, *11*, 1584–1588.

[52] Muñoz, P. A.; Márquez, S. L.; González-Nilo, F. D.; Márquez-Miranda, V.; Blamey, J. M. Structure and Application of Antifreeze Proteins from Antarctic Bacteria. *Microb. Cell Factories* **2017**, *16*, 1–13.

[53] Wang, S.; Cai, X.; Wang, L.; Li, J.; Li, Q.; Zuo, X.; Shi, J.; Huang, Q.; Fan, C. DNA Orientation-Specific Adhesion and Patterning of Living Mammalian Cells on Self-Assembled DNA Monolayers. *Chem. Sci.* **2016**, *7*, 2722–2727.

[54] Gabig-Cimińska, M.; Węgrzyn, G. An Introduction to DNA chips: Principles, Technology, Applications and Analysis. *Acta Biochim. Pol.* **2001**, *48*, 615–622.

[55] Feng, C.; Ding, H.-m.; Ren, C.-l.; Ma, Y.-q. Designing New Strategy for Controlling DNA Orientation in Biosensors. *Sci. Rep.* **2015**, *5*, 1–9.

[56] Zhuang, X.; Miranda, P. B.; Kim, D.; Shen, Y. R. Mapping Molecular Orientation and Conformation at Interfaces by Surface Nonlinear Optics. *Phys. Rev. B* **1999**, *59*, 12632–12640.

[57] Ostroverkhov, V.; Waychunas, G. A.; Shen, Y. R. New Information on Water Interfacial Structure Revealed by Phase-Sensitive Surface Spectroscopy. *Phys. Rev. Lett.* **2005**, *94*, 2–5.

[58] Tyrode, E.; Johnson, C. M.; Kumpulainen, A.; Rutland, M. W.; Claesson, P. M. Hydration State of Nonionic Surfactant Monolayers at the Liquid/Vapor Interface: Structure Determination by Vibrational Sum Frequency Spectroscopy. *J. Am. Chem. Soc.* **2005**, *127*, 16848–16859.

[59] Soule, M. C.; Blower, P. G.; Richmond, G. L. Effects of Atmospherically Important Solvated Ions on Organic Acid Adsorption at the Surface of Aqueous Solutions. *J. Phys. Chem. B* **2007**, *111*, 13703–13713.

[60] Schrödle, S.; Moore, F. G.; Richmond, G. L. In situ Investigation of Carboxylate Adsorption at the Fluorite/Water Interface by Sum Frequency Spectroscopy. *J. Phys. Chem. C* **2007**, *111*, 8050–8059.

[61] Tang, C. Y.; Huang, Z.; Allen, H. C. Binding of Mg2+ and Ca2+ to Palmitic Acid and Deprotonation of the COOH headgroup Studied by Vibrational Sum Frequency Generation Spectroscopy. *J. Phys. Chem. B* **2010**, *114*, 17068–17076.

[62] Wren, S. N.; Gordon, B. P.; Valley, N. A.; McWilliams, L. E.; Richmond, G. L. Hydration, Orientation, and Conformation of Methylglyoxal at the Air–Water Interface. *J. Phys. Chem. B* **2015**, *119*, 6391–6403, PMID: 25989368.

[63] Yu, C.-C.; Imoto, S.; Seki, T.; Chiang, K.-Y.; Sun, S.; Bonn, M.; Nagata, Y. Accurate Molecular Orientation at Interfaces Determined by Multimode Polarization-Dependent Heterodyne-Detected Sum-Frequency Generation Spectroscopy via Multidimensional Orientational Distribution Function. *J. Chem. Phys.* **2022**, *156*, 094703.

[64] Čáp, I.; Čápová, K.; Smetana, M.; Štefan Borik, In *Electromagnetic and Acoustic Waves in Bioengineering Applications*; Čáp, I., Čápová, K., Smetana, M., Štefan Borik,, Eds.; IntechOpen: Rijeka, 2021; Chapter 3.

[65] Landau, L. D.; Lifshitz, E. M. *Mechanics, Third Edition: Volume 1 (Course of Theoretical Physics)*; Butterworth-Heinemann: Oxford, UK, 1976.

[66] Lotze, S. M. *Architecture and Dynamics of Proteins and Aqueous Solvation Complexes*; 2015.

[67] Sakurai, J. J.; Napolitano, J. *Modern quantum mechanics; 2nd ed.*; Addison-Wesley: San Francisco, CA, 2011.

[68] Smit, W. *The Cool State of Water: Infrared Insights into Ice*; 2016.

[69] Rezus, Y. L. A.; Bakker, H. J. Orientational dynamics of isotopically diluted H_2O and D_2O. *J. Chem. Phys* **2006**, *125*, 144512, (1–9).

[70] Rezus, Y.; Bakker, H. Observation of Immobilized Water Molecules around Hydrophobic Groups. *Phys. Rev. Lett.* **2007**, *99*, 148301, (1–4).

[71] Lipari, G.; Szabo, A. Effect of Librational Motion on Fluorescence Depolarization and Nuclear Magnetic Resonance Relaxation in macromolecules and Membranes. *Biophys. J.* **1980**, *30*, 489—506.

[72] Piatkowski, L. *Water Interacting with Interface, Ions and Itself*; 2011.

[73] Rezus, Y. *Snapshots of Water. Orientational Dynamics of Hydrogen-Bonded Systems*; 2008.

[74] Hamm, P.; Zanni, M. *Concepts and methods of 2D infrared spectroscopy*; Cambridge University Press: Cambridge, 2011; p 109–144.

[75] Boyd, R. W. In *Nonlinear Optics (Third Edition)*, third edition ed.; Boyd, R. W., Ed.; Academic Press: Burlington, 2008; pp 69–133.

[76] Morita, A. *Theory of Sum Frequency Generation Spectroscopy*; Springer: Singapore, 2018.

[77] Lambert, A. G.; Davies, P. B.; Neivandt, D. J. Implementing the Theory of Sum Frequency Generation Vibrational Spectroscopy: A Tutorial Review. *Appl. Spectrosc. Rev.* **2005**, *40*, 103–145.

[78] Parson, W. W. *Modern Optical Spectroscopy: With Exercises and Examples from Biophysics and Biochemistry*; Springer Berlin Heidelberg: Berlin, Heidelberg, 2015; pp 81–122.

[79] Wang, H. F.; Gan, W.; Lu, R.; Rao, Y.; Wu, B. H. Quantitative Spectral and Orientational Analysis in Surface Sum Frequency Generation Vibrational Spectroscopy (SFG-VS). *Int. Rev. Phys. Chem.* **2005**, *24*, 191–256.

[80] Goldstein, H.; Poole, C.; Safko, J. *Classical Mechanics*; Addison Wesley: New York, 2002.

[81] Selig, O. *Ultrasensitive Nonlinear Vibrational Spectroscopy of Complex Molecular Systems*; 2017.

[82] Selig, O.; Siffels, R.; Rezus, Y. L. A. Ultrasensitive Ultrafast Vibrational Spectroscopy Employing the Near Field of Gold Nanoantennas. *Phys. Rev. Lett.* **2015**, *114*, 233004.

[83] Hu, X.-H.; Wei, F.; Wang, H.; Wang, H.-F. α-Quartz Crystal as Absolute Intensity and Phase Standard in Sum-Frequency Generation Vibrational Spectroscopy. *J. Phys. Chem. C* **2019**, *123*, 15071–15086.

[84] Moll, C. J.; Versluis, J.; Bakker, H. J. Direct Evidence for a Surface and Bulk Specific Response in the Sum-Frequency Generation Spectrum of the Water Bend Vibration. *Phys. Rev. Lett.* **2021**, *127*, 116001.

[85] Moll, C. J.; Korotkevich, A. A.; Versluis, J.; Bakker, H. J. Molecular Orientation of Small Carboxylates at the Water–Air Interface. *Phys. Chem. Chem. Phys.* **2022**, *24*, 10134–10139.

[86] Moll, C. Bending and Stretching: A Practical Examination of Molecules at Aqueous Interfaces. Ph.D. thesis, 2022.

[87] Bloembergen, N.; Pershan, P. S. Light Waves at the Boundary of Nonlinear Media. *Phys. Rev.* **1962**, *128*, 606–622.

[88] Feng, R.-r.; Guo, Y.; Lü, R.; Velarde, L.; Wang, H.-f. Consistency in the Sum Frequency Generation Intensity and Phase Vibrational Spectra of the Air/Neat Water Interface. *J. Phys. Chem. A* **2011**, *115*, 6015–6027.

[89] Valenzano, L.; Civalleri, B.; Chavan, S.; Bordiga, S.; Nilsen, M. H.; Jakobsen, S.; Lillerud, K. P.; Lamberti, C. Disclosing the Complex Structure of UiO-66 Metal- Organic Framework: a Synergic Combination of Experiment and Theory. *Chem. Mater.* **2011**, *23*, 1700–1718.

[90] Indulkar, A. S.; Gao, Y.; Raina, S. A.; Zhang, G. G. Z.; Taylor, L. S. Exploiting the Phenomenon of Liquid–Liquid Phase Separation for Enhanced and Sustained Membrane Transport of a Poorly Water-Soluble Drug. *Mol. Pharmaceutics* **2016**, *13*, 2059–2069.

[91] Considerations and Challenges in Studying Liquid-Liquid Phase Separation and Biomolecular Condensates. *Cell* **2019**, *176*, 419–434.

[92] Liquid–Liquid Phase Separation and Its Mechanistic Role in Pathological Protein Aggregation. *J. Mol. Biol.* **2020**, *432*, 1910–1925.

[93] Renbaum-Wolff, L.; Song, M.; Marcolli, C.; Zhang, Y.; Liu, P. F.; Grayson, J. W.; Geiger, F. M.; Martin, S. T.; Bertram, A. K. Observations and implications of liquid-liquid phase separation at high relative humidities in secondary organic material produced by α-pinene ozonolysis without inorganic salts. *Atmospheric Chem. Phys.* **2016**, *16*, 7969–7979.

[94] Song, M.; Liu, P.; Martin, S. T.; Bertram, A. K. Liquid–liquid phase separation in particles containing secondary organic material free of inorganic salts. *Atmospheric Chem. Phys.* **2017**, *17*, 11261–11271.

[95] Counsell, J. F.; Everett, D. H.; Munn, R. J. Phase separation and coalescence in critically quenched isobutyric acid-water and 2,6-lutidine-water mixtures. *Pure Appl. Chem.* **1961**, *2*, 335–338.

[96] Míguez, J. M.; Piñeiro, M. M.; Algaba, J.; Mendiboure, B.; Torré, J. P.; Blas, F. J. Understanding the Phase Behavior of Tetrahydrofuran + Carbon Dioxide, + Methane, and + Water Binary Mixtures from the SAFT-VR Approach. *J. Phys. Chem. B* **2015**, *119*, 14288–14302.

[97] Heskins, M.; Guillet, J. E. Solution Properties of Poly(N-isopropylacrylamide). *J. Macromol. Sci. A* **1968**, *2*, 1441–1455.

[98] Upper and lower critical solution temperatures in poly (ethylene glycol) solutions. *Polymer* **1976**, *17*, 685–689.

[99] Lachwa, J.; Szydlowski, J.; Najdanovic-Visak, V.; Rebelo, L. P. N.; Seddon, K. R.; Nunes da Ponte, M.; Esperança, J. M. S. S.; Guedes, H. J. R. Evidence for Lower Critical Solution Behavior in Ionic Liquid Solutions. *J. Am. Chem. Soc.* **2005**, *127*, 6542–6543.

[100] Goldstein, R. E. Substituent effects on intermolecular hydrogen bonding from a lattice gas theory for lower critical solution points: Comparison with experiments on aqueous solutions of alkylpyridines. *J. Chem. Phys.* **1983**, *79*, 4439–4447.

[101] Karlsson, R. Solubility of water in benzene. *J. Chem. Eng. Data* **1973**, *18*, 290–292.

[102] Brovchenko, I. V.; Oleinikova, A. V. Structural Changes of the Molecular Complexes of Pyridines with Water and Demixing Phenomena in Aqueous Solutions. *J. Chem. Phys* **1997**, *106*, 7756–7765.

[103] Pápai, I.; Jancsó, G. Hydrogen Bonding in Methyl-Substituted Pyridine—Water Complexes: A Theoretical Study. *J. Phys. Chem. A* **2000**, *104*, 2132–2137.

[104] Chernia, Z.; Tsori, Y. Complexation reactions in pyridine and 2,6-dimethylpyridine-water system: The quantum-chemical description and the path to liquid phase separation. *J. Chem. Phys.* **2018**, *148*, 104306.

[105] Marczak, W.; Czech, B.; Almásy, L.; Lairez, D. Molecular clusters in aqueous solutions of pyridine and its methyl derivatives. *Phys. Chem. Chem. Phys.* **2011**, *13*, 6260–6269.

[106] Kostko, A.; Anisimov, M.; Sengers, J. Criticality in aqueous solutions of 3-methylpyridine and sodium bromide. *Phys. Rev. E* **2004**, *70*, 026118, (1–11).

[107] Analyzing of segregation in mixtures of 3-methylpyridine and heavy water by dynamic neutron radiography. *Appl. Radiat. Isot.* **2004**, *61*, 597–602.

[108] Evidence of clustering in an aqueous electrolyte solution: a small-angle X-ray scattering study. *Chem. Phys. Lett.* **1999**, *304*, 180–186.

[109] Davies, N.; Gillard, R. The solubility loop of nicotine:water. *Transit. Met. Chem.* **2000**, *25*, 628 – 629.

[110] Cox, J. D. Phase relationships in the pyridine series. Part II. The miscibility of some pyridine homologues with deuterium oxide. *J. Chem. Soc.* **1952**, 4606–4608.

[111] Grattoni, C. A.; Dawe, R. A.; Seah, C. Y.; Gray, J. D. Lower critical solution coexistence curve and physical properties (density, viscosity, surface tension, and interfacial tension) of 2,6-lutidine + water. *J. Chem. Eng. Data* **1993**, *38*, 516–519.

[112] Balevicius, V.; Gdaniec, Z.; Fuess, H. NMR probing of structural peculiarities in ionic solutions close to critical point. *J. Chem. Phys.* **2005**, *123*, 224503.

[113] Reeves, M.; Brown, A.; Schofield, A.; Cates, M.; Thijssen, J. Particle-Size Effects in the Formation of Bicontinuous Pickering Emulsions. *Phys. Rev. E* **2015**, *92*, 032308.

References

[114] Study of phase behavior of 2,6-lutidine, 2,6-lutidine-N-oxide and water mixture using UNIQUAC model with interaction parameters determined by molecular simulations. *Thermochim. Acta* **2019**, *671*, 110–118.

[115] Zhao, W.; Moilanen, D. E.; Fenn, E. E.; Fayer, M. D. Water at the Surfaces of Aligned Phospholipid Multibilayer Model Membranes Probed with Ultrafast Vibrational Spectroscopy. *J. Am. Chem. Soc.* **2008**, *130*, 13927–13937.

[116] Wong, D. B.; Sokolowsky, K. P.; El-Barghouthi, M. I.; Fenn, E. E.; Giammanco, C. H.; Sturlaugson, A. L.; Fayer, M. D. Water Dynamics in Water/DMSO Binary Mixtures. *J. Phys. Chem. B* **2012**, *116*, 5479–5490.

[117] Groot, C. C.; Bakker, H. J. Proteins Take up Water Before Unfolding. *J. Phys. Chem. Lett.* **2016**, *7*, 1800–1804.

[118] Yan, C.; Kramer, P. L.; Yuan, R.; Fayer, M. D. Water Dynamics in Polyacrylamide Hydrogels. *J. Am. Chem. Soc.* **2018**, *140*, 9466–9477.

[119] Fenn, E. E.; Moilanen, D. E.; Levinger, N. E.; Fayer, M. D. Water Dynamics and Interactions in Water–Polyether Binary Mixtures. *J. Am. Chem. Soc.* **2009**, *131*, 5530–5539.

[120] Sturlaugson, A. L.; Fruchey, K. S.; Lynch, S. R.; Aragón, S. R.; Fayer, M. D. Orientational and Translational Dynamics of Polyether/Water Solutions. *J. Phys. Chem. B* **2010**, *114*, 5350–5358.

[121] Lifschitz, A. M.; Rodgers, J. M.; Samet, C. Matrix and Polymer Soft-Landing Isolation of Selected Acids with Pyridine and Poly(4-vinylpyridine): A Comparative Infrared Spectroscopic Study of Hydrogen Bonding. *J. Phys. Chem. B* **2012**, *116*, 211–220.

[122] Shimizu, S.; Watanabe, N.; Kataoka, T.; Shoji, T.; Abe, N.; Morishita, S.; Ichimura, H. *Ullmann's Encyclopedia of Industrial Chemistry*; John Wiley Sons, Ltd, 2000.

[123] Hunger, J.; Tielrooij, K.-J.; Buchner, R.; Bonn, M.; Bakker, H. J. Complex Formation in Aqueous Trimethylamine-N-oxide (TMAO) Solutions. *J. Phys. Chem. B* **2012**, *116*, 4783–4795.

[124] Perakis, F.; Hamm, P. Two-Dimensional Infrared Spectroscopy of Supercooled Water. *J. Phys. Chem. B* **2011**, *115*, 5289–5293.

[125] Petersen, C.; Tielrooij, K.-J.; Bakker, H. J. Strong temperature dependence of water reorientation in hydrophobic hydration shells. *J. Chem. Phys.* **2009**, *130*, 214511, (1–6).

[126] Lomas, J.; Maurel, F. Water and alcohol(s): What's the difference? A proton NMR and DFT study of hetero-association with pyridine. *J. Phys. Org. Chem.* **2008**, *21*, 464 – 471.

[127] Hydration modes of an amphiphilic molecule 2: NMR, FTIR and theoretical study of the interactions in the system water–1,2-dimethoxyethane. *Chem. Phys.* **2011**, *382*, 104–112.

[128] Mishra, B. K.; Sathyamurthy, N. $\pi-\pi$ Interaction in Pyridine. *J. Phys. Chem. A* **2005**, *109*, 6–8.

[129] Hohenstein, E. G.; Sherrill, C. D. Effects of Heteroatoms on Aromatic $\pi-\pi$ Interactions: Benzene−Pyridine and Pyridine Dimer. *J. Phys. Chem. A* **2009**, *113*, 878–886.

[130] Tielrooij, K.-J.; Hunger, J.; Buchner, R.; Bonn, M.; Bakker, H. J. Influence of Concentration and Temperature on the Dynamics of Water in the Hydrophobic Hydration Shell of Tetramethylurea. *J. Am. Chem. Soc.* **2010**, *132*, 15671–15678.

[131] Hamm, P.; Lim, M.; Hochstrasser, R. M. Vibrational relaxation and dephasing of small molecules strongly interacting with water. *Springer Series in Chemical Physics* **1998**, *63*, 514–516.

[132] Woutersen, S.; Bakker, H. J. Resonant intermolecular energy transfer in liquid water. *ACS Symposium Series* **2002**, *820*, 184–197.

[133] DeFlores, L. P.; Ganim, Z.; Ackley, S. F.; Chung, H. S.; Tokmakoff, A. The Anharmonic Vibrational Potential and Relaxation Pathways of the Amide I and II Modes of N-Methylacetamide. *J. Phys. Chem. B* **2006**, *110*, 18973–18980.

[134] He, X.; Yu, P.; Zhao, J.; Wang, J. Efficient Vibrational Energy Transfer through Covalent Bond in Indigo Carmine Revealed by Nonlinear IR Spectroscopy. *J. Phys. Chem. B* **2017**, *121*, 9411–9421.

[135] Lo Nostro, P.; Ninham, B. W. Hofmeister phenomena: An update on ion specificity in biology. *Chem. Rev.* **2012**, *112*, 2286–2322.

[136] Deacon, G.; Phillips, R. Relationships between the carbon-oxygen stretching frequencies of carboxylato complexes and the type of carboxylate coordination. *Coordination Chemistry Reviews* **1980**, *33*, 227–250.

[137] Shirase, S.; Tamaki, S.; Shinohara, K.; Hirosawa, K.; Tsurugi, H.; Satoh, T.; Mashima, K. Cerium(IV) Carboxylate Photocatalyst for Catalytic Radical Formation from Carboxylic Acids: Decarboxylative Oxygenation of Aliphatic Carboxylic Acids and Lactonization of Aromatic Carboxylic Acids. *J. Am. Chem. Soc.* **2020**, *142*, 5668–5675.

[138] Wang, X.; Zhai, L.; Wang, Y.; Li, R.; Gu, X.; Yuan, Y. D.; Qian, Y.; Hu, Z.; Zhao, D. Improving Water-Treatment Performance of Zirconium Metal-Organic Framework Membranes by Postsynthetic Defect Healing. *ACS Appl. Mater. Interfaces* **2017**, *9*, 37848–37855.

[139] Li, H.; Wang, K.; Sun, Y.; Lollar, C. T.; Li, J.; Zhou, H. C. Recent advances in gas storage and separation using metal-organic frameworks. *Mater. Today* **2018**, *21*, 108–121.

[140] Ahamad, M. N.; Khan, M. S.; Shahid, M.; Ahmad, M. Metal organic frameworks decorated with free carboxylic acid groups: Topology, metal capture and dye adsorption properties. *Dalton trans.* **2020**, *49*, 14690–14705.

[141] An Iron Carboxylate-Based Metal-Organic Framework for Furosemide Loading and Release. *J. Mater. Sci.* **2020**, *55*, 13785–13798.

[142] Varghese, H. T.; Panicker, C. Y.; Philip, D.; Sreevalsan, K.; Anithakumary, V. IR, Raman and SERS spectra of disodium terephthalate. *Spectrochimica Acta Part A: Molecular and Biomolecular Spectroscopy* **2007**, *68*, 817–822.

[143] Mondal, M.; Bora, U. Recent advances in manganese(iii) acetate mediated organic synthesis. *RSC Adv.* **2013**, *3*, 18716–18754.

[144] Banerjee, A.; Briceño, B.; Maldonado, A.; Bedoya, L.; Cabrera, E.; Arrieche, D. Lead Tetraacetate in Organic Synthesis. **2021**,

[145] Lehninger, A. L.; Nelson, D. L.; Cox, M. M. In *Lehninger Principles of Biochemistry, Fourth Edition*, fourth edition ed.; Freeman„ Ed.; 2004.

[146] Mitra, S.; Werling, K.; Berquist, E. J.; Lambrecht, D. S.; Garrett-Roe, S. CH Mode Mixing Determines the Band Shape of the Carboxylate Symmetric Stretch in Apo-EDTA, Ca2+–EDTA, and Mg2+–EDTA. *J. Phys. Chem. A* **2021**, *125*, 4867–4881.

[147] Ito, K.; Bernstein, H. J. The Vibrational Spectra of the Formate, Acetate, and Oxalate Ions. *Can. J. Chem.* **1956**, *34*, 170–178.

[148] Woutersen, S.; Mu, Y.; Stock, G.; Hamm, P. Subpicosecond Conformational Dynamics of Small Peptides Probed by Two-Dimensional Vibrational Spectroscopy. *Proc. Natl. Acad. Sci. U.S.A.* **2001**, *98*, 11254–11258.

[149] Kraack, J. P.; Lotti, D.; Hamm, P. Ultrafast, Multidimensional Attenuated Total Reflectance Spectroscopy of Adsorbates at Metal Surfaces. *J. Phys. Chem. Lett.* **2014**, *5*, 2325–2329.

[150] Eddaoudi, M.; Kim, J.; Rosi, N.; Vodak, D.; Wachter, J.; O'Keeffe, M.; Yaghi, O. M. Systematic Design of Pore Size and Functionality in Isoreticular MOFs and Their Application in Methane Storage. *Science* **2002**, *295*, 469–472.

[151] Burrows, A. D. Mixed-Component Metal–Organic Frameworks (MC-MOFs): Enhancing Functionality through Solid Solution Formation and Surface Modifications. *CrystEngComm* **2011**, *13*, 3623–3642.

[152] Xue, D.-X.; Belmabkhout, Y.; Shekhah, O.; Jiang, H.; Adil, K.; Cairns, A. J.; Eddaoudi, M. Tunable Rare Earth fcu-MOF Platform: Access to Adsorption Kinetics Driven Gas/Vapor Separations via Pore Size Contraction. *J. Am. Chem. Soc.* **2015**, *137*, 5034–5040.

[153] Razavi, S. A. A.; Masoomi, M. Y.; Islamoglu, T.; Morsali, A.; Xu, Y.; Hupp, J. T.; Farha, O. K.; Wang, J.; Junk, P. C. Improvement of Methane–Framework Interaction by Controlling Pore Size and Functionality of Pillared MOFs. *Inorg. Chem* **2017**, *56*, 2581–2588.

[154] Wen, Y.; Zhang, J.; Xu, Q.; Wu, X.-T.; Zhu, Q.-L. Pore Surface Engineering of Metal–Organic Frameworks for Heterogeneous Catalysis. *Coord. Chem. Rev.* **2018**, *376*, 248–276.

[155] Wang, X.-F.; Song, X.-Z.; Sun, K.-M.; Cheng, L.; Ma, W. MOFs-Derived Porous Nanomaterials for Gas Sensing. *Polyhedron* **2018**, *152*, 155–163.

[156] Li, B.; Wen, H.-M.; Zhou, W.; Chen, B. Porous Metal–Organic Frameworks for Gas Storage and Separation: What, How, and Why? *J. Phys. Chem. Lett* **2014**, *5*, 3468–3479.

[157] He, B.; Dong, X. Hierarchically Porous Zr-MOFs Labelled Methylene Blue as Signal Tags for Electrochemical Patulin Aptasensor Based on ZnO Nano Flower. *Sens. Actuators B Chem.* **2019**, *294*, 192–198.

[158] Wang, H.-F.; Chen, L.; Pang, H.; Kaskel, S.; Xu, Q. MOF-Derived Electrocatalysts for Oxygen Reduction, Oxygen Evolution and Hydrogen Evolution Reactions. *Chem. Soc. Rev.* **2020**, *49*, 1414–1448.

[159] Cavka, J. H.; Jakobsen, S.; Olsbye, U.; Guillou, N.; Lamberti, C.; Bordiga, S.; Lillerud, K. P. A New Zirconium Inorganic Building Brick Forming Metal Organic Frameworks with Exceptional Stability. *J. Am. Chem. Soc.* **2008**, *130*, 13850–13851.

[160] Winarta, J.; Shan, B.; Mcintyre, S. M.; Ye, L.; Wang, C.; Liu, J.; Mu, B. A Decade of UiO-66 Research: A Historic Review of Dynamic Structure, Synthesis Mechanisms, and Characterization Techniques of an Archetypal Metal–Organic Framework. *Cryst. Growth Des.* **2020**, *20*, 1347–1362.

[161] Khudozhitkov, A. E.; Arzumanov, S. S.; Kolokolov, D. I.; Stepanov, A. G. UiO-66 (Zr) MOF as a Promising Material for Butane Isomers Separation: Evidence Based on the Analysis of the Adsorbed Alkanes Mobility by 2H NMR and Molecular Dynamics Simulation. *J. Phys. Chem. C* **2021**, *125*, 13391–13400.

[162] Virmani, E.; Rotter, J. M.; Mähringer, A.; von Zons, T.; Godt, A.; Bein, T.; Wuttke, S.; Medina, D. D. On-Surface Synthesis of Highly Oriented Thin Metal–Organic Framework Films through Vapor-Assisted Conversion. *J. Am. Chem. Soc.* **2018**, *140*, 4812–4819.

[163] Miyamoto, M.; Hori, K.; Goshima, T.; Takaya, N.; Oumi, Y.; Uemiya, S. An Organoselective Zirconium-Based Metal–Organic-Framework UiO-66 Membrane for Pervaporation. *Eur. J. Inorg. Chem* **2017**, *2017*, 2094–2099.

[164] Liu, X. Metal-organic framework UiO-66 membranes. *Front. Chem. Sci. Eng.* **2020**, *14*, 216–232.

References

[165] Cmarik, G. E.; Kim, M.; Cohen, S. M.; Walton, K. S. Tuning the Adsorption Properties of UiO-66 via Ligand Functionalization. *Langmuir* **2012**, *28*, 15606–15613.

[166] Johnson, B. A.; Bhunia, A.; Fei, H.; Cohen, S. M.; Ott, S. Development of a UiO-Type Thin Film Electrocatalysis Platform with Redox-Active Linkers. *J. Am. Chem. Soc.* **2018**, *140*, 2985–2994.

[167] Sun, Y.; Song, C.; Guo, X.; Liu, Y. Concurrent Manipulation of Out-of-Plane and Regional In-Plane Orientations of NH2-UiO-66 Membranes with Significantly Reduced Anisotropic Grain Boundary and Superior H2/CO2 Separation Performance. *ACS Appl. Mater. Interfaces* **2020**, *12*, 4494–4500.

[168] Yang, F.; Huang, H.; Wang, X.; Li, F.; Gong, Y.; Zhong, C.; Li, J.-R. Proton Conductivities in Functionalized UiO-66: Tuned Properties, Thermogravimetry Mass, and Molecular Simulation Analyses. *Cryst. Growth Des.* **2015**, *15*, 5827–5833.

[169] The Metal–Organic Framework UiO-66 with Missing-Linker Defects: a Highly Active Catalyst for Carbon Dioxide Cycloaddition. *Appl. Energy* **2020**, *277*, 115560.

[170] Feng, L.; Hou, H.-B.; Zhou, H. UiO-66 Derivatives and Their Composite Membranes for Effective Proton Conduction. *Dalton Trans.* **2020**, *49*, 17130–17139.

[171] Wu, H.; Chua, Y. S.; Krungleviciute, V.; Tyagi, M.; Chen, P.; Yildirim, T.; Zhou, W. Unusual and Highly Tunable Missing-Linker Defects in Zirconium Metal–Organic Framework UiO-66 and Their Important Effects on Gas Adsorption. *J. Am. Chem. Soc.* **2013**, *135*, 10525–10532.

[172] Clark, C. A.; Heck, K. N.; Powell, C. D.; Wong, M. S. Highly Defective UiO-66 Materials for the Adsorptive Removal of Perfluorooctanesulfonate. *ACS Sustain. Chem. Eng.* **2019**, *7*, 6619–6628.

[173] Feng, X.; Jena, H. S.; Krishnaraj, C.; Leus, K.; Wang, G.; Chen, H.; Jia, C.; Van Der Voort, P. Generating Catalytic Sites in UiO-66 through Defect Engineering. *ACS Appl. Mater. Interfaces* **2021**, *13*, 60715–60735.

[174] Cirujano, F. G.; Llabrés i Xamena, F. X. Tuning the Catalytic Properties of UiO-66 Metal–Organic Frameworks: From Lewis to Defect-Induced Brønsted Acidity. *J. Phys. Chem. Lett* **2020**, *11*, 4879–4890.

[175] Borges, D. D.; Devautour-Vinot, S.; Jobic, H.; Ollivier, J.; Nouar, F.; Semino, R.; Devic, T.; Serre, C.; Paesani, F.; Maurin, G. Proton Transport in a Highly Conductive Porous Zirconium-Based Metal–Organic Framework: Molecular Insight. *Angew. Chem. Int. Ed.* **2016**, *55*, 3919–3924.

[176] Ling, S.; Slater, B. Dynamic Acidity in Defective UiO-66. *Chem. Sci.* **2016**, *7*, 4706–4712.

[177] Balčiūnas, S.; Pavlovaitė, D.; Kinka, M.; Yeh, J.-Y.; Han, P.-C.; Shieh, F.-K.; Wu, K. C.-W.; Šimėnas, M.; Grigalaitis, R.; Banys, J. Dielectric Spectroscopy of Water Dynamics in Functionalized UiO-66 Metal-Organic Frameworks. *Molecules* **2020**, *25*, 1–11.

[178] Gutierrez, M.; Cohen, B.; Sánchez, F.; Douhal, A. Photochemistry of Zr-based MOFs: Ligand-to-Cluster Charge Transfer, Energy Transfer and Excimer Formation, What Else Is There? *Phys. Chem. Chem. Phys.* **2016**, *18*, 27761–27774.

[179] Liu, J.; Jiang, S.-l.; Zhang, Q. Doping Copper Ions in a Metal-Organic Framework (UiO-66-NH2): Location Effect Examined by Ultrafast Spectroscopy. *Chinese J. Chem. Phys.* **2020**, *33*, 394–400.

[180] Nishida, J.; Tamimi,; Fei, H.; Pullen, S. P.; Ott, S.; Cohen, S. M.; Fayer, M. D. Structural Dynamics Inside a Functionalized Metal-Organic Framework Probed by Ultrafast 2D IR Spectroscopy. *Proc. Natl. Acad. Sci. U.S.A* **2014**, *111*, 18442–18447.

[181] Nishida, J.; Fayer, M. D. Guest Hydrogen Bond Dynamics and Interactions in the Metal–Organic Framework MIL-53(Al) Measured with Ultrafast Infrared Spectroscopy. *J. Phys. Chem. C* **2017**, *121*, 11880–11890.

[182] Yan, J.; Sun, Y.; Ji, T.; Zhang, C.; Liu, L.; Liu, Y. Room-Temperature Synthesis of Defect-Engineered Zirconium-MOF Membrane Enabling Superior CO2/N2 Selectivity with Zirconium-Oxo Cluster Source. *J. Membr. Sci.* **2022**, *653*, 120496, (1–9).

[183] Wang, X.; Lyu, Q.; Sune, K.; Lin, L.-C.; Tang, C. Y.; Yang, F.; Guiver, M. D.; Wuttke, S.; Quang, X.; Dong, Y. Robust Ultrathin Nanoporous MOF Membrane with Intra-Crystalline Defects for Fast Water Transport. *Nat. Commun.* **2022**, *13*, 266, (1–11).

[184] Wilson, E. B. The Normal Modes and Frequencies of Vibration of the Regular Plane Hexagon Model of the Benzene Molecule. *Phys. Rev.* **1934**, *45*, 706–714.

[185] Arenas, J.; Marcos, J. Infrared and Raman spectra of Phtalate, Isophtalate and Terephtalate Ions. *Spectrochim. Acta A Mol* **1979**, *35*, 355–363.

[186] Boerio, F. J.; Roth, P. G. Vibrational Analysis of Terephthalate and Terephthalate-D4 Ions. *Appl. Spectrosc.* **1987**, *41*, 463–467.

[187] Varghese, H. T.; Panicker, C. Y.; Philip, D.; Sreevalsan, K.; Anithakumary, V. IR, Raman and SERS Spectra of Disodium Terephthalate. *Spectrochim. Acta A Mol. Biomol* **2007**, *68*, 817–822.

[188] Andreeva, A. B.; Le, K. N.; Chen, L.; Kellman, M. E.; Hendon, C. H.; Brozek, C. K. Soft Mode Metal-Linker Dynamics in Carboxylate MOFs Evidenced by Variable-Temperature Infrared Spectroscopy. *J. Am. Chem. Soc.* **2020**, *142*, 19291–19299.

[189] Connolly, B.; Aragones-Anglada, M.; Gandara-Loe, J.; Danaf, N.; Lamb, D.; Mehta, J. P.; Vulpe, D.; Wuttke, S.; Silvestro-Albero, J.; Moghadam, P. Z.; Wheatley, A.; Fairen-Jimenez, D. Tuning Porosity in Macroscopic Monolithic Metal Organic Frameworks for Exceptional Natural Gas Storage. *Nat. Commun.* **2019**, *10*, 2345, (1–11).

References

[190] Wieme, J.; Vandenbrande, S.; Lamaire, A.; Kapil, V.; Vanduyfhuys, L.; Van Spey-broeck, V. Thermal Engineering of Metal–Organic Frameworks for Adsorption Applications: A Molecular Simulation Perspective. *ACS Appl. Mater. Interfaces* **2019**, *11*, 38697–38707.

[191] Hydration of Acetic Acid and Acetate Ion in Water Studied by 1D-RISM Theory. *J. Mol. Liq.* **2011**, *164*, 201–206.

[192] Hajari, T.; Van Der Vegt, N. F. Solvation thermodynamics of amino acid side chains on a short peptide backbone. *Journal of Chemical Physics* **2015**, *142*.

[193] Bruce, J. P.; Zhang, K.; Balasubramani, S. G.; Haines, A. R.; Galhenage, R. P.; Voora, V. K.; Furche, F.; Hemminger, J. C. Exploring the Solvation of Acetic Acid in Water Using Liquid Jet X-ray Photoelectron Spectroscopy and Core Level Electron Binding Energy Calculations. *J. Phys. Chem. B* **2021**, *125*, 8862–8868.

[194] Alkyl Ether Carboxylate Surfactants for Chemically Enhanced Oil Recovery in Harsh Field Conditions. *SPE Asia Pacific Enhanced Oil Recovery Conference, EORC 2015* **2015**, 288–298.

[195] Novel Large-Hydrophobe Alkoxy Carboxylate Surfactants for Enhanced Oil Recovery. *SPE J.* **2014**, *19*, 1024–1034.

[196] Roy, S.; Mondal, J. A. Kosmotropic Electrolyte (Na_2CO_3 , NaF) Perturbs the Air/Water Interface through Anion Hydration Shell without Forming a Well-Defined Electric Double Layer. *J. Phys. Chem. B* **2021**, *125*, 3977–3985.

[197] Adams, E. M.; Wellen, B. A.; Thiraux, R.; Reddy, S. K.; Vidalis, A. S.; Paesani, F.; Allen, H. C. Sodium-Carboxylate Contact Ion Pair Formation Induces Stabilization of Palmitic Acid Monolayers at High pH. *Phys. Chem. Chem. Phys.* **2017**, *19*, 10481–10490.

[198] Tyrode, E.; Corkery, R. Charging of Carboxylic Acid Monolayers with Monovalent Ions at Low Ionic Strengths: Molecular Insight Revealed by Vibrational Sum Frequency Spectroscopy. *J. Phys. Chem. C* **2018**, *122*, 28775–28786.

[199] The protonation state of small carboxylic acids at the water surface from photoelectron spectroscopy. *Phys. Chem. Chem. Phys.* **2011**, *13*, 12261–12267.

[200] Minofar, B.; Vácha, R.; Wahab, A.; Mahiuddin, S.; Kunz, W.; Jungwirth, P. Propensity for the Air/Water Interface and Ion Pairing in Magnesium Acetate vs Magnesium Nitrate Solutions: Molecular Dynamics Simulations and Surface Tension Measurements. *J. Phys. Chem. B* **2006**, *110*, 15939–15944.

[201] Minofar, B.; Jungwirth, P.; Das, M. R.; Kunz, W.; Mahiuddin, S. Propensity of formate, acetate, benzoate, and phenolate for the aqueous solution/vapor interface: Surface tension measurements and molecular dynamics simulations. *Journal of Physical Chemistry C* **2007**, *111*, 8242–8247.

[202] Cabaniss, S. E.; McVey, I. F. Aqueous infrared carboxylate absorbances: aliphatic monocarboxylates. *Spectrochimica Acta Part A: Molecular and Biomolecular Spectroscopy* **1995**, *51*, 2385–2395.

[203] Nicholas, N. J.; Franks, G. V.; Ducker, W. A. Selective adsorption to particular crystal faces of ZnO. *Langmuir* **2012**, *28*, 7189–7196.

[204] Hosseinpour, S.; Johnson, C. M.; Leygraf, C. Alkanethiols as Inhibitors for the Atmospheric Corrosion of Copper Induced by Formic Acid: Effect of Chain Length. *J. Electrochem. Soc.* **2013**, *160*, C270–C276.

[205] Nihonyanagi, S.; Yamaguchi, S.; Tahara, T. Direct evidence for orientational flip-flop of water molecules at charged interfaces: A heterodyne-detected vibrational sum frequency generation study. *Journal of Chemical Physics* **2009**, *130*.

[206] Strazdaite, S.; Meister, K.; Bakker, H. J. Orientation of Polar Molecules Near Charged Protein Interfaces. *Phys. Chem. Chem. Phys.* **2016**, *18*, 7414–7418.

[207] Krief, A.; Kremer, A. Synthesis of Alkali Metal Carboxylates and Carboxylic Acids Using "Wet" and "Anhydrous" Alkali Metal Hydroxides. *Chem. Rev.* **2010**, *110*, 4772–4819.

[208] Vandenborre, J.; Truche, L.; Costagliola, A.; Craff, E.; Blain, G.; Baty, V.; Haddad, F.; Fattahi, M. Carboxylate Anion Generation in Aqueous Solution from Carbonate Radiolysis, a Potential Route for Abiotic Organic Acid Synthesis on Earth and beyond. *Earth Planet. Sci. Lett.* **2021**, *564*, 116892.

[209] Wellen, B. A.; Lach, E. A.; Allen, H. C. Surface pKa of Octanoic, Nonanoic, and Decanoic Fatty Acids at the Air–Water Interface: Applications to Atmospheric Aerosol Chemistry. *Phys. Chem. Chem. Phys.* **2017**, *19*, 26551–26558.

[210] Foster, M. J.; Carpenter, A. P.; Richmond, G. L. Dynamic Duo: Vibrational Sum Frequency Scattering Investigation of pH-Switchable Carboxylic Acid/Carboxylate Surfactants on Nanodroplet Surfaces. *J. Phys. Chem. B* **2021**, *125*, 9629–9640.

[211] Achtyl, J.; Buchbinder, A.; Geiger, F. Hydrocarbon on Carbon: Coherent Vibrational Spectroscopy of Toluene on Graphite. *J. Phys. Chem. Lett.* **2012**, *3*, 280–282.

[212] AlSalem, H. S.; Holroyd, C.; Danial Iswan, M.; Horn, A. B.; Denecke, M. A.; Koehler, S. P. K. Characterisation, Coverage, and Orientation of Functionalised Graphene Using Sum-Frequency Generation Spectroscopy. *Phys. Chem. Chem. Phys.* **2018**, *20*, 8962–8967.

[213] von Domaros, M.; Liu, Y.; Butman, J. L.; Perlt, E.; Geiger, F. M.; Tobias, D. J. Molecular Orientation at the Squalene/Air Interface from Sum Frequency Generation Spectroscopy and Atomistic Modeling. *J. Phys. Chem. B* **2021**, *125*, 3932–3941.

[214] Dreesen, L.; Sartenaer, Y.; Peremans, A.; Thiry, P.; Humbert, C.; Grugier, J.; Marchand-Brynaert, J. Synthesis and Characterization of Aromatic Self-Assembled Monolayers Containing Methylene and Ethyleneglycol Entities by Means of Sum-Frequency Generation Spectroscopy. *Thin Solid Films* **2006**, *500*, 268–277.

References

[215] Braunschweig, B.; Mukherjee, P.; Kutz, R. B.; Wieckowski, A.; Dlott, D. D. Sum-frequency Generation of Acetate adsorption on Au and Pt Surfaces: Molecular Structure Effects. *J. Chem. Phys.* **2010**, *133*, 1–8.

[216] Dutta, C.; Mammetkuliyev, M.; Benderskii, A. V. Reorientation of Water Molecules in Response to Surface Charge at Surfactant Interfaces. *J. Chem. Phys.* **2019**, *151*.

[217] Gan, W.; Wu, D.; Zhang, Z.; Feng, R.-r.; Wang, H.-f. Polarization and Experimental Configuration Analyses of Sum Frequency Generation Vibrational Spectra, Structure, and Orientational Motion of the Air/Water Interface. *J. Chem. Phys.* **2006**, *124*, 114705.

[218] Wang, J.; Chen, C.; Buck, S. M.; Chen, Z. Molecular Chemical Structure on Poly(methyl methacrylate) (PMMA) Surface Studied by Sum Frequency Generation (SFG) Vibrational Spectroscopy. *J. Phys. Chem. B* **2001**, *105*, 12118–12125.

[219] Hosseinpour, S.; Roeters, S. J.; Bonn, M.; Peukert, W.; Woutersen, S.; Weidner, T. Structure and Dynamics of Interfacial Peptides and Proteins from Vibrational Sum-Frequency Generation Spectroscopy. *Chem. Rev.* **2020**, *120*, 3420–3465.

[220] Rao, Y.; Comstock, M.; Eisenthal, K. B. Absolute Orientation of Molecules at Interfaces. *J. Phys. Chem. B* **2006**, *110*, 1727–1732.

[221] Santos, C. S.; Baldelli, S. Surface Orientation of 1-Methyl-, 1-Ethyl-, and 1-Butyl-3-methylimidazolium Methyl Sulfate as Probed by Sum-Frequency Generation Vibrational Spectroscopy. *J. Phys. Chem. B* **2007**, *111*, 4715–4723.

[222] Moll, C. J.; Versluis, J.; Bakker, H. J. Direct Observation of the Orientation of Urea Molecules at Charged Interfaces. *J. Phys. Chem. Lett.* **2021**, *12*, 10823–10828.

[223] Goussous, S. A.; Casford, M. T.; Johnson, S. A.; Davies, P. B. A Structural and Temporal Study of the Surfactants Behenyltrimethylammonium Methosulfate and Behenyltrimethylammonium Chloride Adsorbed at Air/Water and Air/Glass Interfaces Using Sum Frequency Generation spectroscopy. *J. Colloid Interface Sci.* **2017**, *488*, 365–372.

[224] Moll, C. J.; Versluis, J.; Bakker, H. J. Bulk Response of Carboxylic Acid Solutions Observed with Surface Sum-Frequency Generation Spectroscopy. *J. Phys. Chem. B* **2022**, *126*, 270–277.

[225] Spinner, E.; Yang, P.; Wong, P.; Mantsch, H. The Vibrational-Spectrum of Sodium Propionate $CH_3CH_3CO_3Na$, $CH_3CD_3CO_3Na$, $CD_3CH_3CO_3Na$ and $CD_3CD_3CO_3Na$ in Aqueous-Solution and in the Solid-State. *Aust. J. Chem.* **1986**, *39*, 475–486.

[226] Dunn, G. E.; McDonald, R. S. Infrared Spectra of Aqueous Sodium Benzoates and Salicylates in the Carboxyl-Stretching Region: Chelation in Aqueous Sodium Salicylates. *Can. J. Chem.* **1969**, *47*, 4577–4588.

[227] Tang, C. Y.; Allen, H. C. Ionic Binding of Na+ versus K+ to the Carboxylic Acid Headgroup of Palmitic Acid Monolayers Studied by Vibrational Sum Frequency Generation Spectroscopy. *J. Phys. Chem. A* **2009**, *113*, 7383–7393.

[228] Lu, Z.; Karakoti, A.; Velarde, L.; Wang, W.; Yang, P.; Thevuthasan, S.; Wang, H.-f. Dissociative Binding of Carboxylic Acid Ligand on Nanoceria Surface in Aqueous Solution: A Joint In Situ Spectroscopic Characterization and First-Principles Study. *J. Phys. Chem. C* **2013**, *117*, 24329–24338.

[229] Simpson, G. J.; Rowlen, K. L. An SHG Magic Angle: Dependence of Second Harmonic Generation Orientation Measurements on the Width of the Orientation Distribution. *J. Am. Chem. Soc.* **1999**, *121*, 2635–2636.

[230] Yamaguchi, S.; Hosoi, H.; Yamashita, M.; Sen, P.; Tahara, T. Physisorption Gives Narrower Orientational Distribution Than Chemisorption on a Glass Surface: a Polarization-Sensitive Linear and Nonlinear Optical Study. *J. Phys. Chem. Lett.* **2010**, *1*, 2662–2665.

[231] Hirose, C.; Akamatsu, N.; Domen, K. Formulas for the Analysis of Surface Sum-Frequency Generation Spectrum by CH Stretching Modes of Methyl and Methylene Groups. *J. Chem. Phys.* **1992**, *96*, 997–1004.

[232] Bagheri, M.; Kiani, F.; Koohyar, F.; Khang, N. T.; Zabihi, F. Measurement of refractive index and viscosity for aqueous solution of sodium acetate, sodium carbonate, trisodium citrate, (glycerol + sodium acetate), (glycerol + sodium carbonate), and (glycerol + trisodium citrate) at T = 293.15 to 303.15 K and atmospheric pressure. *J. Mol. Liq.* **2020**, *309*, 113109.

Summary

Tracking Water Molecules and Carboxylate Ions in Confinement Using Advanced Vibrational Spectroscopy

In this thesis we describe studies of water molecules and carboxylate anions in different types of confinement using linear infrared absorption spectroscopy, femtosecond polarization resolved infrared pump-probe and two-dimensional infrared spectroscopies, as well as heterodyne-detected vibrational sum-frequency generation spectroscopy. In **Chapters 2** and **3** we describe the necessary theoretical background and experimental setups used in the studies.

In **Chapter 4** we study ultrafast dynamics of water molecules in binary mixtures with 2,6-lutidine near lower solution transition temperatures. Due to the formation of strong hydrogen bonds between water molecules and the solute and hydrophobic hydration of the solute, increasing the solute fraction leads to increasing heterogeneity of the hydrogen bond network and deceleration of the reorientational dynamics of the increasing fraction of water molecules. A smaller fraction of water molecules gets enclosed in clusters by the solute molecules. Decreasing the system temperature leads to a decrease of the size of the clusters, thereby increasing the overall hydrophobic surface exposed to water. The decrease of the transition temperature before the critical point is due to domination of the entropic effect of hydrophobic hydration. The increase of the transition temperature after the critical point is due to domination of the enthalpic effect of water-solute hydrogen bonding.

In **Chapter 5** we study ultrafast dynamics of aqueous acetate and terephthalate ions. We find that the interaction of the symmetric (ν_s) and the antisymmetric (ν_{as}) vibrations of the carboxylate anion groups of these ions involves anharmonic coupling and energy transfer. Both vibrational relaxation and energy transfer are faster in the terephthalate than in acetate likely due to a denser manifold of accepting vibrational combination states of the former and solvation effects. We use the obtained results in **Chapter 6** to study vibrational interactions in terephthalate linkers of UiO-66 membranes that we grow on flat c-sapphire substrates. Compared to terephthalate ions in aqueous solution, the cross-sections of the ν_s carboxylate stretch vibration and the ν_{Ph} are strongly enhanced, as a result of the interaction with the Zr^{4+} ions. The ν_s and ν_{as} vibrations of the carboxylate group, as well as the ν_s and the ν_{Ph} vibrational modes show strong vibrational coupling. The ν_{as} and ν_{Ph} modes show a significantly weaker interaction. The ν_s and ν_{as} vibrations show an ultrafast energy exchange and thus relax together with the

same effective vibrational relaxation time constant of ~ 1.3 ps. The absorption of the ν_{Ph} band shows a slower intrinsic vibrational relaxation with a time constant of ~ 6.7 ps. The ν_s and ν_{Ph} modes are observed to be anharmonically coupled and to show energy exchange, with an uphill energy transfer time constant of ~ 6.9 ps. The measured transient absorption signals show a significant non-zero signal at long delay times that is attributed to a hot state resulting from the vibrational relaxation. The ν_{as} show Förster energy exchange with a time constant of ~ 1 ps, which is explained from the close proximity of the carboxylate groups of differently oriented terephthalate linkers.

In **Chapter 7** we study the surface adsorption and orientation of formate and acetate ions at the water-air interface. Both ions have a net orientation with their carboxylate group pointing toward the bulk. The c-axis of these ions is at a nonzero angle with respect to the surface normal and this angle is smaller for acetate than for formate. Even at high bulk concentrations, the surface is not getting saturated with carboxylate ions, and for both ions there is no significant change of the orientation angle when the concentration increases. At high carboxylate concentrations the presence of ions at the surface significantly changes the Fresnel factor of the infrared beam that in turn modifies the lineshapes of the vibrational bands in the spectra. Further, in **Chapter 8** we investigate the orientational properties of carboxylate ions. We compare ions with different substituents: formate, acetate, propionate, hexanoate, octanoate, benzoate and 2-naphthoate. We find that increasing the size of the hydrophobic part of the ion leads to a decrease of the average tilt angle of the carboxylate group of the ions. Finally, we obtain $(\beta_{aac} + \beta_{bbc})/\beta_{ccc}$ and β_{aca}/β_{ccc} ratios for the carboxylate group. The $(\beta_{aac} + \beta_{bbc})/\beta_{ccc} \approx 2$ for aliphatic ions. For the benzoate ion we find $(\beta_{aac} + \beta_{bbc})/\beta_{ccc} \sim 0.5$. This difference can probably be explained from the interaction of the π-electrons of the carboxylate group with the π-electrons of the highly polarizable aromatic ring. For formate, we get a ratio β_{aca}/β_{ccc} of ~ 2 which is larger than the ratio of ~ 1.2 obtained for the other aliphatic ions and the ratio of ~ 0.7 obtained for the benzoate ion.

The obtained results contain valuable information on the structure and ultrafast dynamics of abundant chemical species in confined environments. We believe that it stimulates further progress in related research and technology areas.

Samenvatting

Het volgen van watermoleculen en carboxylaationen in inperking met behulp van geavanceerde vibratiespectroscopie

In dit proefschrift beschrijven we de studies naar watermoleculen en carboxylaationen in verschillende types inperking, met behulp van lineaire infrarood absorptie spectroscopie, femtoseconde polarisatie opgeloste infrarood pomp-probe spectroscopie en tweedimensionale infraroodspectroscopie, alsook heterodyne gedetecteerde vibrationele somfrequentie generatie spectroscopie. In **Hoofdstuk 2** en **3** beschrijven we de nodige theoretische achtergrond en experimentele opstellingen gebruikt in deze studies.

In **Hoofdstuk 4** bestuderen we ultrasnelle dynamica van watermoleculen in binaire mengsels met 2,6-lutidine nabij onderste oplossing overgangstemperaturen. Door de vorming van sterke waterstofbruggen tussen watermoleculen en de opgeloste stof, en door hydrofobe hydratatie van de opgeloste stof, zorgt het verhogen van de opgeloste stof fractie voor een verhoogde heterogeniteit van het waterstofbrugnetwerk en een vertraging van de reoriëntatiedynamica van de toegenomen fractie watermoleculen. Een kleine fractie watermoleculen wordt ingesloten in clusters door de opgeloste moleculen. Het verlagen van de temperatuur van het systeem leidt tot een toename in de grootte van de clusters, en verhoogt daarbij het algehele hydrofobe oppervlak dat aan water blootgesteld wordt. De afname van de overgangstemperatuur voor het kritisch punt komt door de overheersing van het entropisch effect van hydrofobe hydratatie. De toename van de overgangstemperatuur na het kritisch punt komt door de overheersing van het enthalpisch effect van water-lutidine waterstofbruggen.

In **Hoofdstuk 5** bestuderen we de ultrasnelle dynamica van waterige oplossingen van acetaat- en tereftalaationen. We vinden dat bij de interactie van de symmetrische (ν_s) en de antisymmetrische (ν_{as}) vibraties van de carboxylaatanion groepen van deze ionen anharmonische koppeling en energieoverdracht betrokken zijn. Zowel vibrationele relaxatie als energieoverdracht zijn sneller in tereftalaat dan in acetaat, hoogstwaarschijnlijk door een dichtere variëteit van accepterende vibrationele combinatietoestanden van de eerste, en solvatatie effecten. We gebruiken de verkregen resultaten in **Hoofdstuk 6** voor het bestuderen van de vibrationele interacties in tereftalaat linkers van UiO-66 membranen die we groeien op vlakke c-saffier substraten. Vergeleken met tereftalaationen in waterige oplossing zijn de absorptie dwarsdoorsnede van de ν_s carboxylaat strekvibratie en de ν_{Ph} sterk vergroot, als resultaat van de interactie met de Zr^{4+} ionen. De ν_s en ν_{as}

vibraties van de carboxylaatgroep, alsook de ν_s en de ν_{Ph} vibraties vertonen sterke vibrationele koppeling. De ν_{as} en ν_{Ph} vibraties vertonen een significant zwakkere interactie. De ν_s en ν_{as} vibraties vertonen een ultrasnelle energie-uitwisseling en relaxeren dus samen met dezelfde effectieve vibrationele relaxatietijdsconstante van   1.3 ps. De absorptie van de ν_{Ph} piek vertoont een langzamere intrinsieke vibrationele relaxatie met een tijdsconstante van ~ 6.7 ps. We observeren dat de ν_s en ν_{Ph} modi anharmonisch gekoppeld zijn en een langzame energie-uitwisseling vertonen, met een heuvelopwaarts energie-overdrachtstijdsconstante van ~ 6.9 ps. De gemeten transient absorptie signalen vertonen een significant niet-nul signaal bij lange wachttijden, die is toegewezen aan een 'hot state' resulterend van de vibrationele relaxatie. De ν_{as} vertoont Förster energie-uitwisseling met een tijdsconstante van 1 ps, die verklaard is door de nabijheid van de carboxylaatgroepen van verschillend georiënteerde tereftalaat linkers.

In **Hoofdstuk 7** bestuderen we de oppervlakte adsorptie en oriëntatie van formiaat- en acetaationen aan het water-lucht grensvlak. Beide ionen hebben een netto oriëntatie waarbij hun carboxylaatgroep naar de bulk wijst. De c-as van deze ionen heeft een niet-nul hoek ten opzichte van de oppervlakte normaal, en deze hoek is kleiner voor acetaat dan voor formiaat. Zelfs bij hoge bulkconcentraties wordt het oppervlak niet verzadigd met carboxylaationen, en voor beide ionen is er geen significante verandering van de oriëntatie hoek bij het verhogen van de concentratie. Bij hoge carboxylaat concentraties verandert de aanwezigheid van ionen aan het oppervlak de Fresnel factor van de infrarood bundel significant. Dit beïnvloedt de vorm van de vibrationele banden in de spectra. Verder onderzoeken we in **Hoofdstuk 8** de oriëntatie eigenschappen van carboxylaationen. We vergelijken ionen met verschillende substituenten: formiaat, acetaat, propionaat, hexanoaat, octanoaat, benzoaat en 2-naftoaat. We vinden dat het vergroten van het hydrofobe deel van het ion leidt tot een afname van de gemiddelde kantelhoek van de carboxylaatgroep van de ionen. Ten slotte verkrijgen we $(\beta_{aac} + \beta_{bbc})/\beta_{ccc}$ en β_{aca}/β_{ccc} verhoudingen voor de carboxylaatgroep. De $(\beta_{aac} + \beta_{bbc})/\beta_{ccc} \approx$ 2 voor alifatische ionen. Voor het benzoaat ion vinden we $(\beta_{aac} + \beta_{bbc})/\beta_{ccc} \sim$ 0.5. Dit verschil kan waarschijnlijk verklaard worden door de interactie van de p-elektronen van de carboxylaatgroep met de p-elektronen van de hoog polariseerbare aromatische ring. Voor formiaat vinden we een verhouding $\beta_{bbc})/\beta_{ccc}$ van $\sim$ 2 water groter is dan de verhouding van ~ 1.2 verkregen voor de andere alifatische ionen en de verhouding van ~ 0.7 is verkregen voor het benzoaation.

De behaalde resultaten bevatten waardevolle informatie over de structuur en ultrasnelle dynamica van veelvoorkomende chemische verbindingen in ingeperkte omgevingen. Wij geloven dat het verdere vooruitgang in gerelateerde onderzoeks- en technologie velden stimuleert.

Acknowledgements

When the last light warms the rocks and the rattlesnakes unfold, I would like to express my gratitude to people without whom this thesis would not exist. I am very thrilled to write this part which is sometimes referred to as the most read and understood part of any PhD thesis. Hopefully, my passion for using different languages will not make it too confusing.

Allereerst wil ik graag mijn promotor, Huib, bedanken. Ik ben dankbaar voor de mogelijkheid die je mij geboden hebt om bij AMOLF te werken en voor het delen van jouw uitgebreide ervaring en expertise, zowel in de wetenschap als in de algemene werking van de academische wereld. Ik waardeer jouw constante kalmte in situaties die mij nerveus maakten en jouw aandacht voor dringende zaken die invloed hadden op mijn leven. Door onze samenwerking heb ik een dieper begrip gekregen van de uitdagingen bij het succesvol managen van grote organisaties

I would like to thank Stefania for our successful collaboration on the UiO-66 project and becoming my co-promotor. Thank you for being responsive and supportive especially in urgent situations.

Пан Александр, этот тезис вряд ли бы случился без тебя, не хватит никаких слов, чтобы выразить тебе мою благодарность. Сейчас кажется абсолютно ключевым моментом то, что я сразу начал работать именно с тобой. За эти больше чем 4 года мы стали соавторами статьи и песен, мы сделали тысячу вещей вместе, как на работе так и вне её, и ты стал большой частью моей жизни. Надеюсь, что сделаем ещё больше, ведь сорок третья впереди. Дякую за все і особливо за твою силу, спокій та впевненість у будь-яких ситуаціях. Слава тобі та слава Україні! Olivier, you were a pillar of synthetic chemistry in our lasting collaboration on UiO-66 project and always spread positive vibes combined with deep knowledge of your subject, you helped me a lot, thank you for that. Sanghamitra, thank you very much for your contribution to finishing the UiO-66 project and for your constant support inside and outside of work. Your (sometimes overwhelming) optimistic vibes will always stay with me, I value a lot the time we spent together!

The first person I met after moving to Amsterdam happened to be my group member. Carolyn, who could have known that there would be so much to share after that moment! Thank you very much for our collaboration at work, the times were desperate after a year of pandemic and it was so important that you made a couple of measurements which eventually also turned me into a SFG-person and yielded into two articles and chapters of this thesis. Thank you very much for being a good friend, for many handcrafted gifts, for outstanding cooking and baking and eventually becoming my paranymph. I would not make it without you!

The happiness is like that cookie that is waiting for you around the corner. Ik wil graag onze lasertovenaar Jan bedanken. Ik wil nogmaals benadrukken dat jouw bijdrage onmisbaar is voor ons onderzoek. Jouw expertise en hulp met lasers zijn van onschatbare waarde en zonder jou zou het onmogelijk zijn geweest om verder te komen. Ik ben zeer dankbaar voor onze samenwerking en voor het delen van je kennis over SFG. En tot slot wil ik je ook bedanken voor onze vriendschap en de vele interessante gesprekken die we buiten het werk hebben gehad. Laura, thank you very much for making the fantastic cover art for the article on carboxylates at water-air interface, I really enjoyed our collaboration!

Hinco, met jou aan onze zijde leek geen enkel probleem onoplosbaar en je hulp is werkelijk onmisbaar. Ik wil je bedanken voor je onvoorwaardelijke steun bij alle technische uitdagingen, je geduld en het verspreiden van positieve vibes. En last but not least, wil ik je ook bedanken voor de vele gezellige chats in het Nederlands en de fantastische feestjes op de boot die jij en Lianne organiseerden. Dank jullie wel voor alle leuke momenten en herinneringen. Ik wil graag Niels en Dion bedanken voor jullie altijd beschikbare hulp wanneer Hinco niet aanwezig was. Mark en Bob, heel erg bedankt voor jullie hulp bij de chemicaliën en profilometrische metingen. Daarnaast wil ik graag alle technische afdelingen van AMOLF bedanken: Software, Electronics, Mechanical Engineering, Precision Manufacturing en ICT. Zonder jullie onmisbare steun zou ons onderzoek niet eens mogelijk zijn geweest. Vooral ben ik Ricardo Struik, Niels Winkelaar en Ivo Klinkert verschuldigd voor hun hulp in verschillende projecten. Teressa, bedankt voor je uitstekende werk als secretaresse. Sofija, thank you for being an excellent secretary as well, and for sharing many moments at AMOLF and outside. Срећно теби! Oana, dank je wel voor veel hulp met publicatieregels.

Mama Giulia, grazie mille for your care and support when I was making my first steps with Karmijn and thank you for going together through all the doom and gloom of research-in-pandemic times. It's a pitty we could not work together more extensively at the time. Your persistence combined with your chilled and direct demeanour are always an inspiration for me. Alexandra, thank you very much for being a good friend and the office mate, I am very happy I met you. Ευχαριστώ for many meetings at different places and conversations, and especially for the trip to Greece. I appreciate very much your sarcastic and kind personality and attempts to learn Russian language and sharing the passion to Russian music. Wish you all the best in all your endeavours! Roberto, thank you for your optimism, for your help and being an example and sometimes even a mentor in my future career steps. I am especially grateful to you for providing the template for this thesis, you can see that it is rendered in the very likeness of yours. I am very happy I could be a part of the events you organize together with Katya. Thank you both for that! Eliane, ik wil je graag bedanken voor het vertalen van de samenvatting van mijn proefschrift naar het Nederlands. Ik waardeer het echt enorm dat je altijd bereid was om te helpen en je ervaring te delen. Daarnaast wil ik je bedanken voor de

vele gekke headbang-momenten die we samen hebben gehad en voor jouw fijne en rustige persoonlijkheid. Balázs, we shared the office with you for 3.5 years. I want to thank you for that, for making the 'submission button' and for many discussions we had about chemistry, physics and life in general. I wish you luck with the rest of your PhD, szemüveget a bírónak, this guy is so good at never giving up, keep going! Gökçen, I would like to thank you for many chats about 2D-IR, music, and peculiarities of academic life. Ash and Hanna I am so happy you joined the group when I was going through the finishing phase of my PhD. You really helped me to go through by becoming my soulmates, thank you for that. Ash, I wish you luck with your PhD journey, don't forget that you are doing very good. Hanna, I wish you luck with your PhD as well, you are a great researcher i naprawdę bardzo wyjątkową osobą! Kris, thank you very much for bringing your creative vibes to the group, thank you for our discussions, I wish you luck with your further endeavours in science and art and especially in learning Dutch!

I also want to thank all the other nice people who made my time at AMOLF unforgettable: Rahul, Aditi, Fabian, Fotis, René, Andrea, Magda, Giorgio, Agustin, Lukas, Marloes, Iarik, Nebojsa, Nika, Evelijn, Matthias, Mees, Mels, Wessel - good luck to you all!

Елизавета, трудно представить Амстердам без тебя, спасибо, что согласилась стать моим паранимфом. Мы прошли через многое совместно, спасибо, что умеешь слушать и поддерживать, за твою прямоту и честность. Желаю тебе удачи как с твоим PhD, так и после, пусть всё получится. Аня, именно вместе с тобой мы послали мою заявку на позицию в AMOLF, и вот как всё повернулось. Спасибо, что с тобой иногда можно разделить hate и всегда можно выпить кофе, за глубокое понимание моего взгляда на некоторые аспекты жизни и за сладкие посылки из Германии. Пусть жизнь приносит удовольствие. Валентин Иванович, спасибо за то, что делились опытом и мудростью, вы сыграли важную роль в том, чтобы я тут вообще оказался. Кристина, я благодарен тебе за твое тепло, свет и красоту, и особенно за арт-ретрит, я желаю тебе сохранять и поддерживать это. Я многому от тебя научился, спасибо что была со мной на этом сложном пути. Катя, мне очень повезло, что мы встретились с тобой в нашей огранизации, в которой самое главное - это людишки. Спасибо за то, что всегда была хорошим другом, спасибо, что всегда была готова делиться опытом и помогать, я желаю тебе счастья. Николай, я очень рад тому, что нам довелось встретиться, хоть это и произошло в самом конце моего PhD-путешествия. Спасибо за любовь к длинным важным разговорам обо всём, я желаю тебе успехов и стойкости в нашей суровой реальности. Виктор, браток, спасибо за то, что был рядом на протяжении всего пути, твой подход к жизни вызывает моё ува(о)жение, а наши изысканные коллаборации в области искусства всегда будут греть моё сердце. Стайн, спасибо за совместное участие в музыкальных проектах, а так же за taaluitwisseling evenement, верю, что ты можешь прочитать и понять этот текст, и это

очень круто!

Хочу выразить глубокую благодарность сотрудникам и преподавателям Московского Государственного Университета, в особенности, Ю. В. Новаковской, Д. Н. Лайкову, Н. А. Чумаковой, Е. Н. Голубевой, А. Х. Воробьёву, А. В. Богданову, О. И. Громову, В. Ю. Траскину, В. Н. Нуриеву, В. П. Дядченко, А. А. Михалёву, Т. В. Родченко. Мне очень повезло, что я учился у Вас! Спасибо за Вашу работу!

В завершение хочу поблагодарить свою семью. Женя, Миша, Лиза, и Костя, спасибо за вашу поддержку и что были рядом, пусть и, в основном, онлайн. Мама и Валя, вы - опора, я бы не справился без вас, вы всегда со мной. Мама, от всего сердца спасибо, за поддержку и принятие, что бы ни происходило, за желание быть рядом, и за твою любовь.

<div align="center">Занавес?</div>